# Design and development of a spectrograph and polarimeter for the analysis of air plasmas produced by transient luminous events in the mesosphere of the Earth



**Universidad de Granada**

María Passas Varo

Department of Solar System

Instituto de Astrofísica de Andalucía

Programa de Doctorado en Física y Ciencias del Espacio

A thesis submitted for the degree of

*PhilosophiæDoctor (PhD)*

June 2017

Examination date: June 19, 2017

Thesis supervisors:

Dr. D. Francisco J. Gordillo Vázquez       Dr. D. Alejandro Luque Estepa

1. Reviewer:

2. Reviewer: Day of the defense: June 19, 2017

Signature from the head of the PhD committee:

# Abstract

In this work of thesis we describe the design, development and characterization of a new diagnosis instrument intended to perform systematic campaigns of simultaneous measurement of the spectrum and polarization degree of the light emitted by transient luminous events (TLEs) as a ground support to space missions ASIM (ESA) and TARANIS (CNES) to be launched by early and late 2018, respectively.

The GRASSP instrument (GRAnada Sprite Spectrograph and Polarimeter) includes the first medium–high spectrograph specifically designed for the analysis of air plasmas generated by TLEs. All versions of GRASSP have been developed and characterized by our group at the Institute of Astrophysics of Andalusia (IAA, Granada, Spain) and the Institute of Matter Structure (IEM, Madrid, Spain) laboratories, both dependencies of the National Research Council of Spain (CSIC).

We have developed four different versions of GRASSP to date. We installed the first (2012 – 2014) and second (2014 – 2015) versions of GRASSP at the Spanish–German Astronomic Center (CAHA) in Calar Alto, Almería, Spain. Both worked in an autonomous way, without the support of an operator. Every sunset, the system powered on automatically, took the calibration images, opened the blinds of the system and aimed the spectrograph to the region of the sky where a TLE was more probable to appear. This could be done thanks to an aiming algorithm

we developed that queried the databases of the Spanish Weather Agency (AEMET) in real-time and calculated the coordinates of the closest storm. When the system detected a change of the brightness level in the sky, an audio trigger system launched the simultaneous recording of both field image and spectral image to store them in a data repository. This way we could discern the origin of the recorded spectra. Every sunrise, after the observation night, the algorithm closed blinds and switched off all the GRASSP subsystems. From this location we obtained the first TLE images recorded with GRASSP, we recorded several spectra from lightning optical emissions dispersed on clouds and we had the chance of recording a meteoroid spectrum while it passed in front of GRASSP. Unfortunately, from this location we did not record any TLE spectra because of the remoteness of the storms, that occur most frequently in Spain in the Ebro Delta valley. Hence we decided to relocate our spectrograph in a new and compact version of GRASSP. We installed GRASSP versions three (2015 – 2016) and four (2016 – now) in Castellgalí, Barcelona, Spain. This last compact version is currently located within the stormiest region of north-eastern Spain, with a field of view of almost 360 degrees, and it is manually aimed by an experienced colleague (Oscar Van der Velde, from Polytechnic University of Catalonia). Since the installation of the third version of GRASSP we have recorded up to 44 medium–high resolution TLE spectra, that allowed us to quantify, for the first time, the (rotational) temperature of gas surrounding TLEs. It can be done through the spectral fitting of the recorded spectrum to synthetic spectrum that we have modelled, thanks to the high resolution of our spectrograph (0.235 nm) that allows us to fit the rovibrational bands of the nitrogen molecule. This way we can understand TLEs as natural probes of the air

temperature in the Earth mesosphere. It is the first time that systematic campaigns of spectroscopic measurements of TLEs with such high resolution have been developed (the best spectral resolution to date intended to sporadically analyze TLEs spectra is 3 nm), with the goal of feeding a database to statistically characterize the TLEs from a spectroscopic point of view in a near future.

The GRASSP polarimeter is currently in calibration stage within our laboratories. It is intended to be operative from summer 2017.

# Resumen

En esta tesis se describe de manera detallada el diseño y la caracterización de un nuevo instrumento de diagnosis destinado a realizar campañas sistemáticas de medida simultánea del espectro y de la polarización de la luz emitida por eventos luminosos transitorios (o TLEs, del inglés Transient Luminous Events) como apoyo terrestre a las misiones ASIM (ESA) y TARANIS (CNES) que serán lanzadas a comienzos y a finales de 2018, respectivamente.

El instrumento GRASSP (GRAnada Sprite Spectrograph and Polarimeter) incluye el primer espectrógrafo de media–alta resolución diseñado expresamente para el análisis de los plasmas de aire generados por TLEs. Todas las versiones del espectrógrafo se han construido y caracterizado por nuestro grupo en los laboratorios del Instituto de Astrofísica de Andalucía (IAA, Granada, España) y del Instituto de Estructura de la Materia (IEM, Madrid, España), ambas instalaciones del Consejo Superior de Investigaciones Científicas (CSIC).

Hasta la fecha hemos desarrollado cuatro versiones diferentes de GRASSP. Las dos primeras se instalaron en 2012 en el Centro Astronómico Hispano Alemán (CAHA) en Calar Alto, Almería, España. Ambas tenían la peculiaridad de trabajar en modo automático, sin operador. Cada ocaso, el sistema se ponía en marcha automáticamente, tomaba las imágenes de calibración en longitud de onda, abría las persianas y apuntaba el espectrógrafo
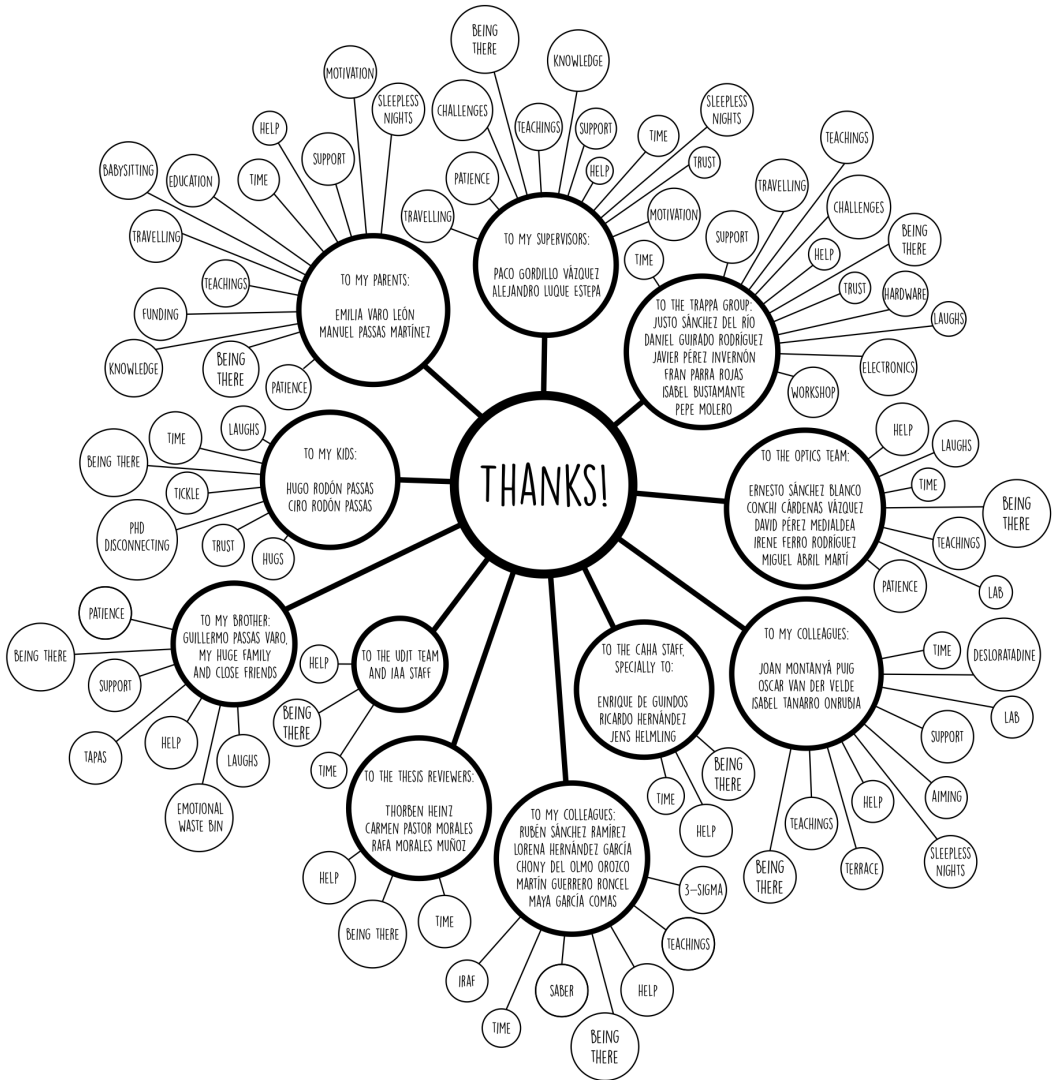
a la región del cielo donde era más probable que apareciera un TLE. Esto se conseguía con un algoritmo de apuntamiento desarrollado por nuestro grupo que, en tiempo real, consultaba las bases de datos de la Agencia Estatal de Meteorología (AEMET) y calculaba las coordenadas de la tormenta más cercana. Cuando se detectaba un cambio de brillo en la imagen de campo, un sistema de disparo por audio grababa simultáneamente tanto la imagen de campo como el espectro asociado, de manera que se podía discernir posteriormente el origen del espectro. Todos esos datos se almacenaban en un repositorio que era posteriormente analizado por un técnico. Cada orto, al finalizar la observación, el algoritmo cerraba las persianas y apagaba todos los subsistemas de GRASSP. Desde este emplazamiento obtuvimos las primeras imágenes de TLE tomadas con GRASSP, medimos el espectro de la luz emitida por rayos y dispersada por las nubes y tuvimos la suerte de registrar el espectro de un meteoroide que se cruzó en nuestro camino. Lamentablemente, desde esta ubicación no conseguimos capturar ningún espectro de TLE debido a la lejanía de las tormentas, que ocurren en España con mayor probabilidad en la región del Delta del Ebro. Por este motivo decidimos reubicar nuestro espectrógrafo, esta vez alojado en un nuevo instrumento más compacto. Las versiones tres y cuatro (actualmente funcionando) de GRASSP se instalaron en 2015 en Castellgalí (Barcelona, España) y a diferencia de las dos primeras, el modo de apuntamiento es ahora manual. Como ventaja tenemos la ubicación, en plena zona de tormentas del noreste español, una cobertura de casi 360° de azimuth (cuando antes contábamos con apenas 20°) y la experiencia del operador (Oscar Van der Velde, de la Universitat Politècnica de Catalunya). Desde la instalación de la tercera versión de GRASSP hemos registrado más de 44 espectros de

TLEs, que nos han servido para cuantificar por primera vez la temperatura (rotacional) del plasma de aire generado por los TLEs a través del ajuste del espectro medido con modelos de espectros sintéticos que hemos implementado y que gracias a la alta resolución espectral (0.235 nm) del espectrógrafo nos permite ajustar las bandas vibro–rotacionales de la molécula de nitrógeno. De esta manera podemos entender los TLEs como una sonda natural de la temperatura del aire en la mesosfera. Es la primera vez que se realizan medidas espectroscópicas de TLEs con una resolución tan alta (hasta la fecha la mejor resolución espectral usada para el análisis de espectros de TLEs era de 3 nm) y de una manera sistemática, lo que nos permitirá disponer de una estadística que caracterice los TLEs desde el punto de vista de la espectroscopía.

El polarímetro de GRASSP está aún en fase de calibración en nuestros laboratorios y se prevé que será instalado en el verano de 2017.

To my children

# Acknowledgements



THANKS!

TO MY SUPERVISORS:
PACO GORDILLO VÁZQUEZ
ALEJANDRO LUQUE ESTEPA

TO THE TRAPPA GROUP:
JUSTO SÁNCHEZ DEL RÍO
DANIEL GUIRADO RODRÍGUEZ
JAVIER PÉREZ INVERNÓN
FRAN PARRA ROJAS
ISABEL BUSTAMANTE
PEPE MOLERO

TO MY PARENTS:
EMILIA VARO LEÓN
MANUEL PASSAS MARTÍNEZ

TO MY KIDS:
HUGO RODÓN PASSAS
CIRO RODÓN PASSAS

TO THE OPTICS TEAM:
ERNESTO SÁNCHEZ BLANCO
CONCHI CÁRDENAS VÁZQUEZ
DAVID PÉREZ MEDIALDEA
IRENE FERRO RODRÍGUEZ
MIGUEL ABRIL MARTÍ

TO MY COLLEAGUES:
JOAN MONTANYÀ PUIG
OSCAR VAN DER VELDE
ISABEL TANARRO ONRUBIA

TO MY BROTHER:
GUILLERMO PASSAS VARO
MY HUGE FAMILY
AND CLOSE FRIENDS

TO THE UDIT TEAM
AND IAA STAFF

TO THE CAHA STAFF,
SPECIALLY TO:
ENRIQUE DE GUINDOS
RICARDO HERNÁNDEZ
JENS HELMLING

TO THE THESIS REVIEWERS:
THORBEN HEINZ
CARMEN PASTOR MORALES
RAFA MORALES MUÑOZ

TO MY COLLEAGUES:
RUBÉN SÁNCHEZ RAMÍREZ
LORENA HERNÁNDEZ GARCÍA
CHONY DEL OLMO OROZCO
MARTÍN GUERRERO RONCEL
MAYA GARCÍA COMAS

BEING THERE · MOTIVATION · SLEEPLESS NIGHTS · CHALLENGES · KNOWLEDGE · TEACHINGS · SUPPORT · HELP · TIME · TRUST · PATIENCE · TRAVELLING · BABYSITTING · EDUCATION · FUNDING · LAUGHS · HARDWARE · ELECTRONICS · WORKSHOP · AIMING · TICKLE · HUGS · PHD DISCONNECTING · TAPAS · EMOTIONAL WASTE BIN · DESLORATADINE · LAB · TERRACE · 3-SIGMA · SABER · IRAF

As the former diagram shows, this dissertation would not have been possible without the advice and support of many people.

In clockwise order, first and foremost, I would like to thank my supervisors Francisco Gordillo Vázquez and Alejandro Luque Estepa, for providing me the opportunity and guidance throughout this project: thank you for your time, your patience and for sharing your knowledge with me. Thank you to the TRAPPA group, specially to Justo Sánchez del Río and Daniel Guirado Rodríguez, the UDIT team, the IAA staff, the CAHA staff, Isabel Tanarro from the IEM, Joan Montanyá and Oscar Van der Velde from the UPC, and Ernesto Sánchez Blanco for your help and support these years.

Thank you to my close friends: Arantxa, Ángela, Paloma, Dikra, Alicia, Elena, Tere, María, Rosa, Susana and Ale, for calling me so often and for making me feeling we are so close. Thank you, girls (and boy) for your support, for your good advices and for being my emotional waste bin.

I would also want to give thanks to my huge family (it is huge indeed, I have 25 cousins) for always being there, for their support and for their trusting in me. Also thanks to my brother, Guille, for your unconditional support, for always trusting and challenging me. We will do great things together. Thank you for being so kind, thank you for your good conversation, thank you for opening my mind and thank you for your piano recitals. I love you, bro. Thank you, Hugo and Ciro, for being so patient. Now we are going to spend a lot of time together. I promise. Thank you for your laughs and for making me disconnect. Thank you for pushing me to play with you, to tickle you, to read books to you. Thank you for sharing your happiness with me, for your hugs, for trusting me and for being there. I love you, kids! And

last and not the least, I would specially want to give thanks to my parents: mom, dad, thank you for your help, support and motivation. Thank you for teaching me not to give up and thank you for sharing your knowledge with me. Thank you for believing in my projects and thank you for being there in the good and in the bad moments. Thank you for your time, for taking care of the kids and for taking care of me. Thank you very much for being so generous. Thank you for loving me so much. I am so lucky to have such wonderful parents. I love you!

*María*

# Contents

# List of Figures

# List of Tables

# Chapter 1

# Introduction

> *"Leaving the port of Kingston, Jamaica, at dusk on November 23, 1885, the night was fine and starlit overhead, but about 8 p.m. a heavy bank of cloud obscured the island, and all around the upper edges of this cloud-bank brilliant flashes of light were incessantly bursting forth, sometimes tinged with prismatic hues, while intermittently would shoot vertically upwards continuous darts of light displaying prismatic colours in which the complementary tints, crimson and green, orange and blue predominated. Sometimes these darts of light were projected but a short distance above the cloud-bank, but at others they ascended at considerable altitude, resembling rockets more than lightning. This state of matters continued until about 9.30 p.m., when all display of light ceased. As I have never seen such a phenomenon in any other part of the world, I have deemed it an unusual occurrence, and worthy of record."*
>
> – Tom Mackenzie, *Nature, January 14, 1886*

## 1.1   Transient Luminous Events

Charles Thomson Rees Wilson, a Scottish physicist and meteorologist who received the Nobel Prize in Physics in 1927, described —among other important achievements— the electric field of a thunderstorm and some of its

1

effects. In 1924 he predicted the upper atmosphere ionization due to the electric field of a thundercloud: *"If the field is strong enough to cause ionization by collision for any considerable distance below the original level of the conducting layer, it is possible that sudden discharge of the upper pole of the thundercloud to the upper atmosphere may occur."*, (*Wilson*, 1925).



**Figure 1.1:** Charles Thomson Rees Wilson (*Elsevier Publishing Company*, 1965)

Some clues from ground-based observations indicated that Wilson went in the right direction: *"...continuous darts of light ... ascended to a considerable altitude, resembling rockets more than lightning..."* (*Mackenzie and Toynbee*, 1886); *"... a luminous trail shot up to 15 degrees or so, about as fast as, or faster than, a rocket ..."*(*Everett*, 1903); *"...there were one or more very slender flashes of typical lightning forms from the cloud upwards..."*(*Boys*, 1926); *"...a long weak streamer of a reddish hue... some 50 kilometers high..."*(*Malan*, 1937); *"...flames appearing to rise from the top*

*of the cloud..."*(*Ashmore*, 1950); *"...diffuse, fan-shaped flashes of greenish color extending up into the clear sky..."*(*Wilson*, 1925).

These previous eyewitness reports, in addition to balloon observations of brief flashes over thunderstorms (*Vonnegut and Atkinson*, 1958) and 15 airplane pilots testimonies of high altitude electrical discharges from the top of the clouds to the ionosphere (*Vaughan Jr. and Vonnegut*, 1989) motivated Bernard Vonnegut and Otha H. Vaughan, from the State University of New York and the National Aeronautics and Space Administration (NASA) Marshall Space Flight Center (MSFC) respectively, to try to detect and record these optical emissions from a high altitude aircraft in several attempts; unfortunately, they had no success (*Vonnegut et al.*, 1989).



**Figure 1.2:** Bernard Vonnegut (*Keller*, 1977)

Concurrently, on 12th January, 1989, a group of scientists and researchers at the School of Physics and Astronomy of the University of Minnesota were operating the SKYFLASH Experiment to identify Rayleigh scattering of a horizontal beam passing over photometers directed at the zenith on clear nights near Minneapolis, such as distant lightning events. But they detected a phenomenon they were not expecting: John Randolph Winckler and his graduate student, Robert James Nemzek, identified, among pulses of known origin, some infrequent and unexplained subvisual-level transient luminous

**Figure 1.3:** Otha H. Vaughan (*Vaughan*, 2017)

flashes of a duration around 20 ms, long rise, some polarization and no re-
lated sferic (a burst of electromagnetic radiation emitted by the lightning
stroke that produced the luminous flash) (*Nemzek and Winkler*, 1989).
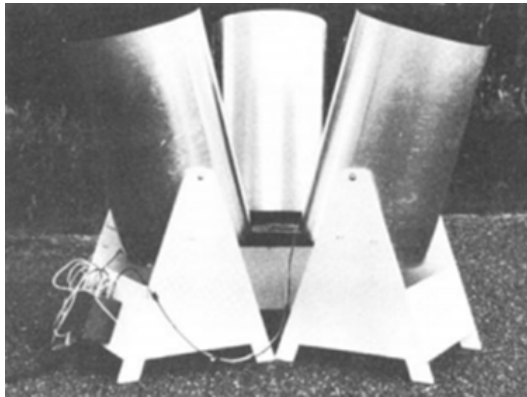


**Figure 1.4:** SKYFLASH photometric telescopes (*Nemzek and Winkler*, 1989)

They didn't know what they were observing until the night of 5 to
6 July, 1989. That night, Winckler and his graduate students, Nemzek
and Robert C. Franz, were testing a low-light-level TV camera intended
for a sounding rocket flight. While observing stars at a distant lightning
storm to calibrate their ground-based instrument, they accidentally recorded
Wilson's prediction for the very first time: two frames of 20 ms huge brilliant
twin-flash columns that they thought extended upwards more than 30 km

from the cloud tops to the stratosphere above a distant thunderstorm (*Franz et al.*, 1990). They immediately noticed that what they had recorded was singular and extraordinary, and confirmed that strong electric fields exist over the top of thunderstorms. Moreover, they realized that this anomalous optical emission could be related to the long events without sferic they had recorded previously, and they hypothesized that cloud-to-stratosphere discharges could generate them (*Franz et al.*, 1990).



**Figure 1.5:** First transient luminous event recorded image (*Franz et al.*, 1990)

Before the University of Minnesota team's recordings, the atmospheric electricity community neglected those anecdotal reports, even when a Nobel Prize winner witnessed one (*Wilson*, 1956). Nevertheless, since the publication of the first observation of a transient luminous event —huge and brief optical emission occurring over thunderstorms, TLE hereinafter— interest in such phenomenon increased and specialists in different scientific disciplines started to study the relationship between tropospheric lightning and the middle and upper atmosphere.

In particular, NASA scientists, concerned about the hazard of TLEs that could impact on aerospace vehicles, immediately started to study these recently discovered energetic events. It was the first systematic observa-

tional campaign of TLEs: Vaughan, Vonnegut and Boeck searched for TLEs in previously recorded observations from space by analyzing the data of the Mesoscale Lightning Experiment (MLE), which used the NASA space shuttle's sensitive payload bay monochrome video cameras to record the Earth's nighttime lightning activity. It was at the 1990 Fall Meeting of the American Geophysical Union where they presented a video documenting the first "cloud-to-stratosphere lightning" recorded from space (*Boeck and Vaughan Jr.*, 1990). This research group acquired seventeen examples of TLEs from space shuttle between October 1989 and November 1991 (*Boeck and Vaughan Jr.*, 1990; *Boeck et al.*, 1991a,b; *Vaughan Jr. et al.*, 1992; *Vaughan Jr.*, 1993a,b, 1994a,b; *Boeck et al.*, 1995) and concluded that the sequence of visible events leading up to a TLE began with a discharge in the thundercloud and could contribute to the global electrical circuit.



**Figure 1.6:** NASA space shuttle's sensitive payload bay monochrome video cameras to record the Earth's nighttime lightning activity (*Boeck and Vaughan Jr.*, 1990)

TLEs became popular worldwide, especially after the broadcasting of full-color video recordings (*Sentman and Wescott*, 1994). While watching a TV program focused on TLEs, Tudor Williams —a welsh head of geography at Abergele Grammar School and Howell's School in Denbigh (Wales)— realized that he had already snapped several rare form of lightning above a
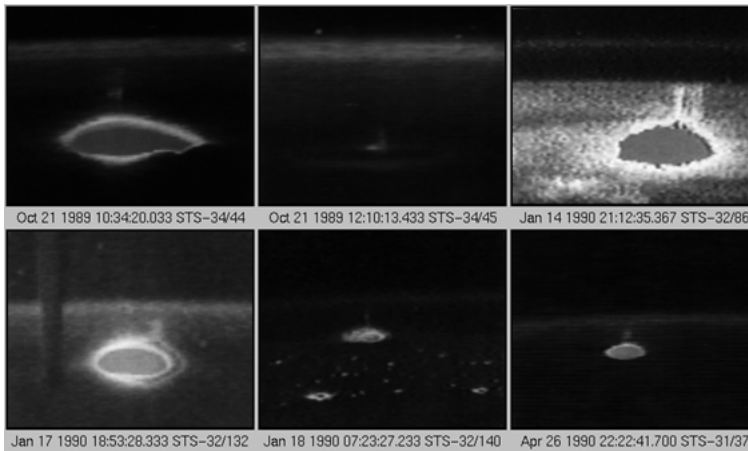
**Figure 1.7:** First TLE images from NASA space shuttle (*Boeck and Vaughan Jr.*, 1990). The ellipsoidal shape is a thundercloud, being the TLE the uprising optical emission

large nocturnal thunderstorm he was observing near Mount Ida, Queensland, Australia in March 1968. He ignored that he was the first person to photograph such extraordinary events, and these pictures were published four decades later, during the American Meteorology Society symposium on Space Weather annual meeting in 2003 (*Lyons et al.*, 2003a). He used a 50 ASA 35 mm transparency film and long exposures to photograph these TLE, revealing a bright blue flame which extended upwards: *"... the outstanding thing that I remember about the upward strokes which I saw was how slowly they formed. The spark rose slowly from the top of the cloud and took a full two seconds to achieve its full height... it faded away rather than shutting off abruptly. This pattern was consistent with every stroke I saw."* (*Lyons and Armstrong*, 2004).

But no matter who made the first TLEs recordings, TLEs themselves are today a subject of study to understand the chemical and physical behavior of the Earth atmosphere.

7

**Figure 1.8:** Upward discharge snapped by Tudor Williams in March 1968

## 1.2 Types of Transient Luminous Events

As Victor P. Pasko mentioned in *Pasko* (2010), *"transient luminous events (TLEs) are large-scale optical events occurring at stratospheric and meso-spheric/lower ionospheric altitudes, which are directly related to the electrical activity in underlying thunderstorms"*.

Two decades of worldwide observational campaigns of TLEs from satellites, space shuttles, aircrafts, balloons or ground-based observatories confirmed that these phenomena occur frequently over thunderstorms. These recordings also allow scientists to catalogue the morphology of these optical emissions: several types of TLEs have been identified since the first observational campaigns were performed. According to their shape, color, duration, altitude, dimension and periodicity, the known types of TLEs can be classified as sprites, halos, elves, blue jets, blue starters, giant blue jets, gnomes and pixies.

### 1.2.1 Sprites

From 1990 to 1993, authors described these kind of TLEs in different ways: *"Large upward electrical discharge"* (*Franz et al.*, 1990); *"vertical light pulse"*

**Table 1.1:** Types of TLEs

| TLE | SHAPE | COLOR | DURATION | ALTITUDE | DIMENSION |
|---|---|---|---|---|---|
| Sprites | Jellyfish - Carrot | Red | 10 - 120 ms | $\sim$40 - 90 km | $\sim$5 - 100 km width |
| | Columniform - Angel | Blue | | | $\sim$40 km height |
| Halos | Ellipsoidal | Red | 2 - 10 ms | $\sim$70 - 85 km | $\sim$50 - 100 km width |
| | | | | | $\sim$10 km height |
| Elves | Flattened toroidal | Red | <1 ms | $\sim$83 - 93 km | $\sim$300 km width |
| | | | | | $\sim$10 - 30 km height |
| Blue Jets | Trumpet-shaped | Blue | 100 - 300 ms | $\sim$15 - 50 km | $\sim$5 km width |
| | Conical | | | | $\sim$20 km height |
| Blue Starters | Conical | Blue | 20 - 90 ms | $\sim$15 - 25.5 km | $\sim$1 km width |
| | | | | | $\sim$5 km height |
| Gigantic Jets | Trumpet-shaped | Blue | 800 ms | $\sim$15 - 90 km | $\sim$15 km width |
| | Conical | Red | | | $\sim$50 km height |
| Gnomes | Conical | Blue | 33 - 136 ms | $\sim$10 km | $\sim$100 m width |
| | | | | | $\sim$1 km height |
| Pixies | Dots | Blue | < 16 ms | $\sim$10 km | $\sim$100 m width |
| | | | | | $\sim$100 m height |

(*Boeck et al.*, 1991a,b), *"cloud-to-stratosphere electrical discharges"* (*Lyons and Williams*, 1993; *Lyons*, 1993, 1994), *"upper atmospheric optical flashes"* (*Sentman and Wescott*, 1993; *Wescott et al.*, 1995), *"cloud to space lightning"* (*Vaughan Jr. et al.*, 1992; *Vaughan Jr.*, 1993a,b), etc.

The term to be used to designate the type of TLE recorded by Franz in 1989 hereinafter was suggested by Davis Sentman after he attended a play of Shakespeare's *"A Midsummer Night's Dream"* in 1993, where some enigmatic characters appeared as *sprites*. The dual jet Sprites94 aircraft campaign conducted by Sentman above Texarkana, Texas/Arkansas, provided the first color recordings of upper atmospheric optical emissions related to thunderstorm systems and allowed to triangulate their physical dimensions and heights (*Sentman et al.*, 1995; *Wescott et al.*, 1995). Since then and the later publication of the video titled *"Red Sprites and Blue Jets"* (*Sentman and Wescott*, 1994; *Sentman et al.*, 1995; *Wescott et al.*, 1995), the term sprite became popular and refers to this variety of TLEs nowadays.



**Figure 1.9:** Red sprite snapped by Oscar Van der Velde in October 2009 from Sant Vicenç de Castellet, Spain. The sprite occurred over a thunderstorm system in southern France some 300 km away

Sprites have been observed worldwide: from space (*Boeck et al.*, 1995; *Yair et al.*, 2004; *Chen et al.*, 2008; *Kuo et al.*, 2011), from aircrafts (*Sentman et al.*, 1995), from balloons (*Bering et al.*, 2004a) and from ground-based observatories in all continents excepting Antarctica (America (*Franz et al.*, 1990; *São Sabbas et al.*, 2010), Europe (*Neubert et al.*, 2008; *Bór*, 2013; *Passas et al.*, 2014), Asia (*Su et al.*, 2002; *Myokei et al.*, 2009; *Jing et al.*, 2008; *Yair et al.*, 2009), Africa (*Williams et al.*, 2010) and Oceania (*Hardman et al.*, 2000)).

József Bór, a researcher of the Hungarian Academy of Sciences, characterized the morphology, dimensions and duration of sprites in 2012 from the compilation and analysis of 489 sprites over Central Europe from Sopron, Hungary. He concluded that sprites can adopt several silhouettes and sizes, from simple column-shape to complex dendritic structures, often appeared in clusters rather than isolated, with these clusters often containing sprites with diverse morphology. He also noticed that sprite clusters occur more frequently above ground than above the sea (*Bór*, 2013).

t = 47.821 ms     t = 49.378 ms     t = 49.508 ms

t = 49.637 ms     t = 49.767 ms     t = 49.897 ms

t = 50.027 ms     t = 50.156 ms     t = 50.286 ms

t = 50.416 ms     t = 50.546 ms     Total integration of the images
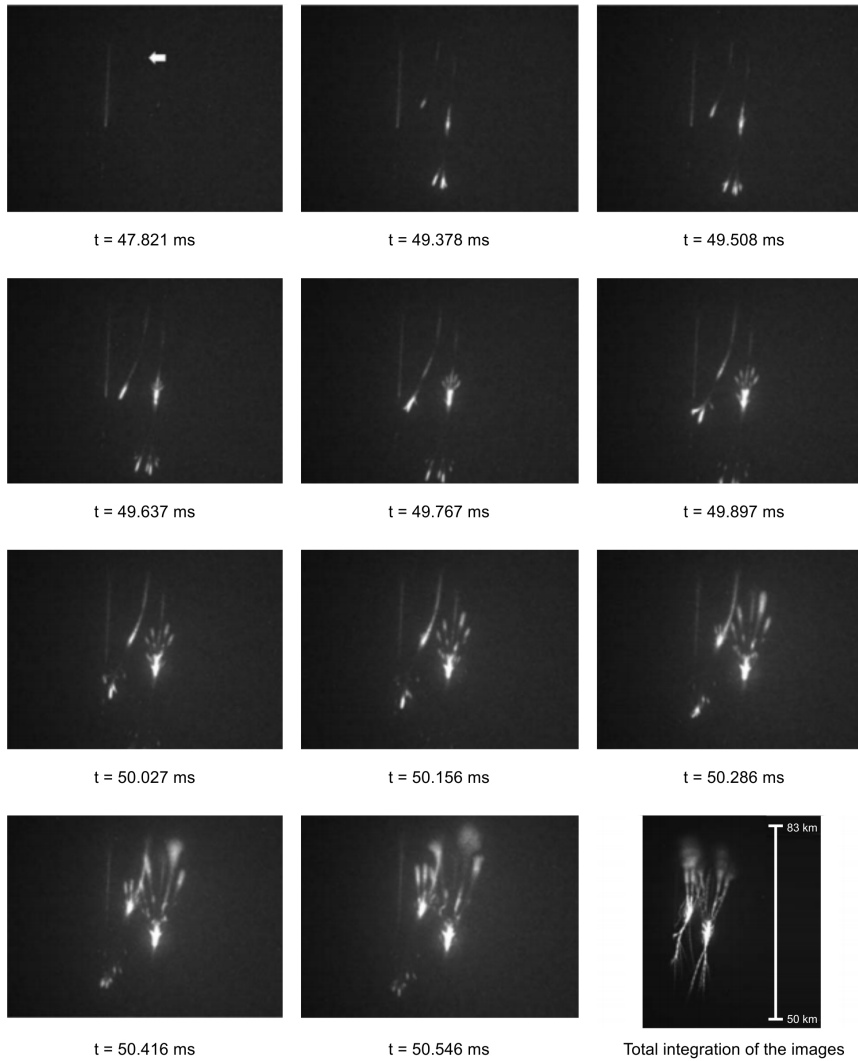
**Figure 1.10:** High speed (7692 frames per second) images of a sprite, snapped the 10th December 2009. The arrow indicates the first sign of the streamer tip of the central sprite element. The time of each image is referenced to the time of the detected parent lightning. The last image corresponds to the composite image of all the frames that compose the video (*Montanyà et al.*, 2010)

Sprites are generally as bright as an intense aurora —up to 1.5 MR (*Kuo et al.*, 2008)—, and sometimes they can be observed with the bare eye. But unlike aurora, they are very brief optical emissions with a main body that commonly lasts from less than 10 ms to 120 ms, with 60 ms being the most frequent duration (*Bór*, 2013). Sprites occur just after a parent lightning, with a maximum delay of hundreds of milliseconds (*Offroy et al.*, 2015) within the Earth upper atmosphere to the mesosphere, between 40 and 90 km above intense thunderclouds, presenting typical lateral dimensions from a few to tens of km and vertical heights up to 40 km (*Montanyà et al.*, 2010). Sprite entities often consist of a reddish intense main body —radiating in the first positive band of molecular nitrogen— that generally begins at 70 $\pm$ 15 km altitude (*Fullekrug et al.*, 2006), expanding downwards with bright positive streamers that become blue —radiating in the second positive band of molecular nitrogen— at low altitudes, commonly propagating upwards with red negative streamers, generally ending in an upper puff of reddish and diffuse light, with a mean streamer propagation speed about $1.5 \times 10^7$ m/s (*Montanyà et al.*, 2010).

The reason why sprites are red in colour at altitudes higher than 55 km and blue below, is due to the gradient of the molecular density and, therefore, to the de–excitation mechanism subjacent. Electrons in the excited state can get de–excited following two different mechanisms: (1) the radiative de–excitation mechanism, by returning to the ground state and emitting a photon in the process and (2) the collisional (quenching) de–excitation mechanism, when the excited electron collides with a nearby molecule or atom, transferring kinetic energy, and no photons are emitted.

In upper regions of the atmosphere the molecular density is very low. Hence, the probability of radiative de–excitation is much higher than the probability of quenching de–excitation, being these emissions red in colour, because the presence of molecular nitrogen excited in its B electronic state, $N_2(B)$, (that radiate in red —first positive system emission— when excited

electrons are radiative de–excited) predominates compared to molecular ni-trogen excited in its C electronic state $N_2(C)$ (that radiate in blue —second positive system emission— in the radiative de–excitation process).

On the other hand, at lower altitudes the molecular density is much higher, so the probability of quenching de–excitation of electrons of neutral nitrogen molecules is higher than the probability of radiative de–excitation of these electrons. But, as the mean lifetime of the excited electrons of the $N_2(C)$ nitrogen molecules is very short (100 times shorter than the mean lifetime of the excited electrons of the $N_2(B)$ neutral nitrogen molecules), their probability to radiate is higher than their probability to collide, so at altitudes below 55 km sprites emit in blue.

Sprites usually show beads of light along the tendrils as well as within the sprite body. It is also frequent to find glows of diffuse light within the main body and at the top of the sprites (*Bór*, 2013).

Sprites are triggered predominantly by positive cloud-to-ground light-ning discharges (+CGs), although not all thunderstorms produce sprites, even those presenting a high number of +CGs: the 1994 Colorado Sprite Campaign concluded that sprites occur most commonly above stratiform precipitation regions of mesoscale convective systems larger than 20,000 km$^2$ (*Lyons*, 1996). As a consequence of the extremely low frequency (ELF) sferic signatures observed related to sprites it is deduced that the +CGs that cause sprites produce as well charge moments of the order of 1000 C km —about an order of magnitude greater than common lightning flashes— (*Williams*, 1998; *Huang et al.*, 1999; *Cummer and Stanley*, 1999). More-over, the probability of sprite generation for lightning with charge moment > 1000 C km in < 6 ms is > 90 % (*Hu et al.*, 2002). So the quasi–electric field from a +CG may induce sprites if the stroke charge moment is high enough. From ELF data, we know that several sprites occur each minute worldwide (*Huang et al.*, 1999).

### 1.2.2 Halos

Gene Wescott and Chris Barrington-Leigh presented the characterization of halos for the first time at the American Geophysical Union meeting in December 1999.

Halos are brief —from 2 to 10 ms duration—, ellipsoidal, reddish, diffuse, descending glows of very weak intensity —about 0.3 MR (*Kuo et al.*, 2008)— which appear approximately between 70 and 85 km above their parent lightning. The dimensions of a halo usually extend about 50–100 km in diameter, and less than 10 km height (*Wescott et al.*, 1999, 2001b; *Frey et al.*, 2007). As sprites, halos are generated by lightning-induced quasi-electrostatic fields (*Offroy et al.*, 2015).

Halos sometimes precede sprites but they are usually observed alone. Spriteless halos are very frequent, being more frequent spriteless halos induced by negative cloud-to-ground lightning discharges (-CGs): they seem to occur between 5 and 7 times more often than spriteless halos induced by +CGs (*Bering et al.*, 2004b).
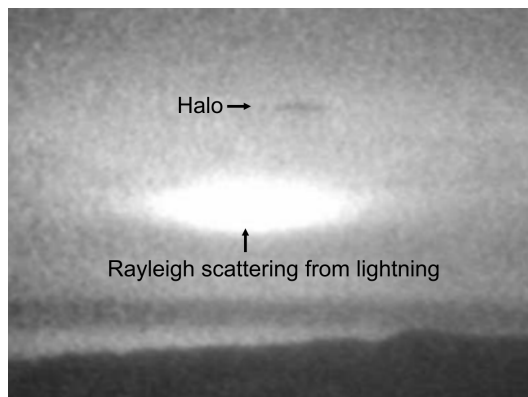


**Figure 1.11:** Halo observation from the Wyoming Infrared Observatory 28/07/1998
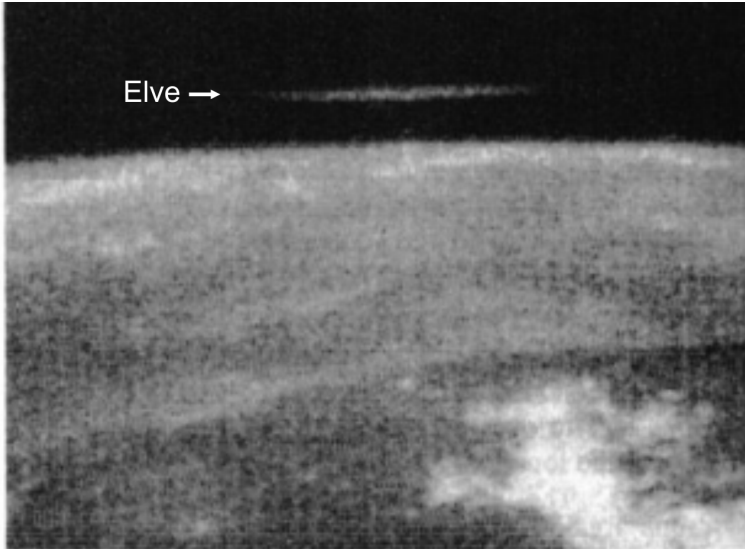
**Figure 1.12:** First image of an ELVE from space shuttle (*Boeck et al.*, 1992)

### 1.2.3 Elves

In April 1991 scientists from Stanford University predicted the modification of the lower ionosphere in lightning-induced electron precipitation events and through VLF heating (*Inan*, 1990; *Inan et al.*, 1991).

The MLE NASA Shuttle Discovery team recorded a new type of TLE the 7th October 1990 while performing Mission STS-41. This rare observations were similar to those described by the Stanford VLF team: a donut-shaped, expanding glow at the altitude of the airglow layer in coincidence with a lightning flash. They presented the video at the 1991 Spring AGU Meeting as well as at the Aerospace Lightning Conference (*Boeck et al.*, 1991b, 1992). Four years later, successful ground-based measurements of this optical emission from Yucca Ridge, near Fort Collins, Colorado, confirmed the existence of this kind of TLEs (*Lyons*, 1996; *Fukunishi et al.*, 1996).

The *"Emission of Light and Very Low Frequency Perturbations From Electro-magnetic Pulse Sources"* or ELVES are the most common type of TLEs (*Chern et al.*, 2014). Elves are morphologically similar to halos, but

they are wider (up to 300 km width), briefer (lasting less than 1 ms), they occur at higher altitudes (up to 93 km) and present a expanding ring shape, hollow in their center when the parent lightning causing it is vertically oriented. If the parent lightning is not vertical they can appear without their characteristic toroidal shape.

Oscar Van der Velde and Joan Montanyà, researchers of the Lightning Research Group of the Electrical Engineering Department at the Technical University of Catalonia, Spain, studied the statistics and variability of the altitude of elves in 2016 from the compilation and analysis of nearly 800 ELVES recorded by a low–light camera in northeastern Spain. They concluded that elves occur above thunderstorms at altitudes between 83 and 93 km, near the base of the ionosphere (*van der Velde and Montanyà*, 2016). They also observed that these reddish diffuse optical emissions of brightness less than 0.17 MR (*Kuo et al.*, 2008) are much weaker in summer than in autumn–winter seasons (*van der Velde and Montanyà*, 2016).

Elves occur related to both positive and negative discharges (*Barrington-Leigh and Inan*, 1999), but only 0.8 % of lightning produce elves: the probability to produce an elve for a lightning with peak current of 88 kA is 50 %, this probability being 100 % if the peak current is higher than 150 kA (*Blaes et al.*, 2016).

Although elves have a very intense typical peak optical intensity, they are so brief that they are not visible with the naked eye so they are quite difficult to detect. They sometimes occur in pairs, separated in time by $\sim$ 80 – 160 $\mu$s (*Marshall et al.*, 2015).

### 1.2.4 Blue Jets

It was 1990 when Vaughan, Boeck and collaborators identified for the first time a new type of TLE while processing the monochrome shuttle video data of the MLE recorded on 21st October 1989 (*Boeck et al.*, 1991a,b). This column-like atmospheric event was observed and described previously in the literature as *"rocket lightning"* (*Mackenzie and Toynbee*, 1886; *Everett*,

1903), and had only been recorded before serendipitously in March 1968 as already mentioned.
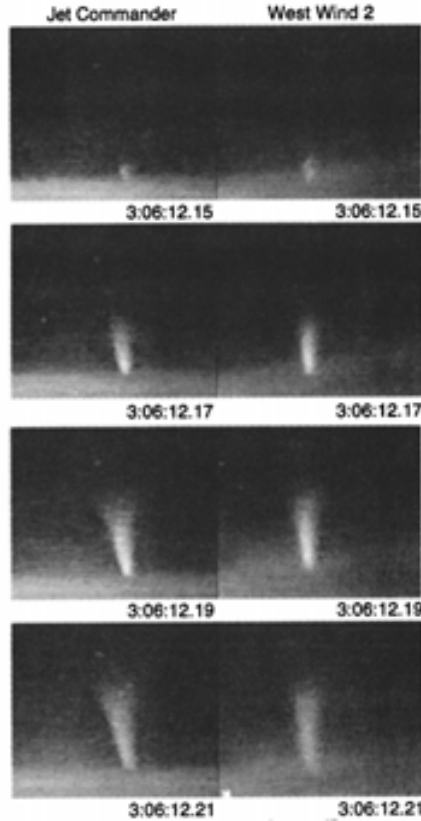


**Figure 1.13:** First high resolution recording of a blue jet (*Wescott et al.*, 1995)

This phenomenon consisted of *"a jet of light rising like a rocket from the cloud anvil"* (*Boeck et al.*, 1991a,b), but the image was not calibrated and no morphologic parameters were extracted.

Within the Sprites94 aircraft campaign, the so-called blue jets were triangulated and characterized, consisting of a slow-moving cone beam of bright blue light with a total optical brightness higher than 6.76 MR calculated from a 2–minutes time exposure photograph (*Wescott et al.*, 2001a) propagating upwards from the top of the thunderstorms at speeds of $\sim$

$10^5$ m/s, reaching terminal altitudes of 40—50 km, and opening itself with streamer-like filaments as a fan near its top and lasting from 100 ms (*Wescott et al.*, 1995; *Pasko*, 2008) to 450 ms (*Suzuki et al.*, 2012).

Professor Paul R. Krehbiel —from New Mexico Tech Univeristy in USA— and collaborators combined several observational results with theoretical models to try to understand the mechanisms developing blue jets, concluding that upward discharges are analogous to cloud-to-ground lightning: *"The modelling indicates that blue jets occur as a result of electrical breakdown between the upper storm charge and the screening charge attracted to the top cloud; they are predicted to occur 5-10 s or less after a cloud-to-ground or intracloud discharge produces a sudden charge imbalance in the storm"* (*Krehbiel et al.*, 2008).

### 1.2.5  Blue Starters

Another kind of TLE was discovered during the productive Sprites94 aircraft campaign: the *blue starters* are similar to the previously described blue jets, but ending at much lower altitude. They are bright and blue in color, start at the cloud top (15 - 18 km) and rise up to a maximum of 25.5 km in altitude (*Wescott et al.*, 1995).

The optical duration of blue starters observed from space seems to last from 1 ms (*Kuo et al.*, 2015) to 150 ms (*Suzuki et al.*, 2012), being their spatial average brightness 130 kR at at 427.8 nm of $N_2$ and 1.2 MR at 337 nm of $N_2$, attenuating as they rise (*Kuo et al.*, 2015).

Blue starters occur in the same area that -CGs, but they are not synchronous with them (*Wescott et al.*, 1996).

### 1.2.6  Gigantic Blue Jets

The evening of the 14th September 2001, Victor P. Pasko and colleagues were observing a cluster of thunderstorm cells from the Arecibo Observa-
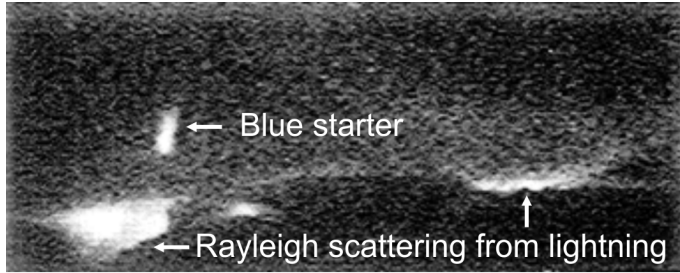
**Figure 1.14:** First image recorded of a blue starter (*Wescott et al.*, 1996)

tory in Puerto Rico, when a huge optical emission occurred. They recorded a video where the first gigantic blue jet was registered: it started at the top of the thundercloud anvil, as a normal intracloud discharge, and propagated upwards reaching around 70 km altitude, doubling in size a common blue jet. It lasted less than 0.8 s and it developed at $0.5 \times 10^5$ m/s speed during the first 0.16 s, increasing to $2.7 \times 10^5$ m/s during the next 0.16 s. Then, it split in two very rapidly and rose upwards at $2 \times 10^6$ m/s. At an altitude of 42 km —region where the upper limits of the blue jets and the lower limits of the sprites typically are— the giant blue jet developed some characteristics often observed in sprites (*Pasko et al.*, 2002). Since Pasko's first recordings, researchers have observed gigantic blue jets worldwide (*Su et al.*, 2003; *Cummer et al.*, 2009; *Yang and Feng*, 2012; *van der Velde et al.*, 2007; *Soula et al.*, 2011) providing an evidence that they might conform a component of the global electric circuit, connecting the thunderstorm and the ionosphere directly (*Yang and Feng*, 2012). After analyzing the distributions and occurrence rates of gigantic blue jets recorded from space, Alfred B. Chen and collaborators concluded that these kind of TLEs occur predominantly over maritime storms (*Chen et al.*, 2008).

### 1.2.7 Gnomes and Pixies

In August 1990, a new extraordinary event was observed but not recorded: *"...lightning bolts discharging to great heights from a pinkish glowing region*
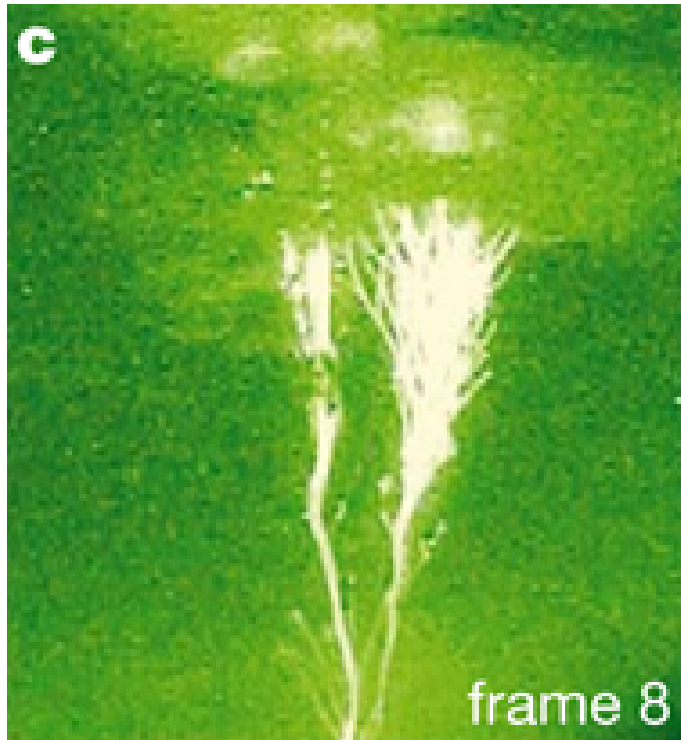
**Figure 1.15:** First image recorded of a gigantic blue jet (*Pasko et al.*, 2002)

*atop a rapidly building mesoscale convective system (MCC) moving east into the plains*" (*Lyons et al.*, 2003b). The same phenomenon was described by project technical manager Thomas Nelson while flying on a commercial aircraft in July 1994: *"Near sundown, while the plane was circumnavigating a large MCC, a brilliant, long lasting (500 ms) lightning-like column shot from the cloud top to at least twice the height of the parent cumulonimbus"*.

During the summer of 2000, a group of researchers were conducting the Severe Thunderstorm Electrification and Precipitation Study (STEPS 2000) campaign from the Yucca Ridge Field Station, near Fort Collins, Colorado, to investigate the dynamical, microphysical and electrical characteristics of thunderstorms, principally those producing +CG. The night of 22nd July 2000 they detected some unusual events: Goofy Nocturnal Optical Mesospheric Emissions from Something, or *gnomes*, are brief (33–136 ms), up-
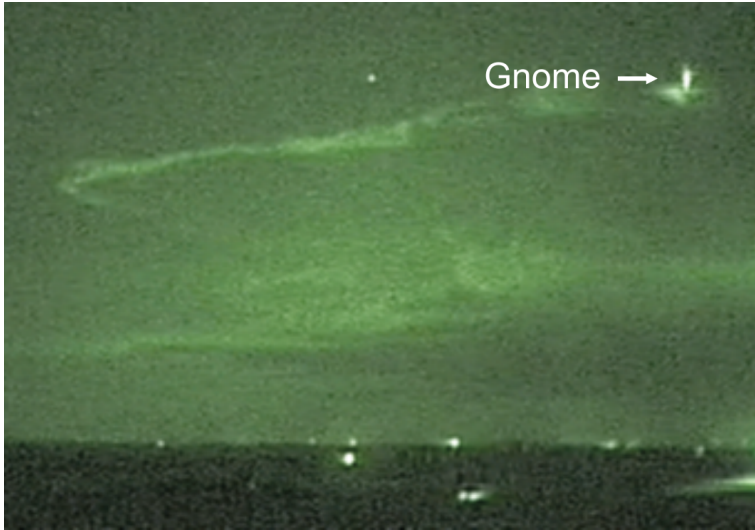
**Figure 1.16:** First image recorded of a gnome (*Lyons et al.*, 2003b)

ward propagating lightning–like cones no faster than 100 m/s, estimated to be less than 200 m wide and up to no more than 1 km above the cloud top; they seemed to be brighter —with an optical brightness higher than 220 kR— and more compact in shape than blue starters, although they could be also a type of them. Moreover, that night they observed another form of TLE: *pixies* are bright dots of light —with an optical brightness higher than 110 kR— of < 16 ms duration and 100 m size. They rose upwards from the top of the thundercloud and no cloud-to-ground or intracloud lightning flashes are related to these observations so they could be another kind of blue starter, although they seem to be much more compact than those. But the lack of blaze which characterize blue starters may suggest they conform a new kind of TLE (*Lyons et al.*, 2003b).

## 1.3   Spectroscopy of TLEs

Spectroscopy is a very useful tool to identify chemical properties and physical processes taking place in distant plasmas, such as their chemical composition, temperature or electron density.
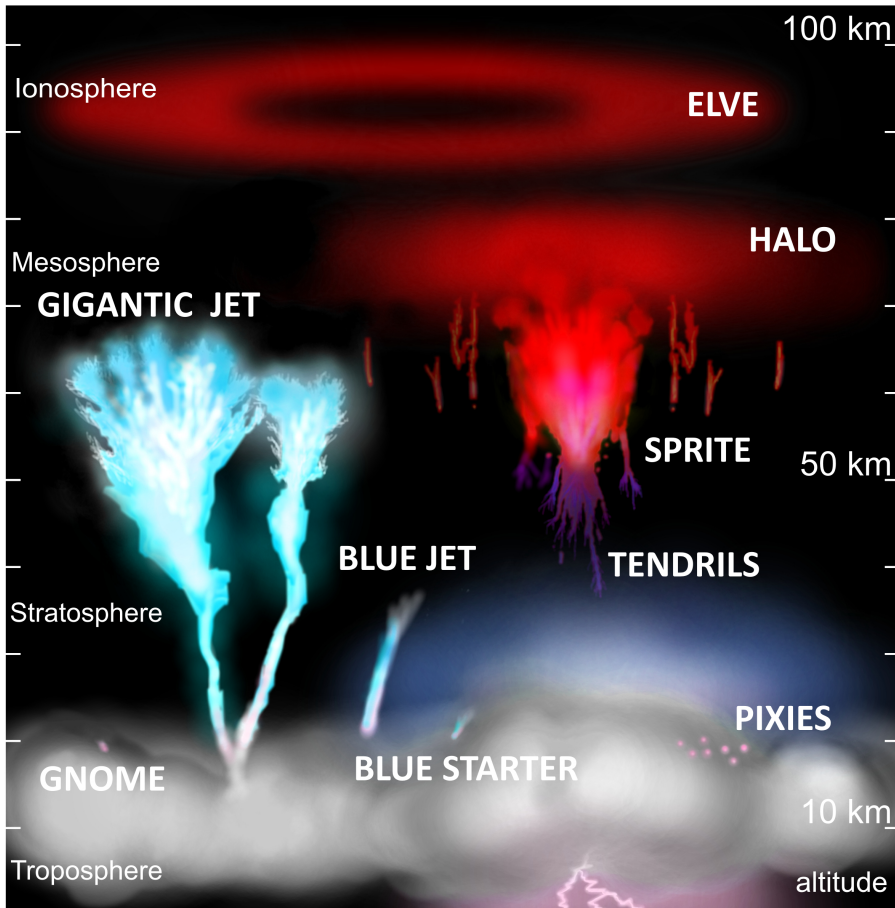
**Figure 1.17:** Schematic representation of known TLEs

Since the impressive color image of the sprite that Sentman and Wescott recorded in 1994, several spectroscopic measurements have been performed to identify the spectral features of these unusual optical emissions in the visible and near infrared (NIR) range by imaging spectroscopy (*Mende et al.*, 1995; *Hampton et al.*, 1996; *Heavner*, 2000; *Morrill et al.*, 1998, 2002; *Bucsela et al.*, 2003; *Kanmae et al.*, 2007, 2010a), filtered photometers (*Armstrong et al.*, 1998, 2000) and filtered intensified CCD-cameras (*Suszcynsky et al.*, 1998; *Morrill et al.*, 2002).

It was the summer of 1995 when —almost simultaneously— two differ-

ent groups of researchers decided to analyze the spectral features of TLEs for the first time in the visible and near infrared (NIR) wavelength range, from 450 nm to 840 nm. The group led by Steve Mende, from Lockheed Martin Palo Alto Research Laboratory in California, collected their data on July 16, 1995 from an observation site near Fort Collins, Colorado, and published their results in December 1995. They used a CCD —vertical— slit spectrograph —used before in auroral and airglow investigations— of 9 nm spectral resolution with a spectral range between 450 nm and 800 nm (*Mende et al.*, 1995). The data they presented was not corrected by the system instrumental spectral response. On the other hand, the group guided by Donald Hampton, from the University of Alaska Fairbanks, published their results a month later, in January 1996, although their data was collected on June 22, 1995 from the High Altitude Laboratory, on Mount Evans, Colorado, a fortnight before Mende did. They employed the Deehr spectrograph: an intensified CCD TV —horizontal— slit spectrograph, previously used for auroral studies (*Deehr*, 1961; *Hallinan et al.*, 1985). They combined two different slits in order to reach 6 and 10 nm spectral resolutions —with a spectral range between 540 nm and 840 nm— and recorded spectra of sprites of different shapes and halos at 30 frames per second. The data they presented was corrected with the response function of the spectrograph (*Hampton et al.*, 1996). Both groups reached the same conclusions practically at the same time: (1) they identified four spectral features of a sprite "body" spectrum in the 600–700 nm region as the $N_2$ first positive system (1PG), corresponding to the transition between electronic states $B^3\Pi_g \rightarrow A^3\Sigma_u^+$ of neutral $N_2$ and (2) they noticed that the spectra lacked other features such as the $N_2^+$ Meinel or the $N_2^+$ first negative system (1NG), indicating that the electron energy causing the excitation was low and the mechanism responsible for sprites produced little or no ionization between 70 km and 90 km altitude (*Mende et al.*, 1995; *Hampton et al.*, 1996). As they were investigating in the same direction, they decided to work together and they determined the molecular internal energy distribution in

the $N_2(B^3\Pi_g)$ state from the fluorescence measured during the observations of sprites mentioned above (*Green et al.*, 1996).

Moreover, Hampton and his team analyzed two spectra from different regions of the same sprite, corresponding to the low altitude "tendrils" (blurred motion of rapidly moving point-like structures (*Liu and Pasko*, 2005; *Stenbaek-Nielsen et al.*, 2007)) from the Wyoming Infrared Observatory on Jelm Mountain in 1996 (*Bucsela et al.*, 2003). They extended the wavelength range of observation to 900 nm and simultaneously used two horizontal slit spectrographs to analyze the spectra of the sprite at 53 km and 57 km, respectively: (1) the Deehr TV spectrograph of 6 nm to 9 nm spectral resolution —used before— and (2) the Fogle spectrograph, of 9 nm to 13 nm resolution (*Fogle*, 1966; *Morrill et al.*, 1998). Besides the former $N_2(B^3\Pi_g)$ system identification, they distinguished a variety of sprites —the columniform sprites– with a shape and a spectrum that presented several differences if compared to "normal" sprites (*Wescott et al.*, 1998). They also detected some evidences of $N_2^+$ Meinel bands in the spectrum belonging to the higher zone of the TLE (*Green et al.*, 1996; *Morrill et al.*, 1998; *Bucsela et al.*, 2003).

As sprites are blue at lower altitudes (*Sentman et al.*, 1995), spectroscopy of blue emissions was also developed. In the summers of 1996, 1997 and 1998, the research group led by Russell A. Armstrong used photometers of spectral resolution of 30 nm, 10 nm to 20 nm and 9.6 nm from Yucca Ridge Field Station, near Fort Collins, Colorado, to identify the emissions of the $N_2(B^3\Pi_g)$ (665 nm), the $N_2^+$ 1NG (427.8 nm) and the $N_2$ second positive (2PG) (399.8 nm) band systems respectively in spectra of scattered lightning, sprites and elves. They observed that the ratio of the intensity of the $N_2$ 2PG emission to that of $N_2^+$ 1NG emission could be used to discriminate among sprites, elves and lightning. Furthermore, they concluded that the source of the $N_2$ 2PG and the $N_2^+$ 1NG emissions in sprites was the initial ionization event, and was not a result of the secondary electron

impact excitation, which was apparently the primary source of the red nitrogen first positive emission. They also reported photometric evidences for a *"continuing current"* associated with the lightning event that gives rise to delayed sprites and indicated the presence of $N_2^+$ 1NG emissions during the initial phase of the sprite (*Armstrong et al.*, 1998; *Suszcynsky et al.*, 1998).

The first near–ultraviolet spectral observations of TLEs were recorded in 1998 from an aircraft during the Energetics of Upper Atmospheric Excitation by Lightning (EXL98) campaign, a collaboration between the University of Alaska Fairbanks, the Naval Research Laboratory and the Air Force Research Laboratory. These researchers analyzed the altitude–resolved spectral features of 1NG and 2PG of $N_2^+$ and $N_2$ TLEs by inspecting their spectra in the near ultraviolet (NUV), visible, NIR and medium infrared (MIR) wavelengths. To do so, they employed two instruments: (1) a camera with a narrow passband filter centered at 427.8 nm with a spectral resolution of 1.44 nm for observation of $N_2^+$ 1NG (*Wescott et al.*, 2001a; *Morrill et al.*, 2002) and (2) a NUV and blue (320 nm - 460 nm) horizontal slit spectrograph of $> 4$ nm resolution (*Heavner et al.*, 2010). The EXL98 campaign obtained several results: (1) electrons with energies of at least 18.6 eV were required to describe the nitrogen ion emissions (*Heavner*, 2000), (2) the blue component of blue jets and blue starters was mainly due to the $N_2$ 2PG band (*Wescott et al.*, 2001a; *Heavner et al.*, 2010) and (3) physical and chemical processes in sprites depended on altitude: for regions higher than 55 km, optical emissions in sprites were due to excited neutrals —$N_2$ 2PG— and below that altitude, these emissions derived from both excited neutrals and excited ions —$N_2^+$ 1NG— almost in the same proportion, indicating a relative enhancement in ionization in tendrils (*Morrill et al.*, 2002).

The only spectrum to date of a sprite halo was obtained for the first time during observations from Mount Evans, Colorado, and it is essentially identical to spectra of the uppermost region of sprites (*Wescott et al.*, 2001b).

TLE spectroscopic imaging from space was —and it is currently being— also developed. The Michelson Interferometer for Passive Atmospheric

**Figure 1.18:** EXL98 Gulfstream II aircraft and NIR camera. (a) The aircraft, with the specialized windows covered for protection when not in flight. (b) Two of the quartz windows. In the left window the Color, Wide field of view (FOV) and Narrow FOV cameras are mounted and in the right window the NIR and NUV imagers. The center window is the standard Gulfstream Plexiglass. (c) The interior of the aircraft; observations could only be made out of the left-hand side. (d) The NIR imaging camera (*Siefring et al.*, 2010)

Sounding (MIPAS) was an international collaboration (Germany, Belgium, Italy, France, Spain, The Netherlands, United Kingdom and Canada) and consisted of a Fourier–transform mid–infrared —from 4150 to 14600 nm— emission spectrometer. It was launched on March 2002 as a part of the core payload of European Space Agency (ESA) ENVISAT, and operated until April 2012, providing data with a mean spectral resolution from 0.025 to 0.0625 $cm^{-1}$ (*Glatthor et al.*, 2017). These observations, combined with theoretical models, also allowed to indirectly study sprite–induced chemical perturbations in the mesosphere (*Arnone et al.*, 2008).

The Imager of Sprites and Upper Atmospheric Lightning (ISUAL) in-
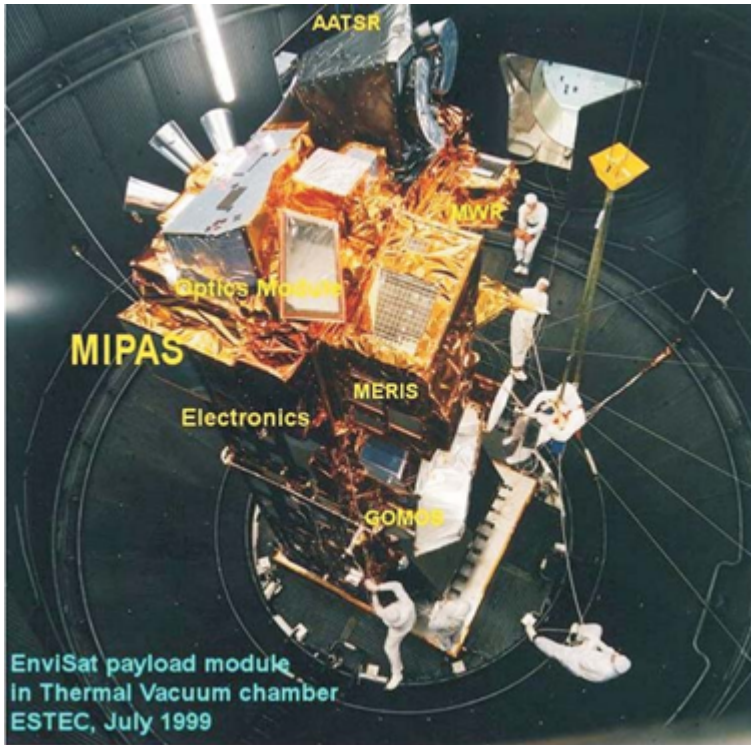
**Figure 1.19:** MIPAS module installed on ESA EnviSat (*Fischer et al.*, 2008)

strument is another international collaboration for the study of TLEs, in this case between Taiwan, Japan and USA. It was installed onboard the FORMOSAT-II satellite and it was operative between 21 May 2004 and 22 August 2016 to analyze transient optical atmospheric phenomena. It consisted of a bore–sighted intensified CCD sprite imager equipped with a six–filter wheel, a six–channel spectrophotometer —covering the spectral range from the far ultra violet (FUV) to the NIR— and a two–channel (red/blue) array photometer to compile TLEs, auroral and lightning data to understand the mechanisms producing these optical emissions and analyze the regions where they occur. The data collected to date show evidences of FUV emissions in the sprite spectrum and the best spectral resolution employed was 6.5 nm (*Mende et al.*, 2004, 2006; *Frey et al.*, 2004; *Adachi et al.*,

2006). Since 2004, ISUAL has recorded more than 35,000 TLEs (see figure 1.21), obtaining an estimated global occurrence of 24 TLEs per minute, with the most common being elves (73.65 %), followed by blue jets (13.51 %), sprites (6.53 %), halos (6 %) and gigantic blue jets (0.30 %) (*Chern et al.*, 2014).
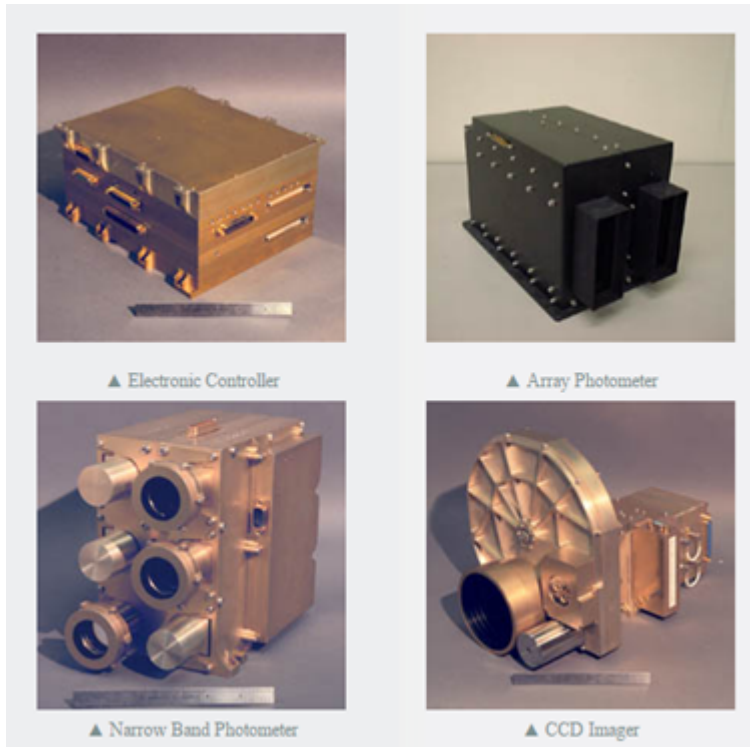


**Figure 1.20:** ISUAL instrument components [http://www.nspo.org.tw]

Meanwhile, in 2005, the research team of the University of Alaska Fairbanks analyzed an altitude–resolved sprite spectra from the Langmuir Laboratory near Socorro, New Mexico (USA). They showed that the vibrational population in the upper electronic state producing the $N_2(B^3\Pi_g \rightarrow A^3\Sigma_u^+)$ bands varied with altitude as well, and reported that the spectrum was similar to that of laboratory afterglow at high pressure (200 mTorr), although they did not detect evidences of $N_2^+$ Meinel bands. They employed a vertical slit spectrograph of 3 nm spectral and 3 ms temporal resolution, within
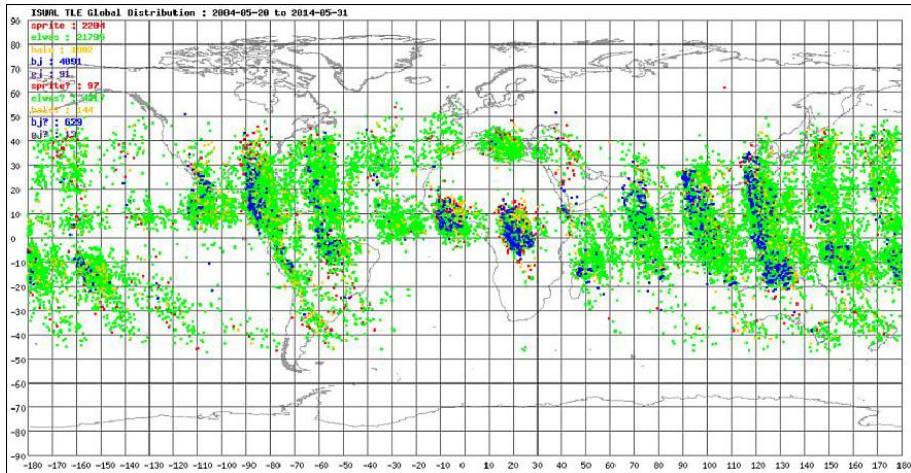
**Figure 1.21:** Global distribution of 35,165 TLEs observed by ISUAL from 4 July 2004 to 31 May 2014 (see legend at left upper corner: green for elves, red for sprites, orange for halos, blue for blue jets, and black for gigantic jets), image credit: China University of Science and Technology, Taiwan and NSPO [https://directory.eoportal.org/web/eoportal/satellite-missions]

the (red) visible range from 640–820 nm (*Kanmae et al.*, 2007). In a subsequent study, they also observed spatially– and temporally–resolved sprite streamer head spectra using a slit–less spectrograph at 10,000 fps with 12 nm spectral resolution, which allowed them to estimate the rotational temperature of the air surrounding TLEs using kinetic models (*Kanmae et al.*, 2010b). Furthermore, they used the same high-speed slit-less spectrograph during an aircraft campaign to characterize blue sprite spectra and confirmed the more energetic nature of sprite streamer heads compared with column shaped glows (*Kanmae et al.*, 2010a).

The different types of TLEs occurring in the Earth's atmosphere from the lower stratosphere to the upper mesosphere can be considered as natural probes to learn about the properties of the middle and upper atmosphere of our planet through remote determination of key properties such as the gas temperature or the degree of excitation and ionization of atoms and molecules caused by TLEs in the atmosphere. In this regard, systematic

spectroscopic campaigns of optical emissions from all sort of TLEs can allow us to remotely determine important atmospheric properties that would be difficult to obtain in other ways. Unfortunately the spectrographs used in the dispersed TLE spectroscopic campaigns carried out so far were originally designed for aurora spectroscopy (*Hallinan et al.*, 1985) and the best spectral resolution achieved to date is ~3 nm that it is not enough to spectrally resolve the different low-lying vibrational transitions of the $N_2$ 1PG.

## 1.4   Polarimetry of TLEs

Polarimetry allows to measure and identify the direction and degree of polarization of light. It can be used in remote sensing applications to analyze the polarimetric properties of optical emissions from distant plasmas.

It seems that polarimetry of TLEs was firstly registered in January and May 1989, just before the identification of the first sprite. While analyzing data from the SKYFLASH experiment, which was intended to identify Rayleigh scattering of a horizontal beam passing over three photometric telescopes including polaroid sheets above their mirrors, Nemzek and Winckler detected *"moderate but definite"* polarization of light coming from short duration flashes that lasted more than 20 ms (*Nemzek and Winkler*, 1989; *Winckler et al.*, 1993). These unexplained events with no sferics and long rise time and duration were later identified as TLEs.

Since then, polarimetry of TLEs was ignored until 2010, when our group decided to build a polarimeter to study whether this property of light is present in TLEs.

## 1.5   Motivation

From the status of knowledge before, we find that (1) no systematic spectroscopic campaigns dedicated to observe TLEs have been developed from ground, (2) the best spectral resolution handled to analyze TLE spectra to

date is 3 nm, and it is insufficient to estimate the temperature of the gas surrounding TLEs and (3) there is a lack of study of polarimetric properties of TLEs, even when there are some evidences suggesting that such feature of light could be present in TLEs emissions.

These facts motivated us to design and develop a ground–based instrument designed to simultaneously measure the polarization and the spectra of the light emitted from TLEs with medium-high spectral resolution in an automatic and systematic way. Because it has been developed in Granada, Spain, we have called our instrument GRASSP, as an acronym of GRAnada Sprite Spectrograph and Polarimeter. This instrument is intended to be a ground support of the Atmosphere Space Interaction Monitor (ASIM), an approved European Space Agency (ESA) project to be installed in the International Space Station (ISS) which will be launched in late 2017 – early 2018.

GRASSP includes the first medium–high resolution spectrograph designed to analyze the spectrum of TLEs in the visible–near infrared band (695 nm – 795 nm) with a spectral resolution better than 0.5 nm, so we can estimate the gas temperature of the gas surrounding TLEs among other characteristics. GRASSP also bears the first polarimeter designed to achieve the type and degree of polarization of the light emitted by TLEs by calculating the four Stokes parameters of TLEs optical emissions in a single shot.

As GRASSP is a custom instrument, we have also designed and developed the software tools to control its inner subsystems and to reduce GRASSP spectroscopic data. Besides, to make measurements reliable, we have calibrated both the spectrograph and the polarimeter in our dependencies.

## 1.6   Content

This introduction summarizes the state of knowledge to date of imaging, spectroscopy and polarimetry of TLEs. We now briefly comment on the

contents of the different chapters of this thesis.

Chapter 2 describes thoroughly the different versions of GRASSP and its components under a hardware perspective. Chapter 3 describes thoroughly the different versions of GRASSP spectrographs, and their calibration processes. Chapter 4 describes thoroughly the GRASSP polarimeter and its calibration process. Chapter 5 describes the GRASSP automatic control system under a software perspective, and also depicts the acquisition and TLEs data reduction software tools. Chapter 6 summarizes the results we have achieved in the course of these years of research and proposes future lines of study. And, finally, chapter 7 is devoted to conclusions.

# Chapter 2

# Experimental device

*"A peculiar species of lightning, bearing a strong resemblance to ascending rockets, was witnessed on the evening of July 22 by two of the professors in Sibpur Engineering College, Howrah, near Calcutta [...]"*

– J. D. Everett, *Nature, October 22, 1903*

## 2.1 Instrument overview

As described in chapter 1, transient luminous events (TLEs) are a kind of brief optical and electrical phenomena that occur in the Earth mesosphere and stratosphere related to lightning in electrically active storms. They emit in different regions of the electromagnetic spectrum, including the visible range, appearing at altitudes between 15 km and 93 km and lasting between less than a millisecond to up to a second. Since their first recording, several sporadic spectroscopic measurements helped to understand the influence of TLEs over the Earth mesosphere. However, so far, the best spectral resolution used was R = $\lambda/\Delta\lambda$ = 215 ($\Delta\lambda$ = 3 nm) (*Mende et al.*, 1995; *Hampton et al.*, 1996; *Kanmae et al.*, 2007) and these measurements corresponded to punctual observational campaigns.

Nemzek and Winckler detected polarization of light from TLEs accidentally for the first time in 1989 (*Nemzek and Winkler*, 1989; *Winckler et al.*, 1993) and, since then, this property of light has been ignored, even when it could reveal chemical and electrodynamical mechanisms taking place within TLEs.

As mentioned in chapter 1, our group intends to study TLE optical emissions with medium–high spectral resolution and, simultaneously, to characterize their polarization if there is any. The objective is to start spectroscopic and polarimetric field campaigns of TLE in Spain as a ground support of the Atmosphere Space Interaction Monitor (ASIM) mission of ESA, to be launched by early 2018. To do so, we have developed the GRASSP instrument: a ground–based visible (695 - 795 nm) grating spectrograph and polarimeter, to measure simultaneously the polarization and the spectra of the light emitted from these TLEs with a spectral resolution of R = $\lambda/\Delta\lambda$ = 3309 ($\Delta\lambda$ = 0.23 nm).

It is worth highlighting that, so far, we have developed two different versions of GRASSP and we have installed them at two different locations.

The first version of GRASSP (GRASSP v1.0) worked automatically in a methodical way: by consulting a real-time lightning database, a telescope mount aimed automatically the spectrograph (the polarimeter was not operative then) to the region of the sky where a TLE was predicted to appear. The spectral range of this first version of GRASSP was 100 nm (660 nm to 760 nm) with a mean spectral resolution of R = $\lambda/\Delta\lambda$ = 1247 ($\Delta\lambda$ = 0.58 nm).

As sprites and halos are red in their upper region —due to the nitrogen first positive emission— we selected the spectral range between 660 and 760 nm. We tried to build the spectrograph to estimate the gas temperature surrounding TLEs by analyzing their spectra, and it is only possible when the spectral resolution is between 0.1 nm and 0.5 nm (*Simek and DeBenedictis*, 1995; *Parra-Rojas et al.*, 2013b). Unfortunately, this first spectrometer only reached a mean spectral resolution of 0.58 nm.

GRASSP v1.0 was installed in October 2012 at the terrace of the 2.2 m dome of the German–Spanish Astronomical Center at Calar Alto, Sierra de Los Filabres, north of Almería (Andalucía, Southern Spain), where its housing is still fixed at 2,168 meters above mean sea level, 37.2231° N latitude and 2.5458° W longitude. The housing was placed on an aluminum sloped fixed structure oriented to 45° azimuth from the north and 10° elevation in order to observe the western Mediterranean Sea zone, a region where TLE activity in Europe seemed to be frequent (37° N – 50° N; 2° W – 14° E with an elevation of 10° – 35° above the horizon).

After several months of testing —and up to 52 TLE recorded— we found out that it was possible to improve the spectral resolution changing the analog to digital converter board, from CCIR 170, 795 × 596 px (H × V) to SDI HR (1920 × 1080 px (H × V)). And we also noticed that the triplet of OI around 777.19 nm could be involved in the chemical processes taken place in TLEs (*Parra-Rojas et al.*, 2013b). So, in July 2014, we decided to shift the spectral range of GRASSP v1.0 between 695 nm and 795 nm and we improved its spectral resolution to 0.23 nm, maintaining its location. We named this upgrade as GRASSP v1.1.

During an annual meeting and five months of observation later, we realized that campaigns carried out by our colleagues from the north of Spain captured ten times more TLE activity than our team: TLE main activity occur in latitudes between 40° – 43° N, whereas electrically active storms barely happen between 37° – 39° N (see figure 2.1). Moreover, as the TLEs we captured occurred far away from our location, their shapes covered a very small proportion of the CCD, being very difficult to fit them over the spectrograph narrow slit. In two years of observations we recorded several TLE images, but none of them matched the spectrograph slit area: 52 TLEs and 0 TLE spectra in two years (see figure 2.2).
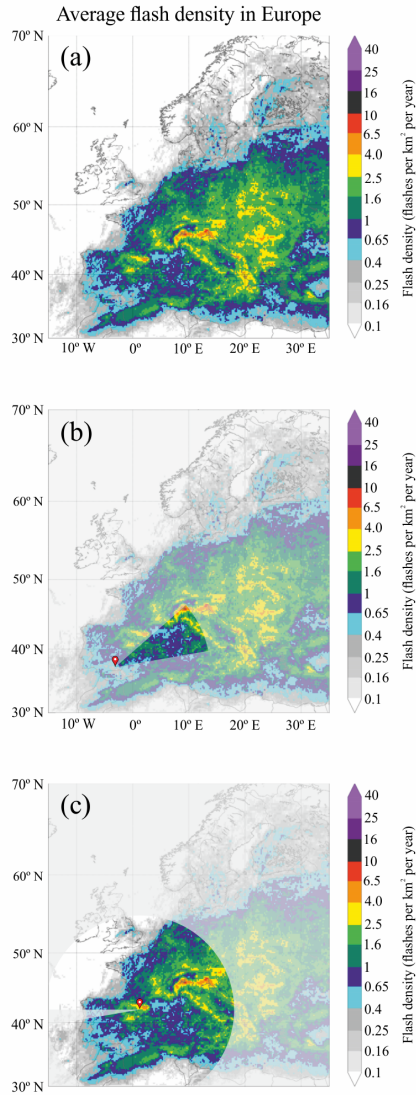
**Figure 2.1:** (a) Average flash densities observed in Europe between January 2008 and 31 December 2012 (*Anderson and Klugmann*, 2014). (b) FOV from CAHA Observatory, Almería, Spain (GRASSP v1.x). (c) FOV from Castell-galí, Spain (GRASSP v2.x)

On the other hand, most TLE images recorded by our northern colleagues filled the whole CCD. If our instrument had been exposed to such close phenomena, several spectra would have been recorded. It was clear that our location was not optimal. So we started a close collaboration with the Universitat Politècnica de Catalunya (UPC) team and we decided to develop a new instrument to be installed at Castellgalí (Barcelona, Spain), at 275 meters above the mean sea level, 41.6768° N latitude and 1.8399° E longitude to improve GRASSP statistics of spectroscopy of TLEs.
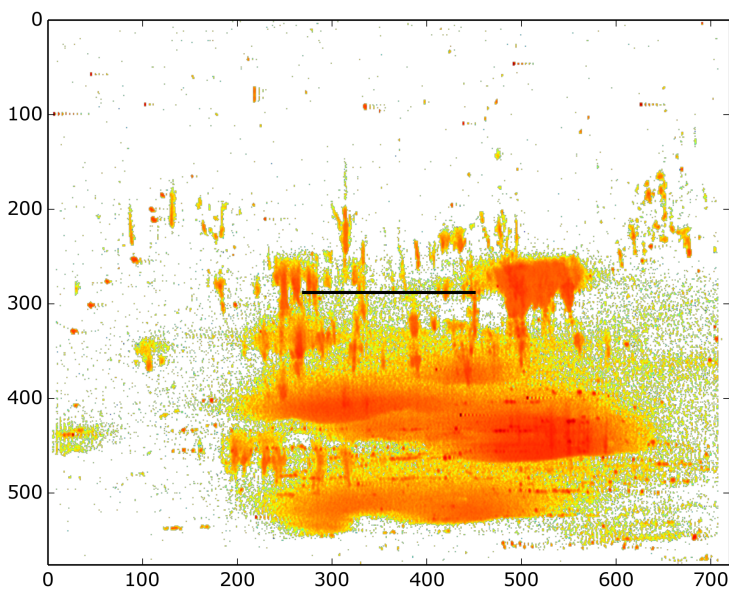


**Figure 2.2:** Slit position of GRASSP v1.x (black) superimposed to a synthetic image generated from the overlapping of all the TLE images recorded from CAHA. No TLE spectrum was detected

As introduced in chapter 1, the final goal of our team is to support the ASIM mission when it is launched, and it is statistically easier to measure spectra and polarization of TLE if we are located at the optimum place. The first option we thought was to move the entire automatic system (GRASSP

v1.1) to Castellgalí but, as it was very difficult to do so, we designed and developed a new version of GRASSP (GRASSP v2.x): a compact instrument we only operate when climate conditions are appropriate for TLEs to appear. If there are any chances of electrically active thunderstorms within the observation area, once the system is wavelength calibrated and remotely controlled from Granada, our partner and colleague Oscar Van der Velde manually aims GRASSP v2.x to the region of the sky where his experience suggests a TLE is going to show up. The spectral range and resolution of GRASSP v2.x is the same as its former version (695 – 795 nm and 0.23 nm). The housing is installed on a movable structure which will be fully described below. It can be oriented horizontally between -60° NW and 170° NW, spinning around 230° azimuth and it can be also moved in elevation from -10° to 60°. It is worth noting that GRASSP v2.0 worked from May 2015 to May 2016, when the internal PC stopped working. In that period, we obtained the first TLE spectra ever recorded worldwide with medium–high resolution. From that date onwards, a new PC is currently controlling all subsystems. This newest version of GRASSP (GRASSP v2.1) has recorded more than 44 TLE spectra to date.

All versions of GRASSP share a common hardware and software. In this chapter I will describe GRASSP hardware, pointing the upgrades between the different versions of GRASSP.

## 2.2  GRASSP common hardware

As mentioned before, GRASSP is a remotely controlled medium-high resolution spectrograph and a polarimeter. It consists of a combination of commercial and customized subsystems.

The commercial common subsystems of GRASSP are a computer, a static IP switch, a field camera, an audio trigger and a weather station. They are fully described below.

The spectrograph and the polarimeter are customized hardware common to all versions of GRASSP, but as they were designed and developed by our team, I will describe them separately in chapters 3 and 4, respectively.

### 2.2.1 PC

The computer that manages GRASSP v1.x and GRASSP v2.0 is a commercial desktop HP Elite 7000 MT with an Intel Core i5–750 @ 2.67 GHz processor, of 4 GB RAM, $1 \times$ PCIex16 and runs under Microsoft Windows XP Professional 2002 Service Pack 3 OS. We have modified the electronics of the power on button of the PC to allow switching it on and off remotely.

On the other hand, the computer that manages GRASSP v2.1 is an industrial PC, UNO-3083G, a very compact automation computer with high-performance Intel Core i7–3555LE @ 2.5 GHz processor, of 8 GB RAM, $1 \times$ PCIex16 + $2 \times$ PCI expansion slots that runs under Microsoft Windows 7 Pro x64 Service Pack 1 OS. This computer can be switched on and off remotely by controlling the power supply through the automaton I will describe below.

We have chosen these operating systems to avoid incompatibilities with the drivers of the devices connected. We use a total of 5 USB ports and 2 RS232 ports from all available. We have also installed a USB extension to control keyboard and mouse from outside the housing.

### 2.2.2 Static IP switch



**Figure 2.3:** Conceptronic C100BRS4H broadband router switch

All versions of the GRASSP instrument are controlled remotely thanks to a Conceptronic C100BRS4H broadband switch (see figure 2.3). It is powered by a 12 V direct current (VDC) supply of 500 mA and it has 4 local area network (LAN) and 1 wide area network (WAN) RJ–45 ports. The connections between the PC, the automaton and the internet are shown in figure 2.4.
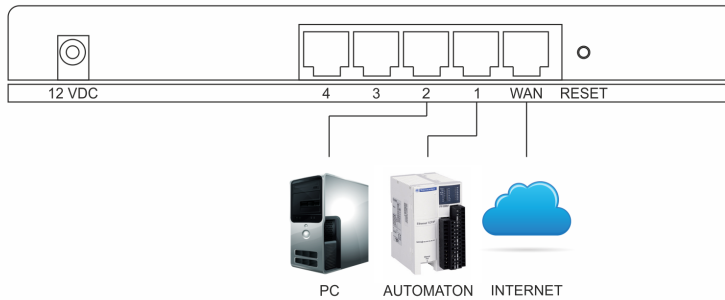


**Figure 2.4:** Schematic of the switch connections

### 2.2.3   Field camera



**Figure 2.5:** Watec WAT-902H2 ultimate

The wide field camera (see figure 2.5) records the night images and helps to discern the origin of the recorded spectrum. It consists of a Watec 1/2"

Charge Coupled Device (CCD hereinafter): a WAT-902H2 ultimate with a 3005VX4 sensor low light monochrome camera of high sensitivity. Its dimensions are $35.5 \times 40 \times 63$ mm$^3$ (width $\times$ height $\times$ length) and it weighs 98 grams. It is powered by a supply of 12 VDC and a current of 110 mA (1.32 W). The number of total pixels of the CCD is 795 (H) $\times$ 596 (V) with a unit cell size of 8.6 $\mu$m (H) $\times$ 8.3 $\mu$m (V). An auto iris function allows the camera to produce visible images in light levels as low as 0.0001 lux with a signal to noise ratio better than 50 dB. Its field of view (FOV hereinafter) is 21.6 (H) $\times$ 17.4 (V) degrees thanks to the f/1.4 and 16 mm focal length lens it has attached. The gain control and the back–light compensation can be manually controlled and the composite video signal output is through a Bayonet Neill-Concelman (BNC hereinafter) connector. We have switched the gamma correction and the electronic shutter off. The automatic gain control has been set to the highest level and the camera has been focused to infinity. It records at a frame rate of 25 frames per second (fps) with a shutter speed mode control of 1/50. The wide field camera specifications are summarized in table 2.1.

**Table 2.1: GRASSP Wide Field Camera**

| | |
|---|---:|
| Wavelength range | 400 nm – 1000 nm |
| Horizontal resolution | 600 lines |
| Signal to noise ratio | 50 dB |
| Automatic gain | 5 – 60 dB |
| Frame rate | 25 fps |
| Field of view | 21.6° $\times$ 17.4° |
| A/D converter | Honestech Trivid 4.0 HD |
| Total pixels | 795 $\times$ 596 px (H $\times$ V) |

A Honestech Trivid 4.0 HD analog to digital video capture system (see figure 2.6) wires the Watec Camera through a BNC connector with the PC through a USB 2.0 host controller port. It supplies a color precision of 8 bits and a high definition format support of 795 (H) $\times$ 596 (V) pixels.

**Figure 2.6:** Honestech TriVid video capturer

### 2.2.4 Audio trigger

We have implemented an audio trigger system to start recording both the wide field camera and the spectrograph images simultaneously. This is possible thanks to a buffering system, which continuously stores the 30 last recorded frames of both the spectrograph and the wide field camera. When a change in brightness is detected in the wide field camera recording, an audio trigger is launched. A 3.5 mm male to male jack cable (see figure 2.7) is connected to the headphones output and the microphone input of the computer, so the PC can receive the sound emitted and triggers the spectrograph recording, saving also all buffered images.



**Figure 2.7:** Male to male jack wire

### 2.2.5  Weather station



**Figure 2.8:**  PCE-FWS 20 meteorological station, solar unit and outdoor temperature and humidity sensors

The GRASSP instrument uses a weather station to automatically control the inner and outer levels of temperature and humidity. The PCE-FWS 20 meteorological station (see figure 2.8) is a multi–functional device measuring 230 mm × 150 mm, which allows the accurate detection of temperature and relative humidity, both indoor and outdoor, among other weather conditions. Data can be date– and time–stamped to ensure that they can be analyzed effectively long after being collected. It transmits the indoor temperature and humidity data from the device to the computer through a USB port. The outdoor data are transmitted from the external sensors to the meteorological station via radio each 48 seconds, being the transmission range up to 100 m in the open air. These external sensors are powered by a solar unit. The operating temperature and humidity ranges of the meteorological station are summarized in table 2.2.

### 2.2.6  Thermal system

An external intercooler and a 300 W heater working at 220 V are installed to keep the temperature inside GRASSP v1.x and v2.x housings between 20 and 30 degrees Celsius. Both are painted in black to minimize its albedo
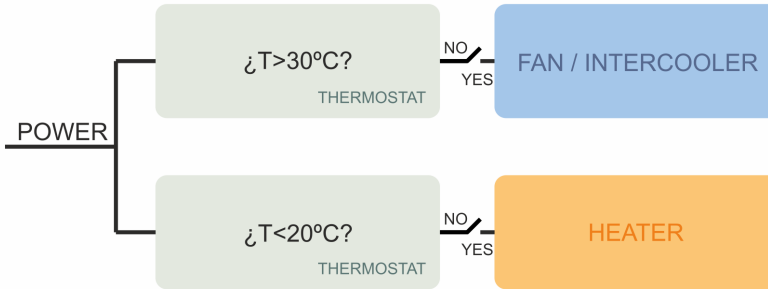
**Figure 2.9:** Block diagram of GRASSP thermal system

and they are controlled by two relays activated by two different thermostats. A block diagram of the thermal system is shown in figure 2.9.

**Table 2.2: PCE-FWS 20 meteorological station**

| Technical specifications | Operating temperature | Humidity |
|---|---|---|
| Indoor | [0 , + 60 °C] ± 0.1 °C | [1 ,99 %] ± 1 % |
| Outdoor | [-40 , + 65 °C] ± 0.1 °C | [1 ,99 %] ± 1 % |

## 2.3 GRASSP v1.x

As mentioned in the instrument overview, the two first versions of GRASSP are similar. The only difference is the spectrograph spectral range and resolution, and it will be described separately in chapter 3. In this section I will describe the common hardware that GRASSP 1.0 and 1.1 share.

### 2.3.1 GRASSP v1.x hardware outline

GRASSP v1.0 and v1.1 consist of a spectrograph and a polarimeter managed by several subsystems, all of them housed in an aluminum isothermal box, presenting a frontal window with blinds to protect the equipment from daylight. The components of GRASSP —besides the common hardware
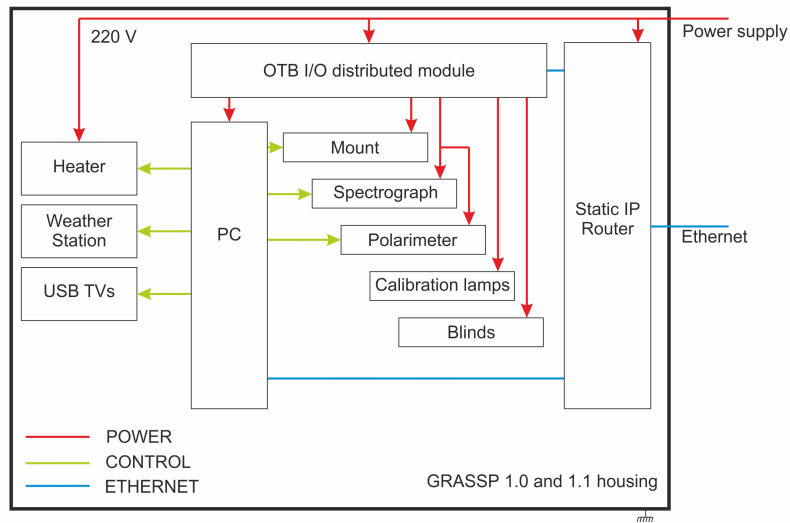
**Figure 2.10:** Schematic of GRASSP v1.x hardware

described above— are a housing, an automaton, a telescope mount, a control camera, a calibration system, a heating system and a system of blinds. GRASSP v1.x is connected to CAHA's uninterruptible power supply (UPS) of 40 KVA to provide emergency power to all loads when the input power source fails. Every sunrise, all subsystems are sequentially switched off. An automatic restart system is also developed to switch off all subsystems every morning in case of fail. The hardware scheme of GRASSP v1.x is shown in figure 2.10.

### 2.3.2 GRASSP v1.x housing

GRASSP v1.0 and v1.1 housing (see figures 2.11 up – right and 2.12 bottom – right) consists of an isothermal box of 80 kg weight and dimensions of 80 × 130 × 100 cm$^3$ (width × length × height). It is made of a welded hollow cube opened on its upper and lower faces, placed over an aluminum base

**Figure 2.11:** GRASSP v1.x housing images. Up–left: Justo Sánchez del Río installing the spectrograph on the telescope mount at the Instituto de Astrofísica de Andalucía (IAA) dependencies. Up–right: GRASSP v1.x housing at the IAA workshop. Bottom–left and right: GRASSP v1.x inner subsystems

and attached to it through hinges which are installed at the bottom of its front face.

The lateral and rear faces of the cube are made of corrugated aluminum, and the front face includes a $80 \times 80$ cm$^2$ double–glass window. The mean transmittance (T) of each glass is 69% in the band between 700 and 800 nm, defined as the fraction of incident light at a specified wavelength that passes through a sample,

$$T = \frac{I}{I_0} \qquad (2.1)$$

being $I_0$ the incident light and being I the transmitted light intensity that strikes the spectrograph and the polarimeter (see figure 2.13).

The transmittance curve of a single glass of all GRASSP versions is
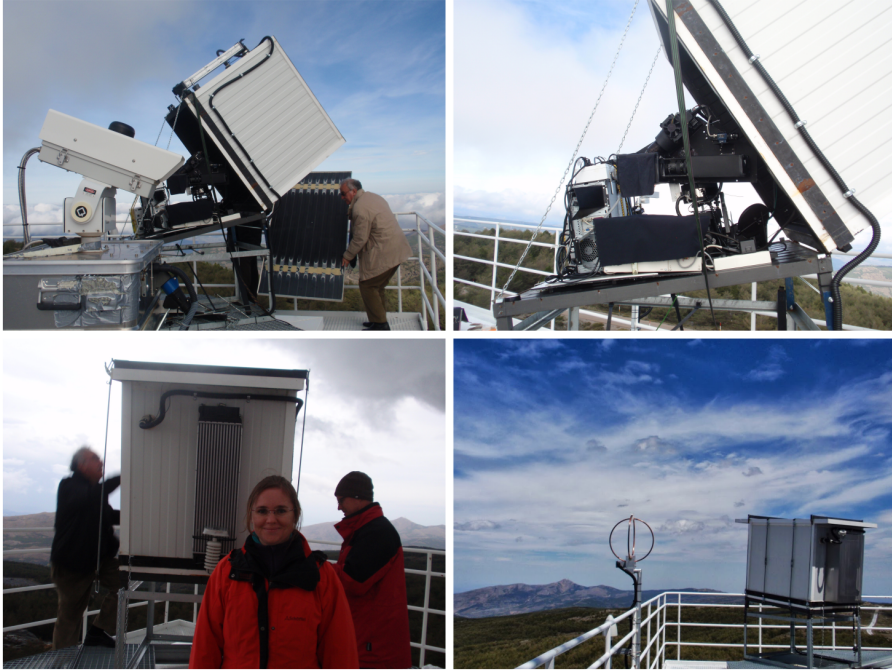
**Figure 2.12:** Installation process of GRASSP v1.x at CAHA Observatory. Up–left: Justo Sánchez del Río carrying the GRASSP v1.x cover. Notice how the housing is opened through hinges. Bottom–left: from left to right, Justo Sánchez del Río, María Passas Varo and Jens Helmling, member of CAHA Observatory staff

represented in figure 2.14.

We installed a double–glass window with an air gap between them to isolate GRASSP v1.x housing and to avoid water condensation: a single–glass window would be insufficient to isolate GRASSP v1.x due to the large size of the window glass.

The housing is equipped with remotely controlled inner blinds, of 90 cm × 70 cm dimensions, which are installed behind the window to protect the camera sensors from daylight. They are made of aluminum and are controlled with a gear under two different operation modes: normal mode and forced mode. Normal mode is activated every night once the calibration measurements are finished: the automaton powers on the blinds gear and
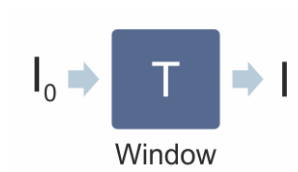
**Figure 2.13:** Incident light ($I_0$) passing through GRASSP window, with transmittance T
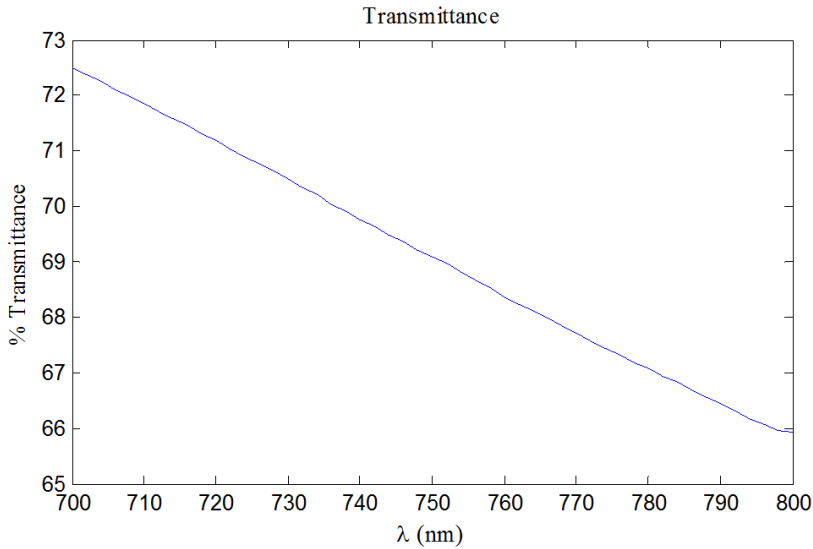


**Figure 2.14:** GRASSP window transmittance curve

the blinds are opened. Although it is not allowed to open the blinds in daylight, a forced mode has been developed to do so: firstly, the automaton switches off all cameras to protect their sensors from overexposure and then, it powers on the blinds gear to open the blinds. It can be done by sending a train of pulses from the PC to the automaton and previously, to the blinds gear. The full process will be explained in chapter 5. A movable corrugated aluminum roof of dimensions $130 \times 80 \times 10$ cm$^3$ (width $\times$ length $\times$ height) covers the hollow cube and it is secured manually with locks to avoid moisture and water getting inside the box. All the junctions are sealed with vacuum gasket tape. The box can be opened manually by

folding it up through the hinges installed at the bottom of its front face by pulling up the handles fixed to the bottom of its rear face, once the locks are opened.

The rear face of the housing presents several small drains at its bottom to evacuate possible condensation water from inside the case. It also presents two input/output ports. The first consists of a circular port of 8 cm diameter sealed through a screw plastic cap located at the right bottom corner of the mentioned rear face, and allow us to connect a screen, a mouse, a keyboard and an USB device to the inner PC of GRASSP v1.x without opening the box. The second one is a basic port sealed to a corrugated plastic tube located at the left top corner of the rear face of the housing, through which the ethernet, power supply and ground wires reach the GRASSP instrument. A $25 \times 15 \times 65$ cm$^3$ (width $\times$ length $\times$ height) radiator is also installed on this rear face of the housing, being protected with a $50 \times 20 \times 70$ cm$^3$ (width $\times$ length $\times$ height) perforated aluminum plate. The solar unit and the outdoor temperature and humidity sensors of the weather station are placed over the radiator to register the temperature changes and the humidity level. The corrugated aluminum external surface is white to maximize its albedo and its internal surface is black to avoid reflections inside to minimize its albedo.

### 2.3.3   GRASSP v1.x automaton

The GRASSP v1.x automaton is a Schneider Electric OTB1E0DM9LP (see figure 2.15), an optimized terminal block (OTB) network interface module with built–in inputs and outputs which switches on and off all GRASSP v1.x subsystems, through a Modbus protocol based software we have implemented (`GRASSP1x.m`). It will be thoroughly described in chapter 5.

The automaton also allows us to remotely identify the inner PC status (on/off) by consulting its registers. It has an ethernet port which uses a maximum of 3 simultaneous transmission control protocol (TCP) connections. It also has 12 discrete inputs, 6 relays and 2 source transistors outputs

**Figure 2.15:** Schneider Electric OTB1E0DM9LP

and terminal blocks for wiring. It works with a rated power voltage of 24 VDC.

To remotely control the automaton, we have fixed its IP manually through the encoder wheels combined with another MATLAB tool we have developed (`ChangeIP.m`) which will be fully described in chapter 5. The automaton outputs are connected respectively to the PC, the calibration lamps, the blinds, the mount limit switches, the spectrograph and the polarimeter.

A schematic of the connections between GRASSP v1.x subsystems and the automaton is represented in figure 2.16. A set of 6 relays are connected to the OTB outputs, so the different subsystems can be powered on and off remotely.

The PC power supply of GRASSP v1.0 could be connected and disconnected remotely. However, in the upgrade of the system –GRASSP v1.1— we decided to control the limit switches of the mount instead. As the automaton just provides 8 outputs, we determined to keep the power supply of the PC permanently (see the bridge on the relay R2 in figure 2.16), although it still can be powered on and off remotely thanks to the reset PC

relay connected to the PC power on/off button.

There are two operation modes to open the blinds: (1) a normal mode, which opens the blinds during night–time and (2) a forced mode, that opens the blinds during day–time and switches the cameras off to protect the CCDs from overexposure. During night–time, the *opening blinds* command of `GRASSP1x.m` sends a pulse of 24 VDC to a relay to open the blinds.

A *watchdog* timing relay changes its state if the input signal does not repeatedly cycle on and off. During day–time, when the forced mode is set, `GRASSP1x.m` sends a train of pulses to a *watchdog* timing relay of 740 $\Omega$ in monostable retriggerable mode and keeps the blinds opened. Watchdog timer relays are intended to detect software failures. If the software stops re-triggering, that is, sending 24 VDC pulses every 20 s, the relay immediately stops acting and the blinds are closed.

Another relay is used to restart the whole system once a day during one minute.

### 2.3.4 GRASSP v1.x mount

An iOptron MiniTower telescope altazimuth mount (see figure 2.17) can hold a standard payload of 11 kg thanks to its aluminum worm wheel, brass worm gear and two dovetail adaptors. The motor of the mount is a dual-axis DC servomotor, working at 12 VDC and it can operate at 9 different slew speeds ($1\times$, $2\times$, $8\times$, $16\times$, $64\times$, $128\times$, $256\times$, $512\times$ and MAX) although we reach speeds of 0.5 °/s maximum to improve the accuracy of the positioning system. The hand controller of the mount has a USB port which is connected to the computer. This will allow firmware upgrading. A USB2COM driver is needed to simulate the USB port to a RS–232 serial port to communicate the mount with the PC. The mount has an automatic over–current protection and an automatic clutch protection for both axes. A ground wire is also installed. We have modified the internal GPS to totally control the mount without depending on any commercial astronomical soft-ware. In order to avoid possible collisions when moving both spectrograph

and polarimeter, we have limited the elevation and azimuth movements by using limit switches that power off the mount when they are pressed. The FOV of the telescope mount is then 20° azimuth and 10° elevation from horizontal position. The mount also has installed two position indicators to check the azimuth and elevation coordinates, that move simultaneously with the mount. A vertical panel is also installed so that two marks indicate if the mount is positioned horizontally when the indicators match with them. By inspecting the position of these indicators compared with the horizontal marks you can also discern whether the mount is working properly. The limit switches system is a useful tool to restart the mount position remotely and automatically. There are six limit switches installed in GRASSP and they are controlled through the automaton: the boundaries limit switches and the horizontal position limit switches.

The boundaries limit switches are four and they are located in the maximum and minimum allowable positions of elevation and azimuth, i.e. the maximum elevation position, the minimum elevation position, the maximum azimuth position and the minimum azimuth position, defining the borders of the system.

The horizontal position limit switches are two and they are installed to control if the horizontal position is reached. They are located in horizontal elevation position (0° elevation) and horizontal azimuth position (45° azimuth).

The mount is feed alternatively through two different power supplies: a main power supply, which is the normal case, and an auxiliary power supply.

When one of the boundaries limit switches is pressed, the main power supply is interrupted and a software command connects the auxiliary power supply through a relay. This is done to avoid internal crashes and gear releases. The mount stops immediately and passes to be controlled through the PC. Then, a software tool we have implemented (`mount.m`) which will be fully described in chapter 5, commands a slow movement against the direction that provoked the limit switch to be pressed.

When the limit switch is released, `mount.m` disconnects the auxiliary power supply and connects the main power supply again. Then, `mount.m` restarts the mount position so it is supposed to aim to horizontal position. If the horizontal position is not reached —because the horizontal limit switches are not pressed— the final user can control the mount manually by using `mount.m` supported by the webcam installed on its rear face.

A scheme of the electronics that controls the limit switches status and the mount movements is shown in figure 2.18.

### 2.3.5    GRASSP v1.x control camera

The webcam that aims the rear part of the telescope mount helps to control the mount position remotely in case of failure: it could happen that the mount software stores a horizontal position and the corresponding limit switches are not pressed, so the system detects an error. If this happens, the system resets itself. But in rare occasions it does not do it properly, so we can use the rear webcam to move the mount under manual mode to the position we need and restart the entire system manually with the software tool `mount.m` which will be fully described in chapter 5. To do so, we use a Creative LIVE! CAM SYNC HD webcam (see figure 2.19) that has a sensor of 1.0 megapixel high definition (HD) distributed as $1280 \times 720$ pixels (horizontal $\times$ vertical). It has fixed lens focusing of f/2.4 and 1.92 mm of focal length and it is connected to the PC through a USB port.

### 2.3.6    GRASSP v1.x wavelength calibration system

The calibration system consists of a Quartz Tungsten Halogen (QTH) spectral lamp working at 230 V and 50 Hz, which emits a flat spectrum and a neon bulb installed on a power supply holder (see figure 2.20). The bulb is made of glass and contains neon gas at a pressure of 0.2 mbar. The length of the bulb is 260 mm, its width being 10 mm. The power supply voltage is of 5000 V (maximum) and it works with 10 mA current. Its dimensions are

120 mm × 90 mm × 370 mm (width × length × height ) each. The system aims in first instance to the neon bulb, switches it on through a software we implemented –`calibration1x.m`— which will be fully described in chapter 5, and records the light emission with 4 different ICCD gains to image each spectrum line with similar intensity. Notice that in a given spectrum some lines are more intense than others and, while these lines are saturated, others cannot be seen. The only way to characterize the full CCD in wavelength is to rise up the ICCD gain slowly to record all the spectrum lines with similar intensity to generate a synthetic spectrum without saturated lines. Once the neon images are recorded, `calibration1x.m` switches the neon bulb off, and aims GRASSP v1.x to a mirror that reflects the collimated light emitted by the QTH, switches it on and records the flat spectrum with 4 different ICCD gains to proceed the same as in the case of the neon lamp. The lamps can be switched on and off through the relays operated by the automaton.

The flat lamp was installed in GRASSP v1.x to provide the spectral inhomogeneities of the system to further correct them from the recorded spectra. But since the instrumental function of the system, which will be fully described in chapter 3, already includes these inhomogeneities, we finally did not use the flat spectral images.
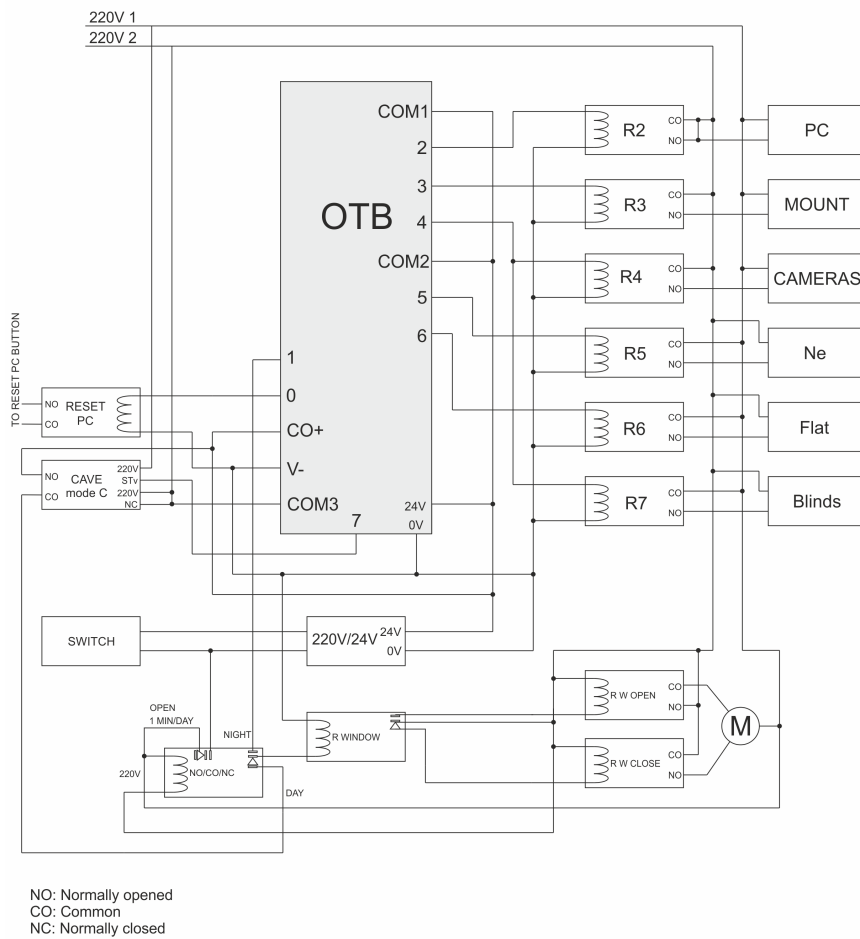
**Figure 2.16:** Schematic and connections of the Schneider Electric OTB1E0DM9LP for GRASSP v1.x

**Figure 2.17:** iOptron MiniTower telescope altazimuth mount
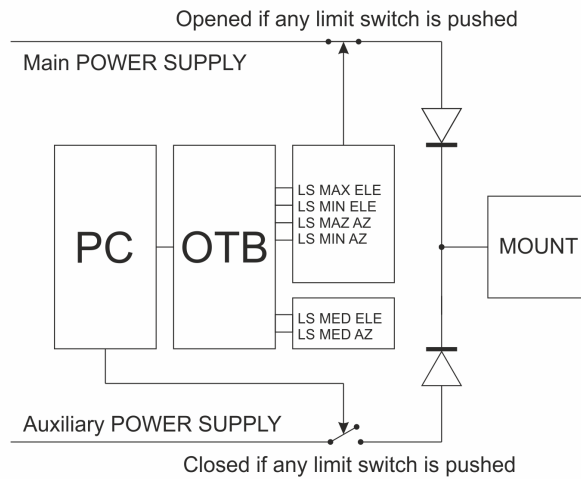


**Figure 2.18:** Limit switches system connection schematic

**Figure 2.19:** Creative LIVE! CAM SYNC HD webcam



**Figure 2.20:** Spectral lamps (right) and their power supply (left)

## 2.4   GRASSP v2.x
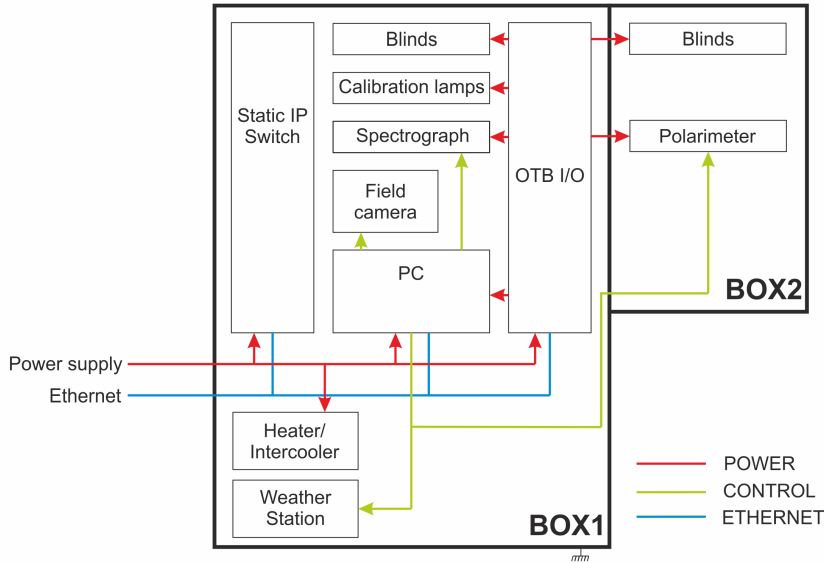


**Figure 2.21:** Schematic of GRASSP v2.x hardware

As mentioned in the instrument overview section, GRASSP v2.x was designed and developed to improve the TLE recordings statistics. The characteristics of the spectrograph and the polarimeter are the same as in GRASSP v1.x and will be described in chapters 3 and 4. Below I will describe the specific hardware of GRASSP v2.x.

### 2.4.1   GRASSP v2.x hardware outline

GRASSP v2.x consists of a medium-high resolution spectrograph and a polarimeter aimed manually with remotely controlled internal subsystems. Its housing is a result of a combination of two aluminum isothermal boxes – BOX1 and BOX2—, presenting both a frontal window with blinds to protect the equipment from daylight. The hardware components of GRASSP v2.x

—besides the common hardware described before— are a housing, an automaton, a calibration system, a heating system and a blinds system. The hardware scheme of GRASSP v2.x is shown in figure 2.21.

## 2.4.2 GRASSP v2.x housing



**Figure 2.22:** GRASSP v2.x at Castellgalí

As described before, GRASSP v2.x housing (see figure 2.22) consists of two aluminum isothermal boxes, BOX1 and BOX2, placed over an altazimuth manual mount. BOX1 contains the spectrograph, the control system, a thermal system, the calibration system and a static IP router. It consists of a welded hollow isothermal box opened on its upper face of 50 kg weight and dimensions of $60 \times 123 \times 53$ cm$^3$ (width $\times$ length $\times$ height). There is a window performed on its front face which is supplied with manual and automatic horizontal blinds systems (see figure 2.23 (a) and (b)). The manual blinds system consists of an external aluminum sheet of 3 mm thick and $38.3 \times 36.2$ cm$^2$ (width $\times$ height) which can be moved through rails to avoid sunlight overexposure of the internal instruments.
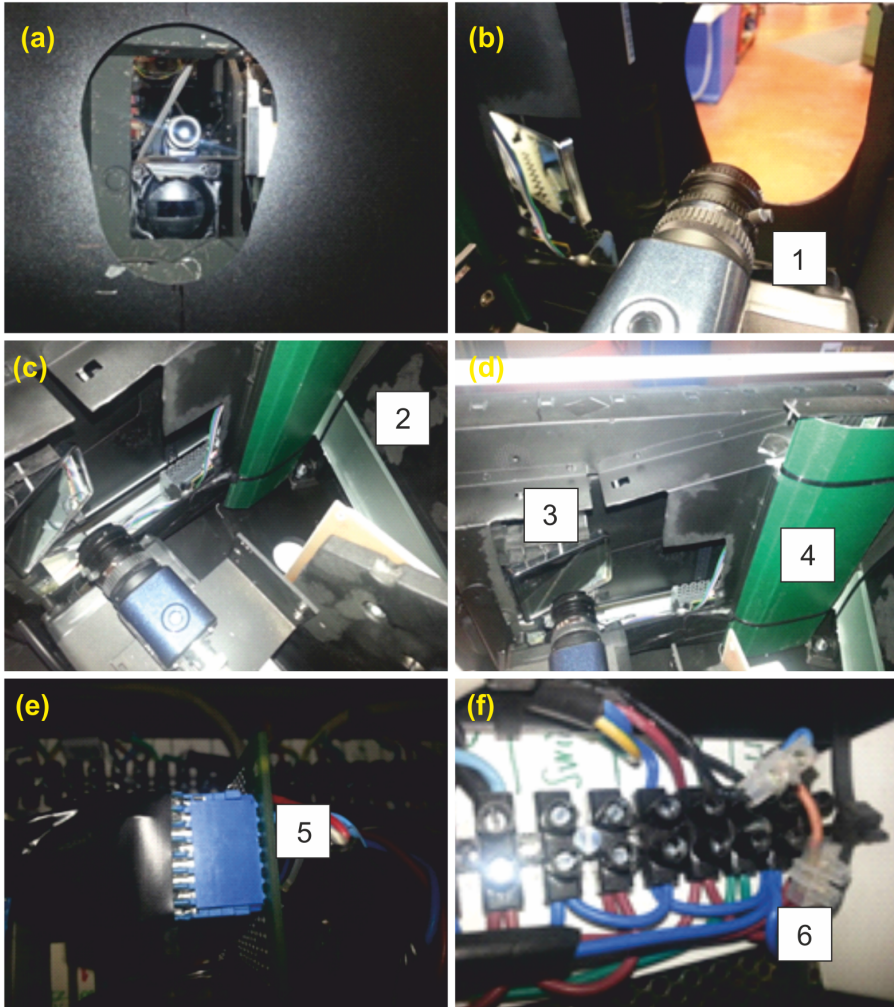
**Figure 2.23:** (a) Window performed on BOX1 front face viewed from outside. (b) Picture taken from the inner side of BOX1. Number 1 indicates the field camera location and the spectrograph input. Blinds are opened. (c) Number 2 indicates the location of the calibration box and the diffusing glass. (d) Number 3 indicates the mirror location and number 4 shows the blinds system electronics. (e) Number 5 is the blinds system electronic connector. (f) Number 6 is the power supply cable at the main shutter controller

We decided to install the external shutter because there is not a system to avoid the internal blinds to open during daylight. The automatic blinds system consists of an internal flexible PVC sheet moved horizontally by a motor through rails (see figures 2.24 and 2.25). The blinds system also participates in the calibration system: when blinds are closed, a 45° mirror installed on the rails that move the PVC sheet is placed so that the incident light of the calibration bulbs reach the spectrograph slit (see figure 2.23 (c) and (d)).

A movable aluminum housing cover of dimensions $123 \times 60 \times 5$ cm$^3$ covers BOX1 to avoid moisture and water getting inside. It is sloped to allow water to flow along. All the junctions are sealed with vacuum gasket tape.
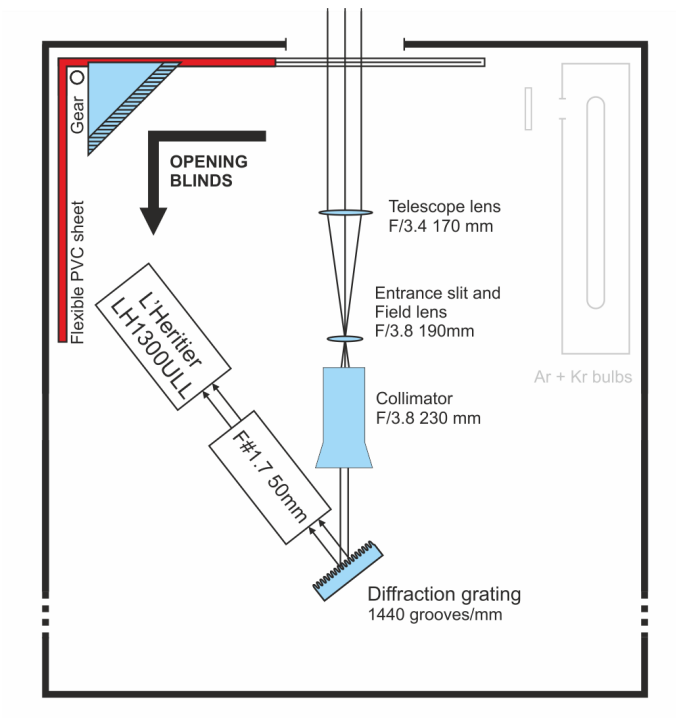


**Figure 2.24:** Schematic of the GRASSP 2.0 spectrum acquisition system

The rear face of the BOX1 presents two input/output ports. The first

one allows us to connect a screen, a mouse, a keyboard and an USB device to the inner PC of GRASSP v2.x without opening the box. The second one is a basic port sealed to a corrugated plastic tube located at the bottom face of the housing, through which the ethernet, power supply and ground wires reach the GRASSP v2.x instrument. A $25 \times 15 \times 65$ cm$^3$ (width $\times$ length $\times$ height) radiator is also installed on the bottom face of the BOX1, being protected with a $50 \times 20 \times 70$ cm$^3$ (width $\times$ length $\times$ height) perforated aluminum plate. The solar unit and the outdoor temperature and humidity sensors of the weather station are placed over the radiator to register the temperature changes and the humidity level.
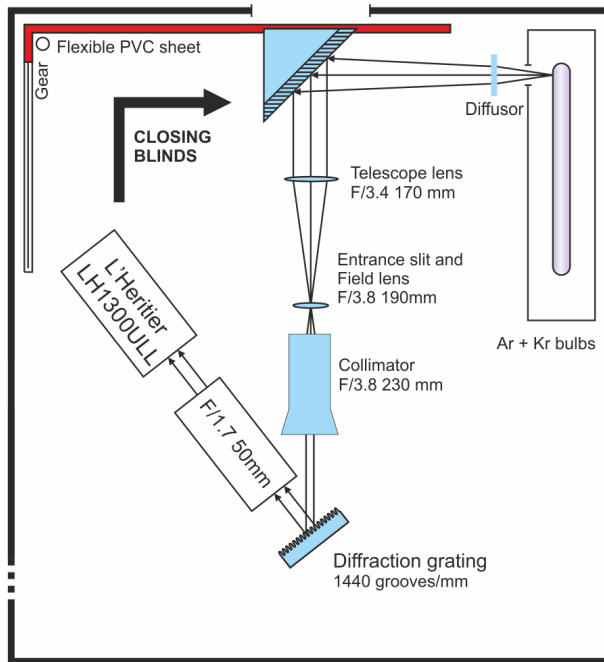


**Figure 2.25:** Schematic of the GRASSP v2.x wavelength calibration system

BOX2 —of 6 kg weight and dimensions of $32 \times 58 \times 32$ cm$^3$ (width $\times$ length $\times$ height)– will contain the polarimeter. It consists of a welded hollow isothermal box opened on its upper face. As in BOX1, there is a

circular window performed on its front face which is supplied with manual and automatic vertical blinds systems (see figure 2.26). The blinds are made of a black flexible PVC sheet.
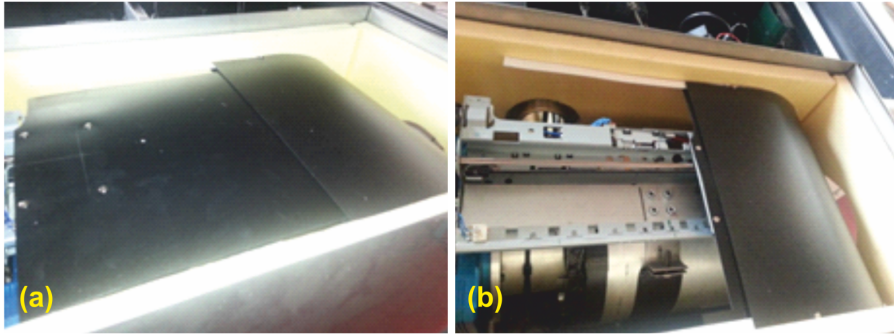


**Figure 2.26:** (a) BOX2 with opened blinds. (b) BOX2 with closed blinds. Rails and polarimeter are shown up

The manual blinds system consists of an aluminum sheet of $32 \times 32$ cm$^2$ and 0.3 mm thick joint to the aluminum roof through hinges, that pivots downwards to cover the polarimeter window. The roof of the polarimeter housing is also sloped. The automatic blinds system is similar as the spectrograph one, excepting this one lacks a calibration mirror.

Both blinds are commanded through the MATLAB application we have developed, `calibration2x.m`, which will be fully described in chapter 5.

The rear face of both boxes presents several small drains at their bottom to evacuate possible condensation water from inside. The external surface is white to maximize its albedo and its internal surface is black to avoid reflections inside, minimizing its albedo.

The glass installed in both spectrograph and polarimeter windows –and hence its mean transmittance— is identical to the one we employed to build GRASPP v1.x housing, being a single–glass in this case due to the small size of both windows.
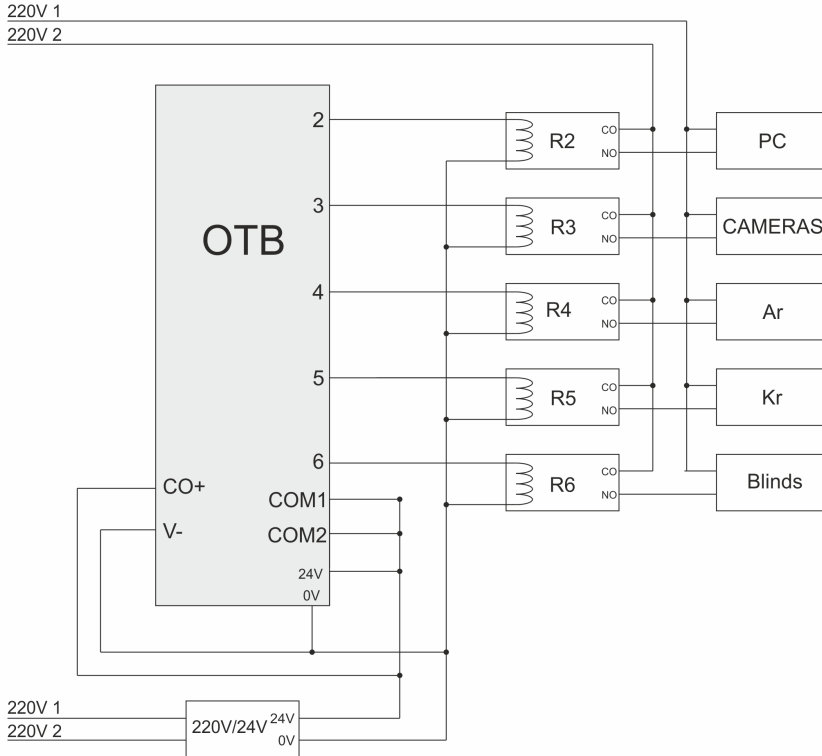
**Figure 2.27:** Schematic of the Schneider Electric OTB1E0DM9LP automaton for GRASSP v2.x

### 2.4.3 GRASSP v2.x automaton

GRASSP v2.x automaton is also a Schneider Electric OTB1E0DM9LP. The connections between GRASSP v2.x subsystems and the automaton is represented in figure 2.27. It is controlled by `GRASSP2x.m`, a software tool we developed that will be thoroughly described in chapter 5.

The automaton outputs are connected through relays to the PC power supply, the calibration lamps, the blinds and the spectrograph (since the polarimeter is not installed yet).

The PC power supply of GRASSP v2.x is connected and disconnected remotely.

### 2.4.4 GRASSP v2.x mount

The altazimuth manual mount is an aluminum structure which can rotate from 0° to 360° azimuth and from −10° to 60° elevation. As the mount is installed at the terrace of a building, there is a blind angle in azimuth, being the total observable area from −60° NW to 170° NW, spinning around 230° azimuth. The structure consists of a fixed circular azimuth ring base of 105 cm diameter and a moving circular base attached to it which can spin thanks to rolling bearings. From this structure two sets of three posts each coincide at 120 cm height, where BOX1 is attached to the structure shaft (see figure 2.28). Counterweights are also installed to keep the centre of gravity aligned to the elevation axis of the instrument.



**Figure 2.28:** GRASSP v2.x mount manufacturing process at the Astrophysics Institute of Andalusia mechanics workshop. On the figure on the left, Isabel Bustamante Díaz from IAA staff

### 2.4.5 GRASSP v2.x wavelength calibration system

As mentioned before, figure 2.25 shows the calibration system that consists of a set of two bulbs (argon and krypton) installed within two different power supply holders inside a black metallic box perforated with a 1 cm diameter hole. This output feeds a white diffusing glass so the beam is directed at the surface of a 45° mirror reaching the entrance slit of the spectrometer only when the blinds system is closed.

The bulbs and their power supplies are similar as that used in the calibration system of GRASSP v1.x.

The system records in first instance the spectrum of the argon bulb. To do so, it switches on the argon lamp through a software tool we implemented –`calibration2x.m`— which will be fully described in chapter 5, and records the emission lines of argon with four different iCCD gains to build a synthetic spectral image with no saturated spectral lines, as described for GRASSP v1.x.

Once the argon images are recorded, the `calibration2x.m` software switches the argon bulb off, switches the krypton bulb on, and records the krypton emission lines with 4 different iCCD gains to proceed the same as in the case of argon. The lamps can be switched on and off remotely through the relays operated by the automaton.

# Chapter 3

# Spectrographs

*"A storm one evening in the autumn had passed directly over the village of Wing in Rutland and moved away to the north, leaving a clear starlit sky above the thundercloud, with the stars of the Great Bear in their lowest position far above. When the storm was distant about ten miles and more, for every flash seen in the rain cloud and below, and simultaneous with it, there were one or more very slender flashes of typical lightning form from the cloud upwards and many times as long as the usual kind of lightning below."*

– C. V. Boys, *Nature, November 20, 1926*

## 3.1   Spectroscopy of TLEs

Since Dave Sentman and Gene Wescott recorded the first colour images of TLEs in 1994 (*Sentman and Wescott*, 1994), the spectral features of TLE became an object of study until the present. From TLE spectra we can study not only the chemical species involved in such phenomenon, but also the dynamics taking place within them.

The colour of TLEs can vary from blue to red, as we mentioned in the introduction of this thesis. And it is well known that the red colour that the upper region of sprites and haloes exhibit is due to the first positive group

(1PG) of $N_2$ (*Mende et al.*, 1995), which is associated with the transition from the upper electronic state $B^3\Pi_g$ to the lower electronic state $A^3\Sigma_u$ (see figure 3.1).

As mentioned before, it is possible to determine the rotational temperature of TLE plasmas or the degree of excitation and ionization of atoms and molecules caused by TLEs in the atmosphere analyzing the emitted spectrum. And hence, it is possible to estimate the surrounding gas temperature through the calculated rotational temperature. There are, at least, three methods to do so: (1) the so-called Boltzmann plot method, which needs high spectral resolution —from 0.005 nm to 0.05 nm— to extract the rotational temperature from the plasma spectrum (*Herzberg*, 1950), (2) the method proposed by Milan Simek and Santolo De Benedictis in 1995, which needs a medium–high spectral resolution —from 0.1 to 0.5 nm— to calculate the plasma rotational temperature by means of comparing the relative intensity of several peaks of its spectrum (*Simek and DeBenedictis*, 1995) and (3) a method based on the numerical fitting of synthetic spectrum to the measured one, which needs an instrument spectral resolution better than 0.5 nm (*Parra-Rojas et al.*, 2013a). Unfortunately, to date, none of the instruments deployed to analyze TLE spectra from 450 to 840 nm presents enough spectral resolution to extract the rotational temperature of TLE plasmas with a fair degree of accuracy, as the best resolution handled is 3 nm and none of the methods referenced before can be used.

Hence, one of the main objectives of the work of this thesis is to study TLE optical emissions in the visible-near infrared band with a spectral resolution better than $\Delta\lambda = 0.5$ nm to determine, among other characteristics, the gas temperature of TLE plasmas. To do so, we decided to build a ground-based medium-high resolution spectrograph remotely controlled to capture TLE spectra in a systematic way.
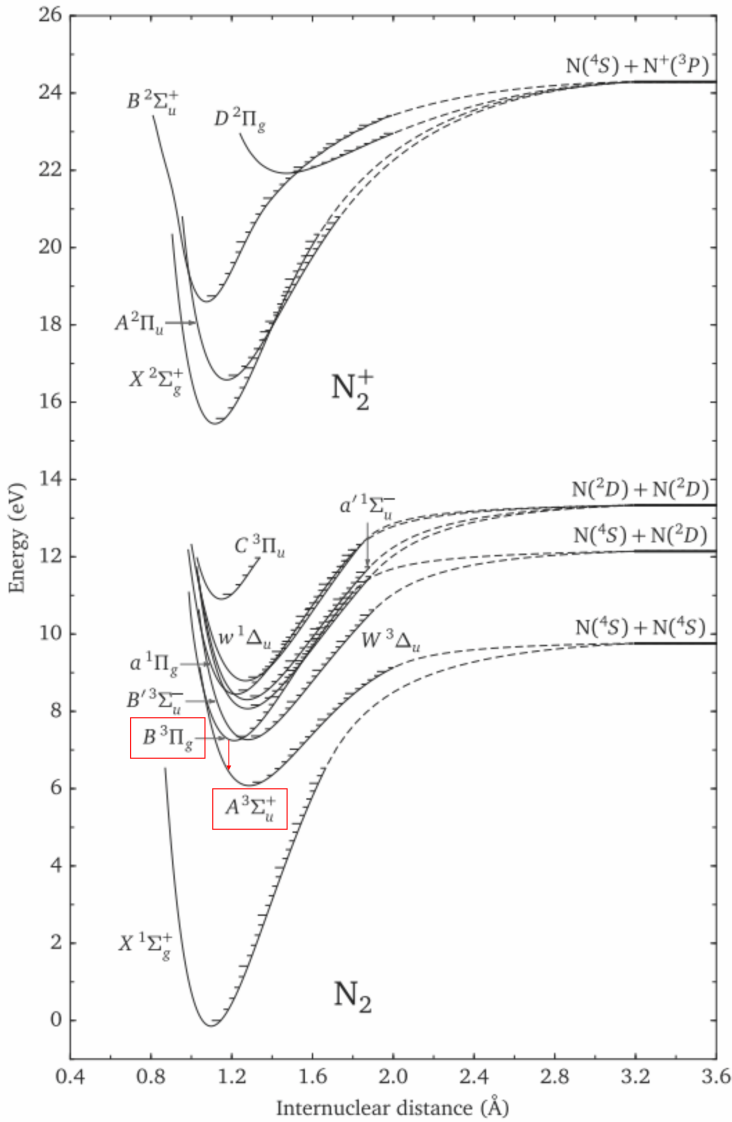
**Figure 3.1:** Simplified potential-energy diagram of the $N_2$ molecule and $N_2^+$ ion. Each curve represents the sum of the electrostatic potential energy of the nuclei and the electronic energies as a function of the internuclear distance, and defines the potential energy for vibrational motion of the nuclei. The vibrational energy levels are shown as tick marks within the respective curves (*Kanmae*, 2014)
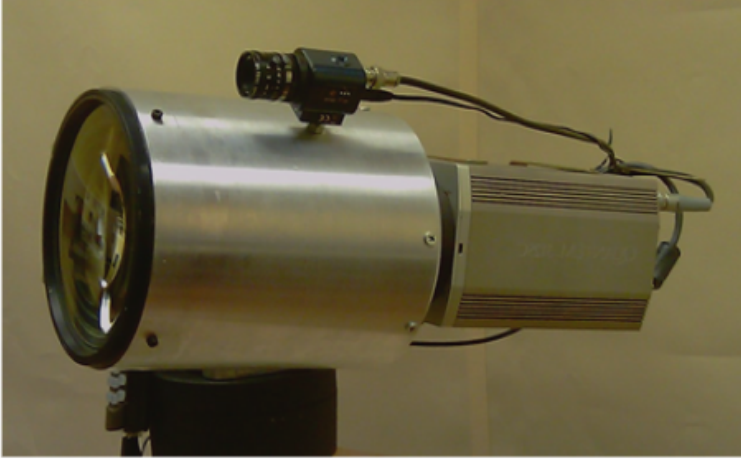
**Figure 3.2:** Sprite Etalon Spectrograph

In first instance, we designed and developed a Fabry-Pérot narrow-band spectrograph: the so-called Sprite Etalon Spectrograph (SES – see figure 3.2) (*Passas et al.*, 2011). It worked in the band between 665 nm and 675 nm with high resolution (R = $\lambda/\Delta\lambda$ = 5500; $\Delta\lambda$ = 0.13 nm).

Unfortunately, during SES calibration we noticed that, although the spectrograph resolution was high, the coating of one of the reflectors created interference and two modes of the same spectral line appeared at different radii. This effect implied a duplication of all spectral lines making it impossible to discern between them, specially when analyzing spectral molecular bands.

So we discarded the etalon concept and opted for a slit spectrograph, renouncing to high spectral resolution in favor of the spectral range. So in 2011 we designed and developed a new grating spectrograph, SPEC1, this time with a free spectral range of 100 nm between 660 nm and 760 nm and a spectral resolution of R = $\lambda/\Delta\lambda$ = 1247 ($\Delta\lambda$ = 0.58 nm). This spectrograph, SPEC1 (see figure 3.3), was installed within the so called GRAnada Sprite Spectrograph and Polarimeter —GRASSP— at the 2.2 dome of the Centro Astronómico Hispano-Alemán (CAHA) Observatory in Calar Alto, Almería, Spain. SPEC1 participated in a two-year observational

campaign and recorded several lightning spectra. Unfortunately, although the GRASSP v1.0 field camera captured more than 50 TLEs during this period, no TLE spectra were recorded since the spectrograph slit covered a very narrow region of the sky and all thunderstorms occurred far away from its location.
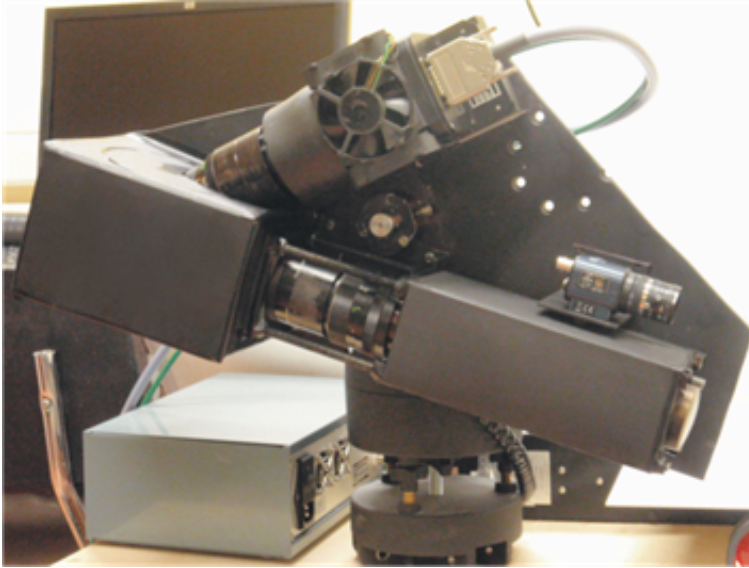


**Figure 3.3:** SPEC1

Meanwhile, as mentioned in Chapter 2, we noticed that the triplet line of OI around 777.19 nm (typical emission line in lightning spectra) could be somehow involved in the chemical processes taking place within TLEs (*Parra-Rojas et al.*, 2013b), but our system was not able to reach such wavelengths. Thus, we decided to upgrade SPEC1 maintaining its optical design. The objective was to shift its spectral range to the near infrared and to improve the spectral resolution by narrowing the slit and enlarging the dimensions of the image by installing a better analog-to-digital board. The new version of the spectrograph, SPEC2, has a spectral range between 695 nm and 795 nm with a spectral resolution of $R = \lambda/\Delta\lambda = 3309$ ($\Delta\lambda = 0.235$ nm). In July 2014 we installed SPEC2 within GRASSP v1.1

and we recorded several spectral images of lightning and five frames of a meteor passing through the spectrograph slit (*Passas et al.*, 2016a). Regrettably, again, although the field camera recorded many TLEs, none of them matched the slit position and no spectra were recorded with enough intensity to extract any valuable information. The reason it was so difficult to record a TLE spectrum from CAHA Observatory was that electrically active thunderstorms mostly occur in northern Spain, far away from CAHA (see figure 2.1), so the area of TLEs covering the field camera sensor is very small. In addition, the slit spectrograph is very narrow so it covers just a tiny area of the field camera sensor (see figure 2.2).

In December 2014, during an annual meeting of the Thunderstorm Effects in the Atmosphere-Ionosphere System (TEA-IS) team, we noticed that our colleagues from the Universitàt Politècnica de Catalunya (UPC team), recorded many huge TLEs from the north of Spain. So we decided to start a close collaboration with them integrating SPEC2 within a new instrument (GRASSP v2.x) and placing it in the north of Spain to improve the likelihood of the detection of TLEs spectra.

Since the installation of SPEC2 in May 2015 in Castellgalí, Barcelona, we have detected 44 high-resolution TLEs spectra. We notice that the observation area we cover from the Castellgalí observation site is much wider than from the CAHA Observatory site. Moreover, the probability of observing a TLE is much higher from the Castellgalí site, basing on the average flash densities in Europe from January 2008 until December 2012 (see figure 2.1).

## 3.2   GRASSP spectrographs

In this section we describe the different spectrographs we have developed for the GRASSP instrument: first we will roughly define the optical designs of the etalon and slit spectrographs, respectively, followed by the thorough description of the characterization of the slit spectrographs. As we finally

did not install the SES instrument, its characterization process will not be described in this thesis.
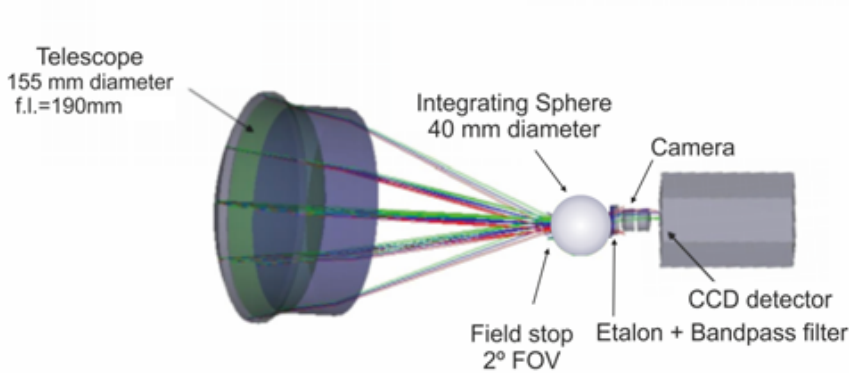


**Figure 3.4:** Sprite Etalon Spectrograph optical scheme

Figure 3.4 shows the optical scheme of the *Sprite Etalon Spectrograph* (SES), which consists of a 155 mm aperture telescope of f/3.4 and 190 mm focal length, a 20 mm diameter etalon and a band pass filter from 640 to 660 nm. The field of view of SES is 4° in diameter. The SES detector is a Peltier–cooled Electron Multiplying Charge Coupled Device (EMCCD) QuantEM of $512 \times 512$ pixels and 16 $\mu$m/px. The mean quantum efficiency of the EMCCD is 90% within the spectral range.

Figure 3.5 shows the optical design of SPEC1 and SPEC2: it consists of a f/3.4 and 170 mm focal length lens telescope which gathers an optical beam at its focal plane, where a field lens (f/3.8, 190 mm focal length) is placed just before the focal plane, where the slit is located, in order to match the pupil position to the collimator entrance pupil. Otherwise a larger vignetting would affect the FOV as we move out of axis.

The slit is oriented horizontally to optimize the likelihood of TLEs detection and has an selectable width. Resolution is driven by slit width once grating, camera and collimator focal lengths are fixed. The slit cannot be narrowed beyond Nyquist sampling at the detector. Moreover photon flux
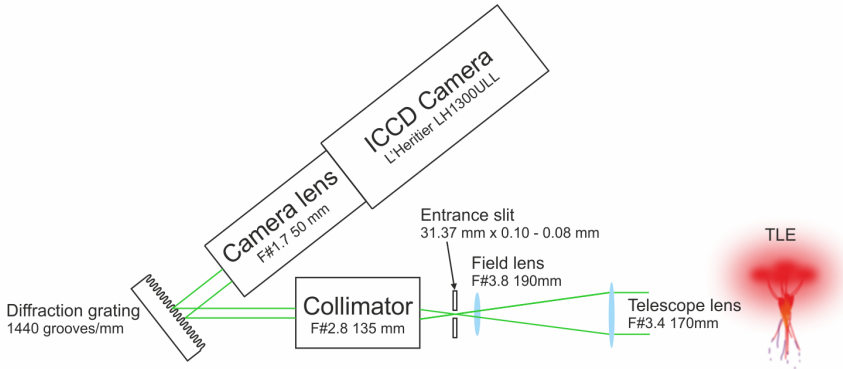
**Figure 3.5:** SPEC1 and SPEC2 optical scheme

is proportional to the slit area, thus the narrower the slit is, the less photons reach the iCCD.

The dimensions of the slit are 0.10 mm × 31.37 mm (width × length) in SPEC1, and 0.08 mm × 31.37 mm (width × length) in SPEC2. We measured the field of view of the spectrograph by recording the spectrum of a star from the top to the bottom of the spectrograph iCCD, and matching the pixel coordinates of the star in the field camera images so we estimated the length and position of the slit superimposed to the field camera sensor (see figure 3.6). As the FOV of the field camera is 21.6° × 17.4° (H × V) and the area that the slit covers on the field camera CCD is about 4 px × 200 px (width × length) for SPEC1 and 3 px × 200 px (width × length) for SPEC2, the FOV of SPEC1 is then $0.12 \pm 0.03° \times 6.00 \pm 0.03°$ and $0.09 \pm 0.03° \times 6.00 \pm 0.03°$ for SPEC2.

The bore sighting of the camera and spectrograph were pre calibrated using star images. This allowed the precise determination of the spatial position of the spectrograph slit in the imaging camera field of view and accurate real time pointing of the spectrometer through the imaging camera. This technique also permitted the recording of the two dimensional image of the sprite simultaneously with the sprite spectra.

A f/2.8 and 135 mm focal length collimator is placed following the field lens. After the 1440 grooves/mm and 70×70 mm aperture diffraction grating and a camera lens of f/1.7 and 50 mm focal length, a commercial monochrome intensified CCD (iCCD) L'Heritier LH 1300 ULL XVGA camera provides the spectral pattern.
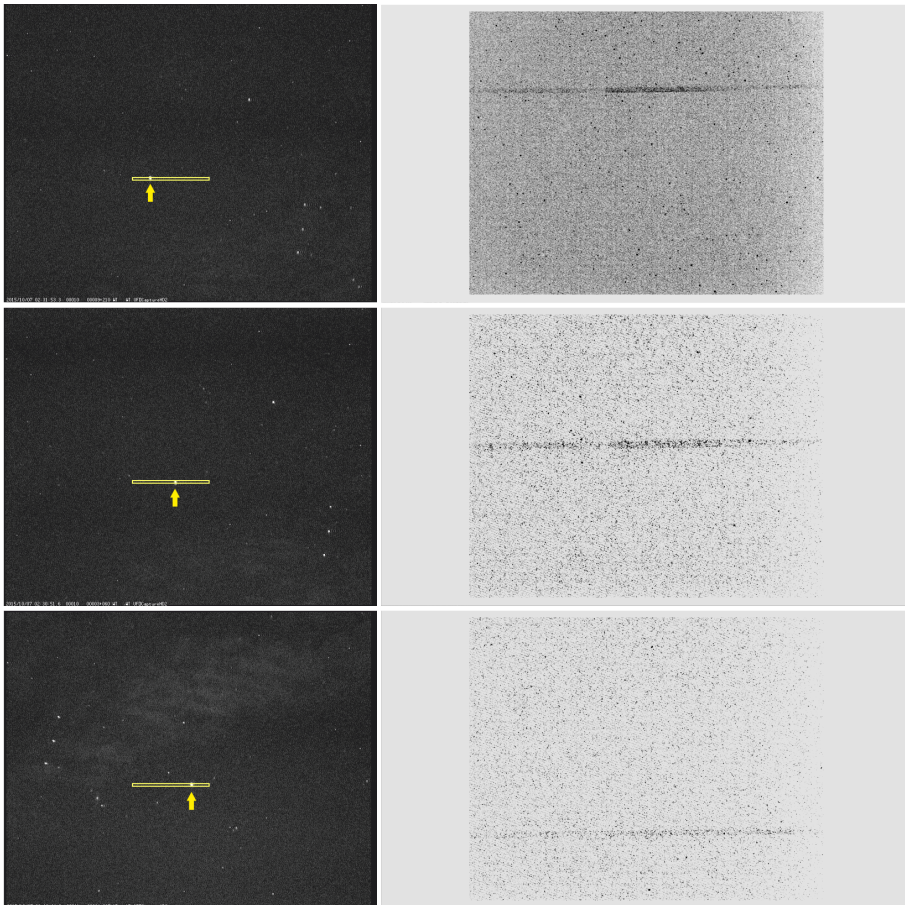


**Figure 3.6:** Stars over different regions of the slit (left) and their relative raw spectra (right)

The streak tube of the image intensifier is a Photonis Super Gen S25 photocathode of 17 mm diameter with spectral response up to 950 nm, equipped with a P20 phosphor, with a decay (persistence) time of tens of ms (*Hoess and Fleder*, 2000). It is powered at 40 W maximum. The Super Gen S25 sensitivity reaches its maximum value in the 700—800 nm spectral range. In particular it varies between 65.7 and 67.7 mA/W for wavelengths between 700 and 800 nm, peaking at 750 nm. Its quantum efficiency ranges between 11.6 % at 700 nm and 10.2 % at 800 nm. The gain of the iCCD is manually adjustable in three different stages (figure 3.7): (1) the exposure time stage, (2) the photocathode intensifier tube gain (TG) stage and (3) the electronic gain stage. First, we can set the exposure time from 10 $\mu$s to 40 ms, this parameter being the time during which the CCD collects photons thanks to an electronic shutter. This concept is different from the frame rate, which is always 25 fps (40 ms). When setting the exposure time to a value under 40 ms, there is a loss of information corresponding to the period that the CCD is not collecting any photons. This is the reason we set the exposure time to the maximum value (40 ms): as TLEs last few ms, this exposure time maximizes the likelihood of the recording of the optical event. Once the exposure time is set, we can also increase the gain of the photocathode intensifier tube from 0 dB to 60 dB. The final stage consists of an electronic gain from 0 dB to 30 dB, obtaining a maximum intensification of 90 dB besides the selected exposure time.

A conical fiber taper adapts the 17 mm diameter to the 11 mm diameter entry face of the 2/3 CCD, being the demagnification factor 0.63. The CCD is a Sony ICX285AL interline solid-state image sensor of 1360 (H) × 1024 (V) pixels and 17.7 $\mu$m/px.

The iCCD is cooled by a Peltier system controlled by the PC through a RS232 connector.

All different features of the camera are remotely controlled by GRASSP inner PC through a USB connector according to the instructions com-

manded by a MATLAB software that we have developed for that purpose which will be fully described in chapter 5.

The information above is fully described in (*Passas et al.*, 2016b).
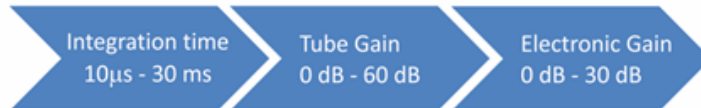


**Figure 3.7:** L'Heritier iCCD gain stages

In SPEC1, a CANOPUS ADVC-55 analog-to-digital video converter (see figure 3.8 – left) digitizes the L'Heritier iCCD output. A FireWire IEEE—1394 connector wires the converter output to the computer. The CCIR 170 format support we use is 576 (V) × 720 (H) pixels and it supplies a colour precision of 8 bits. It is wired to the L'Heritier Camera through a serial digital interface (SDI) input.
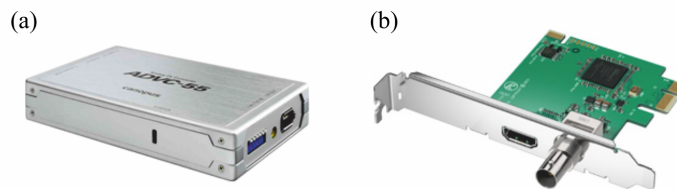


**Figure 3.8:** (a) CANOPUS ADVC-55 analog to digital video converter (SPEC1). (b) BlackMagic Design DeckLink Mini Recorder analog to digital converter board (SPEC2)

In SPEC2, a Blackmagic Design Decklink Mini Recorder analog to digital board (see figure 3.8 – right) digitizes the L'Heritier iCCD output. The HD format support we use is 1080 (V)× 1920 (H) pixels. It supplies a colour precision of 10 bits, although we select only 8—bit precision due to

software compatibilities. The computer interface is a PCI Express of 1 lane, compatible with 1, 4, 8 and 16-lane PCI express slots. It is wired to the L'Heritier Camera through a SDI input.

The differences between SPEC1 and SPEC2 —different slit width and different analog to digital digitizer— result in a significant improvement in the spectral and spatial resolutions of the spectrograph, as we will see in the following sections. The different versions of the GRASSP instrument, their ubications and related spectrographs are shown in figure 3.9.

Table 3.1 shows a comparative between SPEC1 and SPEC2.

**Table 3.1: SPEC1 and SPEC2 features**

| Features | SPEC1 | SPEC2 |
|---|---|---|
| Wavelength range | 660 nm  760 nm | 695nm - 795 nm |
| Mean spectral resolution | 0.56 nm | 0.23 nm |
| Mean resolving power | 1365 | 3309 |
| Linear dispersion | 0.156 nm | 0.078 nm |
| Time resolution | 10 $\mu$s - 40 ms | 10 $\mu$s - 40 ms |
| Slit size | 31.37 mm $\times$ 0.10 mm (H $\times$ V) | 31.37 mm $\times$ 0.08 mm (H $\times$ V) |
| Field of view | $6.00 \pm 0.03°\times 0.12 \pm 0.03°$ (H $\times$ V) | $6.00 \pm 0.03°\times 0.09 \pm 0.03°$ (H $\times$ V) |
| A/D converter | Canopus ADVC55 | BlackMagic Design |
| Total pixels | 795 $\times$ 596 px (H $\times$ V) | 1920 $\times$ 1080 px (H $\times$ V) |
| Effective pixels | 641 $\times$ 320 px (H $\times$ V) | 1280 $\times$ 630 px (H $\times$ V) |
| Operative period | Jun 2012 — Jul 2014 (GRASSP v1.0) | Sep 2014 — Feb 2015 (GRASSP v1.1) |
| | | May 2015 — May 2016 (GRASSP v2.0) |
| | | May 2016 — now (GRASSP v2.1) |
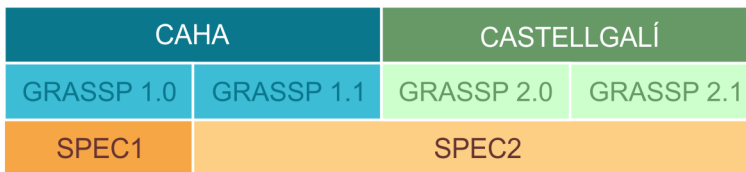


**Figure 3.9:** Different versions of the GRASSP instrument, their ubications and related spectrographs

### 3.2.1 Characterization of SPEC1

The goal of this section is to fully characterize the SPEC1 spectrograph. First, we will calibrate SPEC1 in wavelength to calculate the distortion correction array that will allow us to straighten the recorded spectra. Then, we will calculate its spectral response and we will obtain the SPEC1 spectral and spatial resolutions. Finally, we will check the instrument reliability by comparing a spectrum of an air lamp obtained with SPEC1 with the spectrum of an air plasma generated in a hollow cathode reactor and measured with a commercial Jobin Yvon Horiba FHR1000 spectrometer.

#### 3.2.1.1 Spectrograph calibration

Calibration of measuring instruments is necessary to establish their accuracy and to determine the traceability of the measurement to standards.

We have calibrated every version of the GRASSP spectrograph to analyze the measurements reliably.

The complete calibration of the spectroscopic system consists of three tasks: (1) a wavelength calibration, which assigns an absolute wavelength to each pixel of the iCCD, (2) a distortion correction, which straightens the curved spectrum image and (3) a flux calibration, which provides the spectral sensitivity of the spectrograph. Distortion correction and wavelength calibration are performed whenever a spectrum is recorded; the instrument function is calculated just once.

#### *Wavelength calibration and distortion correction*

Digital images are arrays of pixels. They have a finite number of rows (horizontal) and columns (vertical). The coordinates of a pixel determine its position in the array, so every pixel is identified by means of its row and column numbers. The values of the pixels determine the number photons that reached each element of the array. We will refer to this parameter as

the relative intensity of the pixel, that ranges between 0 and 255 since we use an 8-bits digitizer.

In slit imaging spectroscopy, images show the spectral pattern of the light striking the spectrograph slit. When recording the spectrum of a luminous event through a slit spectrograph, both spatial and spectral information are recorded simultaneously. If we divide the slit in 596 subelements —as SPEC1 iCCD has 596 rows— the light striking on each subelement of the slit projects a spectrum in a row of the iCCD (see figure 3.10).
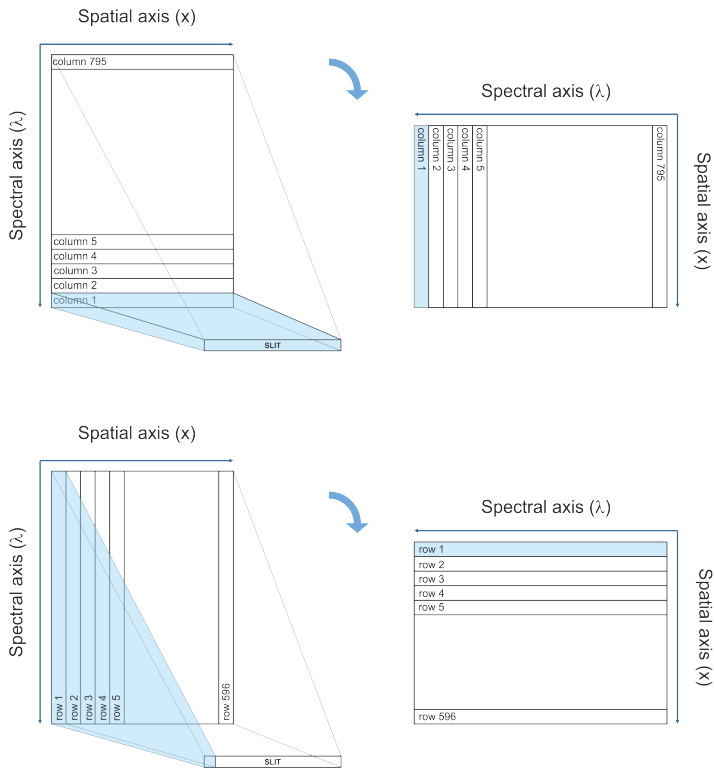


**Figure 3.10:** Projection of the light striking on the slit over the iCCD

The spatial information is the image seen through the slit while being boresighted to the luminous event. In an ideal spectrograph this spatial information is obtained by integrating every row of the spectral pattern.

On the other hand, in an ideal spectrograph the spectral information is obtained by integrating every column of the spectral pattern.

All long slit spectrographs where dispersion is provided by standard diffraction gratings in a collimated beam provide curved slit images. These are unavoidable and depend on the grating entrance/exit angles and the number of lines per mm. Moreover, camera field distortion will also happen in a much smaller degree at the detector. So, to extract reliable information from our spectrum, first we have to straighten this undesirable effect by calibrating the spectral image in wavelength.
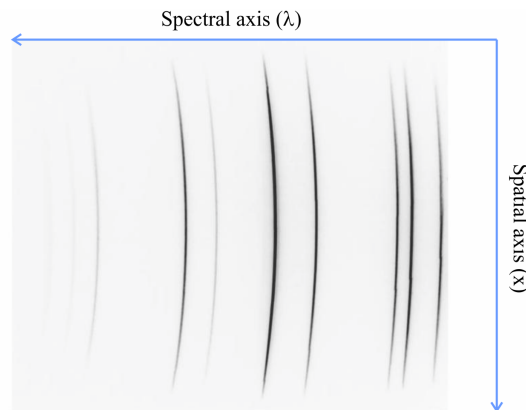


**Figure 3.11:** Spectral pattern of a Ne lamp as it is detected by the iCCD

*Wavelength calibration*

The goal is to obtain a correspondence array between every pixel coordinate in the iCCD and a single wavelength. To do so, first, we illuminate the spectrograph with a collimated beam from a spectral lamp. We choose an element with spectral lines around the wavelength range we are interested in, ensuring that there are enough emission lines —with high enough relative intensities— covering all the targeted spectral range.

Atomic spectral databases are useful to find a proper spectral lamp. As we are interested in the spectral range from 660 to 760 nm, in SPEC1 we used a neon lamp, which shows spectral lines with high relative intensity

from 659.90 to 754.00 nm. In figure 3.11 we plot the spectral pattern of the collimated beam of the neon lamp. We notice that (1) the pattern is curved, (2) some lines are brighter than others, (3) lines do not fill the whole height of the iCCD and (4) the spectral (horizontal) axis is inverted: the longest wavelengths appear on the left side of the iCCD and the shortest appear on the right side of the iCCD, in descending order.

It is very convenient to cover the whole iCCD with spectral lines of similar brightness to calibrate the spectrograph reliably and correct the spectral curvature. However this cannot be done using a single spectral image since it shows all spectral lines with different brightnesses. The goal is to build up a synthetic spectrum showing up spectral lines with similar brightness covering the whole iCCD, and the more the better. So, as the iCCD of SPEC1 is intensified, we can increase the gain of the system so the weaker spectral lines can show up, despite the saturation of the brighter ones.

Hence, we recorded several spectral images with different gain values; then, we trimmed them vertically, so all spectral lines appeared in every row of the spectrum, and also horizontally, showing up only the region of the iCCD where we could extract information. Finally, as the spectral (horizontal) axis is inverted in the process of acquisition of the spectral pattern, we flipped these trimmed images to show up the spectral axis in increasing order (see figure 3.12).

We built up our synthetic spectrum from the trimmed spectral images related to each gain value by selecting the spectral lines with similar brightness. This process is shown in figure 3.13.

Then, we assigned each pixel to a certain wavelength. But, as spectral lines width covers more than a pixel due to the spectral resolution of the system, we have to find the pixel corresponding to the maximum intensity peak of these lines to assign it to a certain wavelength. To do so, for every row of the synthetic spectral pattern we calculated the coordinates of the pixel corresponding to the center of the full width half maximum of each
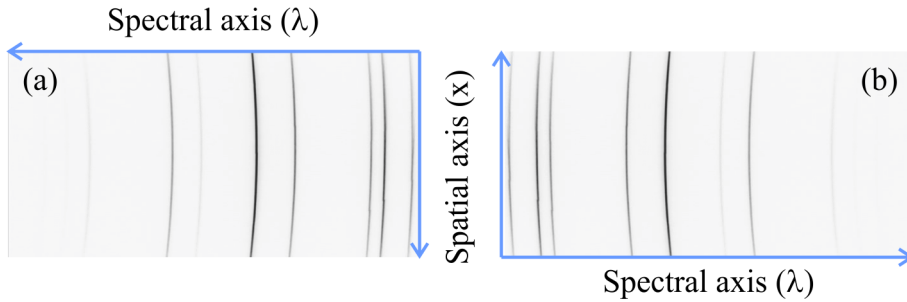
**Figure 3.12:** (a) Trimmed spectral pattern of the Ne lamp on the detector. (b) Trimmed and flipped spectral pattern of the Ne lamp on the detector

spectral line. Thus, we got a cloud of pixels defining each Ne spectral line that we fitted with a cubic curve to obtain a one-pixel-width curve for each spectral line of Ne, as it is shown in figure 3.14. Next, we identified the corresponding wavelengths by comparing the distances between spectral lines to the well-known gaps of Ne spectrum (*Kramida et al.*, 2015). Finally, we assigned the coordinates of each pixel from the one-pixel-width curves to the wavelengths we identified for every row. Then, we fitted these coordinates with a cuadratic curve for each row, as figure 3.15 shows. As we built up the synthetic spectral pattern of Ne by copying and pasting each spectral line —with their own background— over a zero-array, there is a background offset around them. Anyway, this offset does not affect in the calculation of the FWHM of each spectral line.

This process generated a calibration array to correct the curvature of the spectra recorded with SPEC1 hereinafter, associating every pixel coordinate in the iCCD to an absolute wavelength.
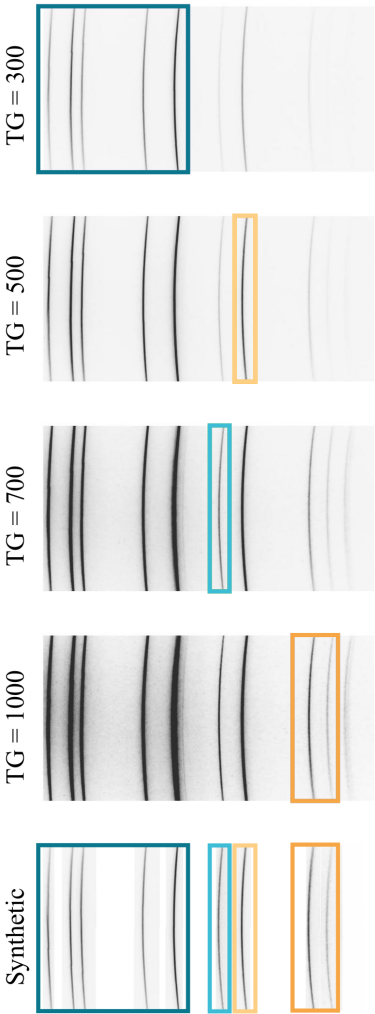
**Figure 3.13:** Synthetic spectrum of Ne
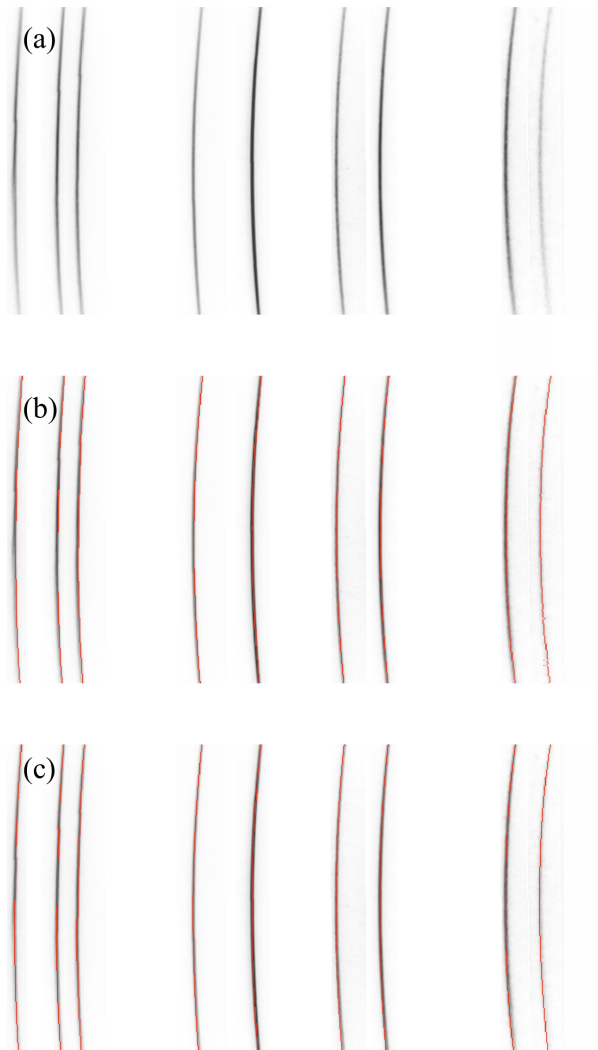
**Figure 3.14:** a) Synthetic spectrum of Ne. b) Cloud of pixels over the maximum intensity in spectral lines of Ne. c) Fitting curves overlapping Ne spectrum
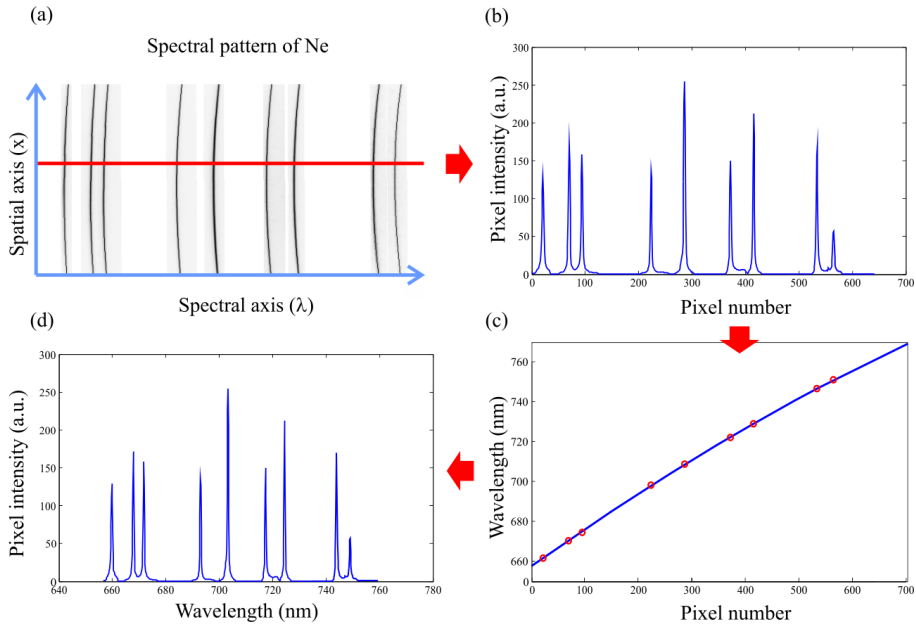
**Figure 3.15:** (a) Trimmed and flipped spectral pattern of the Ne lamp on the detector. Row 100 is shown in red. (b) Plot of row number 100 as a function of the pixel number. (c) Red circles show the wavelength assignment to the pixels corresponding to the mean FWHM of each spectral line for row number 100. The blue solid line shows the fitting curve that assigns a wavelength to each pixel of the iCCD for row number 100. (d) Plot of row number 100 as a function of the wavelength.

### Distortion correction

Distortion correction of a spectrum consists in straightening it so every column of the spectral image is related to an unique wavelength.

To do so, we need three arrays of the same dimensions: (1) the spectral image, an array of pixels whose elements are associated to a relative intensity value, (2) the calibration array, which was calculated before and whose elements are associated to an absolute wavelength and (3) an auxiliary array, where the straightened spectrum will be stored. Each column of the auxiliary array is assigned to an unique and equidistant wavelength. This is done by dividing the spectral range of SPEC1 by the number of columns

of the effective sensor.

Next, we round the wavelength values of the calibration array to the closest wavelength of the auxiliary array columns. Then we shift every row of the calibration array, and therefore we shift also the spectral image, so that the relative intensities of the pixel coordinates with the same wavelength value are aligned in the same column of the auxiliary array. If two or more pixels of the same row of the calibration array are rounded to the same wavelength value, we calculate the mean value of their intensity in the spectral image and we store this value in the auxiliary array, being the row contracted. If after rounding the calibration array values there is a lack of a certain wavelength in a row, we interpolate between the intensities of the neighbour pixels of the spectral image row, and store this value in the auxiliary array, being the row expanded in this case.

Figure 3.16 shows the resultant spectrum of the Ne lamp after wavelength calibration and distortion correction.
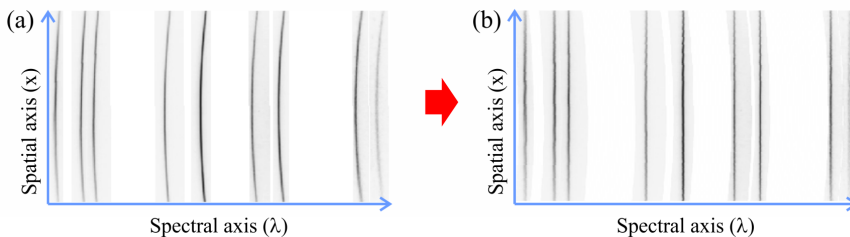


**Figure 3.16:** Curvature correction for the Ne spectral pattern

### *Instrument function*

Every spectroscopic system is wavelength and intensity dependent: its inner components themselves behave heterogeneously, responding to the intensity of incident beams differently. So, a spectrograph by itself is not able to reproduce the observed intensity of light faithfully as a function of the wavelength.

The way we can loyally translate the incident intensity of light in the iCCD into spectral radiance is by correcting the spectral image by the instrument function of the spectroscopic system. The instrument function of a spectroscopic system represents its spectral sensitivity as a function of the wavelength, and we have calculated it following the steps defined in *Fantz* (2006), basically comparing a known spectral response to the one obtained with the instrument we want to characterize.
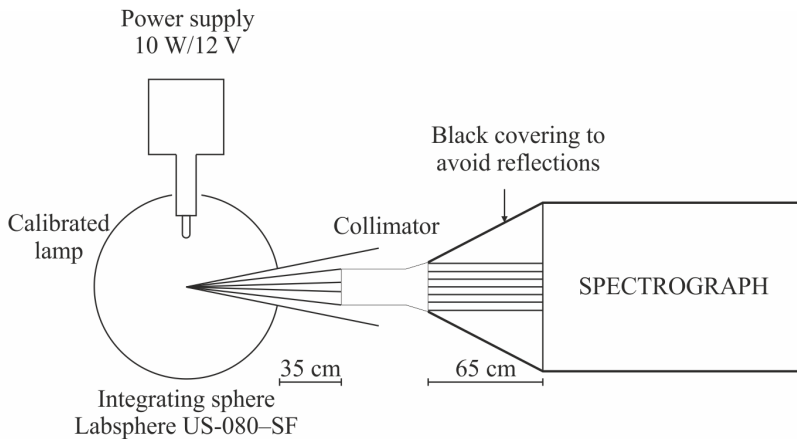


**Figure 3.17:** Flux calibration setup of GRASSP spectrographs

To do so, we obtained the spectral radiance of a calibrated Quartz Tungsten Halogen (QTH) spectral lamp with SPEC1 with a set of different gains and exposure times. Figure 3.17 shows the setup of the measurements: we introduced the QTH lamp within a standard integrating sphere (Labsphere US-080SF) of 8" coated with Spectraflect $BaSO_4$ base paint, with a known wavelength dependent reflectance ($R_{US-080-SF}(\lambda)$). The output light was collimated to reach SPEC1, obtaining an iCCD spectral image. We covered part of the system (from the collimator to the spectrograph) with a black cloth to avoid undesirable reflections.

We reduced the spectral data from SPEC1 as follows:

1. We obtained the raw data from directly recording the spectrum of the QTH through SPEC1 as shown in figure 3.17.

2. We selected one frame ($Frame_i$) and the next ($Frame_{i+1}$) of the recorded spectrum.

3. We corrected the P20 phosphor persistence effect of the phototube of the iCCD (see below) using equation

$$I = Frame_{i+1} - 0.79 Frame_i, \qquad (3.1)$$

obtaining the spectral image $I$.

4. We subtracted bias and background spectral images from $I$, obtaining the spectral image $I_c$.

5. We trimmed $I_c$ so it fitted the wavelength calibration area, obtaining $I_{trimmed}$.

6. We flipped $I_{trimmed}$ to set the spectral axis from left to right, obtaining $I_{flipped}$ (see figure 3.18 (a)).

7. We applied the wavelength calibration and distortion correction array calculated previously to $I_{flipped}$ to straighten the spectrum, obtaining a relative spectral response of our system to the calibrated QTH lamp for each row of the iCCD $I_{corrected}$ (see figure 3.18 (b)).

8. We smoothed every row of $I_{corrected}$ by a fourth degree polynomial so we avoided the noise pattern of the iCCD, obtaining $I_{smoothed}$. All zero values (often found in the borders) were changed to one to avoid dividing by zero. Thus, we obtained the array $QTH_{SPEC1}(\lambda, i)$, where $\lambda$ is the wavelength and $i$ is the row number.

Steps 3) and 4) will be fully described in the data reduction section.

We repeated this process for 8 different gain values to further correct the spectral images according to the gain value they were recorded with. Thus, we obtained 8 different instrument functions, one per the preferred gain value.
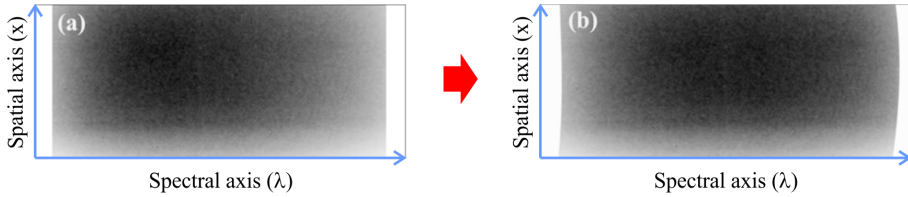
**Figure 3.18:** Curvature and wavelength correction of a QTH lamp spectrum. (a) QTH lamp curved spectrum from SPEC1. Notice that this image does not seem to be curved because the spectral pattern is flat and covers the whole iCCD (b) QTH lamp curved-corrected spectrum. When curvature-correcting a flat spectral image that covers the whole iCCD, the corrected spectral pattern is curved

The manufacturer provided the spectral radiance of this calibrated QTH lamp, which was calculated by using a standard integrating sphere (Labsphere LRS - 4Z 4" Spectralon Luminance radiance sphere) with a known wavelength dependent reflectance $(R_{LRS-4Z}(\lambda))$, and connecting its output through a Sub-Miniature version A (SMA) connector (which is a kind of semi-precision coaxial RF connector) to a spectroradiometer. We have called this spectral radiance as $QTH_{manufactured}(\lambda)$, where $\lambda$ is the wavelength.

Figure 3.19 shows the relative conversion factor of the spectral sensitivity of SPEC1 for row 320, calculated by dividing the manufacturer supplied spectral radiance curve by the relative response of our system for row 320 (*Fantz*, 2006), and corrected by the respective integrating spheres reflectances, according to

$$S_{SPEC1}(\lambda, i) = \frac{QTH_{manufactured}(\lambda)}{QTH_{SPEC1}(\lambda, i)} \frac{R_{US-080-SF}(\lambda)}{R_{LRS-4Z}(\lambda)}. \qquad (3.2)$$

Figure 3.20 depicts the different ways to obtain the spectral response of the QTH spectral lamp: (1) by recording the collimated light from a Spectraflect integrating sphere with SPEC1 and (2) by measuring the light from a Spectralon integrating sphere recorded by a commercial spectroradiometer.

We will further use the instrument function $S_{SPEC1}(\lambda, i)$ to correct every spectrum we record by multiplying this response pixel to pixel. This way we enhance the response of the iCCD within its edges and flatten its center area.

#### 3.2.1.2   Spectral resolution

The spectral resolution ($\Delta\lambda$) of a spectrograph defines the minimum spectral distance between two spectral lines so they can be distinguished. If we consider the spectrograph as a gaussian system whose input is a train of spectral lines, the output is then a train of gaussian curves. The spectral resolution could be interpreted as the standard deviation of the gaussian system so that the lower spectral resolution we have, the more similar would be the output to the input. On the other hand, if the spectral resolution value is high, the output would resemble to a band instead of a train of pulses and we would not be capable to discern among spectral lines. In our case we need high spectral resolution (low value of $\Delta\lambda$) to analyze the emission lines in the rovibronic bands of $N_2(B^3\Pi_g)$.

The Rayleigh criterion is generally accepted for the minimum resolvable detail: two spectral lines can be resolved when the intensity of the saddle point between them is $8/\pi^2$ times the maximum of their irradiance or less (see figure 3.21).

In *Quinten* (2012) we find that if we define the full width half maximum (FWHM or $\delta\lambda$) of an emission line as the spectral width of the peak at the 50% of its maximum irradiance, we obtain that $\delta\lambda \sim 0.8\ \Delta\lambda$. A practical and well-known rule to estimate the spectral resolution of a system is that we can resolve two lines if $\Delta\lambda > \delta\lambda$.

We can also obtain the spectral resolution from the linear dispersion from the spectrometer ($\Delta_{px-w}$), which is defined as the spectral range per pixel that fits the CCD. The spectral resolution is $\Delta\lambda \sim 3\Delta_{px-w}$ (*Quinten*, 2012) .

We define the resolving power of the spectrograph as for a given wavelength $\lambda$ as R = $\lambda/\Delta\lambda$.

Figure 3.22 shows the spectral resolution (top) and the resolving power (bottom) of SPEC1, respectively. We calculated the spectral resolution as the FWHM of each spectral line of Ne and also as three times the linear dispersion of the spectrometer. FWHM of each spectral line varies depending on the gain of the iCCD, so the calculated values of FWHM represent a maximum level for this parameter. Notice that the spectral resolution varies also within the iCCD area. Then, the mean spectral resolution of SPEC1 ranges between 0.47 nm (three times the linear dispersion of the spectrometer) and 0.65 nm (mean value of the calculated FWHM of all spectral lines), while the mean resolving power varies between 1105 and 1624.

The linear dispersion of SPEC1 is 0.156 nm/px.

### 3.2.1.3 Spatial resolution

The spatial resolution ($\Delta x$) of a spectrograph defines the minimum angular distance between two objects so they can be distinguished. It can be calculated following the above mentioned Rayleigh criterion. We can estimate it by measuring the FWHM of a point-source emission in the spatial direction, or we can determine it by means of three times the spatial dispersion the instrument, which defines the FOV that fits a pixel. As the FOV of SPEC1 in the spatial direction is 6° ± 0.03° and the effective length in the spatial direction of the iCCD is 320 px (320 rows), the spatial dispersion of SPEC1 is 67.5 ± 0.4 arcsec/px.

Since all the spectra recorded with SPEC1 belonged to lightning scattering which fully covered the slit, we can not measure the FWHM of a point emission. An estimation of the spatial resolution of SPEC1 in terms of three times the spatial dispersion is 3.38 ± 0.02 arcmin.

#### 3.2.1.4 Instrument reliability and data reduction

With regard the instrument reliability, we compared the spectrum of the light emitted by an arc lamp of dry air measured with SPEC1 with the spectral response measured with a commercial Jobin Yvon HORIBA FHR1000 spectrometer. The air arc lamp was cylindrical, 26 cm long and 0.5 cm width and fed by a DC source of 5 kV and 10 mA, at a pressure of 0.2 mbar.

To do so, we performed the following data reduction steps: (1) phosphor persistence correction and signal to noise ratio enhancement, (2) bias subtraction, (3) background subtraction, (3) trimming and flipping, (4) distortion correction, (5) flux calibration and (6) spectrum extraction.

It is worth to mention that we did not perform the well known flat-field correction because it is intrinsic to the flux calibration process, which compensates the nonuniform response of the spectrograph. Moreover, a flatfield correction does not make any sense when calibrating a single frame due to the scintillation effect of the intensifier tube.

*Phosphor persistence correction and signal to noise ratio enhancement*

As mentioned in chapter 1, the streak tube of the image intensifier is a Photonis Super Gen S25 photocathode equipped with a P20 phosphor, with a decay (persistence) time of tens of ms (*Hoess and Fleder*, 2000). This decay time results in an accumulative effect in the iCCD frames, so a *ghost* of the previous frame is added to the current one. This undesirable effect is corrected by selecting two consecutive frames and applying

$$I_P = Frame_i - 0.79 Frame_{i-1}. \qquad (3.3)$$

We recorded eleven consecutive spectral images, calculating then ten consecutive $I_P$ images by means of equation 3.3. Then, we combined these

$I_P$ images by means of the median value of every pixel at the same coordinates in all images, sketched in figures 3.23 and 3.24, obtaining $I_{PC}$. This way, we enhanced the signal to noise ratio.

### Bias subtraction

Bias images are the count offset generated during the read-out process of the CCDs (*Furuya*, 2010). This offset has to be subtracted from all spectral images. We combined a group of ten bias images by means of the median value of every pixel at the same coordinates in all images. We recorded the images without exposing the iCCD to any incident light building a single bias-combined image ($I_{BIAS}$). The combination process is illustrated in figures 3.23 and 3.24 .

### Background subtraction

We also recorded ten images without switching on the air arc lamp, identifying the background emission of the room where the experiment was being developed. Then, we combined these images by means of the median value of every pixel at the same coordinates in all images. This way we built a single background-combined image ($I_{BG}$).

We subtracted the combined-bias and the combined-background images to the phosphor-corrected image as

$$I_{PBB} = I_{PC} - I_{BIAS} - I_{BG}. \tag{3.4}$$

Figure 3.25 shows the raw spectrum of the air lamp before (a) and after (b) correcting it by the phosphor effect, bias and background.

### Trimming and flipping

Then, we trimmed $I_{PBB}$ so it fitted the wavelength calibration area, obtaining $I_{trimmed}$. Next, we flipped $I_{trimmed}$ to set the spectral axis from left to right, obtaining $I_{flipped}$ (see figure 3.26).

### Distortion correction

The resulting image from the previous steps is curved due to the effects of the optical aberrations of the system. To correct this undesirable effect, we applied the wavelength calibration array calculated before, so we straightened the spectrum of the air lamp, and assigned an absolute wavelength to every pixel of the iCCD, obtaining $I_{straightened}$ (see figure 3.27).

### Flux calibration

The straightened spectrum was multiplied by the instrument function, previously calculated, $S_{SPEC1}$, obtaining $I_{corrected}$ as

$$I_{corrected} = I_{straightened}(i) \cdot S_{SPEC1}(\lambda, i). \tag{3.5}$$

This way we corrected for the nonuniform response of the spectrograph, so that we finally have a spectrum like the one shown in figure 3.28.

### Spectrum comparison

Figure 3.29 shows a comparison between the spectrum of the light emitted by a commercial air lamp at 0.2 mbar as recorded with SPEC1 (obtained by integrating all rows of $I_{corrected}$) and the spectrum emitted by a DC hollow cathode reactor air discharge at 0.23 mbar recorded with a commercial Jobin Yvon HORIBA FHR 1000 spectrometer at a spectral resolution of 0.36 nm. Notice that, although the mean spectral resolution of SPEC1 is 0.58 nm, both spectra show similar structure. Hence, the spectral resolution of SPEC1 is better than 0.58 nm.

The setup of the Jobin Yvon system and the thorough analysis of air spectra will be discussed in chapter 4.
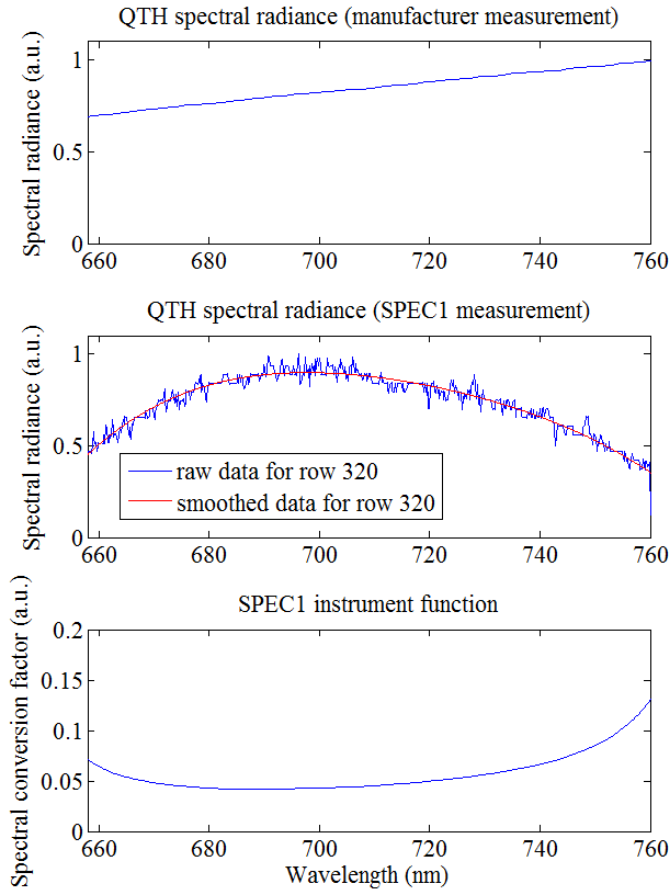
**Figure 3.19:** Top: Spectral radiance of the commercial calibrated QTH lamp (provided by the manufacturer). Middle: Spectral response of SPEC1 to the calibrated QTH lamp for row 320. Bottom: Conversion factor of the spectral sensitivity of SPEC1 for row 320
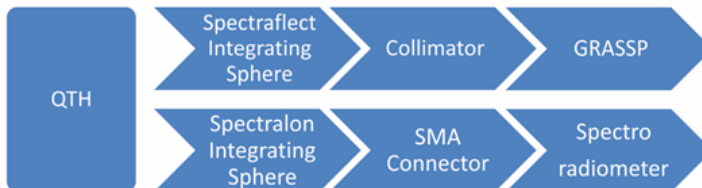


**Figure 3.20:** Different ways to obtain the spectral response of the QTH spectral lamp
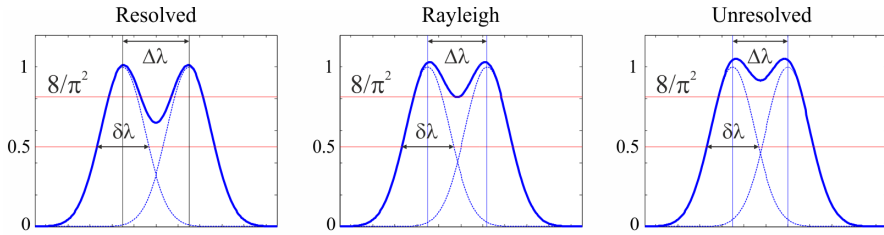
**Figure 3.21:** Rayleigh criterion to discern among spectral lines
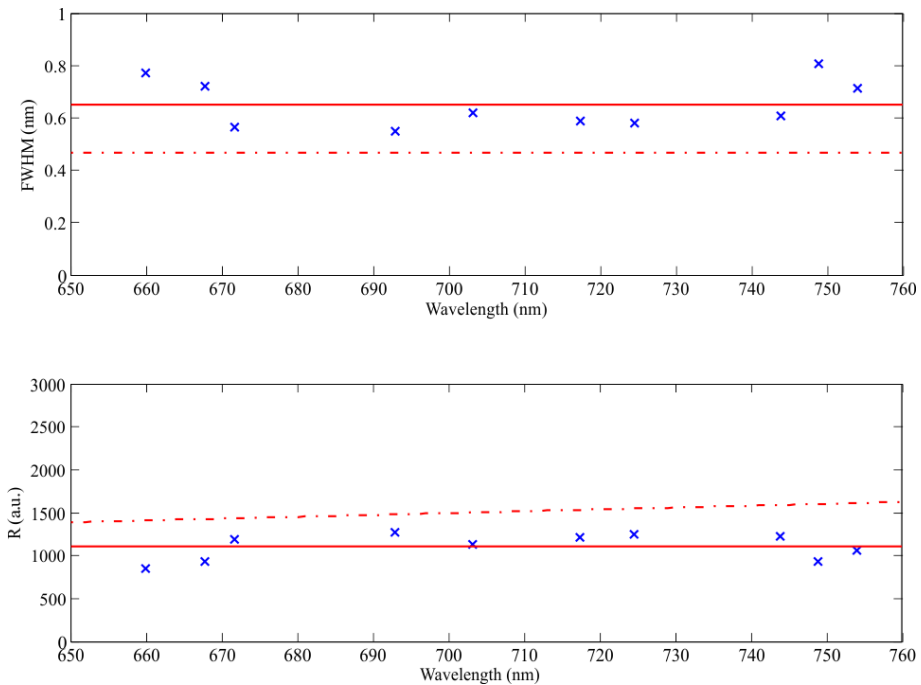


**Figure 3.22:** Spectral resolution (top) and resolving power (bottom) of SPEC1 as a function of the wavelength. (Top) The blue crosses correspond to the calculated FWHM for each spectral line of Ne. The solid line represents the mean FWHM. The dashed line represents the spectral resolution of SPEC1 calculated as $\Delta\lambda \sim 3\Delta_{pixel}$. (Bottom) The blue crosses correspond to the resolving power, calculated as $\lambda/FWHM$, for each spectral line of Ne. The solid line represents the mean resolving power of SPEC1, when it is calculated as $\lambda/FWHM$. The dashed line represents the resolving power of SPEC1 calculated as $\lambda/(3\Delta_{pixel})$
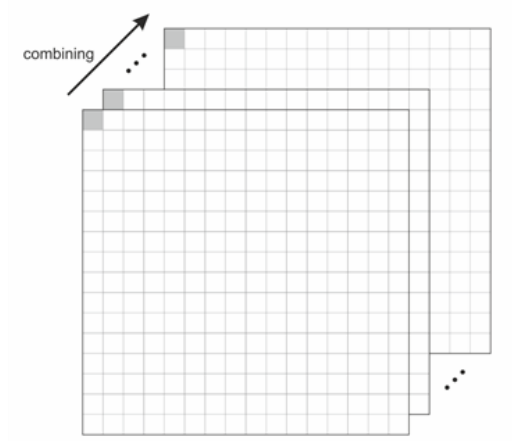
**Figure 3.23:** Pixel by pixel combining method
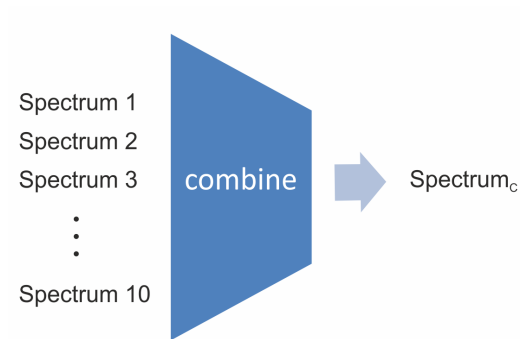


**Figure 3.24:** Combination of spectral images
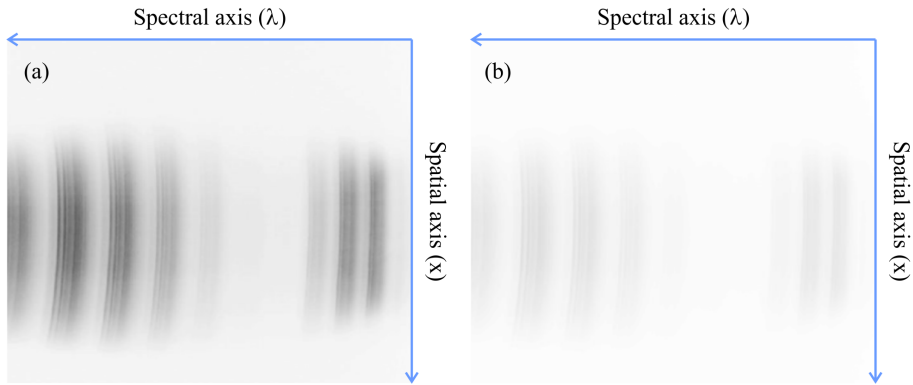
**Figure 3.25:** (a) Air lamp spectrum, raw. (b) Air lamp spectrum, corrected by the phosphor effect, bias and background
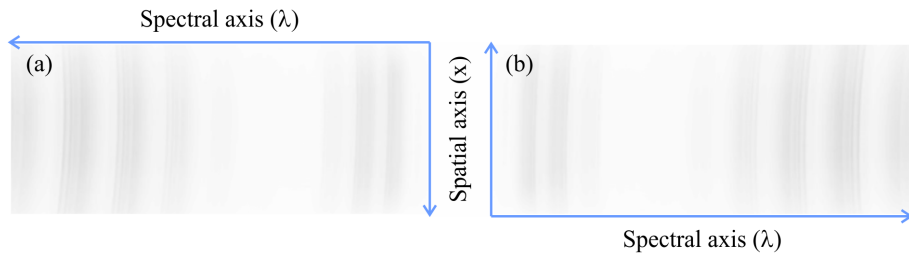


**Figure 3.26:** (a) Air lamp spectrum, trimmed. (b) Air lamp spectrum, trimmed and flipped
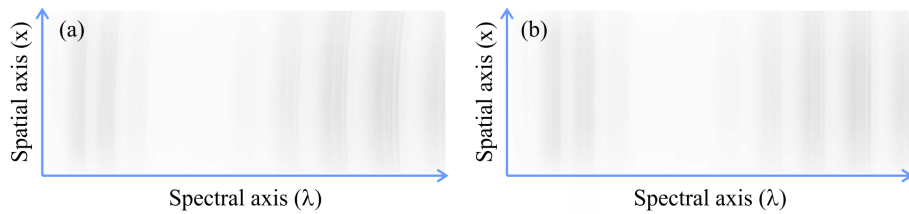


**Figure 3.27:** (a) Air lamp spectrum, trimmed and flipped. (b) Air lamp spectrum, straightened
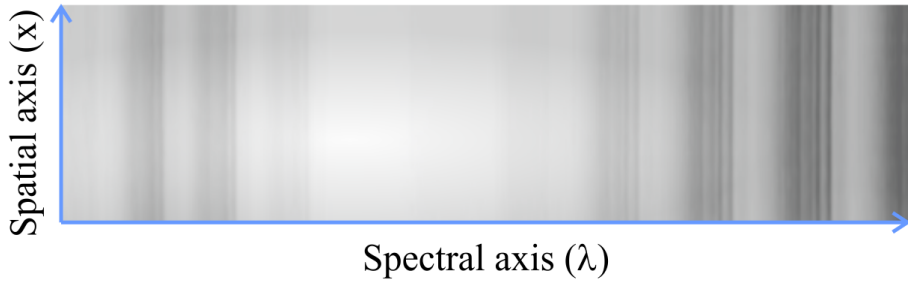
**Figure 3.28:** Air lamp spectrum, trimmed, flipped, straightened and corrected by the instrumental function of SPEC1
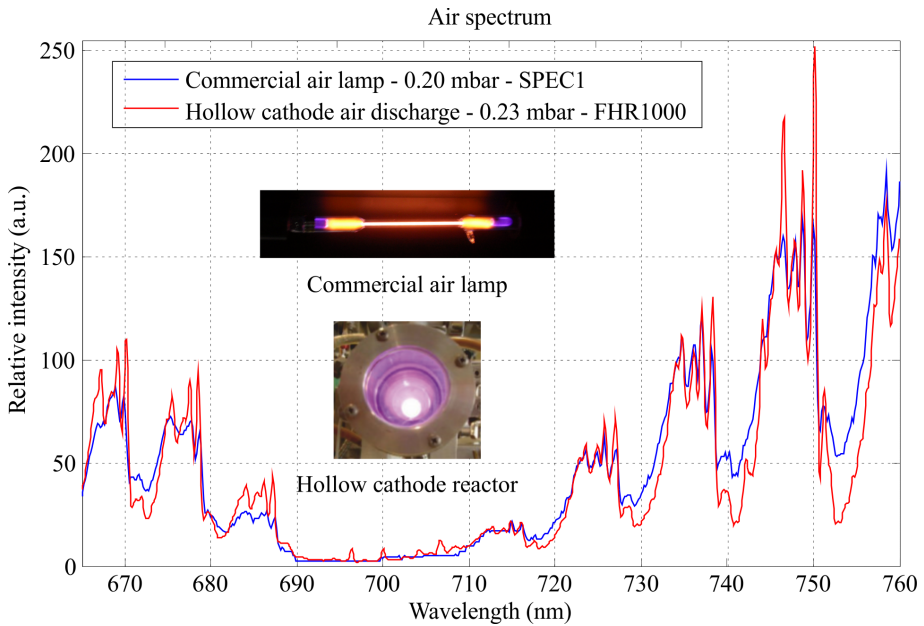


**Figure 3.29:** Air lamp spectrum and hollow cathode air discharge spectrum, measured with SPEC1 and Jobin Yvon Horiba FHR1000 spectrometers, respectively

### 3.2.2 Characterization of SPEC2

In this section we fully characterize the SPEC2 spectrograph following the same steps as in the characterization process of SPEC1: we calibrated SPEC2 in wavelength to calculate the distortion correction array that will allow us to straighten the recorded spectra. Then, we calculated its spectral response, we obtained the SPEC2 spectral and spatial resolutions and, finally, we checked SPEC2 reliability by comparing a spectrum of an air lamp obtained with both SPEC2 and a commercial Jobin Yvon Horiba FHR1000 spectrometer.

#### 3.2.2.1 Spectrograph calibration

As we described in the previous section, the complete calibration of the spectroscopic system consists of three tasks: (1) a wavelength calibration, which assigns an absolute wavelength to each pixel of the iCCD, (2) a distortion correction, which straightens the curved spectrum image and (3) a flux calibration, which provides the spectral sensitivity of the spectrograph.

#### *Wavelength calibration and distortion correction*

*Wavelength calibration*

The procedure to correct the distortion and to wavelength-calibrate SPEC2 is similar to SPEC1, although, as we shifted the spectral range and Ne lacks emission lines above 760 nm, now we need a group of spectral lines distributed between 700 and 800 nm.

To obtain the correspondence array between every pixel coordinate in the iCCD of SPEC2 and a single wavelength, we have to illuminate the spectrograph with a collimated light beam from a spectral lamp of an element whose atomic lines cover this spectral range. Unfortunately, there are no elements completely covering the targeted spectral band. So, to properly calibrate SPEC2 in wavelength, we have to use a combination of spectral lamps providing a calibration pattern.

As we are interested in the spectral range from 700 to 800 nm, in SPEC2 we used an argon lamp, which shows spectral lines with high relative intensity from 696.54 to 772.40 nm, and a krypton lamp, which shows spectral lines with high relative intensity between 758.74 and 785.48 nm.
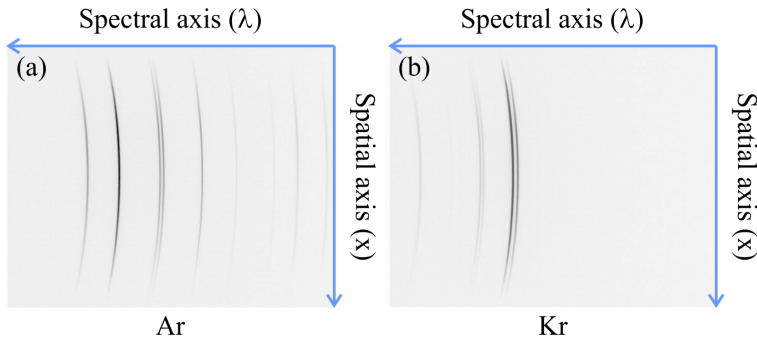


**Figure 3.30:** Raw spectra of Ar and Kr lamps

Figure 3.30 shows the raw spectral patterns of Ar and Kr lamps. We find that they are curved, with some lines brighter than others which do not fill the whole height of the iCCD, and the spectral (horizontal) axis is inverted.

We recorded several spectral images from both atomic lamps, consecutively, with different gain values so the weaker spectral lines showed up, despite the saturation of the brightest; then, we trimmed and flipped them to cover with spectral lines the whole height of the images with similar brightness and to show up the spectral axis in increasing order.

Finally, we selected the spectral lines of similar brightness to build up two synthetic spectra, one for argon and one for krypton. This process is shown in figure 3.31. The resultant synthetic spectrum from combining both argon and krypton synthetic spectra is shown in figure 3.32
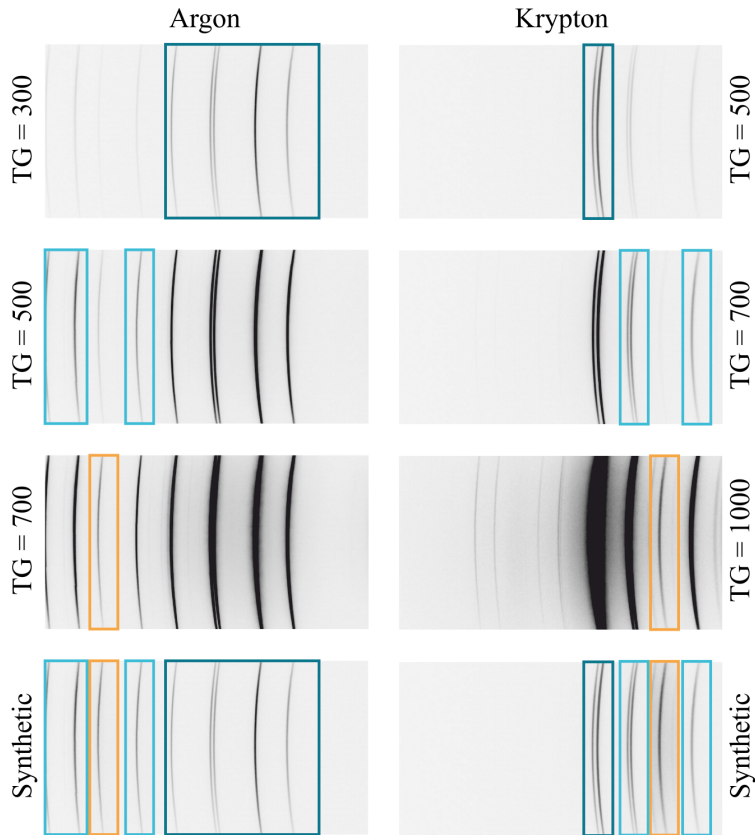
**Figure 3.31:** Synthetic spectrum of Ar and Kr from different values of the iCCD tube gain
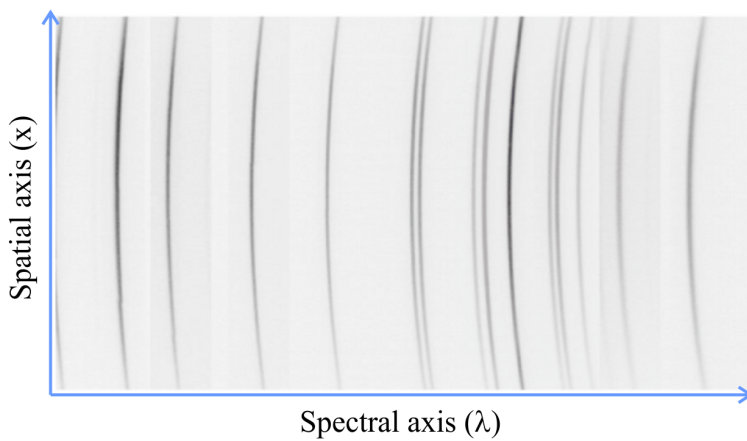


**Figure 3.32:** Synthetic spectrum of Ar and Kr

Then we plotted every row of the synthetic spectral patterns calculating the coordinates of the pixel corresponding to the center of the full width half maximum of each spectral line, obtaining a cloud of pixels defining each Ar or Kr spectral line. Then we fitted these clouds of pixels to a cubic curve to obtain a one-pixel-width curve for each spectral line of Ar and Kr.
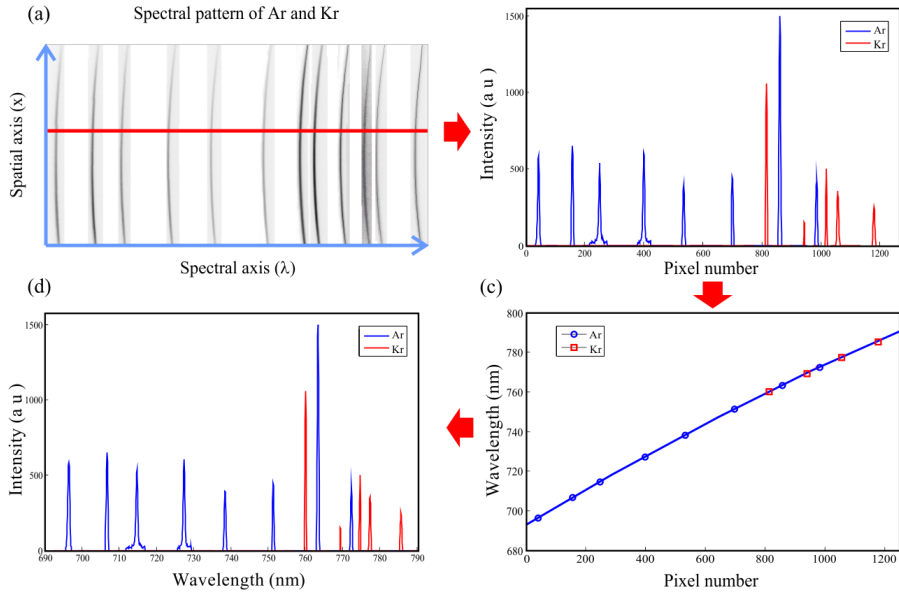


**Figure 3.33:** (a) Trimmed and flipped spectral pattern of the Ar and Kr lamps on the detector. Row 100 is shown in red. (b) Plot of row number 100 as a function of the pixel number. (c) Red squares and blue circles show the wavelength assignment to the pixels corresponding to the mean FWHM of each Kr and Ar spectral line, respectively, for row number 100. The blue solid line shows the fitting curve that assigns a wavelength to each pixel of the iCCD for row number 100. (d) Plot of row number 100 as a function of the wavelength.

Then, we identified the corresponding wavelengths by comparing the distances between spectral lines to the well-known gaps of Ar and Kr spectrum (*Kramida et al.*, 2015).

Finally, we assigned each pixel coordinates from the one-pixel-width curves to the wavelengths we identified for every row. Then we fitted these

coordinates with a cuadratic curve for each row, as figure 3.33 shows.

This process generated a calibration array which was used hereinafter to correct the curvature of the spectra recorded with SPEC2, associating every pixel coordinate in the iCCD to an absolute wavelength.

*Distortion correction*

Once we calculated the array that assigns a wavelength to pixel coordinates in the iCCD, we shifted every row of the iCCD so that all pixel coordinates with the same wavelength number were aligned in the same column of the image. Figure 3.34 shows the resultant spectrum of the Ar and Kr lamps after wavelength calibration and distortion correction.
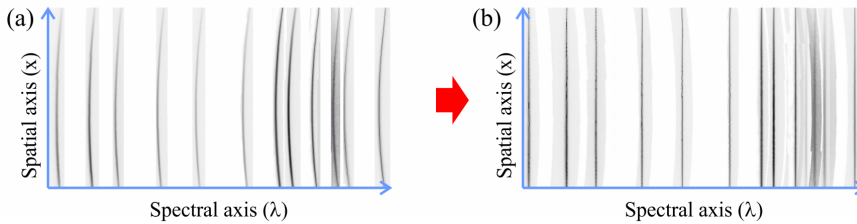


**Figure 3.34:** Curvature correction for the Ar and Kr synthetic spectral pattern

**Instrument function**

We have calculated the SPEC2 instrument function following the steps defined in *Fantz* (2006), by comparing the spectrum of the same calibrated source obtained with both SPEC2 and a calibrated Jobin Yvon Horiba FHR1000 spectrometer, under similar experimental setup (figure 3.17), which is also similar to the setup we used to calibrate the spectral sensitivity of SPEC1.

We measured the spectral radiance of a calibrated QTH spectral lamp using SPEC2 with a set of different gains and exposure times. Then we reduced the spectral data from SPEC2 following the steps described in the previous section. We repeated this process for 8 different gain values to

further correct the spectral images according to the gain values they were recorded with. Thus, we obtained 8 different instrument functions, one per the preferred gain value.
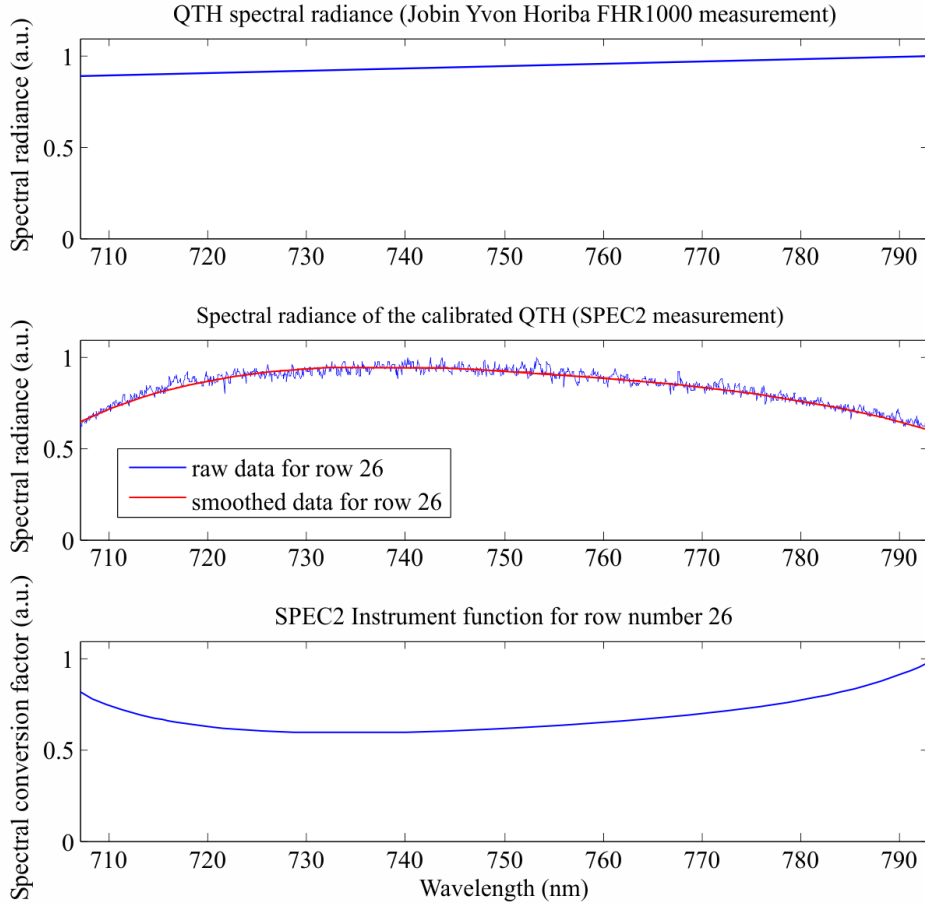


**Figure 3.35:** Up: Spectral radiance of a commercial QTH lamp measured with a calibrated Jobin Yvon Horina FHR1000 spectrometer. Middle: Spectral response of SPEC2 to the QTH lamp for row 26. Bottom: Conversion factor of the spectral sensitivity of SPEC2 for row 26

We repeated these measurements, under the same experimental setup, with the Jobin Yvon Horiba FHR1000 spectrometer.

Figure 3.35 shows the relative conversion factor of the spectral sensitivity of SPEC2 for row 26, calculated by dividing the FHR1000 spectral radiance curve by the relative response of our system for row 26, (*Fantz*, 2006)

$$S_{SPEC2}(\lambda, i) = \frac{QTH_{FHR1000}(\lambda)}{QTH_{SPEC2}(\lambda, i)}. \tag{3.6}$$

As the integrating sphere is the same in both measurements, there is no reflectance correction to apply. Figure 3.36 depicts the different ways to obtain the spectral response of the QTH spectral lamp: (1) by recording the collimated light from a Spectraflect integrating sphere with SPEC2 and (2) by recording the collimated light from a Spectraflect integrating sphere with the Jobin Yvon Horiba FHR1000 spectrometer.

We will further use the instrument function $S_{SPEC2}(\lambda, i)$ to correct every spectrum we record by multiplying it by this spectral response pixel to pixel, enhancing the edges of the iCCD and flattening its center area.
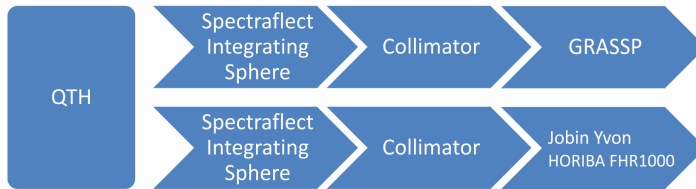


**Figure 3.36:** Different ways to obtain the spectral response of the QTH spectral lamp

#### 3.2.2.2 Spectral resolution

Figure 3.37 shows the spectral resolution (top) and the resolving power (bottom) of SPEC2, respectively. We calculated the spectral resolution as
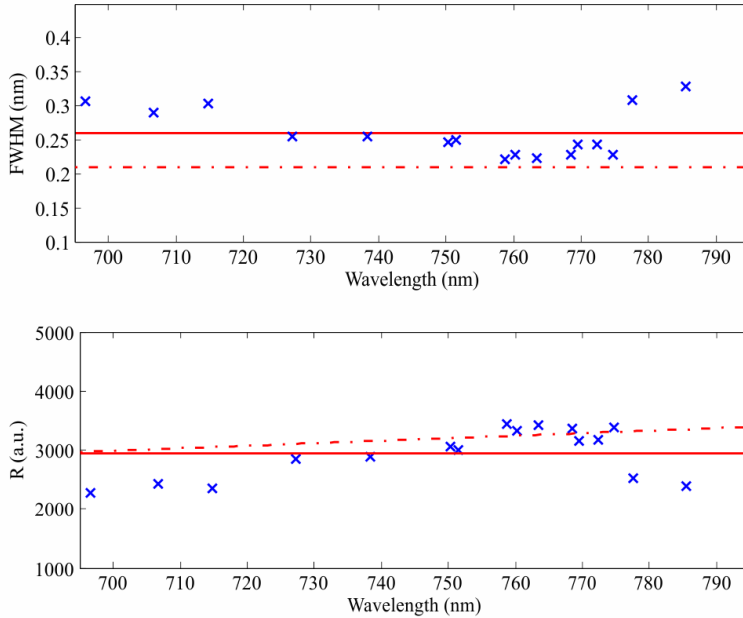
**Figure 3.37:** Spectral resolution (top) and resolving power (bottom) of SPEC2 as a function of the wavelength. (Up) Blue crosses correspond to the calculated FWHM for each spectral line of Ar and Kr. Solid line represents the mean FWHM. Dashed line represents the spectral resolution of SPEC2 calculated as $\Delta\lambda \sim 3\Delta_{pixel}$. (Bottom) Blue crosses correspond to the resolving power, calculated as $\lambda/FWHM$, for each spectral line of Ar and Kr. Solid line represents the mean resolving power of SPEC2, when it is calculated as $\lambda/FWHM$. Dashed line represents the resolving power of SPEC2 calculated as $\lambda/(3\Delta_{pixel})$

the FWHM of each spectral line and also as three times the linear dispersion of the spectrometer. Notice that, again, the spectral resolution varies within the iCCD area. The mean spectral resolution of SPEC2 ranges between 0.21 and 0.26 nm, with mean resolving power ranging between 2939 and 3679.

The linear dispersion of SPEC2 is 0.07 nm/px.

### 3.2.2.3    Spatial resolution

We calculated the spatial dispersion of SPEC2 by measuring the spectrum of a full Moon. Viewed from Earth, the Moon subtends about $32 \pm 3$ minutes of arc (arcmin). Since our spatial dispersion depends on the region of the iCCD, we measured the full Moon spectrum several times, and at different spatial positions of the iCCD. The spectrum of the full moon covered a mean value of $40 \pm 1$ pixels in the spatial axis. This way we found that the mean spatial dispersion of SPEC2 is $48.0 \pm 5$ arcsec/px.

We calculated the mean spatial resolution as three times the spatial dispersion. The mean spatial resolution of GRASSP spectrograph is then $2.4 \pm 0.3$ arcmin. This spatial resolution is worse than the value expected theoretically due to the effect of the photocathode stage over the focal plane of the camera.

### 3.2.2.4    Instrument reliability and data reduction

To test the reliability of SPEC2, we compared the spectrum of the light emitted by a spectral lamp of air measured both with SPEC2 and a commercial Jobin Yvon HORIBA FHR1000 spectrometer, following the steps defined in the characterization of SPEC1: (1) phosphor persistence correction and signal to noise ratio enhancement, (2) bias subtraction, (3) background subtraction, (3) trimming and flipping, (4) distortion correction, (5) flux calibration and (6) spectrum extraction.

In order to not be redundant, we are not going to describe steps one to five since they were defined in the previous section.

We set the configurable parameters of the FHR1000 spectrometer to provide a spectral resolution of 0.02 nm, by selecting a dispersion grating of 1800 lines/mm, a slit of 24 $\mu$m and a mean integration time of 1 s, the detector being a CCD of 26 $\mu$m/px. Then, we convolved the resulting spectrum with gaussian curves of standard deviation of 0.11 nm and 0.18

nm to derive two synthetic spectra with 0.23 nm and 0.37 nm spectral resolution, respectively.

The GRASSP spectrograph was set to 40 ms exposure time and a tube gain of 1200. Due to the setup of the measurement system, lower tube gain values did not allow us to discern all the spectral features of air between 700 and 800 nm. It is worth to mention that we only measured the background images with a maximum value of tube gain of 1000, because the air spectral images images we recorded with a gain value over 1000 seemed to be saturated. When analyzing these data we noticed that the best air spectral images were recorded with a tube gain value of 1200.

We integrated each column of the resulting air lamp spectrum image, measured with GRASSP. Figures 3.38 and 3.39 show the air lamp recorded spectra with both GRASSP and Jobin Yvon Horiba FHR1000 spectrometers.

When we compare both spectra, we find that the height of the peaks are not coincident. This could be a result of the combination of several factors: (1) we subtracted a background level recorded with less tube gain —SPEC2 tube gain of 1000— than the air lamp spectrum measurement —SPEC2 tube gain of 1200—, so the background level may not be accurate; (2) the different ambient lighting during the measurements could also contribute in this height difference; and (3) peaks height also depends on the air plasma temperature, and this can vary depending on the time the lamp has been switched on. Moreover, the spectral resolution of SPEC2 is variable within the iCCD, being better in the central region of the iCCD, the reliability of SPEC2 decreasing as we approach the edges of the iCCD. However, the spectral resolution of the Jobin Yvon Horiba FHR1000 spectrometer is constant for all wavelengths.

Despite these differences, this comparison confirms the reliability of the wavelength and flux calibration of SPEC2 between 715 and 790 nm.
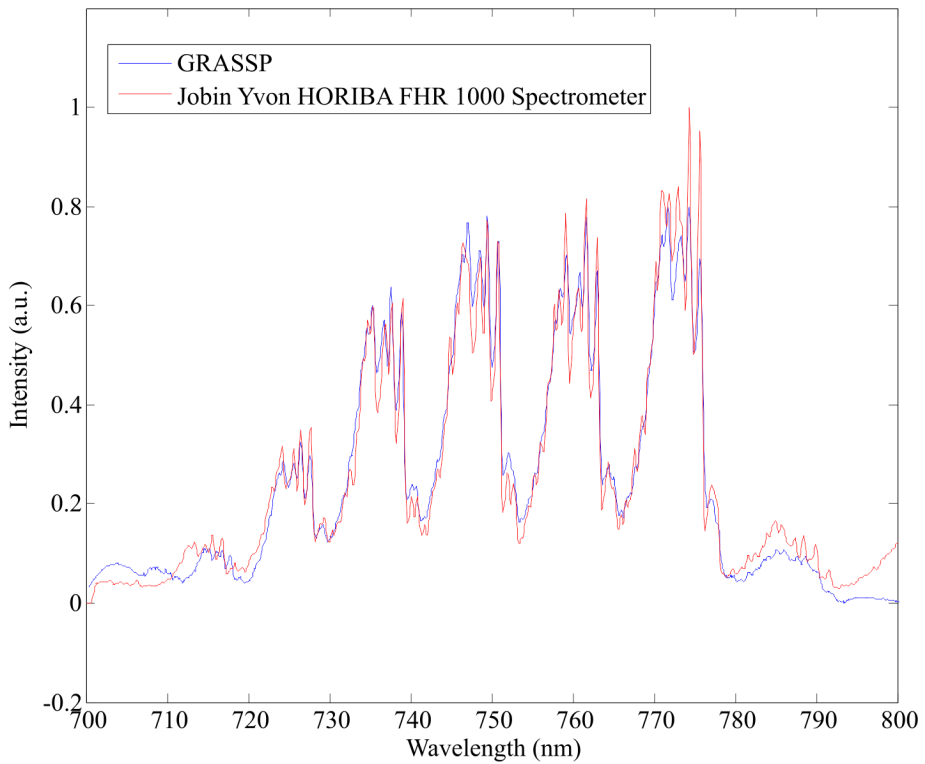
**Figure 3.38:** Spectra of a dry air (0.2 mbar) lamp measured with a commercial Jobin Yvon Horiba FHR1000 spectrometer (red) at 0.36 nm spectral resolution and with GRASSP spectrograph (blue)
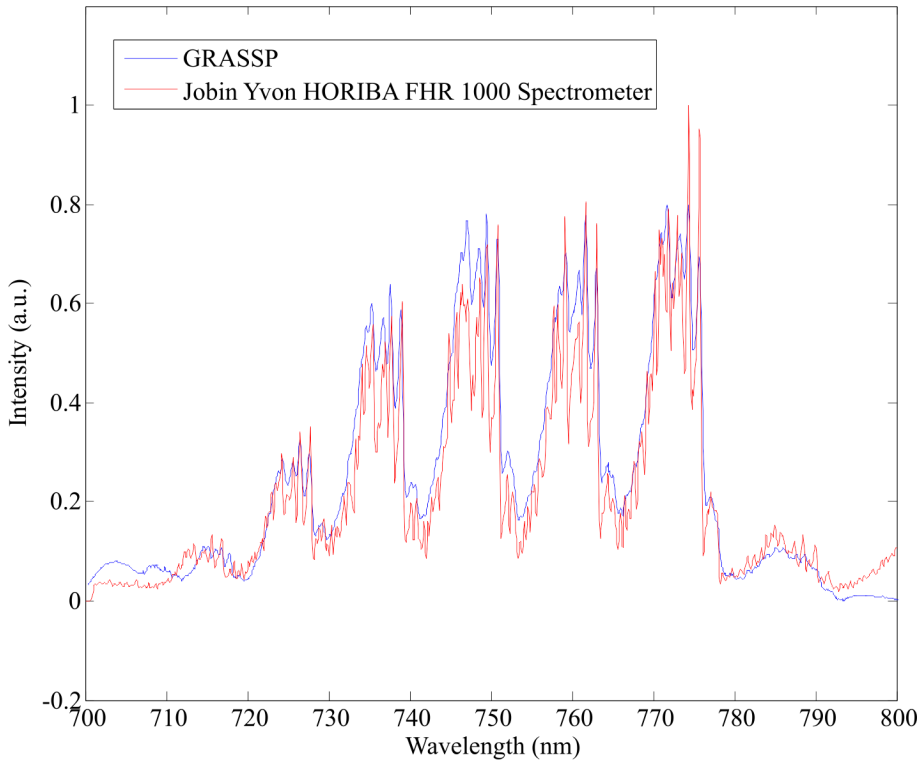
**Figure 3.39:** Spectra of a dry air (0.2 mbar) lamp measured with a commercial Jobin Yvon Horiba FHR1000 spectrometer (red) at 0.23 nm spectral resolution and with GRASSP spectrograph (blue)

# Chapter 4

# Polarimeter

*"We observed vertical lightning nine times on a flight from Glasgow, Montana, to Washington D.C. This observation occurred in mid-April 1965 while cruising at 37,000 feet over mean sea level. The night was clear and the nearby full moon was very bright. Approaching a line of northeast to southwest thunderstorms in eastern Indiana, there was considerable lightning activity. It was beautiful to watch. The clouds were white from the moonlight but firey inside. [...] About a mile or two from the nearest top, a bolt of lightning came straight out the top and went to a point about 2,000 feet above us and shattered in all directions as an egg would do if were thrown against a ceiling. At the point where it shattered there was nothing observable. We climbed to 41,000 feet, and we observed the phenomenon 7 or 8 more times."*

– Dan E. Babcock, colonel United States Air Force retired, *Journal of Geophysical Research, September 30, 1989*

## 4.1   Introduction

Polarimetry campaigns of TLEs have never been carried out. But there are evidences suggesting that the light from TLEs could be polarized: it was 1989 when Nemzek and Winckler detected *"moderate but definite"* polar-

ization of light coming from short duration no–spherics flashes (*Nemzek and Winkler*, 1989; *Winckler et al.*, 1993). These research group later identified these events as TLEs. However, so far, only spectroscopy of TLEs has been paid attention to, whereas polarimetry of TLEs has been ignored.

Hence, our group decided to design and develop the first polarimeter intended to carry out systematic polarimetric campaigns of TLEs, to discern whether or not the light emitted by TLEs is actually polarized, and if it is so, to characterize its polarization.

In this chapter we will describe the GRASSP instrument polarimeter and its calibration process, which is necessary in order to reveal the non-ideal behaviour of linear and circular polarizers in the instrument and to retrieve the polarization state of the incoming light. The GRASSP polarimeter is currently in the testing phase and it is planned to be operative in the summer of 2017.

We will also describe the pipeline to obtain the degrees of linear and circular polarization of the incident light striking the polarimeter.

## 4.2 Definitions and theoretical basis

In this section we will describe the theoretical basis to fully understand the calibration process and the data reduction pipeline of the GRASSP polarimeter.

Linear and circular polarizers are essential parts of the GRASSP polarimeter. And a quarter-wave plate is also necessary for calibration. For all of these elements, an axis is defined. This is contained within the plane of the plate and forms an angle $\gamma$ with respect to the *optical plane.*

The *optical plane* is a reference plane containing the direction of propagation of light. For simplicity, among all possible, we choose the plane where the instrument lays on. During calibration, when the polarimeter is placed on a table, the optical plane is horizontal. But during field operation, when the instrument is pointed at different altitudes, the *optical plane* slopes too.

Let us consider light propagating in the direction of a unitary vector $\hat{m}$. In a plane perpendicular to $\hat{m}$ we choose rectangular axes $l$ and $r$, parallel and perpendicular to the optical plane, respectively. Defining $\hat{l}$ and $\hat{r}$ as the unit vectors along the positive $l$- and $r$-axes, respectively, leads to $\hat{m} = \hat{r} \times \hat{l}$ (see figure 4.1).
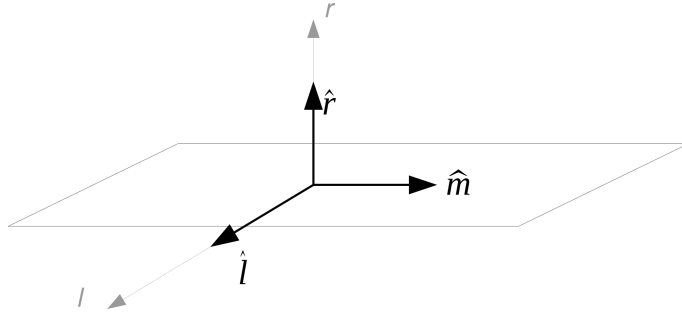


**Figure 4.1:** Unit vector $\hat{m}$ defines the direction of propagation of light. Vectors $\hat{r}$ and $\hat{l}$ are perpendicular and parallel to the optical plane, respectively. $\hat{m} = \hat{r} \times \hat{l}$

Unpolarized light, also called *natural light*, is formed, in a certain point at a certain moment, by a number of non-related (incoherent) electric field vectors vibrating in random directions.

If light is *completely polarized*, the tip of the electric vector $\vec{E}$ will describe a *polarization ellipse* as that shown in figure 4.2.

E. g., for *linearly polarized light* $\beta = 0$ and $\chi$ will be a fixed value. This occurs when the phase gap between perpendicular components $E_r$ and $E_l$ is 0 or $\pi$.

For *circularly polarized light*, the tip of $\vec{E}$ describes a circle and $\beta = \frac{\pi}{4}$. It occurs when the phase gap between components $E_r$ and $E_l$ is $\frac{\pi}{2}$ or $-\frac{\pi}{2}$.

*Partially polarized light* occurs when polarized and natural light are mixed up so a statistical preference for one polarization state over others takes place. In that case, the tip of $\vec{E}$ does not describe an ellipse but a noisy trajectory around an ellipse. Much light in nature is partially polarized.
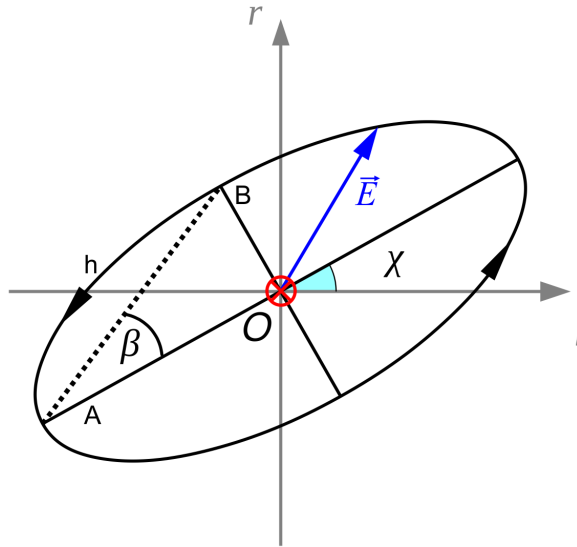
**Figure 4.2:** Polarization ellipse for the electric vector at a point $O$ of the propagating beam. Light propagates into the paper perpendicular to axes $l$ and $r$. Axis $l$ and $r$ are, respectively, parallel and perpendicular to the optical plane. $A$ and $B$ are the semi-major and semi-minor axes of the polarization ellipse, respectively. $\chi$ is the angle subtended by the parallel axis $l$ and the semi-major axis of the polarization ellipse, measured anti-clockwise. $h$ is the sense of rotation of the electric field, and it is positive if anti-clockwise rotating

### 4.2.1 The Stokes parameters

Polarization of light can be determined by giving the magnitudes of the semi-major and semi-minor axes of its polarization ellipse, the angle that the semi-major axis describes with the optical plane, and the sense of rotation of the electric field (parameters $A$, $B$, $\chi$ and $h$ of figure 4.2, respectively). These magnitudes can be measurable through the 4 Stokes parameters of the beam of light ($I$, $Q$, $U$ and $V$) (*Stokes*, 1851).

We can obtain the Stokes parameters $I$, $Q$ and $U$ of a beam of light directly from the measurement of some components of its electric field: $E_0$,

$E_{90}$, $E_{45}$ and $E_{-45}$, with $E_\alpha$ being the projection of the electric field over an axis forming $\alpha$ degrees with the $l$ axis of the polarization ellipse. To obtain the fourth Stokes parameter, $V$, we need to measure the component of the electric field rotating clock and anti-clockwise, respectively, $E_R$ and $E_L$.

The four Stokes parameters are defined as follows:

$$
\begin{aligned}
I &= \left\langle E_0^2 \right\rangle + \left\langle E_{90}^2 \right\rangle = \left\langle E_{45}^2 \right\rangle + \left\langle E_{-45}^2 \right\rangle \\
Q &= \left\langle E_0^2 \right\rangle - \left\langle E_{90}^2 \right\rangle \\
U &= \left\langle E_{45}^2 \right\rangle - \left\langle E_{-45}^2 \right\rangle \\
V &= \left\langle E_L^2 \right\rangle - \left\langle E_R^2 \right\rangle
\end{aligned}
\tag{4.1}
$$

where $\langle \rangle$ stands for the expected value of the electric field component. If we define the Stokes parameters in terms of the parameters of the polarization ellipse, we obtain:

$$
\begin{aligned}
I &= A^2 + B^2 \\
Q &= (A^2 - B^2)\cos(2\chi) \\
U &= (A^2 - B^2)\sin(2\chi) \\
V &= 2ABh
\end{aligned}
\tag{4.2}
$$

So if we can measure the four Stokes parameters of an incident beam of light, we can obtain the parameters that define its polarization ellipse.

## 4.2.2 Linear polarizer

A linear polarizer is a filter that only lets pass through the components of light parallel to its polarization axis. The result is light loosing its components perpendicular to the axis of the linear polarizer (see figure 4.3).

Let us call $\gamma_{LP}$ the angle between the axis of the linear polarizer and the optical plane (figure 4.4), measured anti-clockwise from the plane when looking in the direction of propagation of light ($0 \leq \gamma_{LP} \leq 180°$).

The Mueller matrix $M^{LP}$ associated to a linear polarizer transforms the Stokes vector $\vec{I_0}$ of the incident light into that of the light emerging from the polarizer $\vec{I}$ as $\vec{I} = M^{LP}\vec{I_0}$.
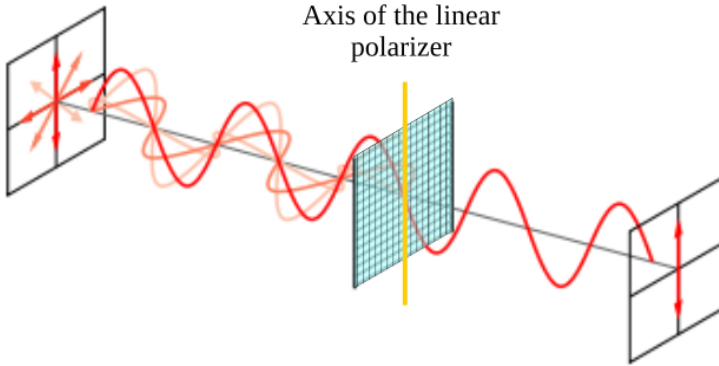
**Figure 4.3:** Natural light is filtered as passing through a linear polarizer. The components of light vibrating parallel to the axis of the linear polarizer remain, while the perpendicular components are absorbed and reflected

The matrix associated to a linear polarizer with its axis at an angle $\gamma_{LP}$ is given by equation 4.3 (*Mishchenko et al.*, 2000):

$$M^{LP}(\gamma_{LP}) = \frac{1}{2} \begin{pmatrix} 1 & C_{LP} & S_{LP} & 0 \\ C_{LP} & C_{LP}^2 & S_{LP}C_{LP} & 0 \\ S_{LP} & S_{LP}C_{LP} & S_{LP}^2 & 0 \\ 0 & 0 & 0 & 0 \end{pmatrix}, \qquad (4.3)$$

where

$$S_{LP} = \sin(2\gamma_{LP})$$
$$C_{LP} = \cos(2\gamma_{LP}).$$

When any kind of polarized, unpolarized or partially polarized light passes through a linear polarizer, emerging light, if any, is linearly polarized in the direction of the axis of the polarizer. Only in case of linearly polarized incoming light with its axis perpendicular to the axis of the polarizer, there will not be any emerging light.

All linear polarizers are broadband effective in the visible range of the electromagnetic spectrum.
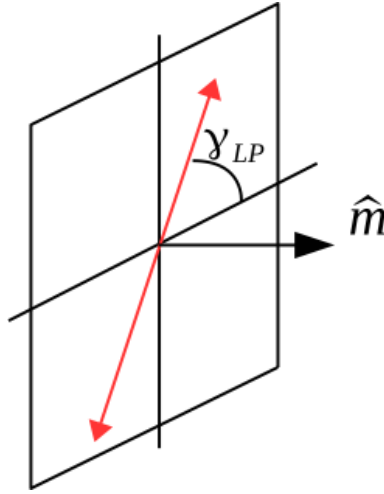
**Figure 4.4:** Angle formed by the axis of the polarizer and the optical direction

### 4.2.3 Quarter-wave plate

A *quarter-wave plate* is not a filter but a retarder, i. e., instead of selectively absorbing certain components of the light beam, it introduces a phase gap between the perpendicular components of the electric field vector of light. In particular, $\frac{\pi}{2}$. In terms of the wavelength $\lambda$, this is $\frac{\lambda}{4}$.

Quarter-wave plates are made of a non-isotropic material. Within this material, the component of light with its electric field vector $\vec{E}$ vibrating in a certain direction *(fast axis)* travels faster than that with $\vec{E}$ vibrating perpendicularly *(slow axis)*. The width of the plate is chosen so that the retardation is exactly $\frac{\pi}{2}$.

The fast axis is called the *optical axis of a quarter wave plate*, and it forms an angle with the optical reference plane that we call $\gamma_Q$. It is measured anti-clockwise from the reference plane when looking in the direction of beam propagation.

The Mueller matrix associated to a quarter-wave plate with its axis at

an angle $\gamma_Q$ is given by *Mishchenko et al.* (2000):

$$M^Q(\gamma_Q) = \begin{pmatrix} 1 & 0 & 0 & 0 \\ 0 & C_Q^2 & S_Q C_Q & -S_Q \\ 0 & S_Q C_Q & S_Q^2 & C_Q \\ 0 & S_Q & -C_Q & 0 \end{pmatrix}, \tag{4.4}$$

where

$$S_Q = \sin(2\gamma_Q)$$
$$C_Q = \cos(2\gamma_Q).$$

The effect of a quarter-wave plate on incoming light as a function of its state of polarization can be deduced just by $\vec{I} = M^Q \vec{I_0}$, but it is simpler to think about the phase shift introduced by the plate.

- Natural → Natural: if light is a collection of waves with uniformly random phase shifs between $E_r$ and $E_l$. If a gap of $\frac{\pi}{2}$ is introduced in each one, the result will still be uniformly random.

- Linear → Circular: If the phase shift between $E_r$ and $E_l$ is 0 or $\pi$ initially and a gap of $\frac{\pi}{2}$ is added or substracted, the phase shift between the components of light coming out of the quarter-wave plate will be $\frac{\pi}{2}$ or $-\frac{\pi}{2}$, which means circularly polarized light.

- Circular → Linear: Suppose the phase shift between $E_r$ and $E_l$ is $\frac{\pi}{2}$ or $-\frac{\pi}{2}$ before passing through the quarter-wave plate. After adding or substracting $\frac{\pi}{2}$ or $-\frac{\pi}{2}$, the new shift will be 0 or $\pi$, which corresponds to linearly polarized light.

### 4.2.4   Half-wave plate

By putting together two quarter-wave plates or doubling the width of one, we get a retardation of $\frac{\lambda}{2}$ . This is called a *half-wave plate*.

There are some materials that can be very affected in their structure by applying an electric voltage to them. Consequently, they can significantly

change their refractive indices in a certain direction and thus they may work as variable retarders. This is called an optical modulator. Its axis is defined again as the fast axis. Let us call $\gamma_M$ the angle formed by the axis of the modulator and the optical plane measured anti-clockwise from the reference plane when looking in the direction of light propagation. And let the retardation induced by the applied voltage be $\phi$. Then, the associated Müller matrix can be written as (*Mishchenko et al.*, 2000):

$$
M^M(\gamma_M) = \begin{pmatrix} 1 & 0 & 0 & 0 \\ 0 & C_M^2 + S_M^2 \cos\phi & S_M C_M (1 - \cos\phi) & -S_M \sin\phi \\ 0 & S_M C_M (1 - \cos\phi) & S_M^2 + C_M^2 \cos\phi & C_M \sin\phi \\ 0 & S_M \sin\phi & -C_M \sin\phi & \cos\phi \end{pmatrix},
$$

$$(4.5)$$

where

$$
S_M = \sin(2\gamma_M)
$$
$$
C_M = \cos(2\gamma_M).
$$

The Müller matrix of a quarter-wave plate is a particular case of the matrix of the modulator.

Retardation is strongly dependent on the wavelength of propagating light. As a consequence, retarders are wavelength-specific. The retardation of crystalline optical modulators and liquid crystals can be adjusted but they can be used only for one wavelength at a time.

### 4.2.5 Circular polarizer

A *circular polarizer* converts natural light into circularly polarized. It is made of a linear polarizer and a quarter-wave plate. Light must pass through the linear polarizer first, as in figure 4.5.

First, any kind of light must pass through a linear polarizer at $45°$ or $-45°$. The linearly polarized light emerging should pass then through a quarter-wave plate with its fast axis at $0°$ or $90°$ from the optical plane.
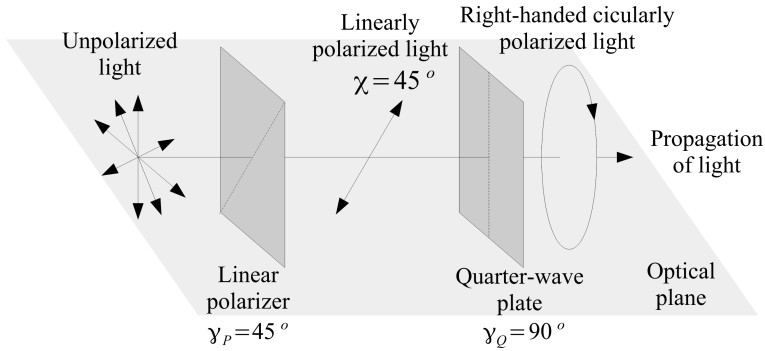
**Figure 4.5:** A circular polarizer consists of a linear polarizer plus a quarter-wave plate. First, light is linearly polarized at $45°$ or $-45°$. Then, it is converted into right- or left-handed, respectively, when passing through the quarter-wave plate

- Any kind of light $\to$ linear polarizer with $\gamma_{LP} = 45°$ $\to$ linearly polarized light at $45°$ with a phase gap $(E_r - E_l)$ of $0°$ $\to$ quarter-wave plate with $\gamma_Q = 90°$ $\to$ right-handed polarized light with a phase gap $(E_r - E_l)$ of $45°$.

- Any kind of light $\to$ linear polarizer with $\gamma_{LP} = 45°$ $\to$ linearly polarized light at $45°$ with a phase gap $(E_r - E_l)$ of $0°$ $\to$ quarter-wave plate with $\gamma_Q = 0°$ $\to$ left-handed polarized light with a phase gap $(E_r - E_l)$ of $-45°$.

- Any kind of light $\to$ linear polarizer with $\gamma_{LP} = -45°$ $\to$ linearly polarized light at $-45°$ with a phase gap $(E_r - E_l)$ of $0°$ $\to$ quarter-wave plate with $\gamma_Q = 90°$ $\to$ left-handed polarized light with a phase gap $(E_r - E_l)$ of $-45°$.

- Any kind of light $\to$ linear polarizer with $\gamma_{LP} = -45°$ $\to$ linearly polarized light at $-45°$ with a phase gap $(E_r - E_l)$ of $0°$ $\to$ quarter-wave plate with $\gamma_Q = 0°$ $\to$ right-handed polarized light with a phase gap $(E_r - E_l)$ of $45°$.

### 4.2.6 Circular analyzer

A *circular analyzer* is an optical device to check whether or not light is circularly polarized and, in such case, it determines how much it is and its sense of rotation.

A couple of crossed linear polarizers can work as a linear polarization analyzer just by subtracting the signal obtained from both. For circular polarization the analysis is not that simple: two circular polarizers could do the job, but they must be flipped so light enters the quarter-wave plate first (figure 4.6).
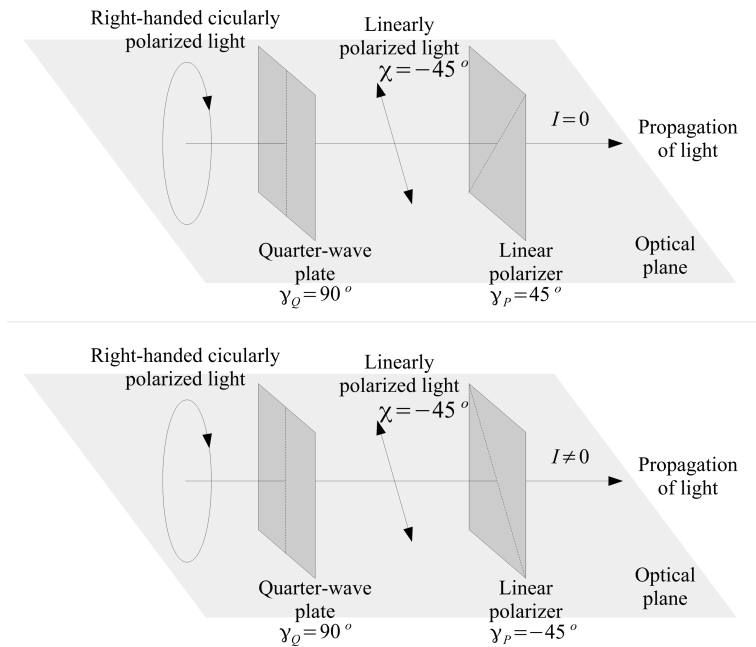


**Figure 4.6:** A circular analyzer consists of two quarter-wave plates plus two linear polarizers. In both cases, circular polarized light passes through the quarter–wave plate, which adds a phase gap of 90°. Then it is converted to linearly polarized light. The axis of the linear polarizers are rotated 90°, so by subtracting the first signal to the second, we can deduce that the incoming light was right-handed (or left-handed) circularly polarized

- Right-handed circularly polarized light with a phase gap $(E_r - E_l)$

of $45° \to$ quarter-wave plate with $\gamma_Q = 90° \to$ linear polarizer with $\gamma_{LP} = -45° \to$ linearly polarized light at $45° \to I = 0$.

- Right-handed circularly polarized light with a phase gap $(E_r - E_l)$ of $45° \to$ quarter-wave plate with $\gamma_Q = 90° \to$ linear polarizer with $\gamma_{LP} = -45° \to$ linearly polarized light at $-45° \to I \neq 0$.

By subtracting the first signal to the second, we can deduce that the incoming light was right-handed circularly polarized.

Equivalently, a quarter wave plate with $\gamma_Q = 0°$ can work with two linear polarizers at $\gamma_{LP} = \pm 45°$.

## 4.3 Wide field imaging polarimeter

We have designed and developed a wide field imaging polarimeter to measure simultaneously the 4 Stokes parameters of the optical emission of a TLE in a single image acquisition, in order to characterize its polarization using a unique CCD.
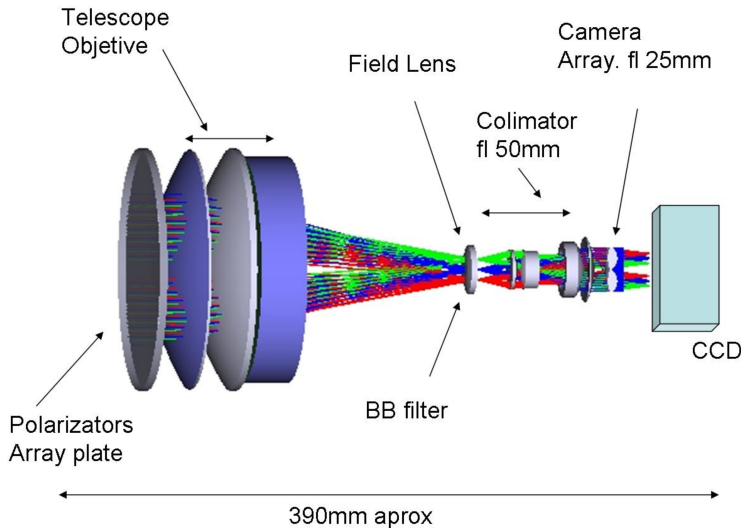


**Figure 4.7:** GRASSP polarimeter basic layout. Two of the six channels are clearly seen

### 4.3.1   Optical description

The polarimeter imaging camera (see figure 4.7) starts with the analyzers plate. It consists of seven circular windows of 48 mm diameter, six of them disposed hexagonally around a center one over a telescope surface (see figure 4.8). An UV protection glass will be installed within the single center window, that will project the wide field image on the CCD; the six remaining windows include four linear polarizers (0°, 45°, 90° and 135°) and two circular polarizers (right and left–handed). After the plate, a large aperture telescope (150 mm) creates a common focal plane where a broadband filter is placed in order to select the wavelength range (550 nm to 775 nm). A field aperture and field lens are also located at this position. The field lens also positions the pupil at the required distance so a collimator can provide a pupil image of the six apertures. At this plane we place a lens array that projects an image on the CCD for each aperture, thus generating six images on a single, large format detector (a CCD of 2048 × 2048 pixels and 15 $\mu$m/px). All these elements are confined in an hollow aluminum cylinder to guarantee environmental protection (see figure 4.9).
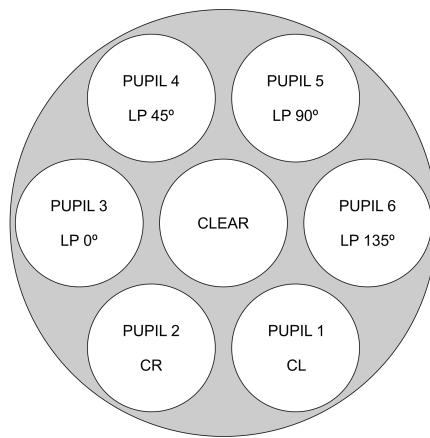


**Figure 4.8:** Geometry of the polarizers plate
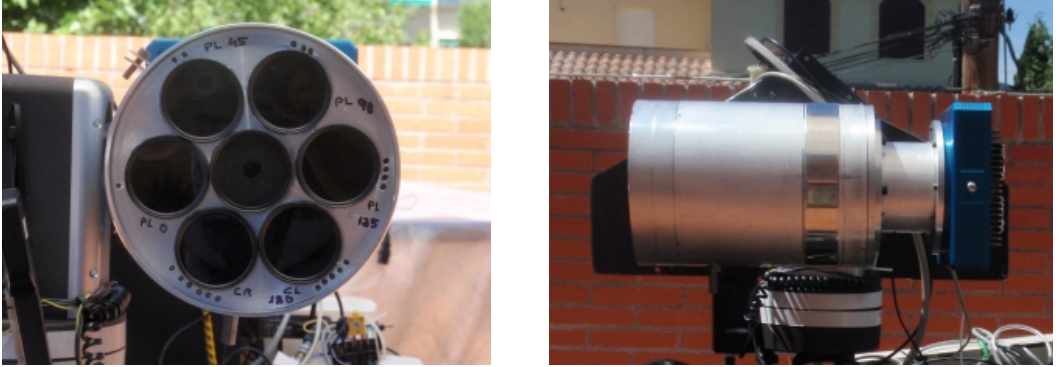
**Figure 4.9:** Front (left) and lateral (right) views of GRASSP polarimeter

| Analyzer | Polarization axis angle (°) | Phase gap |
|---|:---:|:---:|
| Linear polarizer (reference) | 0 | 0 |
| Linear polarizer | 45 | 0 |
| Linear polarizer | 90 | 0 |
| Linear polarizer | 135 | 0 |
| Circular polarizer | 45 | 90 |
| Circular polarizer | 135 | 90 |

**Table 4.1:** Analyzer distribution

### 4.3.1.1   Polarizers plate

The polarizers plate is located at the telescope entrance (the first optical element). This is to avoid the introduction of any instrumental polarization. The size of the polarizers is limited by the 150 mm gathering aperture of the telescope to 48 mm diameter (this is a widely used filter standard size). The analyzers are distributed to table 4.1.

The linear polarizers show a very flat transmission curve between 500 nm and 700 nm (see figure 4.10). This value either refers to the transmission of light polarized linearly in the direction of polarization axis, or to the transmission of unpolarized light through the polarizer. Parallel trans-

mission is the transmission of unpolarized light through two polarizers with their polarization axes aligned in parallel, while crossed transmission is the transmission of unpolarized light through two polarizers with their polarization axes crossed. For ideal polarizers transmission of linearly polarized light parallel to the polarization axis is 100 %, parallel transmission is 50 % and crossed transmission is 0 %.
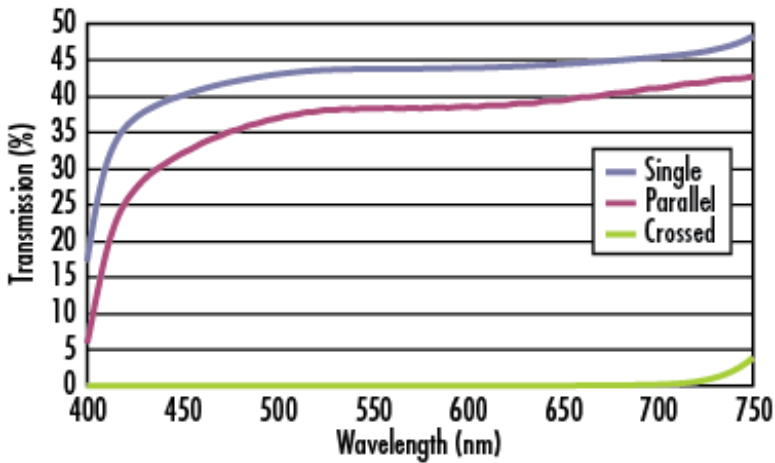


**Figure 4.10:** Transmission test for a polarized linear filter illuminated by polarized light

#### 4.3.1.2   Telescope

The telescope works as a light collector. It is a triplet lens refractor (apochromatic, that is, that minimizes the chromatic aberration), 155 mm in aperture and 190 mm focal length. This makes a very fast unit f/1.22. The telescope focal plane feeds a 18 mm (5° FOV) aperture stop.

#### 4.3.1.3   Filter

We filtered the wavelength range to improve any chromatic effect of the system, specially the telescope and collimator chromatic aberrations. The

filter also allows a good performance of the polarizers, which always have an optimum range, and also decreases the atmosphere wavelength–dependent polarization effects. So we installed two broad band absorption glass filters: a high-pass filter of 550 nm and a low-pass filter of 775 nm. These filters are tilted on the mount to avoid ghost structures.

### 4.3.1.4   Field lens and collimator

The collimator is a commercial objective from Asahi Optical CO (smc-Pentax). This is a 50 mm focal length and f/1.17. A 50 mm focal length plano–convex lens was placed near the focal plane to place the pupil right after the exit of the objective. To avoid any vignetting and in the lack of the optical prescription of the objective, the field lens was placed in a test to guarantee the correct pupil position and the final effective f/ number of the system.

### 4.3.1.5   Camera array

The camera array is placed at the pupil image. Each camera will consist of a 25 mm focal length achromatic doublet. These doublets will be working on a collimated beam (infinite conjugated) for optimum correction. Each camera will be placed on the corresponding image of the aperture. The doublets have an aperture of 9 mm diameter and 22.5 mm focal length.

### 4.3.1.6   CCD detector

The CCD sensor is an Apogee ALTA U3041F (see figure 4.11). It is a large format (4 megapixel) front illuminated detector with 15 micron pixel size. The chip size is 30.7 mm × 30.7 mm which is very well sampled with the 15.5 mm in diameter doublets of the camera optics. This detector was selected to provide the widest affordable FOV. Its main specifications can be found in table 4.2. Figure 4.12 shows the quantum efficiency of the CCD as a function of the wavelength.

**Figure 4.11:** Apogee ALTA U3041F
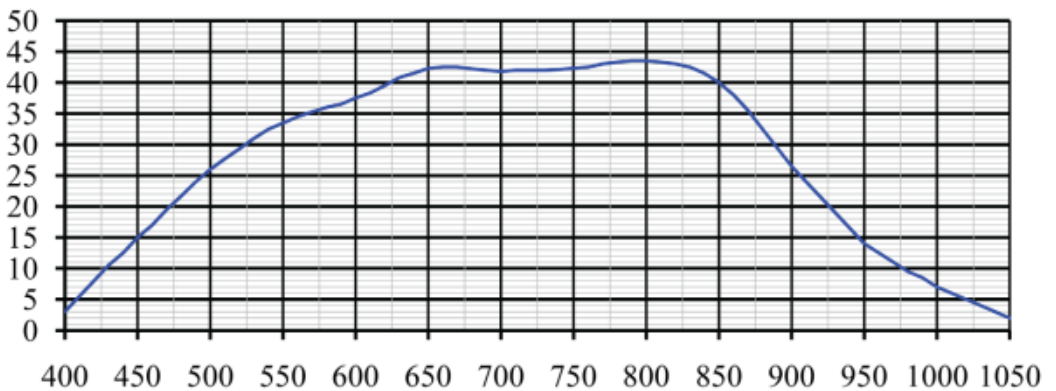


**Figure 4.12:** CCD detector QE in % versus wavelength (nm)

## 4.4  Calibration of the GRASSP polarimeter

The performance of the GRASSP polarimeter (as of any) is not ideal be-
cause of the non-ideal performance of the polarizers and other structural
imperfections of the instrument: the non-perfect alignment of the axes of
all polarizers, the non-perfect orientation of the polarization axes of the

| CCD | Fairchild 3041 |
|---|---|
| **Array Size (pixels)** | 2048 × 2048 |
| **Pixel Size** | 15 × 15 microns |
| **Imaging Area** | 30.7 × 30.7 mm (944 mm$^2$) |
| **Imaging Diagonal** | 43.4 mm |
| **Video Imager Size** | 2.7" |
| **Linear Full Well (typical)** | 100 K electrons |
| **Dynamic Range** | 82 dB |
| **QE at 400 nm** | 3% |
| **Peak QE (800 nm)** | 43.5% |

**Table 4.2:** Main CCD detector specifications

linear polarizers at 0°, 90°, 45° and −45°, etc.

Calibration must be carried out each time when any change of polarizers, reposition of the pupils or any structural change is made in the instrument. For instance, it should be done after focusing.

### 4.4.1 The calibration matrix
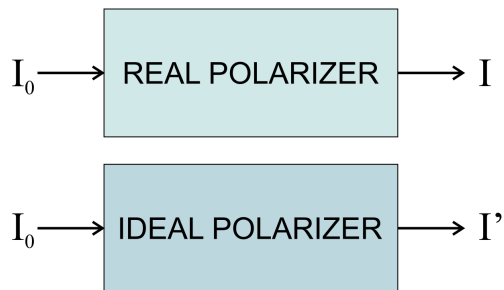


**Figure 4.13:** Stokes vectors of light coming from the source before it goes through any of the polarizers of the polarimeter ($I_0$), and after ($I$) if the polarizer is real and $I'$ if the polarizer is ideal)

The Stokes vector of light coming from the source before it goes through any of the pupils of the polarimeter is noted as in equation 4.6. This is the unknown of our problem.

$$\vec{I_0} = \begin{pmatrix} I_0 \\ Q_0 \\ U_0 \\ V_0 \end{pmatrix} \tag{4.6}$$

The Stokes parameters of light coming on the CCD detector after passing through one of the pupils (non-ideal linear or circular polarizer) are given in equation 4.7:

$$\vec{I} = \begin{pmatrix} I \\ Q \\ U \\ V \end{pmatrix} \tag{4.7}$$

We will note the Stokes vector of light that would come on the CCD detector after passing through an ideal linear or circular polarizer as in equation 4.8.

$$\vec{I'} = \begin{pmatrix} I' \\ Q' \\ U' \\ V' \end{pmatrix} \tag{4.8}$$

The vectors $I_0$, $I$ and $I'$ are represented in figure 4.13. If all polarizers of the instrument were ideal, obtaining the Stokes parameters of the incident light would be as simple as

$$\begin{aligned} I_0 &= I'_{P0} + I'_{P90} \\ Q_0 &= I'_{P0} - I'_{P90} \\ U_0 &= I'_{P45} - I'_{P-45} \\ V_0 &= I'_{CR} - I'_{CL} \end{aligned} \tag{4.9}$$

with $P$ being a linear polarizer and $C$ a circular polarizer, as a combination of a linear polarizer and a quarter wave plate.

Let us call, $I_{P0}$, $I_{P90}$, $I_{P45}$, $I_{P-45}$, $I_{CR}$ and $I_{CL}$ the intensities of light on the detector after passing through actual non-ideal linear and circular polarizers of GRASSP. Let us now define errors in intensity of the non-ideal polarizers as

$$\begin{aligned} I &= I' + \delta I \\ I' &= I - \delta I. \end{aligned} \qquad (4.10)$$

The definition can be extended to the whole Stokes vector, as shown in equation 4.11.

$$\begin{pmatrix} I' \\ Q' \\ U' \\ V' \end{pmatrix} = \begin{pmatrix} I \\ Q \\ U \\ V \end{pmatrix} - \begin{pmatrix} \delta I \\ \delta Q \\ \delta U \\ \delta V \end{pmatrix}. \qquad (4.11)$$

Definitions given in equations 4.10 and 4.11 are valid only for a single measurement.

Let $\left( M'_{ij} \right)$ be the Mueller matrix of an ideal linear or circular analyzer and $(M_{ij})$ the matrix of an actual non-ideal analyzer in our instrument. Then, the errors of the matrix elements $(\delta M_{ij})$ can be defined as:

$$(M_{ij}) = \left( M'_{ij} \right) + (\delta M_{ij}). \qquad (4.12)$$

From equations 4.11 and 4.12 we can derive:

$$\begin{pmatrix} \delta I \\ \delta Q \\ \delta U \\ \delta V \end{pmatrix} = \begin{pmatrix} \delta M_{11} & \delta M_{12} & \delta M_{13} & \delta M_{14} \\ \delta M_{21} & \delta M_{22} & \delta M_{23} & \delta M_{24} \\ \delta M_{31} & \delta M_{32} & \delta M_{33} & \delta M_{34} \\ \delta M_{41} & \delta M_{42} & \delta M_{43} & \delta M_{44} \end{pmatrix} \begin{pmatrix} I_0 \\ Q_0 \\ U_0 \\ V_0 \end{pmatrix}. \qquad (4.13)$$

Equations 4.9, 4.10 and 4.13 lead to:

$$I_0 = I_{P0} + I_{P90} - \left(\delta M_{11}^{P0} + \delta M_{11}^{P90}\right) I_0 - \left(\delta M_{12}^{P0} + \delta M_{12}^{P90}\right) Q_0 -$$
$$- \left(\delta M_{13}^{P0} + \delta M_{13}^{P90}\right) U_0 - \left(\delta M_{14}^{P0} + \delta M_{14}^{P90}\right) V_0$$

$$Q_0 = I_{P0} - I_{P90} - \left(\delta M_{11}^{P0} - \delta M_{11}^{P90}\right) I_0 - \left(\delta M_{12}^{P0} - \delta M_{12}^{P90}\right) Q_0 -$$
$$- \left(\delta M_{13}^{P0} - \delta M_{13}^{P90}\right) U_0 - \left(\delta M_{14}^{P0} - \delta M_{14}^{P90}\right) V_0$$

$$U_0 = I_{P45} - I_{P-45} - \left(\delta M_{11}^{P45} - \delta M_{11}^{P-45}\right) I_0 - \left(\delta M_{12}^{P45} - \delta M_{12}^{P-45}\right) Q_0 -$$
$$- \left(\delta M_{13}^{P45} - \delta M_{13}^{P-45}\right) U_0 - \left(\delta M_{14}^{P45} - \delta M_{14}^{P-45}\right) V_0$$

$$V_0 = I_{CR} - I_{CL} - \left(\delta M_{11}^{CR} - \delta M_{11}^{CL}\right) I_0 - \left(\delta M_{12}^{CR} - \delta M_{12}^{CL}\right) Q_0 -$$
$$- \left(\delta M_{13}^{CR} - \delta M_{13}^{CL}\right) U_0 - \left(\delta M_{14}^{CR} - \delta M_{14}^{CL}\right) V_0. \tag{4.14}$$

Let us define the *calibration matrix* as a $4 \times 4$ matrix with elements:

$$C_{11} = 1 + \delta M_{11}^{P0} + \delta M_{11}^{P90}$$
$$C_{12} = \delta M_{12}^{P0} + \delta M_{12}^{P90}$$
$$C_{13} = \delta M_{13}^{P0} + \delta M_{13}^{P90}$$
$$C_{14} = \delta M_{14}^{P0} + \delta M_{14}^{P90}$$
$$C_{21} = \delta M_{11}^{P0} - \delta M_{11}^{P90}$$
$$C_{22} = 1 + \delta M_{12}^{P0} - \delta M_{12}^{P90}$$
$$C_{23} = \delta M_{13}^{P0} - \delta M_{13}^{P90}$$
$$C_{24} = \delta M_{14}^{P0} - \delta M_{14}^{P90}$$
$$C_{31} = \delta M_{11}^{P45} - \delta M_{11}^{P-45}$$
$$C_{32} = \delta M_{12}^{P45} - \delta M_{12}^{P-45} \tag{4.15}$$
$$C_{33} = 1 + \delta M_{13}^{P45} - \delta M_{13}^{P-45}$$
$$C_{34} = \delta M_{14}^{P45} - \delta M_{14}^{P-45}$$
$$C_{41} = \delta M_{11}^{CR} - \delta M_{11}^{CL}$$
$$C_{42} = \delta M_{12}^{CR} - \delta M_{12}^{PL}$$
$$C_{43} = \delta M_{13}^{CR} - \delta M_{13}^{CL}$$
$$C_{44} = 1 + \delta M_{14}^{CR} - \delta M_{14}^{CL}$$

Then, the set of equations 4.14 can be simplified by matrix notation:

$$(C_{ij}) \begin{pmatrix} I_0 \\ Q_0 \\ U_0 \\ V_0 \end{pmatrix} = \begin{pmatrix} I_{P0} + I_{P90} \\ I_{P0} - I_{P90} \\ I_{P45} - I_{P-45} \\ I_{CR} - I_{CL} \end{pmatrix} \tag{4.16}$$

Matrix $(C_{ij})$ contains information on the deviation from ideal of the linear and circular analyzers of the instrument. In case of an ideal instrument, the calibration matrix would become the identity matrix and equation 4.16 would be equivalent to equation 4.9.

Equation 4.16 is equivalent to a set of 4 linear equations with 4 unknowns: $I_0$, $Q_0$, $U_0$ and $V_0$. The column vector on the right side of the equation can be obtained from one single measurement. If we knew the calibration matrix, the set of equations could be solved so the Stokes parameters of light coming from the source could be retrieved. From those, the degrees of both linear and circular polarization could be obtained as explained in the section 4.5.

The GRASSP polarimeter can be used to investigate both linear and circular polarization of light, but it can also work in a linear-polarization-only mode just by discarding the last of the set of equations 4.14. In matrix notation:

$$
\begin{aligned}
C_{11} &= 1 + \delta M_{11}^{P0} + \delta M_{11}^{P90} \\
C_{12} &= \delta M_{12}^{P0} + \delta M_{12}^{P90} \\
C_{13} &= \delta M_{13}^{P0} + \delta M_{13}^{P90} \\
C_{21} &= \delta M_{11}^{P0} - \delta M_{11}^{P90} \\
C_{22} &= 1 + \delta M_{12}^{P0} - \delta M_{12}^{P90} \\
C_{23} &= \delta M_{13}^{P0} - \delta M_{13}^{P90} \\
C_{31} &= \delta M_{11}^{P45} - \delta M_{11}^{P-45} \\
C_{32} &= \delta M_{12}^{P45} - \delta M_{12}^{P-45} \\
C_{33} &= 1 + \delta M_{13}^{P45} - \delta M_{13}^{P-45}
\end{aligned}
\tag{4.17}
$$

$$
(c_{ij}) \begin{pmatrix} I_0 \\ Q_0 \\ U_0 \end{pmatrix} = \begin{pmatrix} I_{P0} + I_{P90} \\ I_{P0} - I_{P90} \\ I_{P45} - I_{P-45} \end{pmatrix}.
\tag{4.18}
$$

Hereafter we will call $c_{ij}$ the *reduced calibration matrix*. In this linear-polarization mode, only $I_0$, $Q_0$ and $U_0$ would be the unknowns. From those parameters, the degree of linear polarization and the orientation of the axis of polarization could be calculated, but not the degree of circular polarization. This simplification makes sense as circular polarizers are nowadays

far from ideal, present a large stochastic error for our purposes, are quite expensive and they are much more wavelength-dependent than linear polarizers. Our instrument can work as a linear polarization analyzer at this moment and will be updated in the future to include fairly good circular polarization analysis.

### 4.4.2 Calibration in linear-polarimetry-only mode

A non polarized light source must be used for the calibration described in this section. As shown in figure 4.14, a calibration unit must be placed between a source of light and our instrument. In the case of linear-polarimetry-only mode, let us consider an ideal linear polarizer for calibration $LP$, although obviously it is not.
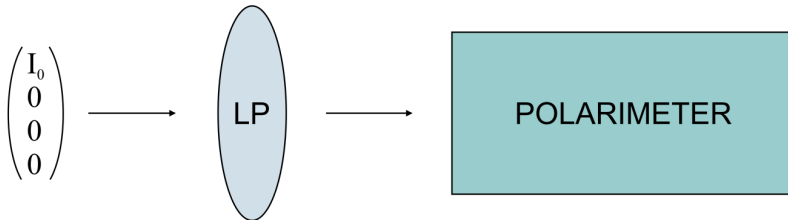


**Figure 4.14:** A linear polarizer placed between the light source and the instrument as a calibration unit in linear-polarization-only mode

$LP$ is placed within a rotating frame. Rotation occurs around the direction of light so the orientation of the axis of $LP$ ($\gamma_{LP}$) changes continuously. An electric engine rotates the frame. It is controlled automatically by an *Arduino* board and a sketch of *Arduino* software we have developed.

Let us call $M^{LP}$ the Mueller matrix of an ideal linear polarizer and $M$ the actual Mueller matrix of the instrument to investigate. The matrix of the whole calibration setup (including the instrument) would be the product

of both.

$$\vec{I} = MM^{LP}\left(\gamma_{LP}\right)\vec{I_0} \tag{4.19}$$

Equation 4.19 refers to all of the Stokes parameters. In particular, the flux reaching the detector of the polarimeter would be:

$$I = \frac{I_0}{2}M_{11} + \frac{I_0}{2}M_{12}\cos\left(2\gamma_{PL}\right) + \frac{I_0}{2}M_{13}\sin\left(2\gamma_{PL}\right). \tag{4.20}$$

Now let us rotate $LP$, stop at a number of positions and take images in each position. Those positions should uniformly cover any 180° range. Simply by imagining the axis of the polarizer rotating, it is clear that the system is equivalent for any orientation $\gamma_{LP}$ and $\gamma_{LP} + 180°$, and we can see the periodicity of 180° of our system in equation 4.3 as well. After measuring at these positions, a table of pairs of data $\left(\gamma_{LP}, I\right)$ is built and a non-linear fit to function given in equation 4.21 is performed.

$$I = \alpha_1^{LP} + \alpha_2^{LP}\cos\left(2\gamma_{LP}\right) + \alpha_3^{LP}\sin\left(2\gamma_{LP}\right). \tag{4.21}$$

From this fitting, we estimated coefficients $\alpha_1^{LP}$, $\alpha_2^{LP}$ and $\alpha_3^{LP}$ with their errors.

Comparing equations 4.20 and 4.21:

$$\begin{aligned}
M_{11} &= 2\alpha_1^{LP} \\
M_{12} &= 2\alpha_2^{LP} \\
M_{13} &= 2\alpha_3^{LP}
\end{aligned} \tag{4.22}$$

As shown in equation 4.17, the reduced calibration matrix $c_{ij}$ is made out of the differential quantities $\delta M_{11}$, $\delta M_{12}$ and $\delta M_{13}$ for four of the pupils of the instrument: $P0$, $P90$, $P45$ and $P-45$. These can be derived from equations 4.22 and 4.12.

Unfortunately, we considered that the linear polarizer in the calibration system was ideal, but it is not. Once we calculate the reduced calibration matrix, next step is to repeat the measurements considering the polarimeter with the reduced calibration matrix $c_{ij}$ as an ideal system and with the

linear polarizer for calibration being non–ideal, so we can estimate the non ideal behaviour of the linear polarizer used in the calibration. Then we have to consider the linear polarizer for calibration with its errors as an ideal system and to calculate again the reduced calibration matrix $c_{ij}$. This process should be repeated until we find a convergent solution.

### 4.4.3 Calibration in complete mode

By this process, all elements of the first row of the Mueller matrix of our polarimeter can be obtained. Again a source of unpolarized light is used.

Now we considered an ideal quarter wave plate $Q$ added to the ideal calibration unit as shown in figure 4.15.
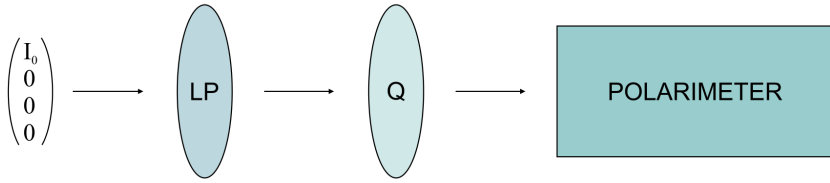


**Figure 4.15:** A linear polarizer and a quarter-wave plate placed between the light source and the instrument as a calibration unit in complete mode.

The Stokes vector in the detector can be calculated by multiplying all Mueller matrices in the path of light:

$$\vec{I} = M M^Q\left(\gamma_Q\right) M^{LP}\left(\gamma_{LA}\right) \vec{I_0} \tag{4.23}$$

In particular, the flux on the detector would be given by:

$$
\begin{aligned}
I = & \tfrac{I_0}{2} M_{11} + \tfrac{I_0}{2} M_{12} \cos\left(2\gamma_{LP}\right) \cos^2\left(2\gamma_Q\right) + \tfrac{I_0}{2} M_{14} \cos\left(2\gamma_{LP}\right) \sin\left(2\gamma_Q\right) + \\
& + \tfrac{I_0}{2} M_{13} \cos\left(2\gamma_{LP}\right) \sin\left(2\gamma_Q\right) \cos\left(2\gamma_Q\right) + \tfrac{I_0}{2} M_{13} \sin\left(2\gamma_{LP}\right) \sin^2\left(2\gamma_Q\right) - \\
& - \tfrac{I_0}{2} M_{14} \sin\left(2\gamma_{LP}\right) \cos\left(2\gamma_Q\right) \cos\left(2\gamma_Q\right) + \tfrac{I_0}{2} M_{12} \sin\left(2\gamma_{LP}\right) \cos\left(2\gamma_Q\right) \sin\left(2\gamma_Q\right)
\end{aligned}
\tag{4.24}
$$

Rotating $LP$ and $Q$ independently, a table of values $(\gamma_{LP}, \gamma_Q, I)$ is built, and a non-linear multiple variable fit is performed to a function as that given in equation 4.25:

$$
\begin{aligned}
I = {} & \alpha_0^{PQ} + \alpha_1^{PQ} \cos(2\gamma_{LP}) \cos^2(2\gamma_Q) + \alpha_2^{PQ} \cos(2\gamma_{LP}) \sin(2\gamma_Q) + \\
& + \alpha_3^{PQ} \cos(2\gamma_{LP}) \sin(2\gamma_Q) \cos(2\gamma_Q) + \alpha_4^{PQ} \sin(2\gamma_{LP}) \sin^2(2\gamma_Q) - \\
& - \alpha_5^{PQ} \sin(2\gamma_{LP}) \cos(2\gamma_Q) \cos(2\gamma_Q) + \alpha_6^{PQ} \sin(2\gamma_{LP}) \cos(2\gamma_Q) \sin(2\gamma_Q)
\end{aligned}
\tag{4.25}
$$

Comparing equations 4.24 and 4.25:

$$
M_{14} = \alpha_3^{PQ} - \alpha_5^{PQ}
\tag{4.26}
$$

Equation 4.22 is still valid for retrieving $M_{11}$, $M_{12}$ and $M_{13}$. These may be obtained from equation 4.25 as well, but it is convenient to get them from data obtained with the simplest calibration setup in order to minimize systematic and stochastic errors.

Again, we considered that the linear polarizer and the quarter wave plate in the calibration system were ideal, but they are not. We have to estimate the errors of the linear polarizer and the quarter wave plate for calibration to completely calculate all the elements of the Mueller matrix of our system. This can be done only by iterating the process until we find a convergent solution.

### 4.4.4 Step-by-step recipe for calibration

The whole process to obtain the calibration matrix (equations 4.15 and 4.17) can be summarized as:

1. Place a linear polarizer $LP$ between the (unpolarized) light source and the instrument.

2. Measure the flux on the detector for a number of orientations of $LP$ uniformly covering $[0°, 180°[$.

3. Use measurements from step 2 to fit the function given in equation 4.21 and obtain $\alpha_1^{LP}$, $\alpha_2^{LP}$ and $\alpha_3^{LP}$.

4. Deduce $M_{11}$, $M_{12}$ and $M_{13}$ from the result of step 2 and equations 4.22.

5. Calculate $\delta M_{11}$, $\delta M_{12}$ and $\delta M_{13}$ from the result of step 3 and equation 4.12.

   If we are measuring circular polarization:

6. Add a quarter wave plate $Q$ between the calibration polarizer and the instrument and measure the flux on the detector for a number of independent orientations of $LP$ and $Q$ uniformly covering $[0°, 180°[$ ranges.

7. Use measurements from step 4 to fit the function given in equation 4.25 and obtain $\alpha_3^{PQ}$ and $\alpha_5^{PQ}$.

8. Obtain $M_{14}$ from equation 4.26 and the result of step 5.

9. Calculate $\delta M_{14}$ from the result of step 7 and equation 4.12.

All measurements have to be corrected by bias, background and flat images before fitting the functions given in equations 4.21 and 4.25.

### 4.4.5   Calibration system and results

To calculate the calibration matrix of the GRASSP polarimeter, we have built a calibration system consisting of an unpolarized light source module, a calibration unit and a refractive telescope.

The unpolarized light source module consists of a hollow aluminum cylinder, held by an aluminum post which is attached to the optical bench by an aluminum plate. It holds a solid and thick circular plate within one of the bases which shows a central drilling, allocating a flattened red LED which is used as the unpolarized source, emitting in all directions. The other base

allocates a thin and solid aluminum circular plate, black in its surfaces to minimize the albedo, presenting 5 pinholes in its center. By connecting the LED to a power supply of 5.1 V through a 500 Ohm potentiometer, we perform a matrix of five parallel beams incident to the rotators module, which is aligned next to the pinhole matrix, so we have a five punctual sources pattern. The output beams reach the telescope module to further arrive GRASSP polarimeter.

The calibration unit consists of two submodules, lined up next to each other. Each submodule consists of a hollow aluminum cylinder with a vertical drilling to let a worm to rotate a sprocket wheel —which is allocated inside the cylinder— thanks to a stepper gear installed over the cylinder and actuated by an Arduino motherboard. We have also installed a limit switch that is activated when a screw attached to the sprocket wheel passes though. The rotator system holds a circular filter mount and an aluminum ring to brace either a linear polarizer (in the first submodule) or a quarter-wave plate (in the second submodule). The rotators are sealed with two methacrylate rings. The attachment to the optical bench is similar to that described before. The calibration unit can be set either as a simple rotating linear polarizer or a combination of rotating linear polarizer and a rotating quarter wave plate.

Before getting to the instrument, light is converted into a plane wave–front by passing through the convergent lens of a refractive telescope. Then it passes through all of the six pupils of the polarimeter and is detected by the CCD camera. The whole optical chain of optical elements for calibration is shown in figure 4.16.

The first step of the calibration process consists of setting the calibration unit to be a single rotating linear polarizer (*LP*), by placing it between the unpolarized source and the polarimeter to calibrate. A stepper motor moved the rotating frame through an Arduino board (previously set with an Arduino sketch `ROTATE.ino`) commanded by a MATLAB software we have developed (`GEAR.m`). These tasks will be thoroughly described in chapter 5.
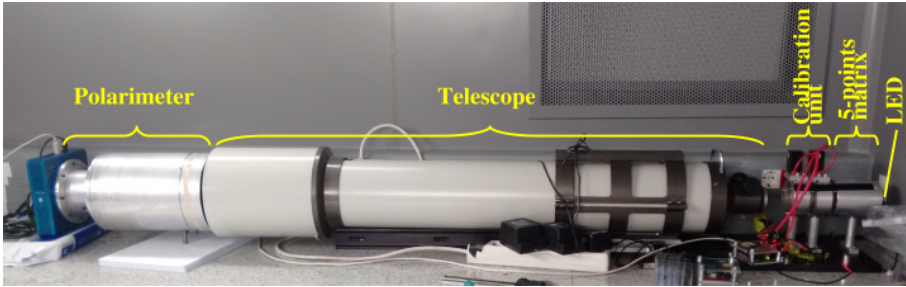
**Figure 4.16:** The whole chain of optical elements in the optical path of light for calibration. Light goes from right to left. In order: led unpolarized source, five points matrix, calibration unit, convergent lens of a diffractive telescope, polarimeter

The range $[0°, 180°[$ was covered in 50 steps, so the angular resolution was $3.6°$. For each step, an image had to be taken by the CCD detector of the instrument and downloaded to a computer. This was a slow but automatic and non–interrupted process that took approximately two hours.

Figure 4.17 shows the flux measurements (circles) for the four of the linear analyzers of the instruments as a function of the angle of the calibration linear polarizer during step 1 of the calibration recipe given in section 4.4.4. A non–linear fitting was performed by using `xmgrace` software (step 2 of section 4.4.4). The fitted function (red solid line) is shown along with the measurements.

Table 4.3 presents the elements of the actual Mueller matrices corresponding to all linear analyzers of the instrument.

|  | $M_{11}$ | $M_{12}/M_{11}$ | $M_{13}/M_{11}$ |
|---|---|---|---|
| Linear polarizer $0°$ | 1 | 0.962192703 | 0.0994895529 |
| Linear polarizer $45°$ | 1 | -0.3004252093 | 0.9308721351 |
| Linear polarizer $90°$ | 1 | -0.8517655945 | -0.3504747471 |
| Linear polarizer $-45°$ | 1 | 0.2023242628 | -0.9138568076 |

**Table 4.3:** Actual values of the elements of the first row of the Mueller matrix of the polarimeter
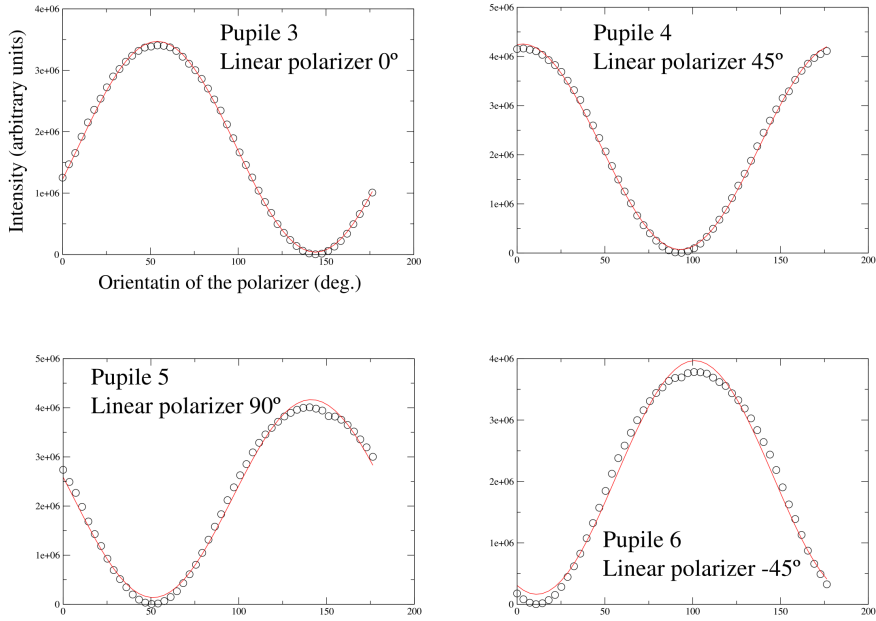
**Figure 4.17:** Measurements (circles) and fitted curve (solid red lines) of the flux going through all of the four linear-analyzer pupils of the instrument

With these values we conclude that we can detect a linear polarization degree of 2 % (see equation 4.27).

Step 5 of the calibration recipe (given in section 4.4.4) was carried out. The quarter-wave plate $Q$ we used to calibrate was indicated for red light (684 nm). As well as the linear polarizer, it was placed in a frame rotated by a stepper motor (figure 4.18) and commanded by a MATLAB routine we developed (`GEAR.m`).

The range $[0°, 180°[$ was covered in 50 steps for each step of $LP$, so 2500 measurements were carried out. This was a non-interrupted automatic process that took, approximately, four days.
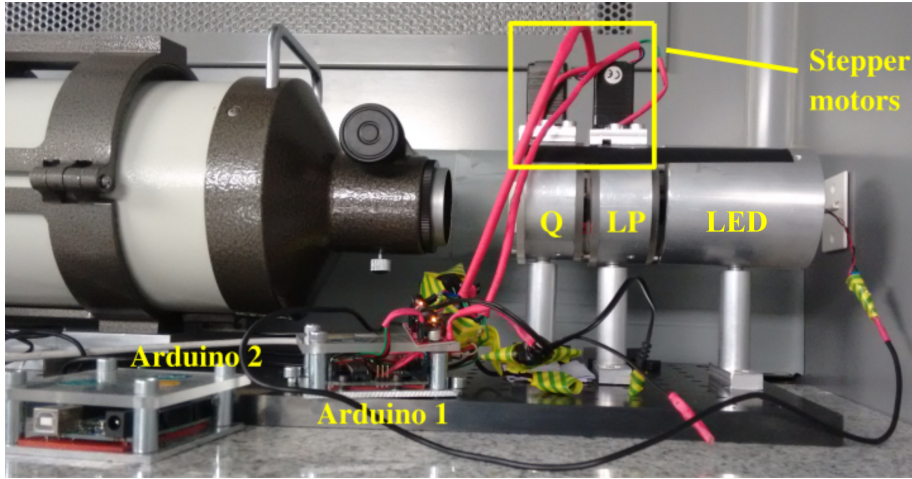
**Figure 4.18:** Calibration unit consisting of a linear polarizer $LP$ (right) and a quarter-wave plate $Q$ (left). Source light goes through the linear polarizer first. $LP$ and $Q$ are embedded within a rotating frame moved by stepper motors controlled by Arduino boards

## 4.5 How to get the degrees of linear and circular polarization

Suppose calibration was already performed and $(C_{ij})$ is known. Then we measure the flux of a certain signal. Light passing through all of the six pupils of the polarimeter goes to the detector at the same time, so one image will contain the information coming from all pupils in six separated regions. The object we are observing will be repeated in all regions with different intensities. Some features of the observed object must be recognized in all regions so we can establish a correspondence between pixels of the six regions and parts of the object. Let us center in a part of the object and localize the corresponding pixel in all of the six regions of the image. The count values at those pictures will be proportional to fluxes $I_{P0}$, $I_{P90}$, $I_{P45}$, $I_{P-45}$, $I_{CR}$ and $I_{CL}$. With all this information, the set of equations given in (4.16) is determined. Now we just solve it and obtain $I_0$, $Q_0$, $U_0$ and $V_0$.

The degrees of linear ($DLP$) and circular ($DCP$) polarization are de-

fined as *Hovenier et al.* (2004):

$$DLP = \frac{\sqrt{Q_0^2 + U_0^2}}{I_0},$$
$$DCP = \frac{V_0}{I_0}. \tag{4.27}$$

The angle $\chi$ formed by the major axis of the polarization ellipse and the optical reference plane can be calculated as follows (*Hovenier et al.*, 2004):

If $Q_0 = 0$ and $U_0 > 0$, $\chi = 90°$, if $Q_0 = 0$ and $U_0 < 0$, $\chi = -90°$, if $Q_0 \neq 0$, $\tan 2\chi = \frac{U_0}{Q_0}$ and $Q_0 \cos 2\chi > 0$.

$$\tag{4.28}$$

In summary, this is the pipeline to retrieve $DLP$, $DCP$ and $\chi$:

1. Measure intensities reaching the CCD detector from each pupil: $I_{P0}$, $I_{P90}$, $I_{P45}$, $I_{P-45}$, $I_{CR}$ and $I_{CL}$.

2. Solve the system of linear equations given in equation 4.16.

3. Use equations 4.27 and 4.28 to get $DLP$, $DCP$ and $\chi$.

# Chapter 5

# Software

*"This was a twilight flight during the summer of 1966 from Randolph Air Force Base to Arizona. [...] There were numerous large cells, and lightning was continuous in all quadrants on this flight. About 50 miles west of San Antonio, Texas, at flight level 41,000 feet over mean sea level, I observed a strong shaft of lightning go directly up and discharge into the ionosphere. It occurred a number of times through the life of the cell. The storm extended above 50,000 feet over mean sea level."*

– Lloyd F. Willett, United States Air Force pilot retired major and meteorologist, *Journal of Geophysical Research, September 30, 1989*

## 5.1 Introduction

Within this chapter we will describe the software we have developed to control all versions of the GRASSP instrument, to reduce the recorded spectral data and to calibrate both the spectrograph and the polarimeter. We will also describe the commercial acquisition software we use for polarimetry (*Nebulosity*) and spectroscopy (*UFO Capture HD2*), which allows to capture both spectra and field images in a synchronous way, so we can discern the region of the TLE we are recording the spectrum of.

First we will describe a software overview and then we will detail each task individually.

## 5.2    Software overview

The GRASSP software tasks can be divided into three main blocks, as can be seen in figure 5.1: (1) the instrument control software, (2) the acquisition software and (3) the data reduction software.

The instrument control software manages GRASSP remotely and allows us to switch on and off all GRASSP subsystems, to change the automaton IP, to set the L'Heritier camera parameters, to calibrate GRASSP spectrograph and to aim the telescope mount to the desired position. We also include in this section the control software that commands the polarimeter calibration system. All these tasks have been developed by the author in MATLAB programming language.

The spectral acquisition software is a commercial application developed by SonotaCo —UFO Capture HD2—, which allows us to record synchronously the field camera images and the spectral images, thanks to an audio trigger system. The polarimetric acquisition software is also a commercial application developed by Stark Labs —Nebulosity— which continuously records polarimetric images and to remotely set the Apogee ALTA U3041F camera integration time.

We have developed a spectroscopic and a polarimetric data reduction software pipeline, which consist of obtaining calibrated and reliable signals from raw spectral and polarimetric images. These tasks have been developed by the author in MATLAB programming language.

### Why MATLAB?

Besides the author's previously expertise on MATLAB, we have chosen this programming language for many reasons: its libraries have a solid amount of functions, its integrated development environment (IDE) makes

the tasks easy to debug, the instrument control toolbox allows us to easily low–level control several devices, the image processing toolbox allows us to extract useful information from the raw spectral and polarimetric images, it is very well documented, it is very easy to develop graphical user interfaces, the MATLAB scientific community is very active and we have access to our institution's MATLAB license.



**Figure 5.1:** GRASSP Software Overview

## 5.3 Instrument Control Software

As we developed two different versions of GRASSP aiming system, in this section we will describe the control software tasks related to each of them as well as the common software they share (see boxes in grey in figure 5.2).

### 5.3.1 Common Software

In this subsection we will describe the common software that both versions of GRASSP share: (1) `ChangeIP.m`, an application to remotely modify the automaton IP, (2) `lheritier.m`, an application to remotely set the iCCD parameters and (3) `LHERITIER.m`, a graphical user interface (GUI) that allows the user to control the L'Heritier camera parameters.

#### 5.3.1.1 `ChangeIP.m`

It is necessary to set a static internet protocol (IP) address to remotely access the automaton. The automaton has a default IP address which is 85.16.x.y, x and y being the two last bytes of the media access control (MAC)

## Instrument Control Software
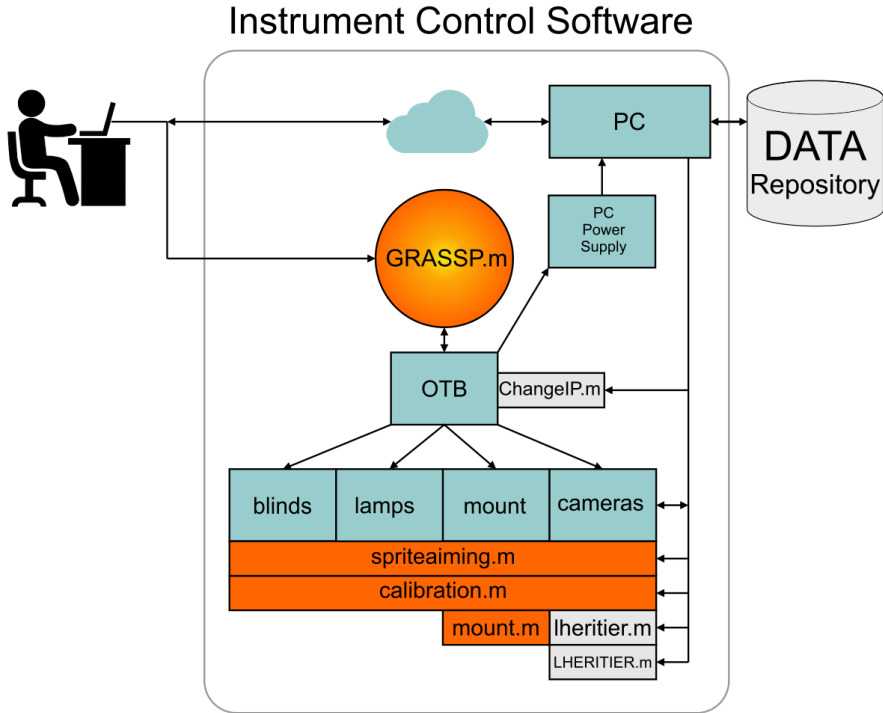


**Figure 5.2:** GRASSP instrument control software scheme

address of the automaton. So we have to change the IP address of the automaton to further access it remotely. We first power off the automaton and set the optimized terminal block (OTB) rotary switch to *Clear IP*. Then, we wait 3 minutes and set the rotary switch to *Stored IP*. Then we change the automaton IP through the application program we developed in MATLAB programming language, `ChangeIP.m`, whose graphical user interface is shown in figure 5.3.

First we obtain the current IP address, subnet mask and gateway values, by pressing the *Get data* button, which reads 6 registers of the automaton, starting from register number 1061. Registers 1061 and 1062 indicate the current IP address (remember: one register is one word of 16 bits, so two registers define a complete IP address of 4 8-bit numbers). Registers 1063 and 1064 indicate the current subnet mask value, and registers 1065 and

**Figure 5.3:** Graphical user interface to remotely change the IP address of the automaton

1066 indicate the current gateway value.

Then, we set the new values of the IP address, subnet mask and gateway by pressing the *Change data* button, which follows the tasks below:

- We access the automaton through its current IP address by a TCP/IP connection.

- We switch the register number 1050 from value '0' to value '1', to enable register writing.

- We change the automaton IP address by writing the new value in registers 1051 and 1052.

- We change the automaton subnet mask by writing the new value in registers 1053 and 1054.

- We change the automaton gateway by writing the new value in registers 1055 and 1056.

- We close the TCP/IP connection.

The next step is to verify if we set the desired values properly by pressing the *Verify data* button, which reads the automaton registers 1051 to 1056. If

we are completely sure that the values are right, we press button *STORE*, which changes the value of the register number 1050 from '1' to '0' and disable registers for writing

We must be careful not to remotely change the automaton IP to a random value: it has to be the static IP address of the observation site, otherwise we could not access the automaton remotely. If we accidentally set a wrong IP address, the only way to restore it again is to manually reboot the automaton IP, with the inconvenience of travelling to the observation site.

The reason we developed this GUI is that, sometimes, the internet supplier can change the fixed remote IP. In this situation, without this GUI, the only way to remotely access to the GRASSP instrument is to physically go to the observation site and manually change the IP. With `ChangeIP.m` we only have to ask the operator to switch on the PC, then we remotely access the PC through *remote desktop* application and change the IP. This GUI has has prevented us from having to travel for several times.

#### 5.3.1.2 `lheritier.m`

The commercial software that controls the L'Heritier camera is a hermetic built-in application program that allows the final user to set several parameters of the iCCD. But since we need the autonomous managing of the camera we developed `lheritier.m`, a routine that allows tasks `calibration1x.m`, `calibration2x.m` and `spriteaiming.m` to configure the L'Heritier camera parameters without the supervision of the final user. In particular, `lheritier.m` changes the tube and electronic gains of the L'Heritier camera, keeping constant the rest of the parameters that can be set.

**L'Heritier communications protocol**

We identified the communication protocol of the L'Heritier iCCD camera

by inspecting the hexadecimal frames sent and received by the PC and the camera while we set the parameters through its commercial software. To do so, we connected the camera to the PC through a RS-232 cable and opened a serial communication through COM3, setting the parity as even and a baudrate of 11500.

Every L'Heritier camera communication frame consists of a total of 28 bytes: a 6-byte fixed header, a 16-byte message body, a 5-byte fixed tail and a cyclic redundancy check (CRC) byte, whose pseudocode is implemented in algorithm 1. A cyclic redundancy check byte is a signature of the frame and it is calculated both by the transmitter and receiver. If this value is not consistent, a message error is generated and the frame is neglected.

---

**Algorithm 1** Calculation of the cyclic redundancy check byte of the L'Heritier camera communication frame.

---

1: **procedure** GETCRC($frame$)
2:     $B \leftarrow frame.size$;                    ▷ We count the number of bytes of the string
3:     $CRC \leftarrow frame(1)$;                          ▷ We get the first byte
4:     **for** $i = 1 : 1 : B$ **do**
5:         $CRC \leftarrow bitxor(CRC, frame(i))$;       ▷ ...and calculate the xor between CRC
    and each word of the frame, recursively.
6:     **return** $bit2hex(CRC, 2)$                       ▷ We return a CRC byte

---

After several attempts at reproducing such frames, we realized that bytes 18 to 20 were synchronizing bytes. These bytes are different whenever the camera is switched on, and have to be the same in the incoming and out-coming frames. So to communicate with the camera, first we have to listen to the frames emmited by the camera and then, to extract these bytes to copy them within bytes 18 to 20 of the frame to be sent back to the camera. The frame structure is represented in figure 5.4. The header and tail bytes are fixed and they delimit the full frame.

**Figure 5.4:** Structure of a L'Heritier camera frame

#### 5.3.1.3 LHERITIER.m

We also developed LHERITIER.m (see figure 5.5), a GUI based in lheritier.m that allows the final user to remotely configure all parameters of the L'Heritier camera:

- **AIT/AGC:** Automatic Integration Time (AIT) and Automatic Gain Control (AGC). This value is set to OFF by default.

- **Electronic offset auto:** This command allows to enable the black level to be set automatically. If this value is set to OFF, then the manual electronic offset parameter has to be set. It is set ON by default and it is recommended to keep this configuration.

- **AIT/AGC preset:** This parameter allows to choose the response time of the system between 1.2 s or 2.4 s. It is set to 1.2 s by default.

- **Frame accumulation:** This parameter allows to enlarge the exposition time from 40 ms to 1 s. It is set to OFF by default. If we set this parameter ON, the *AIT/AGC* parameter will be automatically set to OFF and *Exposure time* parameter is ignored.

- **Outline enhancement:** This parameter enhances the outline of the image. It is set to OFF by default.

**Figure 5.5:** `LHERITIER.m`

- **Outline enhancement preset:** When *Outline enhancement* parameter is ON, we can set the enhancement level by setting this parameter. It is set to '1' by default.

- **Noise reduction:** When switching ON this parameter, we increase the signal to noise ratio (SNR). It is set to ON by default.

- **Test pattern:** When switching this parameter ON, the camera generates a test pattern that allows to verify that it is working properly.

- **Binning:** If this parameter is set to ON, the camera calculates a 2×2 binning of the image enhancing the SNR but losing spatial and spectral resolution. It is set to OFF by default.

- **Exposure time:** We can set this value from 10 $\mu$s to 40 ms. You have to set this parameter (V) from 493 to 1980000, which means a correspondence in seconds of $20.2 \times 10^{-9} V$ s

- **Electronic gain:** It can be set from 0 dB to 29.4 dB. It is set to 0 by default. We can vary the parameter V from 0 to 823, being the correspondence value in dB $20 log(0.0359V)$

- **Tube gain:** It can be set from 0 dB to 60 dB. It is set to 0 by default. We can vary the parameter V from 0 to 1023, being the correspondence value in dB $20 log(V)$

- **Electronic offset:** If *Electronic offset* auto is OFF, it can be set from 0 % to 12.5 % of the video level. This value (V) is set to 255 by default, and it can vary from 0 to 255. The correspondence in percentage of the video level is 0.0488 V.

- **AIT/AGC target level:** This value sets the gain and exposition time parameters in case of AIT/AGC parameter is set ON to reach a certain video level. It is set to 50 % by default and we can vary it from 0 % to 100 %.

- **AIT/AGC max integration time:** It is set to 30 ms by default. We can vary this parameter from 10 $\mu$s to 30 ms.

- **Exposure time for frame:** It is set to 0 micro seconds by default. It can be set from 40 ms to $4 \times 10^{-2} \times 2^{0.1V}$ where V can be set from 0 to 47. Maximum value to set is 1 s.

- **Global and Local High Illumination Reset and Overriding:** These parameters reset the iCCD camera when an overexposure is detected to protect the intensifier tube. They are set OFF by default. The *Global* parameter only triggers when the AIT/AGC parameter is on. The *Local* parameter triggers both in automatic and manual

modes. These parameters are recommended to be OFF (protection activated).

- **Mean value:** When pressing the *GET STATUS* button, it shows the pixel mean value of the images and gives an idea of the saturation level.

- **SET:** When the previous parameters are defined, we press the *SET* button and all the information is sent to the camera.

- **GET STATUS:** This button shows the current values of all parameters of the L'Heritier camera, and checks whether the camera is saturated or not. If the camera is saturated we have to switch the *Global and Local High Illumination Reset* ON and then OFF.

### 5.3.2   GRASSP v1.x

As mentioned in chapter 2, GRASSP v1.x is a spectrograph installed on a telescope mount, within a static hermetic housing. It automatically aims over the closest storm by consulting realtime lightning databases and it can also work in a manual way.

The tasks designed and developed to control the GRASSP v1.x instrument are detailed below:

#### 5.3.2.1   GRASSP1x.m

GRASSP1x.m (see figure 5.6) is an application program that allows the final user to switch on and off all GRASSP v1.x subsystems. It communicates the PC where it is installed to the GRASSP Schneider Electric Advantys OTB automaton through a TCP/IP connection and reads or writes the automaton registers under the Modbus serial communications protocol.
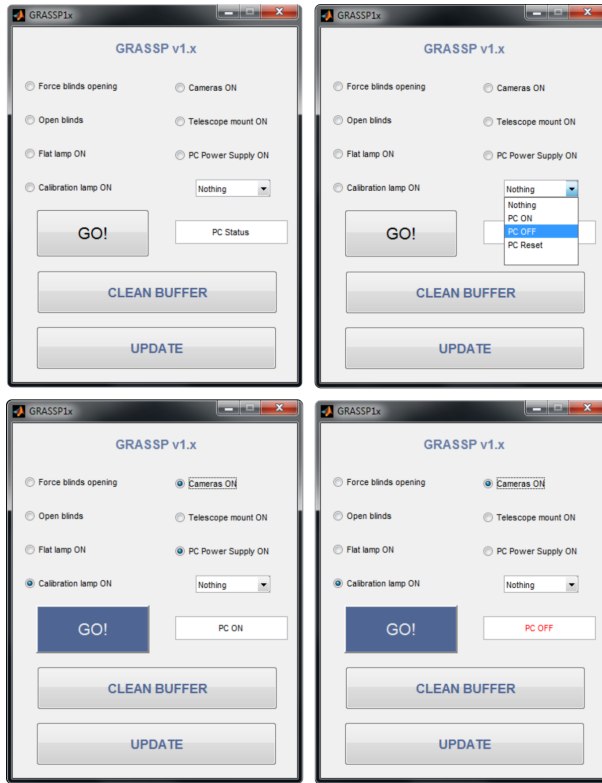
**Figure 5.6:** `GRASSP1x.m`

The Modbus protocol uses 16-bit words divided into two bytes of 8 bits. A Modbus frame starts with a header of 2 words defining the transaction ID and the Modbus ID, followed by a word which contains the Modbus message size (in bytes). The next word starts the Modbus message, and contains the slave address and the supported function we want to command. The following word specifies the register we want to write to or read from, and the last word contains the desired values of the register we want to set. The size of the message varies depending on the command we choose. The Modbus message is ended by a CRC word, calculated from the message bit values. This error finding mechanism is calculated by the sender and the receiver and if it is incongruous, an error signal is generated. Figure 5.7 describes the full structure of a Modbus message.
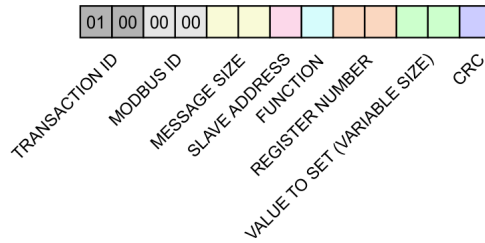
**Figure 5.7:** Structure of a Modbus frame

`GRASSP1x.m` reads and/or writes the automaton register number 100 which commands 8 binary outputs. When setting an output to 1, a signal of 24 VDC is provided. When setting an output to 0, a signal of 0 VDC is provided. Each output feeds a relay which respectively switches on and off the PC, the calibration lamps, the cameras and the telescope mount; two digital outputs also open and close the blinds in two operation modes: a normal mode, during nighttime, and a forced mode, opening the blinds during daytime with the caution of previously switching off the intensified cameras. To avoid keeping the blinds opened in case of a software failure, we developed the *watchdog technique* that consists of sending a train of pulses that feed a timing relay, that changes its state if the input signal does not repeatedly cycle on and off. This way the software sends a train of pulses to keep the blinds opened and, if only a pulse is sent, the blinds are opened and immediately closed. If the software stops sending pulses, the relay immediately stops acting and the blinds are closed.

### 5.3.2.2   `mount.m`

`mount.m` (see figure 5.8) is a graphical user interface that allows the final user to remotely move the telescope mount inside the GRASSP v1.x housing replicating the telescope mount commands —that are implemented in its hand controller pad (see figure 5.9)— adding some extra functionalities. It communicates the GRASSP PC with the telescope mount through the serial port (RS-232) via COM5.
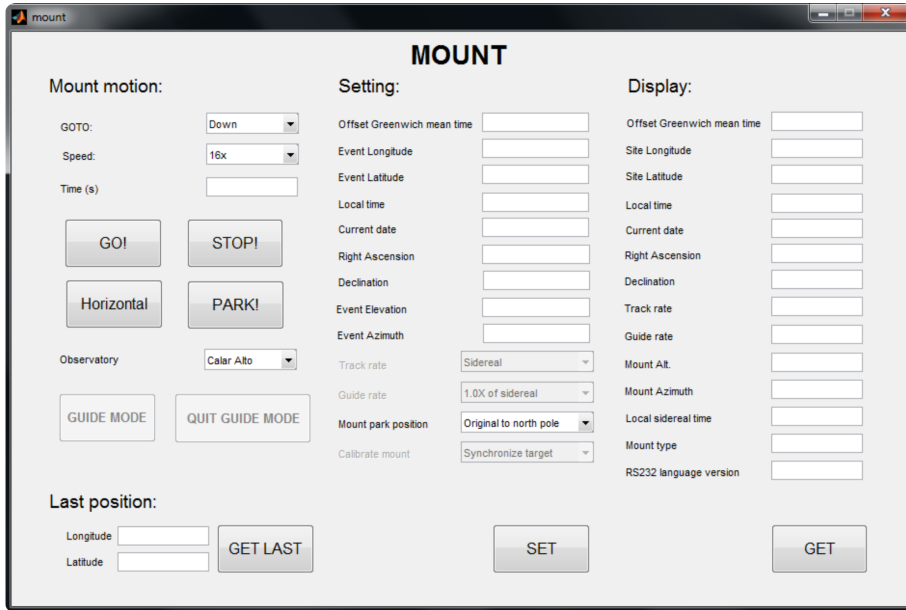
**Figure 5.8:** `mount.m` GUI



**Figure 5.9:** iOptron remote control pad

The frames messaging protocol is defined by iOptron and it represented in figure 5.10: it consists of a 1-word header, a variable-length message body and a 3-word tail. The RS-232 command set of the iOptron telescope mount is defined within appendix G of the GoToNova 8401 hand controller instructions manual (*iOptron*, 2010).
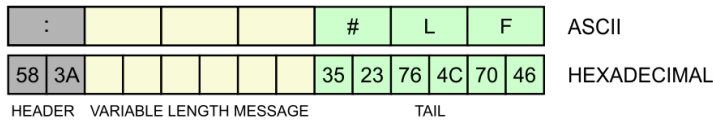


**Figure 5.10:** Structure of an iOptron frame

As we mentioned before, `mount.m` is a graphical user interface divided in 5 areas: mount motion, horizontal and park buttons, last position, setting and display.

As a telescope mount moves as times goes by to aim to the same astronomical object while the Earth rotates, we have removed the inner GPS system of the mount to force it to aim to the coordinates we desire and to keep it still until we decide to move it again.

`mount.m` is supported by a rear webcam which allows the final user to track the telescope mount movements.

### Mount motion

From this panel, the final user can set the mount aiming direction (up, down, left or right), its speed ($16\times$, $64\times$, $256\times$ or $512\times$) and the time the mount shall be moving (in seconds). Then we press the *GO!* button and the mount starts moving to the direction, speed and time we set. If we need to abruptly stop the mount, we press the *STOP!* button.

As there are forbidden positions for the mount not to collide with other subsystems, we installed two aluminum pieces on the azimuth plane and on the elevation plane of the telescope mount respectively. We also installed six limit switches (up – horizon – down and left – center – right; see figure

5.11, up) on a fixed plate so when the aluminum pieces of the mount touch these positions, the power supply of the telescope mount is switched off and it immediately stops. The vertical aluminum plate can press the left, center and right limit switches. The horizontal aluminum plate can press the up, horizon and down limit switches. The limit switches status is stored in a byte, and only 6 bits are used. All these aiming positions are illustrated in figure 5.12. Figure 5.13 shows the aluminum plates over the rear face of the spectrograph.
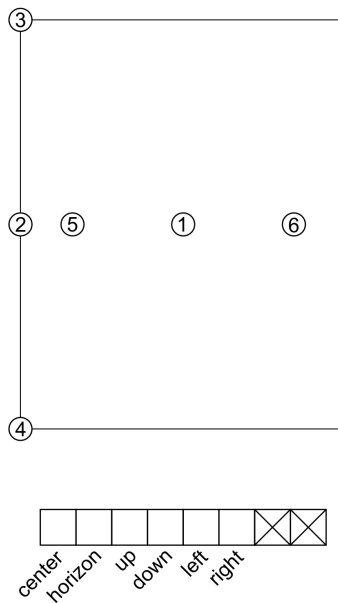


**Figure 5.11:** Limit switches numbered from 1 to 6 and limit switches status register

Every movement of the telescope mount and the reached positions are automatically logged in a document, where the date, time and azimuth and elevation positions are registered once a movement is commanded. This document allows us to track possible errors and we will further refer to it as *log document*.
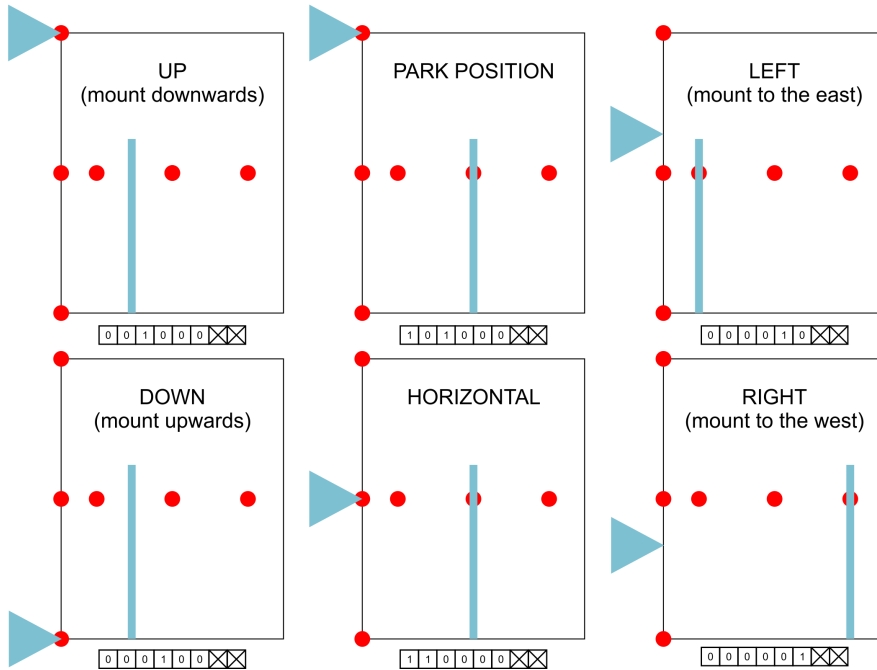
**Figure 5.12:** Limit switches (red circles) and mount positions (blue graphics). Blue triangle is the aluminum plate installed on the elevation plane of the telescope mount. Blue rectangle is the aluminum plate installed on the azimuth plane of the telescope mount

### Horizontal and Park buttons

Horizon and center limit switches help us to aim the mount either to horizon or to the calibration (park) position.

When the final user presses the *Horizontal* button, the system reads the log document, and automatically aims the mount to horizon (horizontal and centered) by following the steps defined in the algorithm 2. Only when the horizontal and center limit switches are pressed, the log document is updated. If after the calculated movements the mount does not press the horizontal and central limit switches, `mount.m` displays an error message so we can manually move the mount to horizon using the rear camera and the *Mount Motion* panel of `mount.m`.

**Algorithm 2** Moving the telescope mount to 0° elevation angle and 55° azimuth.

1: **procedure** HORIZONTAL
2:    $Close.All.Ports()$;
3:    $s \leftarrow Serial(COM5)$;                           ▷ We configure serial COM5
4:    $s.BaudRate \leftarrow 9600$;
5:    $s.StopBits \leftarrow 1$;
6:    $s.DataBits \leftarrow 8$;
7:    $s.Parity \leftarrow none$;
8:    $s.StopBits \leftarrow 1$;
9:    $s.Terminator \leftarrow CR/LF$;
10:    $s.Flush()$;                              ▷ We flush the buffer
11:    $s.Open()$;                             ▷ We open serial COM5
12:    $p \leftarrow GetPosition()$;      ▷ p.Ele and p.Az store the mount elevation angle and azimuth
13:    $bits \leftarrow LimitSwitchesStatus()$;
14:    $MountSpeed \leftarrow: RC0\#LF$;    ▷ We set the mount speed to the slowest option
15:    $MoveSecondsLS \leftarrow 200$;              ▷ Moves the mount 20.66°
16:    $MoveSecondsH \leftarrow 96.80$;             ▷ Moves the mount 10°
17:    $GoToN \leftarrow: Mn\#LF$;            ▷ Moves the mount upwards
18:    $GoToS \leftarrow: Mn\#LF$;            ▷ Moves the mount downwards
19:    $GoToE \leftarrow: Me\#LF$;            ▷ Moves the mount to the east
20:    $GoToW \leftarrow: Mw\#LF$;           ▷ Moves the mount to the west
21:    **if** $bits(3:6) \neq' 0000'$ **then**      ▷ If we are touching a limit switch...
22:       $poweron()$;
23:       **if** $bits(3) ==' 1'$ **then**    ▷ UP limit switch pressed: the mount is aiming downwards...
24:          $MoveMount(GoToN, MountSpeed, MoveSecondsH)$;
25:          $MoveMount(GoToW, MountSpeed, MoveSecondsLS)$;
26:          $poweron()$;              ▷ We power on the mount again...
27:          $MoveMount(GoToE, MountSpeed, MoveSecondsH)$;
28:       **else if** $bits(4) ==' 1'$ **then**    ▷ DOWN limit switch pressed: the mount is aiming upwards...
29:          $MoveMount(GoToS, MountSpeed, MoveSecondsH)$;
30:          $MoveMount(GoToW, MountSpeed, MoveSecondsLS)$;
31:          $poweron()$;
32:          $MoveMount(GoToE, MountSpeed, MoveSecondsH)$;

33:        **else if** $bits(5) ==' 1'$ **then**       ▷ LEFT limit switch pressed: the mount is aiming to the right...

34:            $MoveMount(GoToW, MountSpeed, MoveSecondsLS);$

35:            $poweron();$

36:            $MoveMount(GoToE, MountSpeed, MoveSecondsH);$

37:            $MoveMount(GoToN, MountSpeed, MoveSecondsLS);$

38:            $poweron();$

39:            $MoveMount(GoToS, MountSpeed, MoveSecondsH);$

40:        **else if** $bits(6) ==' 1'$ **then**     ▷ RIGHT limit switch pressed: the mount is aiming to the left...

41:            $MoveMount(GoToE, MountSpeed, MoveSecondsH);$

42:            $MoveMount(GoToN, MountSpeed, MoveSecondsLS);$

43:            $poweron();$

44:            $MoveMount(GoToS, MountSpeed, MoveSecondsH);$

45:     $SavePosition();$      ▷ We save the current position in the log document

46:   $p \leftarrow GetPosition();$

47:   $bits \leftarrow LimitSwitchesStatus();$

48:   **if** $bits(1:2) \neq' 11'$ **then**        ▷ If we are not aiming to horizon...

49:     **if** $p.Ele > 0$ **then** ▷ ...we calculate the direction and the seconds to move the mount

50:       $GoTo \leftarrow: Mn\#LF;$

51:       $MoveSeconds \leftarrow Ele/0.1033;$

52:     **else**

53:       $GoTo \leftarrow: Ms\#LF;$

54:       $MoveSeconds \leftarrow -Ele/0.1033;$

55:     $MoveMount(GoTo, MountSpeed, MoveSeconds);$   ▷ We move the mount in elevation...

56:     **if** $p.Az > 55$ **then**

57:       $GoTo \leftarrow: Mw\#LF;$

58:       $MoveSeconds \leftarrow (p.Az - 55)/0.1033;$

59:     **else**

60:       $GoTo \leftarrow: Me\#LF;$

61:       $MoveSeconds \leftarrow (55 - p.Az)/0.1033;$

62:     $MoveMount(GoTo, MountSpeed, MoveSeconds);$      ▷ ...and in azimuth

63:   $bits \leftarrow LimitSwitchesStatus();$

64:   **if** $bits(1:2) \neq' 11'$ **then**       ▷ If we are still not aiming to horizon...

65:     $DisplayErrorMessage();$     ▷ ...we manually move the mount to horizon using...

66:   **else**         ▷ ...the rear camera and the *Mount Motion* panel of `mount.m`

67:     $SavePosition();$      ▷ We save the current position in the log document

68:   $s.Close();$                   ▷ We close the port
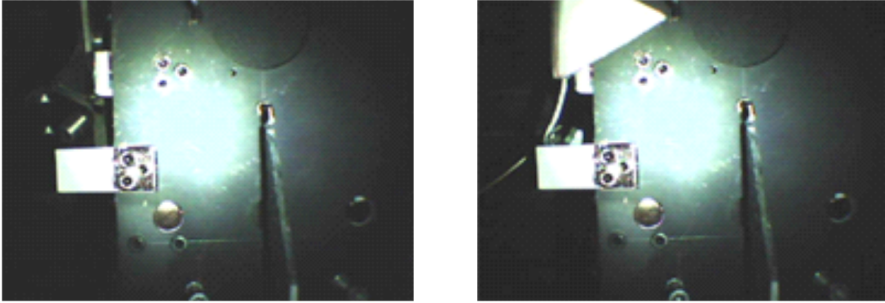
**Figure 5.13:** Rear part of the spectrograph installed on the telescope mount. Left image shows park position. Right image shows horizontal position. These images were recorded by a webcam which allows the final user to track the telescope mount movements

In a similar way, when the final user presses the *Park* button the system reads the log document, and automatically aims the mount to the park position following the steps defined in the algorithm 3. If after the calculated movements the mount does not press the park position limit switches, `mount.m` displays an error message so we can manually move the mount to the parking position using the rear camera and the *Mount Motion* panel of `mount.m`. Only when the down and center limit switches are pressed, the log document is updated.

### Last position

When the final user presses the *Last position* button, the log document is read and the last position is shown. If the log document does not exist, a warning message is shown.

### Setting

From this panel the final user can set several parameters of the telescope mount:

---

**Algorithm 3** Moving the telescope mount to park position.

---

1: **procedure** PARK
2:    $Close.All.Ports()$;
3:    $s \leftarrow Serial(COM5)$;                    ▷ We configure serial COM5
4:    $s.BaudRate \leftarrow 9600$;
5:    $s.StopBits \leftarrow 1$;
6:    $s.DataBits \leftarrow 8$;
7:    $s.Parity \leftarrow none$;
8:    $s.StopBits \leftarrow 1$;
9:    $s.Terminator \leftarrow CR/LF$;
10:   $s.Flush()$;                             ▷ We flush the buffer
11:   $s.Open()$;                             ▷ We open serial COM5
12:   $bits \leftarrow LimitSwitchesStatus()$;
13:   **if** $bits(1:3) \neq' 101'$ **then**            ▷ If we are not aiming to park position...
14:      $Horizontal()$;                          ▷ We aim to horizon...
15:      $GoTo \leftarrow: Ms\#LF$;                   ▷ ...and then we aim downwards
16:      $MountSpeed \leftarrow: RC0\#LF$;
17:      $MoveSeconds \leftarrow 96.80$;
18:      $MoveMount(GoTo, MountSpeed, MoveSeconds)$;
19:   $bits \leftarrow LimitSwitchesStatus()$;
20:   **if** $bits(1:3) \neq' 101'$ **then**         ▷ If we are still not aiming to park position...
21:      $DisplayErrorMessage()$; ▷ ...we manually move the mount to park position
   using the rear camera and the *Mount Motion* panel of `mount.m`
22:   $s.Close()$;                             ▷ We close the port
23:   $SavePosition()$;              ▷ We save the current position in the log document

---

- **Offset Greenwich Mean Time:** The final user can set the offset relative to the Greenwich Mean Time (GMT).

- **Event Longitude and Event Latitude:** The final user can aim directly to certain spatial coordinates.

- **Local Time, Current Date, Right Ascension and Declination:** The final user can set the current time to aim the mount by setting the declination and right ascension parameters, being sure to set the correct GMT.

- **Event Elevation and Event Azimuth:** The final user can aim directly to certain horizontal coordinates.

- **Track Rate and Guide Rate:** The final user can set the track rate either to Sidereal, Solar or Lunar. If the track rate is Sidereal, the final user can also set the guide rate either to $1.0\times$, $0.8\times$, $0.6\times$ or $0.4\times$ of sidereal track rate. We disabled this option, since our mount does not work as a telescope mount itself, but as a remote 2-D linear actuator.

- **Mount Park Position:** The final user can set the mount park position as *original to north pole, left and vertical, left and horizon, right and vertical* and *right and horizon.*

- **Calibrate Mount:** This option is currently disabled. When abled, the final user can calibrate the mount by either synchronizing a target or syncronizing the hand controller coordinate to a commanded coordinate.

All these parameters are commanded when pressing the *SET* button.

### *Display*

From this panel the final user can obtain several parameters from the telescope mount:

- **Offset Greenwich Mean Time:** The final user can get the offset of the Greenwich mean time.

- **Site Longitude and Site Latitude:** The final user can get the stored spatial coordinates of the observation site.

- **Local Time, Current Date, Right Ascension and Declination:** The final user can get the current time and date, declination and right ascension of the telescope mount.

- **Track Rate and Guide Rate:** The final user can get the stored values of the track and guide rates.

- **Mount Elevation and Mount Azimuth:** The final user can get the horizontal coordinates where the telescope mount is currently aiming to.

- **Local Sidereal Time:** The final user can get the local Sidereal time of the telescope mount.

- **Mount Type:** The final user can get the mount type, altazimuth or equatorial.

- **RS232 language version:** The final user can get the RS232 language version of the telescope mount.

### 5.3.2.3 `calibration1x.m`

The calibration process of SPEC1 consists of recording the bias and dark images, before recording several spectra of a commercial Ne lamp, intensified under different gain values to further build a synthetic spectral image with all spectral lines with the same intensity. All this process is embedded

in a MATLAB programming routine called `calibration1x.m` which communicates with the telescope mount through the same messaging protocol as `mount.m` (see figure 5.14). As the SPEC1 spectrograph is installed on a telescope mount, the first step is to aim to the Ne spectral lamp, which is located in the lower region of the GRASSP v1.x housing. Once the telescope mount is parked, `calibration1x.m` switches the L'Heritier camera on and launches the commercial Sonotaco UFO-Capture software, which will be described below. The bias and dark images are recorded, before the Ne spectral lamp is switched on. Then, the gain is increased from 0 to 1500 in steps of 500 in order to enhance the weaker spectral lines of Ne. This way we obtain a video from which we can build a synthetic spectrum showing up all spectral lines with similar intensity. Next step is to switch off the Ne spectral lamp as well as the Sonotaco UFO-Capture software. This process is done automatically, without the supervision of the final user.

We decided not to install a flat lamp in GRASSP v1.x since the instrument functions of SPEC1 already include the system inhomogeneities at different gains.

`calibration1x.m` is launched at the beginning and at the end of every observation night. All these recorded images are necessary to correct the TLE spectral images, so they are stored in a data repository.

### 5.3.2.4   `spriteaiming.m`

We have developed a graphical user interface to aim the GRASSP v1.x mount in a manual or in an automatic mode (see algorithm 4).

Since the observation site is located at $2.5458°$ W longitude, $37.223°$ N latitude and 2160 m altitude, and it aims to a central azimuth of $45°$, the GRASSP v1.x observation area defines a sector of the circle from azimuth $32.5°$ to $57.5°$ and radii of 2000 km (see figures 5.15 and 5.16), defining a grid divided in $10 \times 10$ sectors. The elevation angle varies from $1.2°$ to $5.5°$.
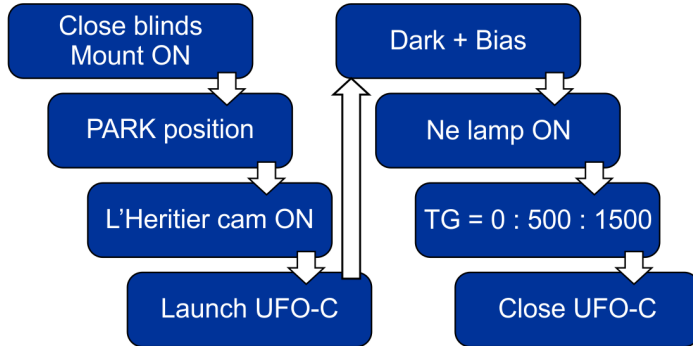
**Figure 5.14:** Flux diagram of `calibration1x.m`

*Automatic mode*

To aim the GRASSP v1.x mount in an automatic mode, we select the *Automatic* option of the select list and press the *GO!* button.

The automatic mode of `spriteaiming.m` queries a realtime lightning database (*Meteorage*, 2017) every five minutes. To track the storm we only take into account the lightning occurred within the preceding hour, that is, we compile lightning data in 12 blocks of five minutes each. From these data, the more relevant lightning are the latest, so we assign a weight to the lightning current peak of each block to enhance the most recent lightning. We plot the weighted lightning data over a grid delimiting the observation area (see figure 5.15), after removing the outer lightning data. This way we can localize the locations where the active storms are. If there are two different storms and they are aligned from the observation site, we aim GRASSP v1.x to the closest sector, because the clouds of the closest storm would cover the TLEs occurring over the furthest one. Then, `spriteaiming.m` displays the most active storm centroid coordinates values and elevation, that will be used to call `mount.m` and aim GRASSP v1.x to the calculated target (see algorithms 4, 5, 6 and 7).
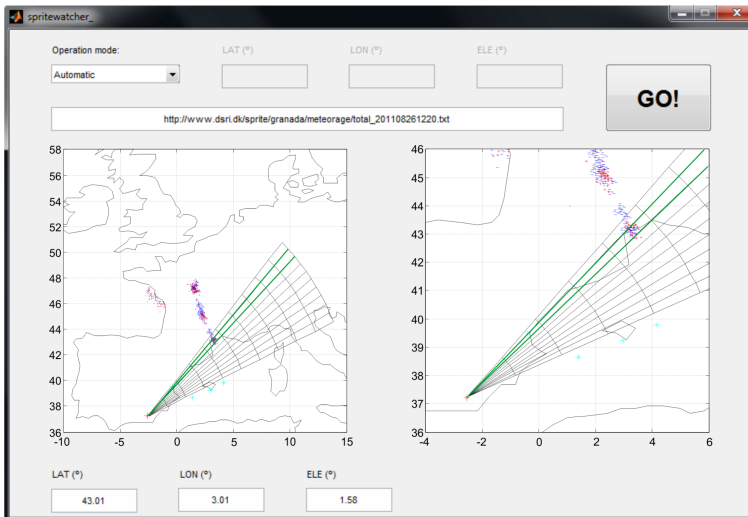
**Figure 5.15:** Automatic mode of `spriteaiming.m` (the most active cluster is pointed at)

*Manual mode*
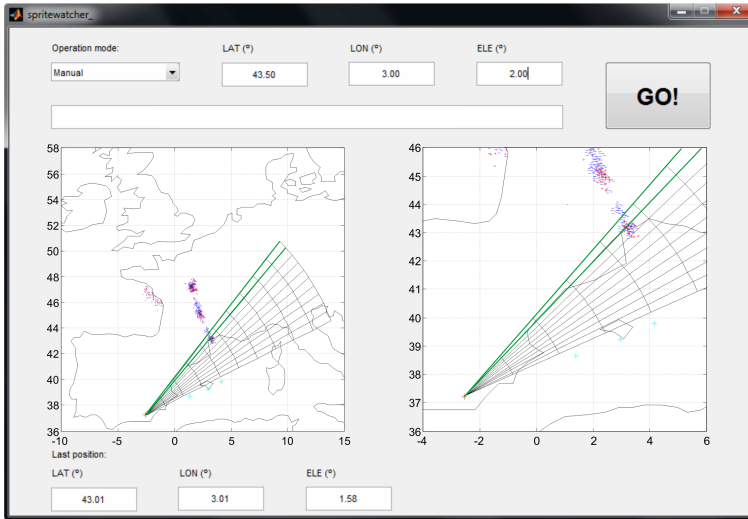


**Figure 5.16:** Manual mode of `spriteaiming.m` (in this case we are forcing GRASSP v1.x to aim to 43.50° N 3° E with an elevation angle of 2°)

If we prefer to aim elsewhere, and aim GRASSP v1.x mount in an manual mode, we select the *Manual* mode within the select list options, command the new coordinates and elevation angle from the upper panel of `spriteaiming.m` and press the *GO!* button (see figure 5.16). This option calls `mount.m` with the commanded values of coordinates and elevation angle.

### 5.3.2.5   `simulator.m`

We have developed a graphical user interface to test the mount movements in a simulated heavy storm scenario (see figure 5.17). As mentioned before, we have plot a grid delimiting the observation area. `simulator.m` generates a set of positive and negative lightning over the observation area, from the last 5 minutes and from the past 55 minutes, in the grid sectors we command. These data are generated over the coordinates of the grid sector or sectors we choose, sampling from a Normal distribution with a dispersion

---

**Algorithm 4** Aiming GRASSP v1.x to the closest storm

---

1: **procedure** SPRITEAIMING
2:     $m \leftarrow aimingMode$;
3:     **if** $m == Automatic$ **then**                      ▷ *Automatic* mode
4:         **do**         ▷ Repeat every 5 minutes until the *Manual* mode is activated
5:             $s \leftarrow CameraStatus()$;
6:             **if** $s == Saturated$ **then**
7:                 $ResetCamera()$;            ▷ Reset the cameras if they are saturated
8:             $t \leftarrow getTime()$;
9:             $d \leftarrow getData()$;
10:            $ActualData \leftarrow ProcessData(d, t, actual)$; ▷ Data within last 5 minutes in the observation area
11:            $PastData \leftarrow ProcessData(d, t, past)$;      ▷ Data within last hour in the observation area
12:            $(lat, lon) \leftarrow CalculateCoordinates(ActualData, PastData)$;
13:            $MountAiming(lat, lon)$; ▷ The mount aims to the desired location, if it is possible
14:            $wait(5, minutes)$;                ▷ Wait 5 minutes
15:            $m \leftarrow aimingMode$;
16:         **while** $m == Automatic$
17:     **else**                               ▷ *Manual* mode
18:         $lat \leftarrow getLat()$; ▷ We get the latitude and longitude from the text area of the GUI
19:         $lon \leftarrow getLon()$;
20:         $MountAiming(lat, lon)$;     ▷ The mount aims to the desired location, if it is possible

---

---

**Algorithm 5** Ignoring the data outside the observation area

---

1: **procedure** PROCESSDATA(data,t,option)
2:     $tam \leftarrow length(data)$;
3:     $j = 1$
4:     **for** $i = 1 : 1 : tam$ **do**
5:         $az \leftarrow GetAzimuth(data(i).lat, data(i).lon, lat_{obs}, lon_{obs})$; ▷ Gets the azimuth from the coordinates of the lightning and the observation site
6:         $ratio \leftarrow GetRatio(data(i).lat, data(i).lon, lat_{obs}, lon_{obs})$;        ▷ Gets the ratio from the coordinates of the lightning and the observation site
7:         **if** $az \geq 35$ & $az \leq 55$ & $ratio \leq 800$ **then**         ▷ If the lightning occurred between 35 and 55 degrees azimuth and closer than 800 km
8:             $NewData(j).sector \leftarrow getSector(data(i))$;       ▷ Assigns the sector of the aiming grid where the lightning belongs to
9:             **if** $option == actual$ & $t - data(i).Time \leq 300$ **then**          ▷ If we are collecting the data within the last 5 minutes...
10:                 $NewData(j) \leftarrow data(i)$;
11:             **else if** $option == past$ & $t - data(i).Time < 3600$ & $t - data(i).Time > 300$ **then**      ▷ Or if we are collecting the data between the last hour and the last 5 minutes...
12:                 $NewData(j) \leftarrow data(i)$;
        **return** $NewData$;

---

---

**Algorithm 6** Calculating the coordinates to aim to

---

1: **procedure** CALCULATECOORDINATES(ActualData,PastData)
2:    $WeightedPastData \leftarrow WeightData(PastData)$;
3:    $Data \leftarrow ActualData + WeightedPastData$;
4:    **if** $\neq isEmpty(Data)$ **then**
5:       $grid \leftarrow FillGrid(Data)$; $\triangleright$ We fill the observation area $10 \times 10$ grid with the lightning
6:       $s \leftarrow FindSector(grid)$;      $\triangleright$ We find the most active (and closest) sector, to identify the most active storm
7:       $StormData \leftarrow GetStorm(Data, s)$;      $\triangleright$ We select the data belonging to the most active sector and adjacent
8:       $tam \leftarrow length(StormData)$;
9:       $lat \leftarrow 0$;
10:       $lon \leftarrow 0$;
11:       **for** $i = 1 : 1 : tam$ **do**    $\triangleright$ We calculate the centroid of the most active storm
12:          $lat \leftarrow lat + StormData(i).lat$;
13:          $lon \leftarrow lon + StormData(i).lon$;
14:       $lat \leftarrow lat/tam$;
15:       $lon \leftarrow lon/tam$;
16:    **else**
17:       $p \leftarrow GetPosition()$;
18:       $lat \leftarrow p.Lat$;
19:       $lon \leftarrow p.Lon$;
      **return** $(lat, lon)$;

---

---

**Algorithm 7** Moving the mount of GRASSP v1.x

---

1: **procedure** MOUNTAIMING(lat, lon) $bits \leftarrow LimitSwitchesStatus()$;
2:      **if** $bits(3:6) \neq' 0000'$ **then**
3:          $Horizontal()$;                   ▷ If a limit switch is pressed, aim to horizon
4:      $az \leftarrow GetAzimuth(lat, lon, lat_{obs}, lon_{obs})$;          ▷ Gets the azimuth from the coordinates of the storm and the observation site
5:      $ele \leftarrow GetElevation(lat, lon, lat_{obs}, lon_{obs})$;          ▷ Gets the elevation angle from the coordinates of the storm and the observation site. We aim to a hypothetic sprite occurring at 70 km altitude
6:      **if** $az < 32.5$ **then**         ▷ If the coordinates are outside the observation area...
7:          $az \leftarrow 32.5$;                       ▷ ...we aim to the nearest boundaries
8:      **else if** $az > 57.5$ **then**
9:          $az \leftarrow 57.5$;
10:      **if** $ele < 1.2$ **then**
11:          $ele \leftarrow 1.2$;
12:      **else if** $ele > 5.5$ **then**
13:          $ele \leftarrow 5.5$;
14:      $p \leftarrow GetPosition()$;               ▷ We get the current aiming coordinates
15:      $MovAz \leftarrow az - p.Az$;
16:      $MovEle \leftarrow ele - p.Ele$;
17:      $MountSpeed \leftarrow: RC0\#LF$;       ▷ We set the mount speed to the slowest option
18:      **if** $MovAz > 0$ **then**
19:          $GoTo \leftarrow: Mw\#LF$;
20:          $MoveSeconds \leftarrow MovAz/0.1033$;
21:      **else**
22:          $GoTo \leftarrow: Me\#LF$;
23:          $MoveSeconds \leftarrow -MovAz/0.1033$;
24:      $MoveMount(GoTo, MountSpeed, MoveSeconds)$;       ▷ We move the mount in azimuth
25:      **if** $MovEle > 0$ **then**
26:          $GoTo \leftarrow: Mn\#LF$;
27:          $MoveSeconds \leftarrow MovEle/0.1033$;
28:      **else**
29:          $GoTo \leftarrow: Ms\#LF$;
30:          $MoveSeconds \leftarrow -MovEle/0.1033$;
31:      $MoveMount(GoTo, MountSpeed, MoveSeconds)$;       ▷ We move the mount in elevation
32:      $SavePosition()$;          ▷ We save the current position in the log document

---

value we also set. The values we have to command to generate the lightning data are:

- Sector numbers where the simulated storm is going to be centered, delimited by commas

- Dispersion value of the lightning cluster

- Observatory

- Number of current positive lightning to be generated

- Number of current negative lightning to be generated

- Number of past positive lightning to be generated

- Number of past negative lightning to be generated

When these values are set, we press the *GENERAR* button, so a cloud of lightning is plotted over the map. Notice that the oldest data are weighted as described before.

Once the lightning data are generated as we desire, we press the *PROCE-SAR* button and outer lightning data are removed. Then we can choose between five aiming options:

- Aim to the storm cluster with the most lightning strokes

- Aim to the storm cluster with the most positive lightning strokes

- Aim to the storm cluster with the most negative lightning strokes

- Aim to the storm cluster which sum of positive lightning strokes is the highest

- Aim to the storm cluster which sum of negative lightning strokes is the highest
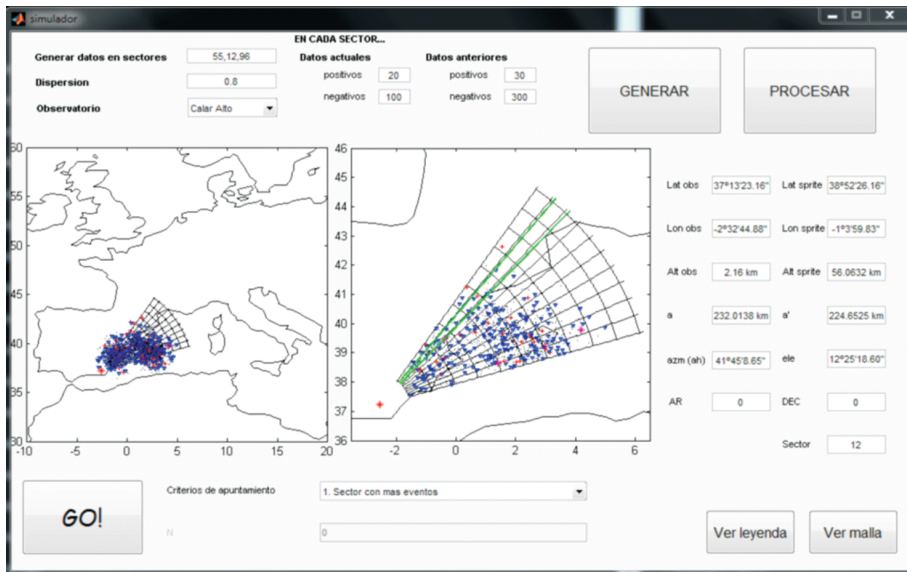
**Figure 5.17:** `simulator.m`

When the aiming option is selected, we press the *GO!* button and `simulator.m` calculates the target coordinates and elevation angle to call `mount.m` and move the telescope mount. The calculated values are displayed so we can check the aiming system reliability by inspecting the mount at the laboratory.

### 5.3.3 GRASSP v2.x

As mentioned in chapter 2, GRASSP v2.x consists of a spectrograph within a hermetic housing installed on an alt-azimuthal mount. It is manually aimed, but their inner systems and data management are remotely operated.

The tasks designed and developed to control the GRASSP v2.x instrument are detailed below:

#### 5.3.3.1 GRASSP2x.m

`GRASSP2x.m` is a simpler version of `GRASSP1x.m` that allows the final user to switch on and off all GRASSP v2.x subsystems under the Modbus serial

179

communications protocol.

`GRASSP2x.m` switches on and off the PC power supply, the Ar and Kr calibration lamps, the cameras and the blinds, and also displays their status (see figure 5.18). The blinds can only be opened if the intensified cameras are powered off. The PC is powered on as soon as its power supply is on. It can be powered off either directly from the GRASSP v2.x PC or remotely by turning the power supply off from the final user's PC through `GRASSP2x.m.` To switch it on again, it is necessary that the power supply passes from OFF to ON.

The automaton register programming protocol is similar as the `GRASSP1x.m` version.



**Figure 5.18:** `GRASSP2x.m`

#### 5.3.3.2 `calibration2x.m`

The calibration process of SPEC2 consists of recording several spectra of the commercial Ar and Kr lamps, intensified under different gain values to build a synthetic spectral image with all spectral lines with roughly the same intensity. `calibration2x.m` is a version of `calibration1x.m` as far as it measures the spectra from two different spectral lamps but, as GRASSP v2.x has been designed with a static calibration system, no mount movements are involved. We decided not to install a flat lamp in GRASSP v2.x since the instrument function of SPEC2 already includes the system inhomogeneities at different gains.

calibration2x.m is launched at the beginning and at the end of every observation night. All these recorded images are necessary to correct the TLE spectral images, so they are stored in a data repository whenever an event is detected. This is an automatic process and it is launched without the supervision of the final user.

The full process is synthesized in figure 5.19.
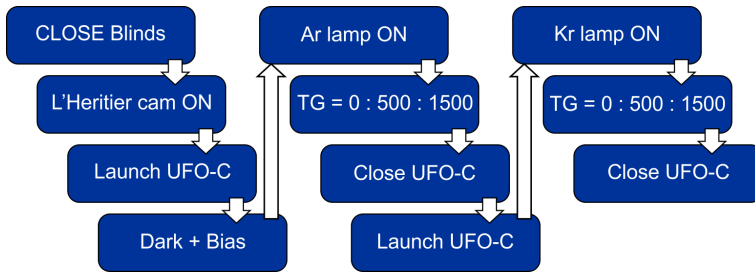


**Figure 5.19:** Flux diagram of calibration2x.m

### 5.3.4 Polarimeter calibration software

As described in chapter 4, we designed and developed a polarimeter calibration system consisting of an unpolarized light beam passing through a calibration array directed to a rotators module allocating either a linear polarizer or a linear polarizer plus a quarter wave plate. Once the light passes through the polarizers it is collected by the polarimeter through a refractive telescope. By analyzing all the combinations of the rotating polarizers, we could extract the calibration matrix of our system.

In this section we will thoroughly describe the tasks and routines we have developed to control the polarimeter calibration system:

- LOOP.m: A script developed in MATLAB, to sequentially launch GEAR.m and NEB.bat

- GEAR.m: A software tool, developed in MATLAB, to command the Arduino motherboard.

- `NEB.bat`: A batch script to launch *Nebulosity* software (which will be described later) every time the rotators change their position.

- `ROTATE.ino`: An Arduino sketch to move the rotators whenever receiving a command.

### 5.3.4.1 `LOOP.m`

`LOOP.m` (figure 5.20) is a MATLAB script that rotates sequentially the linear polarizer gear and the quarter wave plate gear. We have to sweep the linear polarizer gear 180° in 50 steps. And we have to sweep the quarter wave plate gear 180° in 50 steps for each position of the linear polarizer gear. To do so, `LOOP.m` is a script that launches `GEAR.m` tool to move each rotator to a certain location, and when the final position is reached, `LOOP.m` launches `NEB.bat` script to automatically record an image with GRASSP polarimeter, resulting 2500 differently polarized images which will allow us to calculate the minimum degree of polarization that GRASSP polarimeter is able to detect.

### 5.3.4.2 `GEAR.m`

`GEAR.m` (see algorithm 8) is a MATLAB tool that commands the `ROTATE.ino` sketch through the serial port to move the desired gear a desired number of steps. `GEAR.m` can also restart the commanded gear by moving forward the rotator until it reaches the initial position.

### 5.3.4.3 `NEB.bat`

`NEB.bat` (figure 5.21) is a batch script to launch `nebulosity.neb` software every time the rotators change their position. We have set up the integration time to 1.5 s and a delay of 1 s between captures (see figure 5.22).

---

**Algorithm 8** GEAR Algorithm

---

1: **procedure** GEAR(gear, reset, steps)
2:     $Close.All.Ports()$;
3:     $s \leftarrow Serial(COM4)$;                        ▷ We configure serial COM4
4:     $s.BaudRate \leftarrow 9600$;
5:     $s.StopBits \leftarrow 1$;
6:     $s.DataBits \leftarrow 8$;
7:     $s.Parity \leftarrow none$;
8:     $s.StopBits \leftarrow 1$;
9:     $s.Terminator \leftarrow CR/LF$;
10:    $s.Flush()$;                                    ▷ We flush the buffer
11:    $s.Open()$;                                     ▷ We open serial COM4
12:    $aux \leftarrow gear * 2^8 + reset * 2^7$;
13:    $Word1 \leftarrow Bin(aux, 8)$;
14:    $Word2 \leftarrow Bin(steps, 8)$;
15:    $frame \leftarrow [Word1 : Word2]$;
16:    $s.Write(frame, sync)$;                         ▷ We transmit the frame
17:    $pause(t)$;
18:    $s.Close()$;                                    ▷ We close the port

---

#### 5.3.4.4  ROTATE.ino

ROTATE.ino is an Arduino sketch developed to move the calibration rotators according to the requirements of GEAR.m (see algorithm 9). The algorithm consists of receiving a frame of 16 bits, where the first byte specify the rotator to be moved (bit 1) and whether the rotator has to be reset (bit 2); the last byte specify the steps to be moved. This sketch is compiled just once, before launching GEAR.m or NEB.bat. This is the only way the Arduino motherboard can interpret the commands of GEAR.m.

---

**Algorithm 9** ROTATE Algorithm

---

1: **procedure** ROTATE
2:     $word \leftarrow Serial.read();$
3:     $gear \leftarrow word[0];$
4:     $reset \leftarrow word[1];$
5:     $steps \leftarrow word[8:15];$
6:     **if** $gear$ **then**                                  ▷ We have to move gear 1
7:         **if** $reset$ **then**
8:             $LS1 \leftarrow Digital.read(SW1);$
9:             **while** LS1==0 **do**
10:                 $IncreaseStep1();$
11:                 $LS1 \leftarrow Digital.read(SW1);$          ▷ Until it reaches the limit switch
12:         **else**
13:             $cont = 0;$
14:             **while** cont ¡ steps **do**
15:                 $IncreaseStep1();$
16:                 $cont + +;$                        ▷ Or until it rotates the commanded steps
17:     **else**                                        ▷ We have to move gear 2
18:         **if** $reset$ **then**
19:             $LS2 \leftarrow Digital.read(SW1);$
20:             **while** LS2==0 **do**
21:                 $IncreaseStep2();$
22:                 $LS2 \leftarrow Digital.read(SW2);$          ▷ Until it reaches the limit switch
23:         **else**
24:             $cont = 0;$
25:             **while** cont ¡ steps **do**
26:                 $IncreaseStep2();$
27:                 $cont + +;$                        ▷ Or until it rotates the commanded steps

---

184
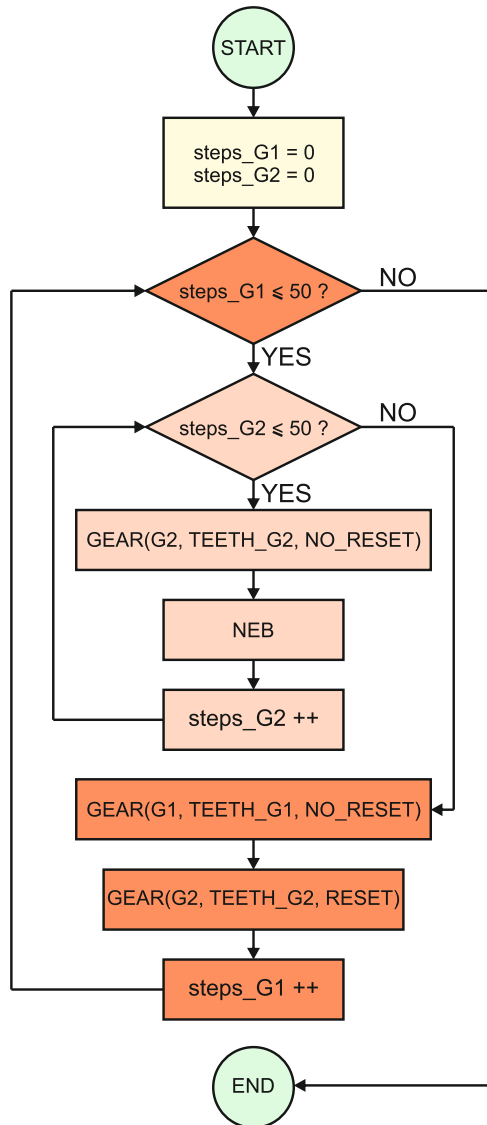
**Figure 5.20:** LOOP flow chart

```
@ECHO OFF

START nebulosity.neb
PING 1.1.1.1 -n 1 -w 100000 >NUL
CD C:\Archivos de programa\Nebulosity2
TASKKILL /im Nebulosity.exe /f

EXIT
```

**Figure 5.21:** `NEB.bat`

```
SetDirectory C:\Documents and Settings\MATLAB\autobot
Connect 1
SetShutter 0
SetName P
SetDuration 1500
Delay 1000
Capture 1
```

**Figure 5.22:** `nebulosity.neb`

## 5.4    Acquisition Software

Within this section we will describe two commercial software intended to both acquire spectroscopic and polarimetric images: SonotaCo UFO-Capture HD2, to record raw spectral images, and Nebulosity, to acquire polarimetric images.

### 5.4.1    SonotaCo UFO-Capture HD2

SonotaCo UFO-Capture is a commercial software intended to detect movement by recording a sequence of images when a change in the background brightness is detected. The basis of this software is to store a buffer of images which are processed in realtime every 40 ms. When motion is detected, a trigger is launched and UFO-Capture starts recording from the beginning of the buffer until the event has stopped. This trigger can either emit a sound, or can perform an action when the motion has ended. If no motion is detected, but an external trigger is received, UFO-Capture starts recording from the beginning of the head-buffer until filling the tail-buffer (both parameters are set by the user). Figure 5.23 outlines the SonotaCo UFO-Capture functionality and figure 5.24 shows its graphical user interface.

If no trigger is received, the buffered images are overwritten.

The user can draw an image mask to ignore the movement occurred in that area. The user can also set a scintillation mask to ignore the scintillation of stars or planes passing through.

Particularly, we launch two instances of UFO-Capture simultaneously. The main one is connected to the Watec field camera, and when motion is detected an audio trigger is launched. The secondary UFO-Capture window is connected to the spectrograph camera. When an audio trigger is detected, it starts recording the head-buffer of images until 50 frames later. This way we can synchronously record the field image of a TLE and its related spectrum.
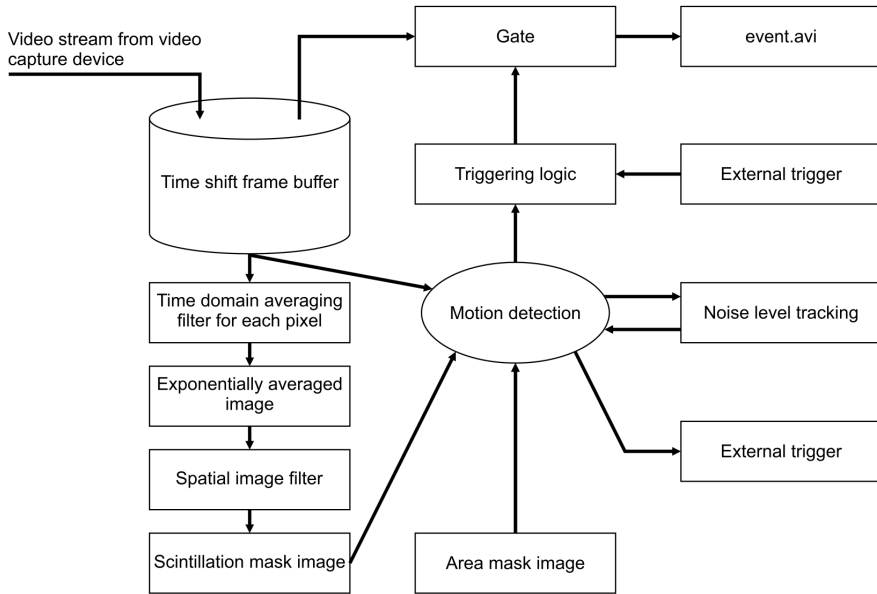
**Figure 5.23:** *UFO Capture* flux diagram courtesy of SonotaCo (*SonotaCo*, 2017). This process is performed every 40 ms

There are two main areas in every UFO-Capture window: the left-side area, which consists of several setting parameters divided in four tabs, and the right-side area, which shows an image display and an upper panel of two tabs.

We are going to briefly describe the main parameters that can be set in UFO-Capture.

### 5.4.1.1 Left-side area panels

These panels are described below and their user interfaces are depicted in figure 5.25.

#### *Input tab*

From this tab we can choose the video capture device, as well as the size of the frame, the frame rate and whether or not the signal is interlaced.
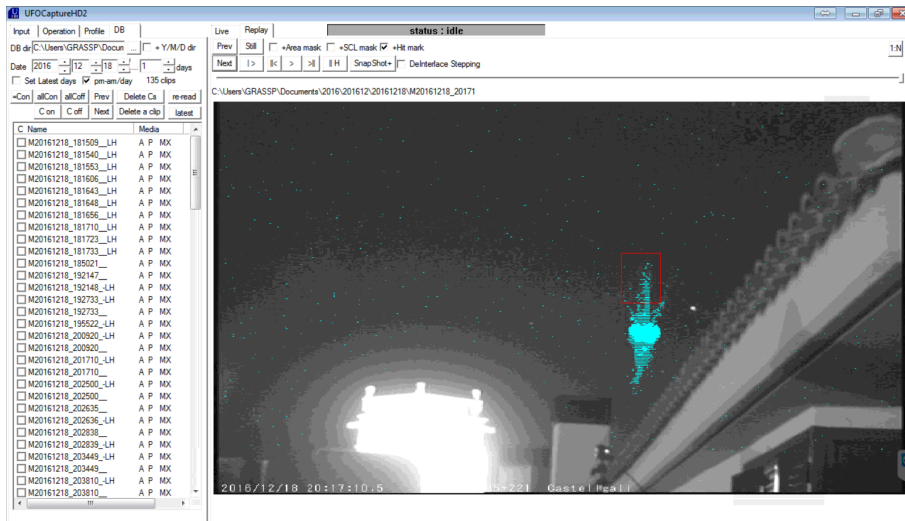
**Figure 5.24:** *UFO Capture* GUI. The detected event is highlighted in cyan with a red rectangle around the area where the brightness of the pixels change the most

We can also choose the audio capture device, and the compression codec we will use to store the videos.

The *Frame Shift* panel allows to set the number of frames in the head and tail buffers, as well as the number of frames that will be used to calculate the change of brightness between pixels.

The *Video Trigger* panel configures the detection area (which we can also edit within UFO-Capture) and the scintillation mask. We can set the parameters related to both masks from this panel.

The *Optional Trigger* panel enables the audio trigger or the time interval trigger. Both triggers are optional.

The *Super Impose* panel sets the timestamp format. We can choose whether the image time is UTC or not. We can also superimpose the scintillation and area masks.

### Operation tab

From this tab we can choose the detection to start when UFO-Capture
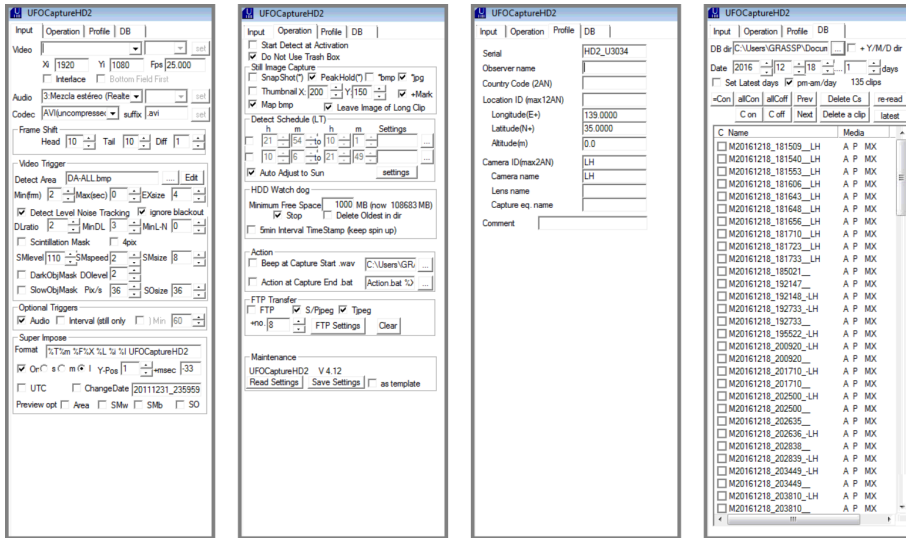
**Figure 5.25:** *UFO Capture* left-side area panels. From left to right: input, operation, profile and database

is activated. We can also choose to use the trash box or not.

The *Still Image Capture* panel configures the snapshot of the image that triggers the motion.

The *Action* panel selects the action (script execution or sound emission) to be launched when movement is detected.

The *Maintenance* panel shows a *Save Settings* button which stores all the configured parameters. There is also a *Read Settings* button to load previously stored settings.

We do not use the rest of the setting parameters in this tab.

### Profile tab

The *Profile* tab allows to set the metadata of the recorded videos: serial number, observer name, country code, location ID, latitude, longitude and altitude of the observation site, camera ID and user's comments.

**Database tab**

From the *Database* tab we can choose the directory where the videos will be stored (data repository) and we can add a year–month–day child–directory. We can also select a video from this tab and watch it in the right-side area display. This tab also allows us to delete either the selected clip or all clips.

### 5.4.1.2   Right-side area panels

**Live tab**

This tab is shown in figure 5.26. It consists of four buttons, three bars and a video display.
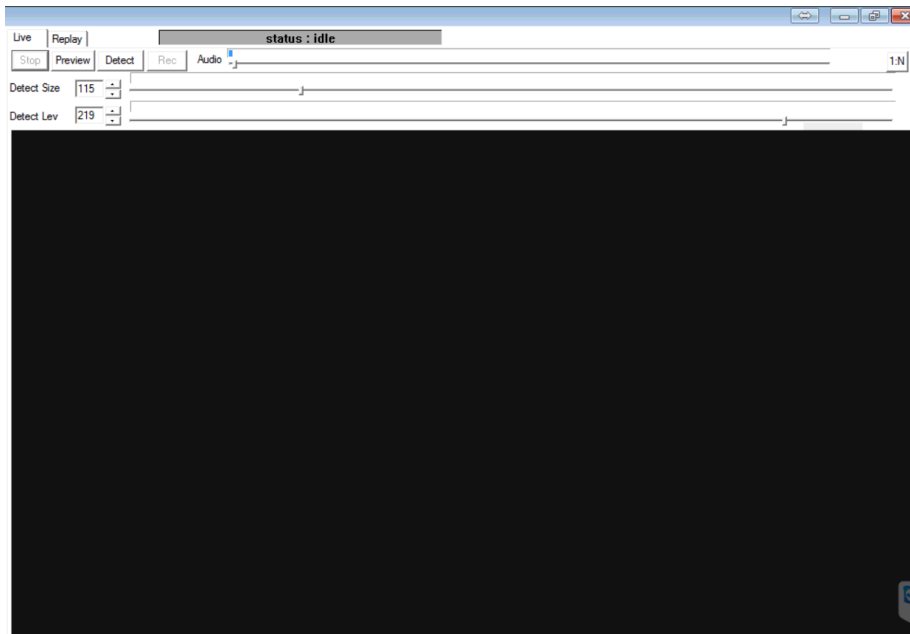


**Figure 5.26:** *UFO Capture* live tab. As the *STOP* button is pressed, no image is shown

The *Preview* button shows the realtime images captured by the camera

in the lower display, but they are not stored in the buffer.

The *Detect* button starts storing images in the buffer and, when motion is detected, it starts recording until the movement stops. Realtime images captured by the camera are shown up in the lower display.

The *Rec* button starts recording, even if no motion is detected. Realtime images captured by the camera are shown up in the lower display.

The *Stop* button stops recording abruptly. No images are shown in the lower display.

The *Audio* bar sets the threshold from which the audio trigger starts recording the video. We set this value very low so we do not miss any audio trigger.

The *Detect Size* bar and its editable area set the size threshold from which the size–trigger starts recording the video. If a change in brightness is detected in a smaller number of pixels than the value set by the threshold, the size–trigger is not launched and the video is not recorded.

The *Detect Level* bar and its editable area set the brightness threshold from which the brightness–trigger starts recording the video. If there is a change in the brightness of pixels, but their brightness level is lower than the detect level threshold, the brightness–trigger is not launched and the video is not recorded.

### Replay tab

This tab is shown in figure 5.27. It consists of eleven buttons, four selection boxes and a video display.

The *Prev* and *Next* buttons select the previous or the next stored video.

The *Still* button shows the image that launched the trigger. Masks can be superimposed. Also the detected event can be highlighted.

Lower buttons are the well-known commands of a video reproducer: Play, pause, forward, rewind, play movie from the top and move to detect start frame.
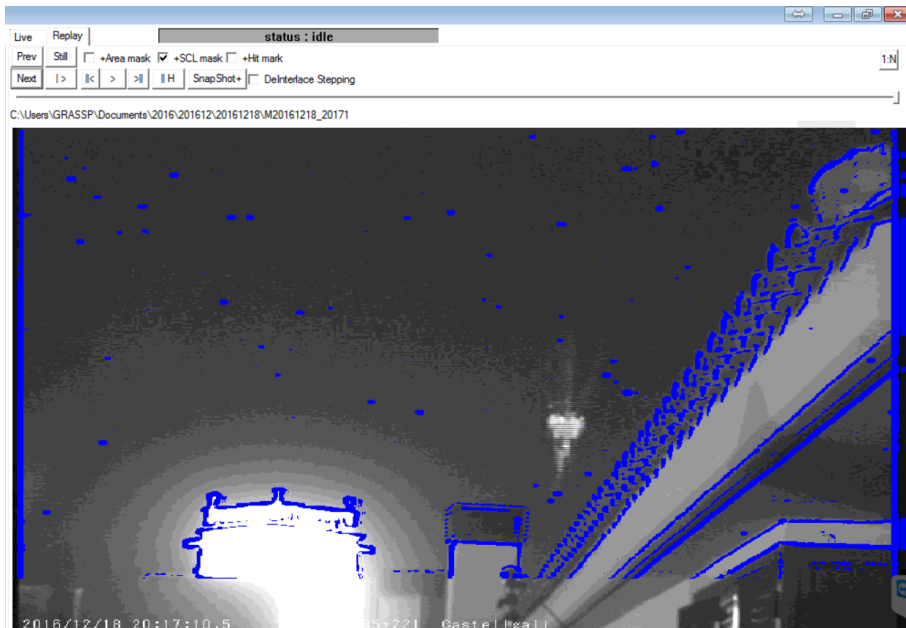
**Figure 5.27:** *UFO Capture* replay tab. Scintillation mask is superimposed in blue. Notice that, although the area mask option is not checked, the scintillation mask does not appear in the lower area of the image

One frame is composed by two interlaced fields. The *De-Interlace Stepping* option allows to watch the video frame by frame (if it is OFF) or field by field (if it is ON).

### 5.4.2 Nebulosity

Figure 5.28 shows the *Nebulosity* graphical user interface. It is a simple and flexible commercial software developed for astrophotography with the possibility of selecting the exposure time from 3 ms to up to several minutes. We use *Nebulosity* to record the TLEs polarimetric images through the Apogee camera described in chapter 4 to extract the four Stokes parameters from a single image.
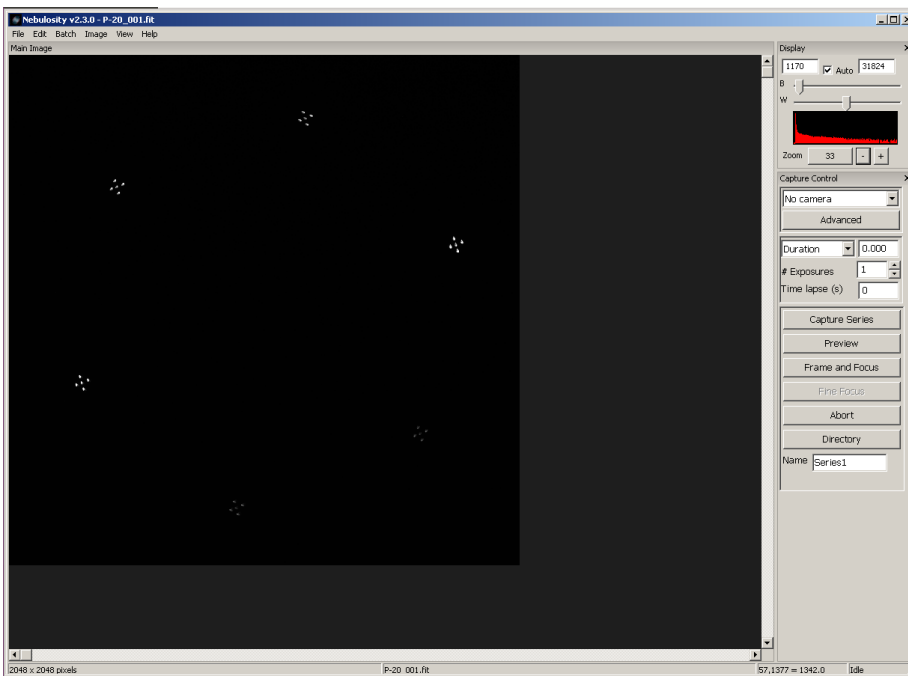


**Figure 5.28:** *Nebulosity* screenshot

## 5.5   Spectroscopic Data Reduction Software

The tasks to reduce raw spectral images are well–known in the spectro-
graphic community and are described in chapter 3. We followed the Subaru–
Faint Object Camera and Spectrograph (FOCAS) data reduction cook–book
(*Furuya*, 2010), which defines the steps to reduce long–slit spectrograph
data using the traditional Image Reduction and Analysis Facility (IRAF),
a general–purpose software system for the reduction and analysis of astro-
nomical data. But, although IRAF can be very useful when the studied
spectral range is wider than 200 nm, it is not recommended when the cov-
ered spectral range is narrower. We decided therefore to develop our own
custom IRAF tasks in MATLAB programming language to reduce GRASSP
spectroscopic data.

The results we show in chapter 6 were derived by calling the MATLAB
tasks we specifically designed and developed for every different observation.
These tasks replicated the IRAF environment, and they were called man-
ually from the command line. But since the installation of GRASSP v2.x
in Castellgalí in May 2015, the number of detected spectra increased sig-
nificantly and hence, so did the time we spent in reducing such data. So
we decided to develop a graphical user interface (GUI) that compiles these
independent tasks and scripts, simplifying the processes of calibration and
data reduction and minimizing programming errors.

We have developed three main software packages to obtain a wavelength
spectrum (I vs $\lambda$) from a spectral raw image: (1) the wavelength calibration
and distortion correction software, (2) the instrument function calculation
software and (3) the data reduction software. We will thoroughly describe
them below.

### 5.5.1 Wavelength calibration and distortion correction software

`calibration.m` is a GUI intended to calculate the calibration array to be used to transform a single raw spectral image to a measurable spectrum through an off-line pipeline. It consists of five sequential layers that allow the user to interact in order to calculate the calibration array. The first layer of `calibration.m` is shown in figure 5.29. The user selects four different images from the argon lamp spectrum videos, to build up a synthetic image which will be used to calculate the calibration array.
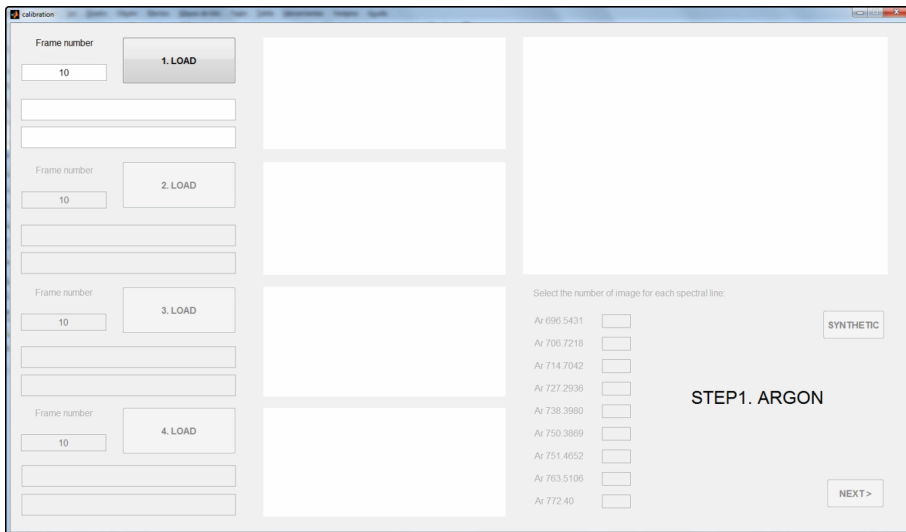


**Figure 5.29:** `calibration.m` GUI
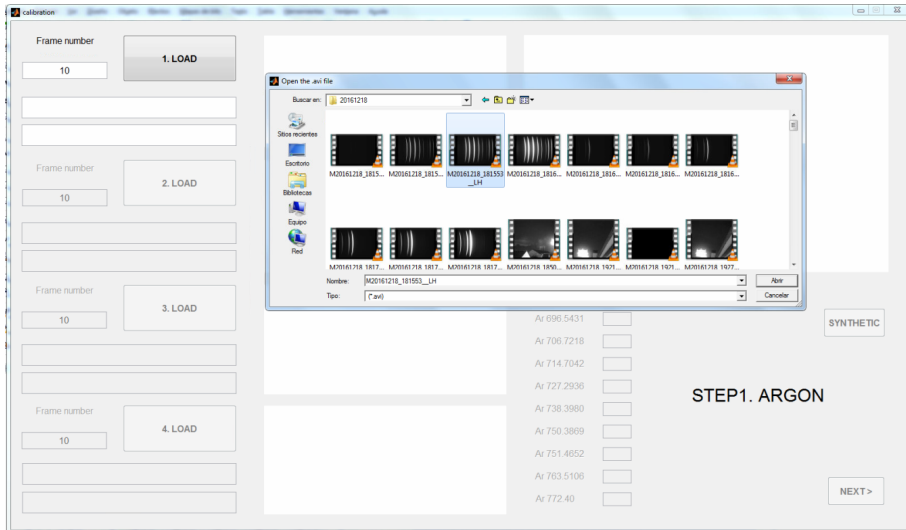
**Figure 5.30:** `calibration.m` GUI. A dialog box helps to select the spectral video
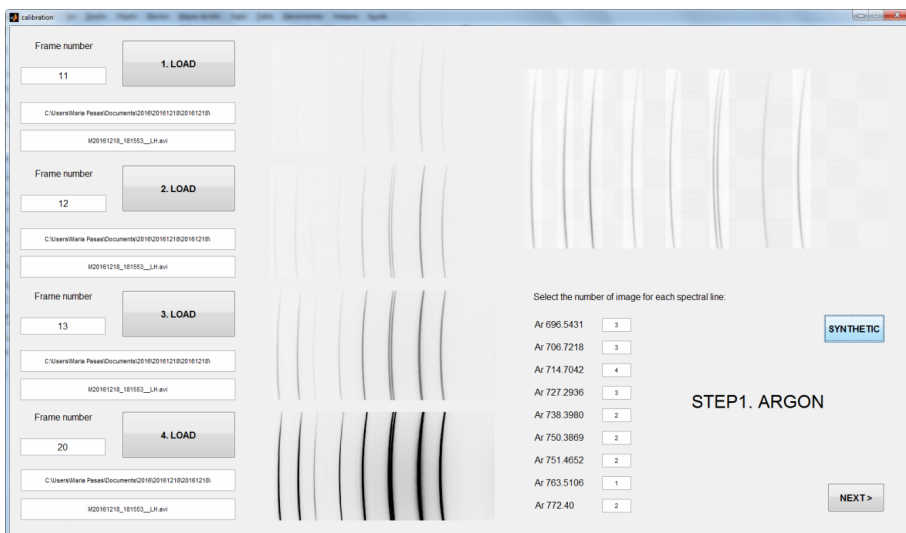


**Figure 5.31:** `calibration.m` GUI. Synthetic argon spectrum with all spectral lines with similar intensity (right). The synthetic spectrum can be built only when the four spectral images are loaded

The user selects a frame number and when pressing the *LOAD* button, a dialog box appears so the user can visually choose the argon spectral video by selecting it from the file directory system (see figure 5.30).

Then, the selected frame is trimmed, flipped and plotted in the nearby axes (see figure 5.31 left).

When the four spectral images are loaded, the next step is to select the similar–intensity spectral lines of each frame and press the *SYNTHETIC* button, so the synthetic spectrum is built and shown up in the axes on the right (see figure 5.31 right).

When we are sure that the synthetic spectrum we built shows up all the argon spectral lines with the same intensity, we press the *NEXT* button and the second layer of `calibration.m` appears. As figure 5.32 shows, from this layer we build a synthetic spectrum from the krypton spectral images following the same steps described before.
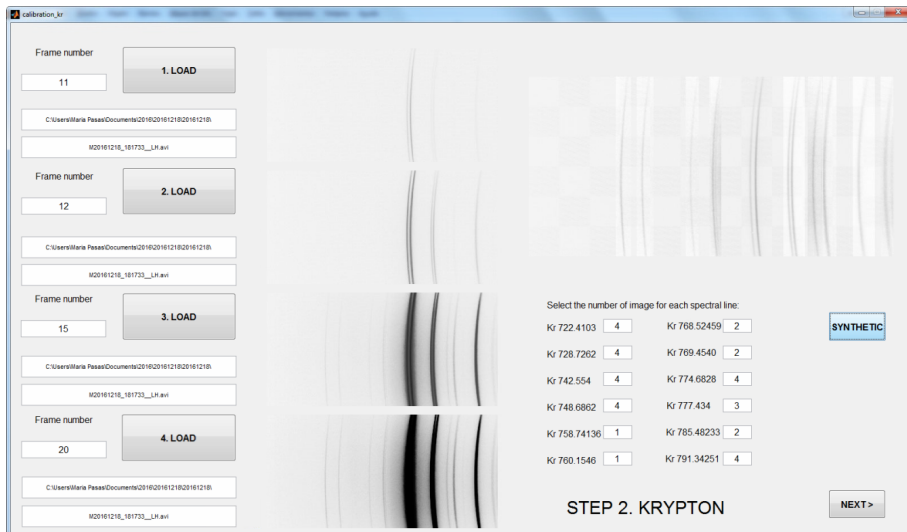


**Figure 5.32:** `calibration.m` GUI. Synthetic krypton spectrum with all spectral lines with similar intensity (right)

The next layer shows up the synthetic argon spectrum (see figure 5.33) and from it, `calibration.m` builds up a one–pixel–width spectrum.
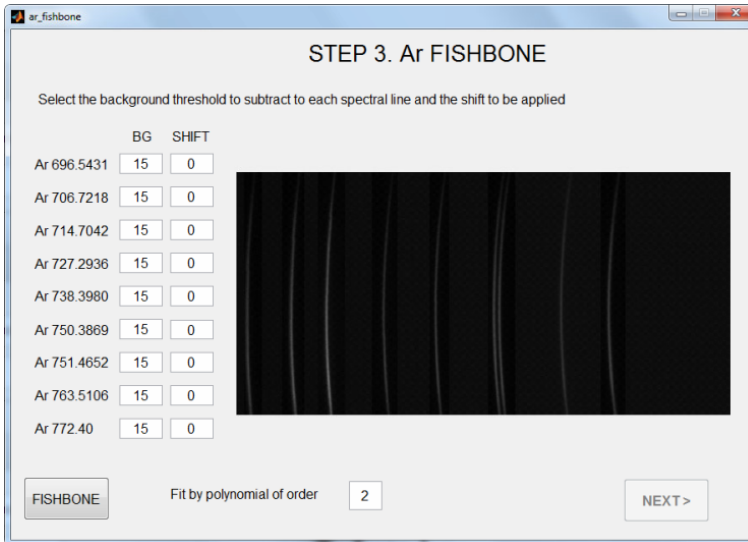
**Figure 5.33:** `calibration.m` GUI. Synthetic argon spectrum and editable threshold and shift levels

To do so, we find the peaks in every row of the synthetic spectrum of argon, and then we plot these peaks over the synthetic spectrum to check whether the clouds of pixels overlap the spectral lines or not. Sometimes, when the signal-to-noise ratio is very poor, the peaks are not found properly. A solution is to filter out the signal below a background threshold, at a level that can be commanded by the final user. Figure 5.34 shows the spectral line 763.5106 nm of argon with a dispersed cloud of pixels, with a threshold background level 15, resulting impossible to fit.

When setting the threshold background level to 20, the cloud of pixels overlaps the spectral line and no noise is detected: now the fitting is accurate (see figure 5.35 ).

Next step is to fit these clouds of pixels to a polynomial. The final user can set the order of the polynomial, being quadratic polynomials the preferred option.

Fitting very close spectral lines can be a difficult task. The solution we adopted was to use the previously fitted curve as a limit between both

spectral lines, so we separate the pixels of the cloud before and after the limit curve. Then we fit each group of pixels to a different curve. If we do not separate the cloud of pixels into two groups, the fitting software assumes that there is only one cloud of pixels and fits only one curve instead of two.
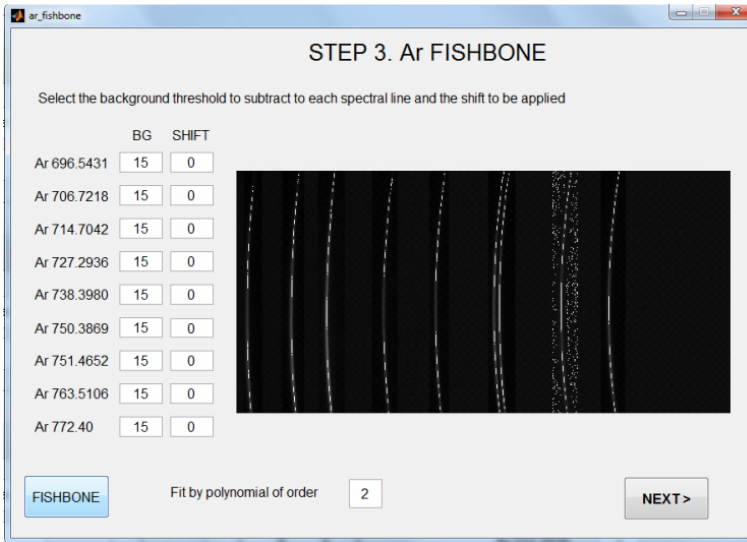


**Figure 5.34:** `calibration.m` GUI. Cloud of pixels over the synthetic spectrum maxima. Notice that the spectral line 763.5106 nm of argon shows a very dispersed cloud of pixels around it, resulting impossible to fit. The background threshold is 15
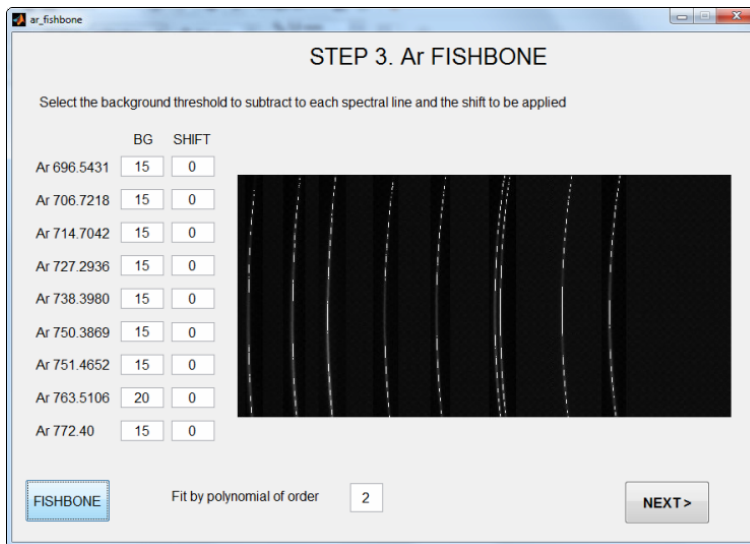
**Figure 5.35:** `calibration.m` GUI. Cloud of pixels over the synthetic spectrum maxima. The background threshold level is set to 20 for the spectral line 763.5106 nm of argon. No dispersion is detected and fitting is possible now

Sometimes we have to shift the limit curve to group the pixels properly and this can be done by setting the *shift* parameter of the third step of the `calibration.m` GUI. For instance, figure 5.36 seems to be a good fitting, but if we zoom (see figure 5.37) we find that there is a little shift we have to correct.
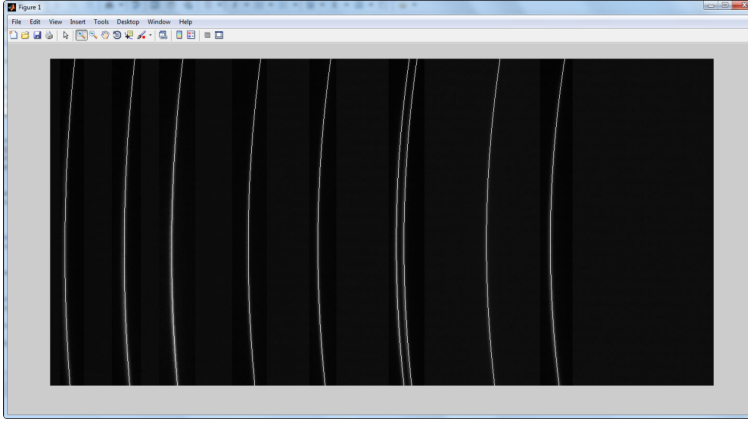


**Figure 5.36:** Fitting of the cloud pixels of the argon synthetic spectrum peaks
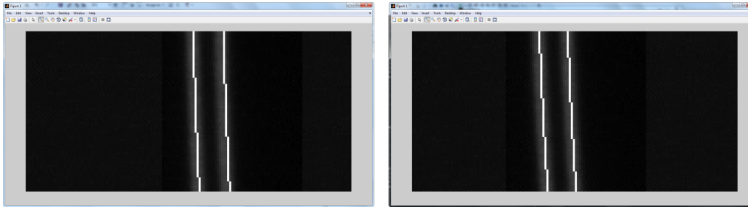


**Figure 5.37:** Zoom of the fitting of the cloud pixels of the argon synthetic spectrum peaks. Notice that there is a shift in the fitting

To do so, we shift the limit curve one pixel to the left for spectral line 751.4652 nm of argon (see figure 5.38) and the resulting spectrum is plotted in figure 5.39.
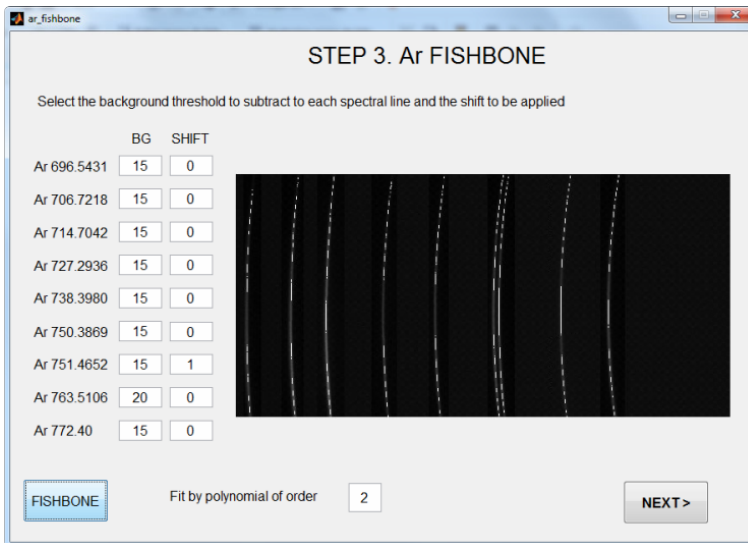
**Figure 5.38:** `calibration.m` GUI. Cloud of pixels over the argon synthetic spectrum maxima. We have set a shift of one pixel to the spectral line 751.4652 nm of argon
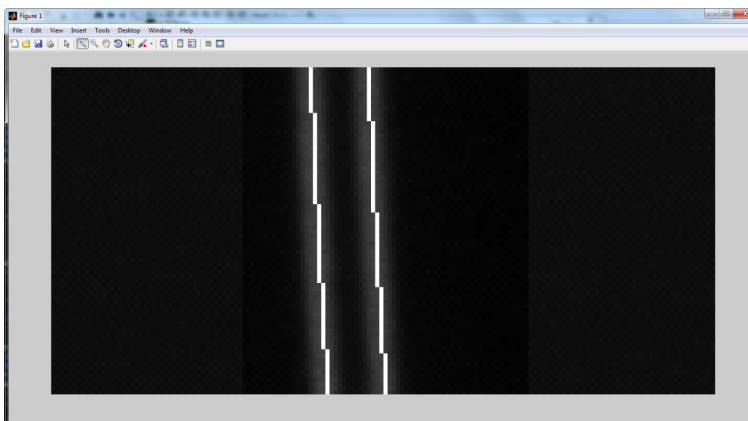


**Figure 5.39:** Zoom of the fitting of the cloud pixels of the argon synthetic spectrum peaks. We set a shift of one pixel in `calibration.m` GUI and the fitting curve overlaps the synthetic spectrum
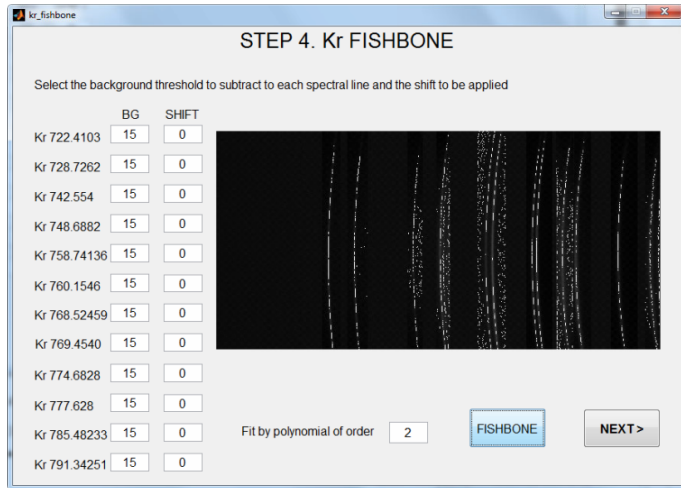
**Figure 5.40:** `calibration.m` GUI. Cloud of pixels over the krypton synthetic spectrum maxima. Background threshold should be increased

Once we determine that the argon fitting is accurate, we push the *NEXT* button and repeat the same process with the synthetic spectrum of krypton (see figures 5.40 and 5.41).

When the krypton fitting is accurate, we push the *NEXT* button so `calibration.m` launches a new layer and generates an argon–krypton *fishbone* pattern (see figure 5.42 down–left).

For every row of this *fishbone* pattern we assign a correspondence between pixel number and wavelength. Then we fit a polynomial of order 2 to these data, so every pixel of every row of the spectral image is associated to a wavelength (see figure 5.42 up–left).

When pressing the *Ar* button, `calibration.m` plots the calculated argon synthetic spectrum (see figure 5.42 up–right) and its straightened version (see figure 5.42 down–right). `calibration.m` also plots the resultant argon spectrum so we can check whether the spectral fitting is accurate.
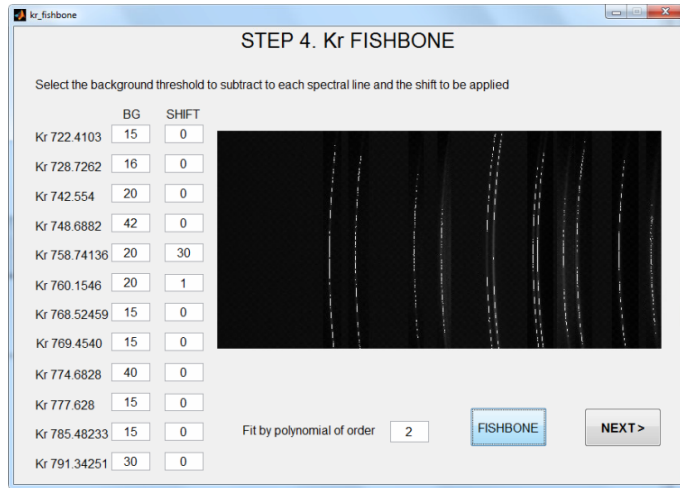
**Figure 5.41:** `calibration.m` GUI. Cloud of pixels over the krypton synthetic spectrum maxima. We have set shifts and background thresholds to fit the spectral pattern
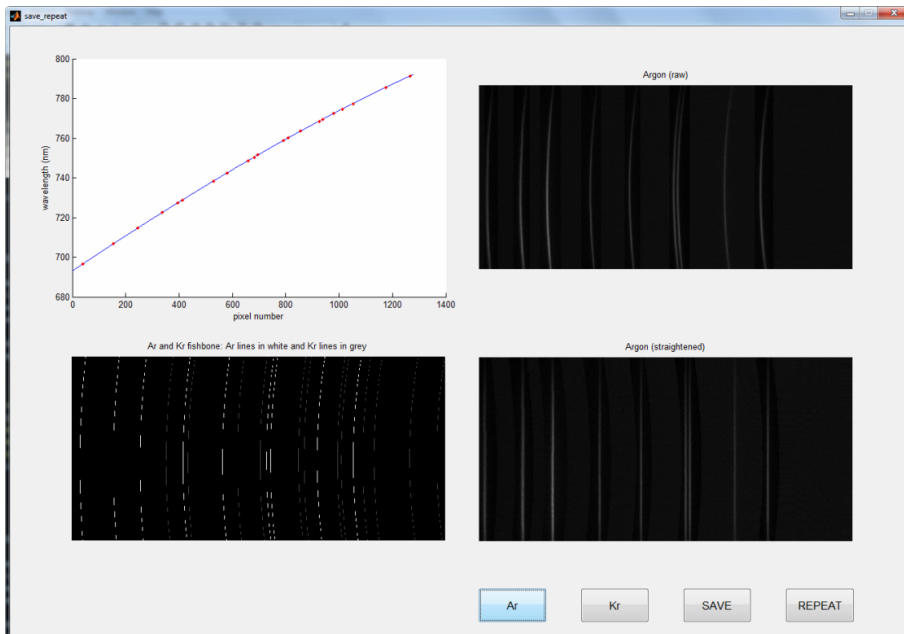


**Figure 5.42:** `calibration.m` GUI. From left to right and from up to down: (1) pixel number – wavelength fitting for row number 100 (2) argon synthetic spectral image (raw) (3) argon and krypton *fishbone* from the synthetic spectral images (4) argon synthetic spectral image (straightened)

When pressing button *Kr* the calculated krypton synthetic spectrum is plotted (see figure 5.43 up–right) and also does its straightened version (see figure 5.43 down–right). `calibration.m` also plots the resultant krypton spectrum so we can check whether the spectral fitting is accurate or it is not.
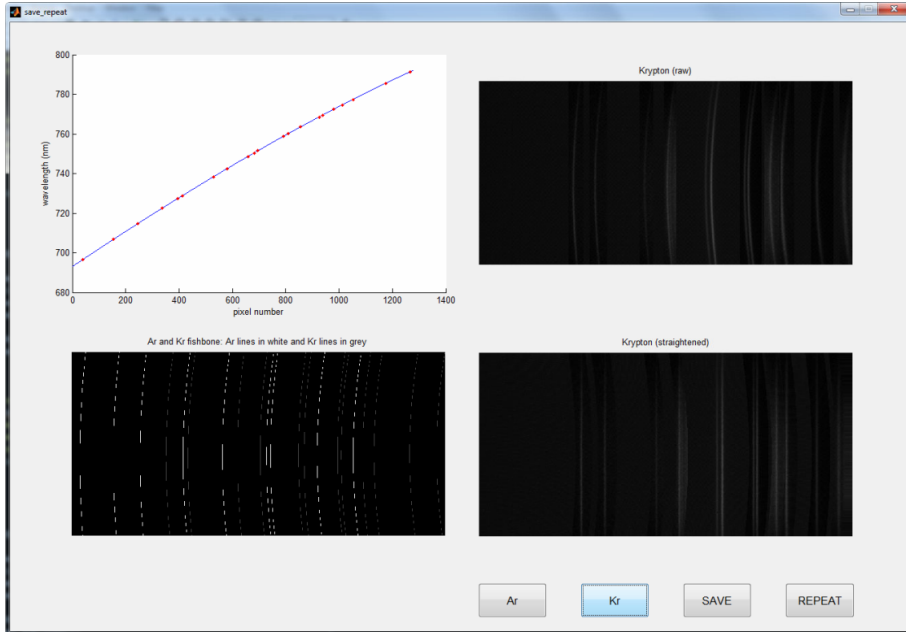


**Figure 5.43:** `calibration.m` GUI. From left to right and from up to down: (1) pixel number – wavelength fitting for row number 100 (2) krypton synthetic spectral image (raw) (3) argon and krypton *fishbone* from the synthetic spectral images (4) krypton synthetic spectral image (straightened)

If we find that the fitting is not accurate, we can repeat the whole process by pressing the *REPEAT* button. On the other hand, if we find that the fitting is accurate, we press the *SAVE* button, which launches a dialog box to save the calibration array so we can use it to reduce further spectroscopic images.

The pipeline of this process is shown in figure 5.44.
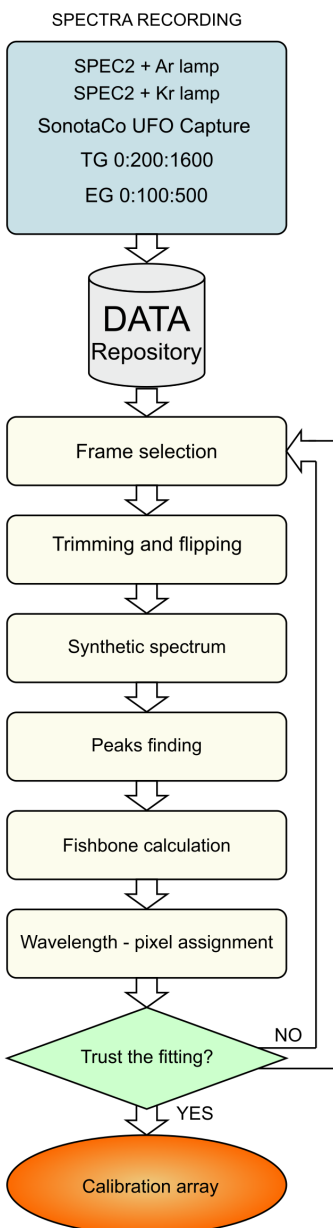
**Figure 5.44:** `calibration.m` GUI pipeline

SPECTRA RECORDING

SPECx + QTH

SonotaCo UFO Capture

TG 0:200:1600

EG 0:100:500

DATA
Repository

Frame selection

Phosphor persistence correction

Bias and background subtraction

Trimming and flipping

Distortion correction

Row smoothing

QTH spectral response from SPECx

Instrument function

QTH spectral response from a
commercial spectrograph
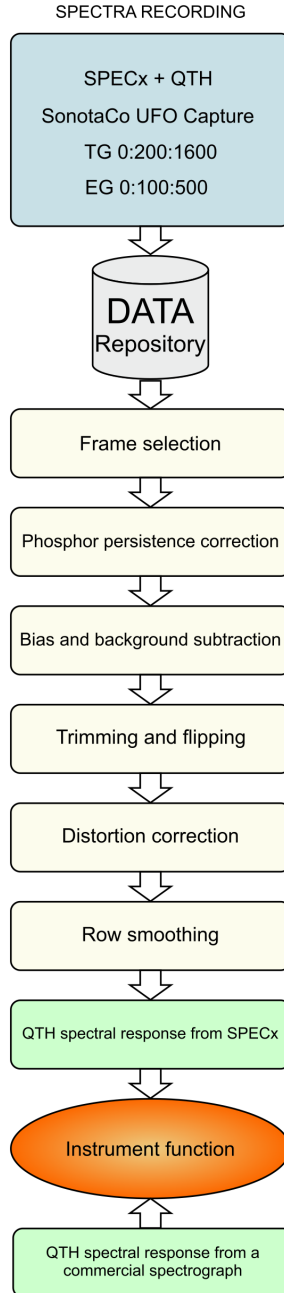
**Figure 5.45:** Pipeline of the calculation of the instrument function of SPEC1
and SPEC2
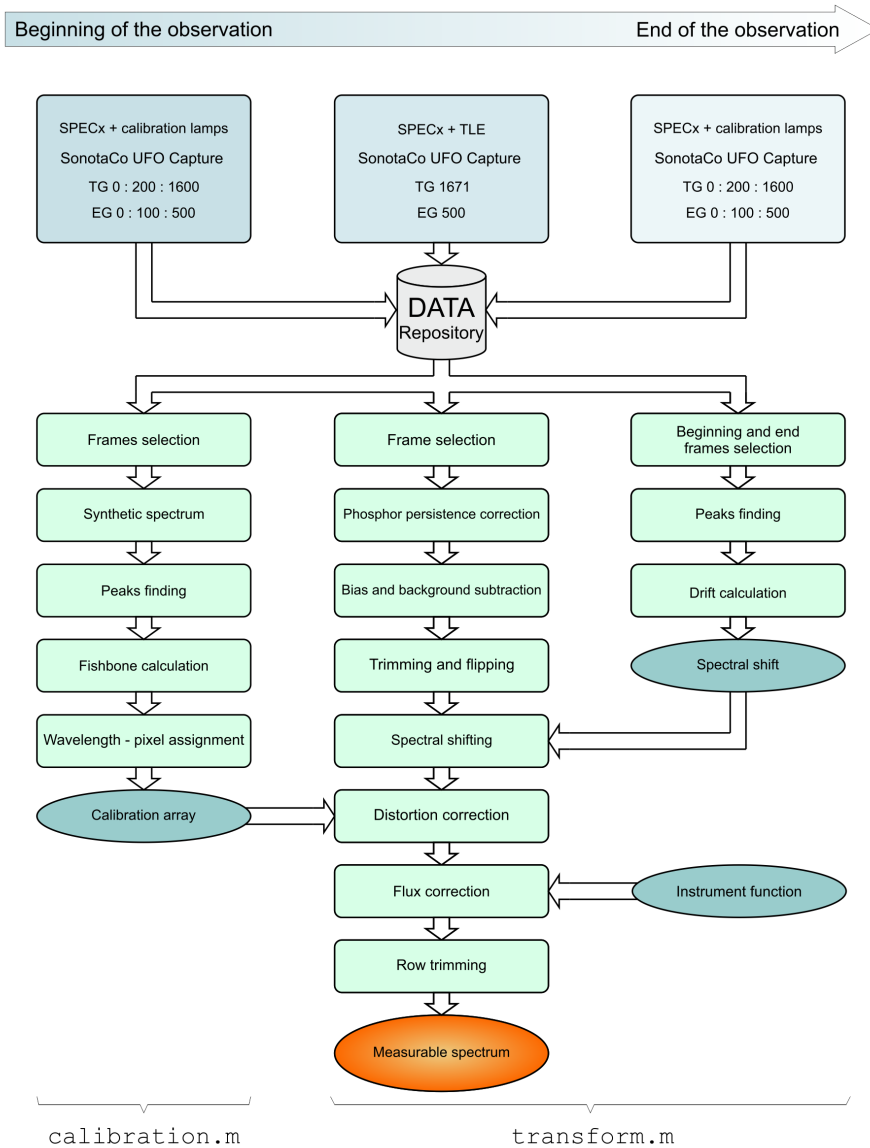
**Figure 5.46:** GRASSP data reduction pipeline

### 5.5.2 Instrument function calculation software

`InstrumentFunction.m` is a software application intended to calculate the spectral response of SPEC1 and SPEC2. In chapter 3 we thoroughly described the steps to calculate the instrument function of both spectrographs, and here we present the pipeline diagram to better understand the process (see figure 5.45). As this calculation was only made once, we did not develop a GUI.

### 5.5.3 Data reduction software pipeline

As mentioned before, the observational data presented in chapter 6 were reduced through an off-line pipeline, based on IRAF–inspired command–line tasks. In this section we will depict them within the thorough description of `transform.m`, a GUI to reduce spectroscopic data that we developed for our own specific requirements.

The figure 5.46 shows the `transform.m` and the `calibration.m` GUI pipelines, conforming the data reduction whole process. Notice that the instrumental function is not calculated within this process. `transform.m` GUI is shown in figure 5.47.
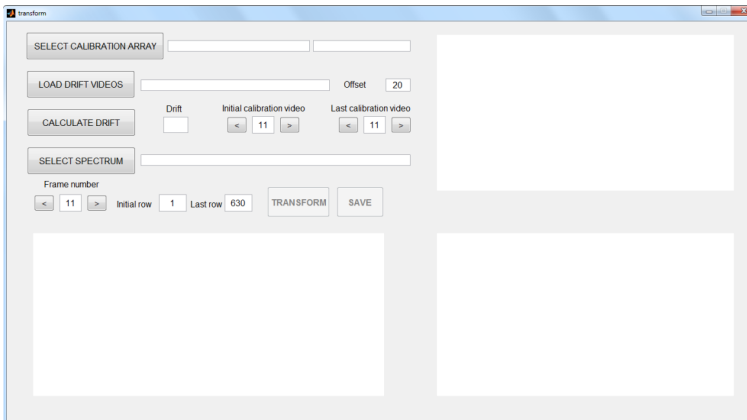


Figure 5.47: `transform.m` GUI

First step is to load the calibration array (see figure 5.48). When the user presses the *SELECT CALIBRATION ARRAY* button, a dialog box shows up to select the calibration array calculated in `calibration.m`.
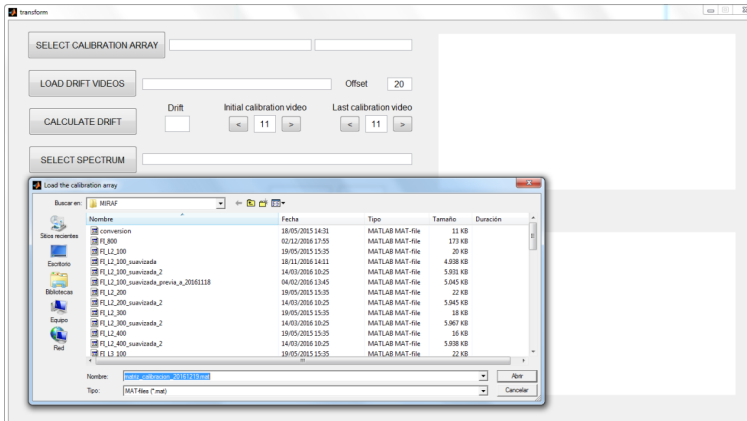


**Figure 5.48:** `transform.m` GUI. When pressing the *SELECT CALIBRA-TION ARRAY* button, a dialog box shows up

Next step is to calculate the pixel drift due to the increase of temperature inside the GRASSP housing during the observation. To do so, the final user presses the *LOAD DRIFT VIDEOS* button to select an Ar (or Kr) spectrum at the beginning and at the end of the observation night by selecting different frames so both spectra show up all the spectral lines with the same intensity level (see figure 5.49). Then, the final user selects a threshold that filters out the signal below. When pressing the `CALCULATE DRIFT` button, the beginning and the final calibration spectra are convolved with a gaussian curve and the peaks of both are detected. Next step is to calculate the pixel difference between similar peaks, and the mean value of this calculated drift is shown and saved (see figure 5.50).
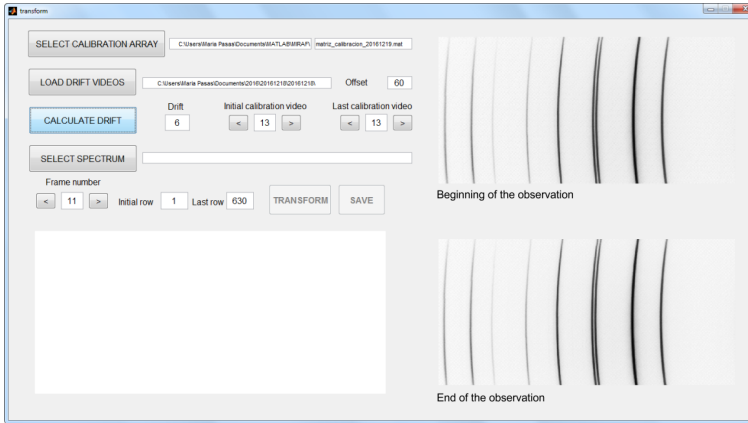
**Figure 5.49:** `transform.m` GUI. When pressing the *LOAD DRIFT VIDEOS* button, a dialog box shows up and the user selects two calibration spectra videos: one at the beginning and one at the end of the observation night. Then the final user selects —with the naked eye— the video frames so all spectral lines show up with similar intensity level in both videos
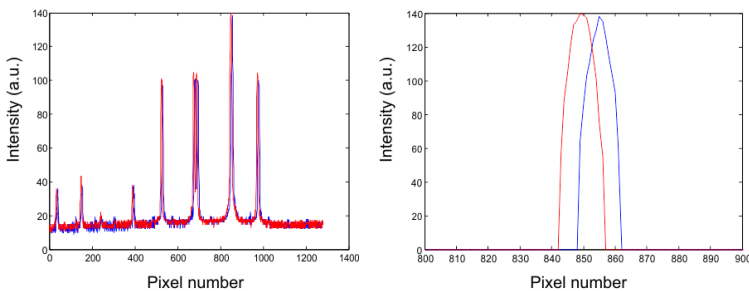


**Figure 5.50:** Drift calculation. Blue spectrum was recorded at the beginning of the night. Red spectrum was recorded at the end of the night. Right figure is a zoom of the left figure

Once we have calculated the temperature drift, the next step is to select the spectrum to analyze. The *SELECT SPECTRUM* button pops a dialog box (see figure 5.50) so the final user can select the video of the spectrum to analyze. When a TLE is detected, the region overlapping the slit is plotted in the spatial axis and its spectrum is plotted in the spectral axis. The final user can step the video frame by frame, and two graphs are plotted at the bottom of the layer: the graph on the right plots the spatial information of the spectral video frame, that is, the sum of the pixels of every row of the frame; the graph on the left plots the spectral information (not corrected by distortion yet), that is, the sum of the pixels of every column of the frame. The final user can easily find a spectrum by inspecting the spatial information: when a spectrum is detected some peaks corresponding to the TLE structure appear on the figure to the right. Once the final user has selected the TLE spectrum frame, the next step is to select the area of the image of highest SNR, that is, to select the rows where the spatial information shows well–defined peaks (see figure 5.51).
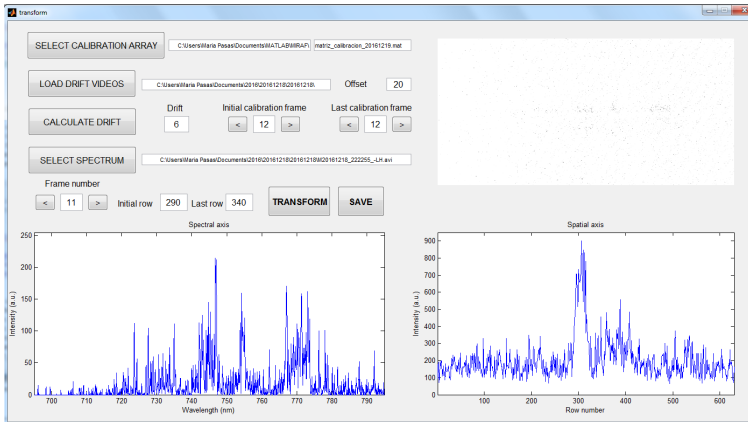


**Figure 5.51:** `transform.m` GUI. Left–bottom figure shows the spectral information of the video frame number 11. Right–bottom figure shows the spatial information of the video frame number 11. Next step is to select rows where the spatial signal is more relevant to enhance the SNR, that is, between 280 and 330 in this case

When the final user is sure to have selected the rows that enhance the SNR of the spectrum, the next step is to press the *TRANSFORM* button. `transform.m` corrects then the phosphor persistence effect as we described in chapter 3 and subtracts the bias and the background to the phosphor–corrected image. `transform.m` trims and flips the resulting image, and shifts the image as a function of the calculated temperature drift and the date and time of the image.

Next step is to transform the resultant spectral image with the calibration array we calculated with `calibration.m` to correct the curved spectral features (distortion correction). Once the spectrum is straightened, it is multiplied by the instrumental function of SPEC2 so we correct the inhomogeneities of the system. To conclude, the resultant image is trimmed again by the selected rows to enhance the SNR, and the pixels of every column are summed, so a measurable spectrum is generated in the left–bottom axes and the trimmed and corrected image is displayed in the right–bottom axes. The final user can repeat this process, varying the initial and final row number to choose the best SNR option. Once the best spectrum is generated, the final user presses the *SAVE* button, and a `*.dat` file is stored.
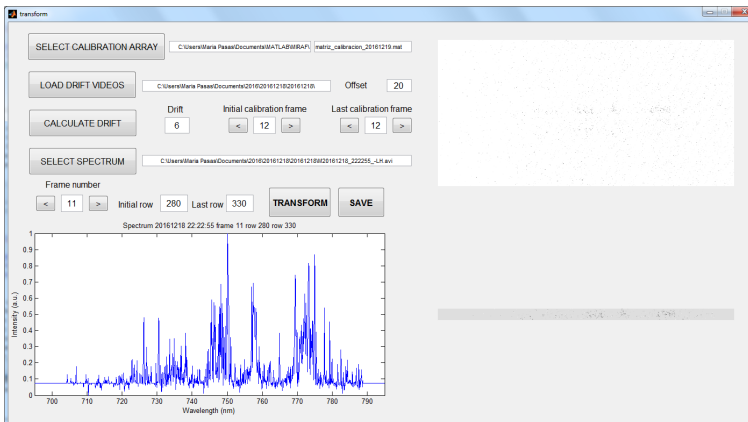


**Figure 5.52:** `transform.m` GUI. Left–bottom figure shows the trimmed and corrected spectrum of the video frame number 11 for rows between 280 and 330. Right–bottom figure shows the trimmed and corrected spectrum image

The tasks to reduce raw polarimetric images are defined in chapter 4. As the polarimeter is currently under testing, we have not developed a custom software to extract the polarization degree from a raw polarimetric image.

## 5.6 Conclusions

We have developed two software packages to both control all GRASSP subsystems and to reduce the spectroscopic data.

The instrument control software is intended to:

- Remotely switch on and off all GRASSP subsystems (`GRASSPv1x.m` and `GRASSPv2x.m`)

- Remotely change the automaton IP (`ChangeIP.m`)

- Remotely set the L'Heritier camera parameters (`lheritier.m` and `LHERITIER.m`)

- Remotely calibrate GRASSP spectrograph (`calibration1x.m` and `calibration2x.m`)

- Remotely aim the telescope mount to the desired position (`mount.m`)

- Automatically control the gears and the cameras of the polarimeter calibration system

The data reduction software is intended to:

- Calibrate SPEC1 and SPEC2 in wavelength and correct the distortion of the raw spectral images through an intuitive GUI (`calibration.m`)

- Calculate the instrument function of SPEC1 and SPEC2 (`InstrumentFunction.m`)

- Perform a data reduction software pipeline through an intuitive GUI (`transform.m`)

All these tasks have been developed by the author in MATLAB programming language.

The spectroscopic acquisition software is a commercial application developed by SonotaCo —UFO Capture HD2—, which allows us to record synchronously the field camera images and the spectral images and stores them in a data repository. The polarimetric acquisition software is a commercial application developed by Stark Labs —Nebulosity—, which allows to remotely set the Apogee ALTA U3041F camera integration time.

# Chapter 6

# Results

*"My sighting occurred in June 1983 approximately 200 miles south-southeast of Manila. [...] As the three of us in the cockpit were discussing the storm size and activity, suddenly a bolt of lightning discharged vertically. The bolt appeared to come from the approximate center of the storm and was perpendicular to the surface of Earth. The bolt was also observed by a U.S. Air Force C-141 aircraft which was circumnavigating the storm. They reported they too had seen a lightning bolt go straight up into nowhere."*

— W. L. McDonough, Jr., United States Naval Aviator *Journal of Geophysical Research, September 30, 1989*

## 6.1   Observation of TLEs

Since the first version of GRASSP was installed, our group has recorded several images of TLEs, lightning and also meteoroids.

We published the first results of GRASSP imagery in the journal IEEE Transactions on Plasma Science on June 2014 (*Passas et al.*, 2014). We presented two images of sprites and halos from August to November 2013, captured by GRASSP 1.0 at the 2.2 m dome terrace of the CAHA Observatory, Sierra de Los Filabres, north of Almería (Andalucía, Southern Spain), at 2,168 meters above mean sea level, 37.2231° N latitude and 2.5458° W

longitude. GRASSP 1.0 aimed automatically to the closest storm by consulting the real-time lightning database provided by the Spanish Meteorology Agency (AEMET).
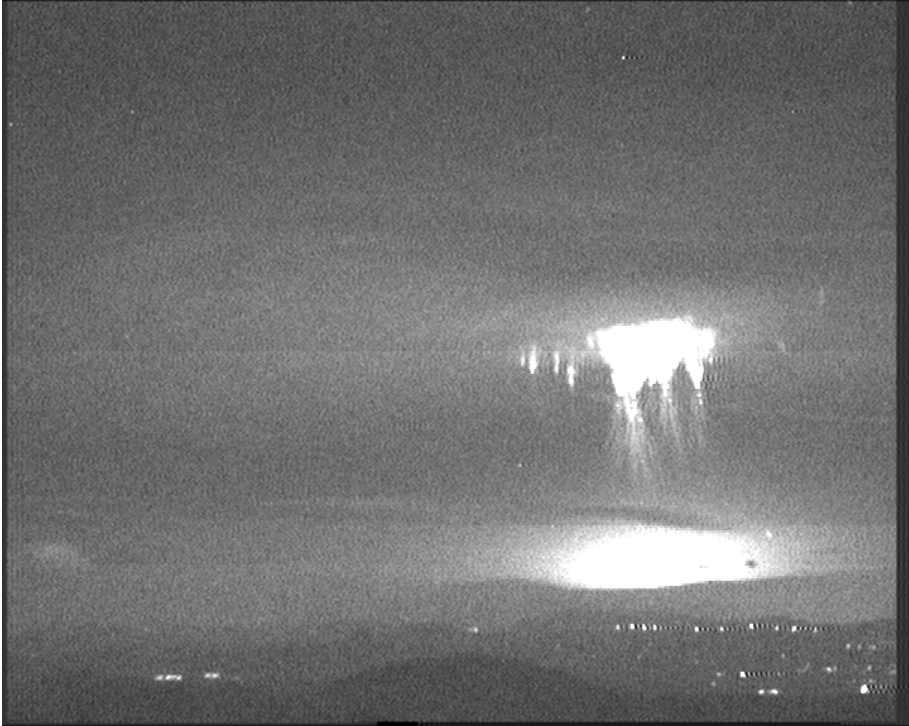


**Figure 6.1:** Sprites emerging from a halo seen as a diffuse disc of light with a diameter of up to 100 km. Sprite plasma streamers are visible as filaments due to the low speed of the imaging system. This photo was taken from CAHA Observatory at 19:43:38.285 UTC, November 15, 2013. The bright flash in the bottom part corresponds to the causating parent lightning located at 40.36° N latitude and 1.80° E longitude (close to Balearic Islands, Spain) (*Passas et al.*, 2014)

Sprites and halos usually occur over a mean horizontal distance of 25 km from the parent lightning strike.

Figure 6.1 shows a set of nine different sprites exhibiting striking features emerging from a halo, serving as the initial stage of sprite generation, formed at an approximate altitude of 80 km and about 500 km distant from the

observatory.

The observed vertical structuring in the three sprites shown in the center of figure 6.1 responds to the interplay between three physical time scales: 1) the net dissociative attachment time scale $(\tau_a)$ ; 2) the ambient dielectric relaxation time $(\tau_d)$ scale (inversely proportional to the ambient ion and electron conductivities); and 3) the time scale for the development of an individual electron avalanche into a streamer $(\tau_s)$ (*Pasko et al.*, 1998).

As reported in (*Pasko et al.*, 1998), the interplay between these three parameters creates three unique altitude regions visible in the three sprites shown in the center of figure 6.1: 1) the top diffuse region $(\tau_d < \tau_a, \tau_d < \tau_s)$; 2) the transition region $(\tau_d > \tau_a, \tau_d > \tau_s)$ in the middle is characterized by strong attachment of ambient electrons before the onset of the electrical breakdown; and 3) the streamer region $(\tau_d > \tau_a, \tau_d > \tau_s)$ in the bottom is also characterized by the strong attachment as well as by individual electron avalanches and local inhomogeneities evolving into streamers. Due to the 40 ms exposure time of our camera, the fast moving sprite streamers (with speed of about $10^7$ m/s) are observed as tendrils in figure 6.1.

Figure 6.2 shows a set of column (left/center sides), carrot (center/right sides), and wishbone-like (left side) sprites where there is no halo.

Contrarily to the lightning optical emissions from excited nitrogen and oxygen atoms and atomic ions, the very intense visible optical emissions from sprites and halos are controlled by the electron impact excitation of nitrogen $(N_2)$ molecules and the radiative decay and collisional quenching of the $N_2$ electronically excited states (*Gordillo-Vázquez et al.*, 2012). In particular, while halos (at approximately 80 km) emit only a reddish diffuse light associated to the first positive group (1PG) of $N_2$, sprites emit in red (upper part, 80–55 km) due to the 1PG of $N_2$ and in blue (lower part, 55–30 km) due to the second positive group (2PG) of $N_2$ since the emitting states of 1PG and 2PG $N_2$ are quickly quenched below 55 and 30 km, respectively.

**Figure 6.2:** Column and carrot type sprites images, recorded by GRASSP 1.0 at 20:40:38.239 UTC, November 15, 2013. The distant lights in the bottom of the image correspond to nearby villages. The causating parent lightning was at 40.37° N latitude and 1.72° E longitude (close to Balearic Islands, Spain) (*Passas et al.*, 2014)

## 6.2 Observation of lightning spectra

The night of 9th – 10th July 2013 there were up to 1065 positive and 1430 negative lightning strokes in the area between 37°–45°N and 2°W–14°E (figure 6.3). GRASSP v1.0 instrument captured 49 spectra of light from lightning scattered on clouds between 660 and 760 nm.
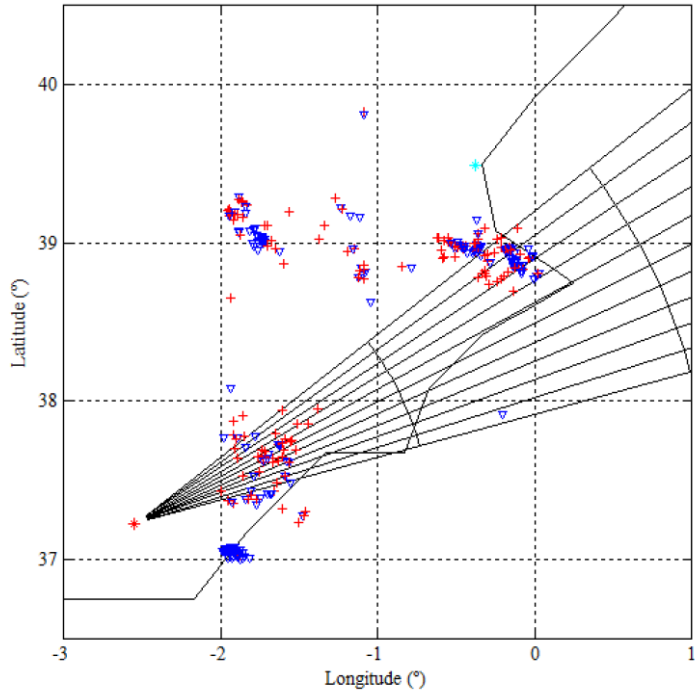
**Figure 6.3:** 9th–10th July 2013 lightning activity map. Red crosses represent positive strokes. Blue inverted triangles represent negative strokes. Red asterisk depicts CAHA observatory coordinates. Cyan asterisk depicts Barcelona coordinates. Data provided by the Spanish State Meteorology Agency — Agencia Estatal de Meteorología (AEMET)—

Figure 6.4 shows the iCCD image of the spectrum of the light scattered on clouds from a lightning occurred on the 10th July 2013 at 03:21:36 UTC, being the lightning stroke coordinates $1.9325°$ W – $38.0766°$ N. This spectral image was trimmed, flipped, distortion-corrected and flux-corrected by SPEC1 instrumental function. Figure 6.5 shows the resultant spectrum from integrating all the rows of the corrected iCCD image 6.4.
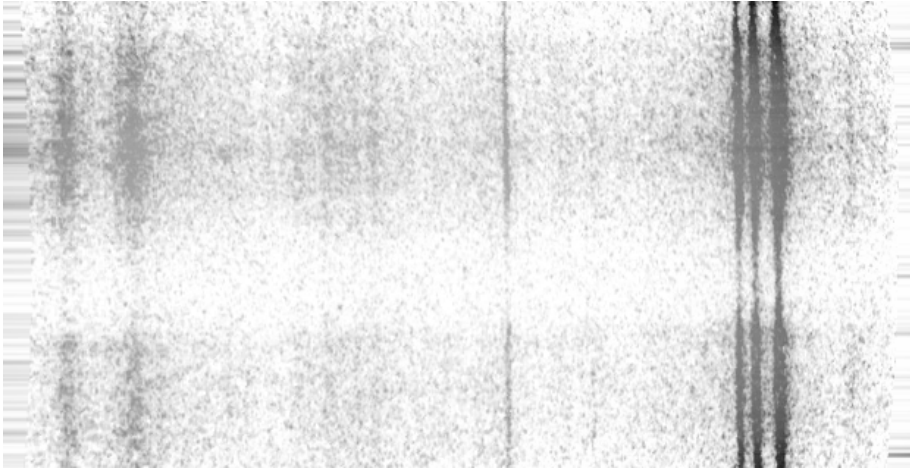


**Figure 6.4:** iCCD image of the spectrum of light from lightning scattered on clouds, trimmed, flipped, corrected, straightened and corrected by SPEC1 instrument function. It was recorded on the 10th of July 2013 at 03:21:36 UTC

From spectrum 6.5, we identified emissions from atmospheric species taking into account the signal over an upper limit of 2 and 3-sigma (see table 6.1). We calculated sigma as the root mean square value (RMS) of the background signal of the image. The limits of 3-sigma and 2-sigma identify spectral lines with a confidence of 99.87 % and 97.73 % respectively.

Spectra of lightning have been studied for decades (*Salanave*, 1961; *Wallace*, 1964; *Orville*, 1968; *Orville and Salanave*, 1970; *Walker*, 2015). The species we have identified in the spectrum of the light of lightning scattered by clouds within the spectral range between 660 and 760 nm are coincident to those.

| Wavelength (nm) | | $\Sigma$ intensity (A.U.) | |
|---|---|---|---|
| Measured | Theory | Identification | Measured |
| 660.9 | 661.056 | N II | 0.1022 |
| **664.3** | **664.496** | **N I** | **0.161** |
| 665.5 | 665.651 | N I | 0.1045 |
| **672.3** | **672.262** | **N I** | **0.182** |
| 703.3 | 703.241 | Ne I | 0.1025 |
| **715.6** | **715.670** | **O I** | **0.187** |
| **724.6** | **724.517** | **Ne I** | **0.118** |
| **738.3** | **738.398** | **Ar I** | **0.114** |
| **739.6** | **739.864** | **N I** | **0.129** |
| **740.5** | **740.624** | **N I** | **0.160** |
| **742.3** | **742.364** | **N I** | **0.712** |
| **744.2** | **744.229** | **N I** | **0.837** |
| **746.8** | **746.831** | **N I** | **1** |
| **747.9** | **747.644** | **O I** | **0.272** |
| **750.3** | **750.387** | **Ar I** | **0.176** |
| 751.5 | 751.465 | Ar I | 0.1034 |

**Table 6.1:** Identified lines in the spectrum from lightning emissions scattered on clouds, over 2- and 3-sigma. Spectral lines over 3-sigma are bold-typefaced
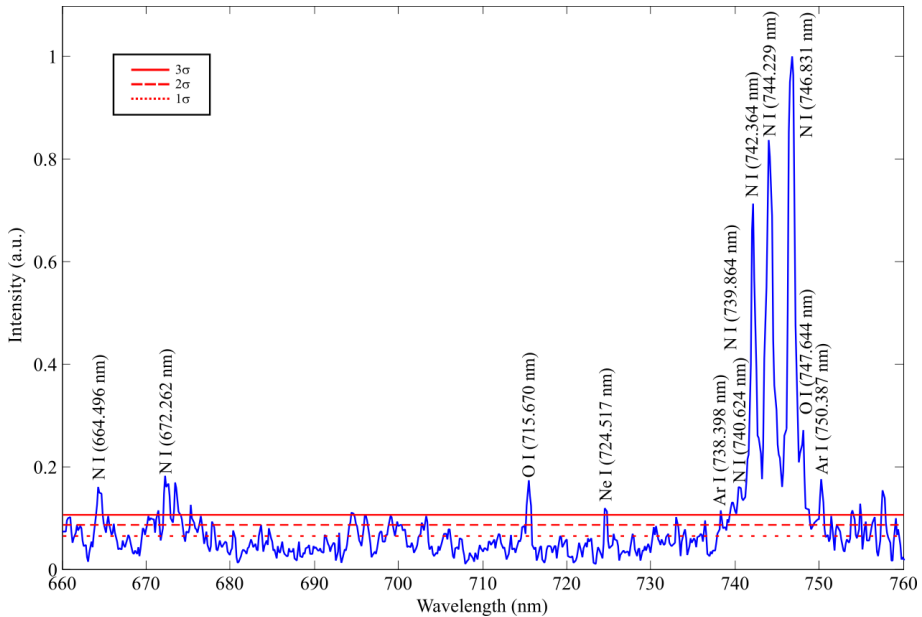
**Figure 6.5:** Lightning spectrum, correspondent to figure 6.4. Dotted red line represents the 1-sigma level. Dashed red line represents the 2-sigma level. Solid red line represents the 3-sigma level. Identified spectral lines over 3-sigma are shown

As the spectral resolution of SPEC1 is 0.56 nm and the N I triplet over 744 nm is well resolved, we can estimate the electron density ($N_e$) for different temperatures if we analyze the Stark (pressure) broadening of N I spectral line at 744.229 nm within the hypothesis of considering that it is isolated. Stark broadening of well-isolated lines from neutral atoms is mainly caused by electron-atom collisions (*Gordillo-Vázquez et al.*, 2005) and its FWHM ($d$) is related to $N_e$ (cm$^{-3}$) by means of equation 6.9 (*Befeki*, 1976):

$$d = 2W \frac{N_e}{10^{16}} (\mathring{A})$$
(6.1)

where $W$ is the electron impact parameter which is temperature dependent. For N I spectral line 744.229 nm $W$ varies between 0.299 Å and 0.785 Å for temperatures ranging from 2,500 K to 40,000 K, respectively (table
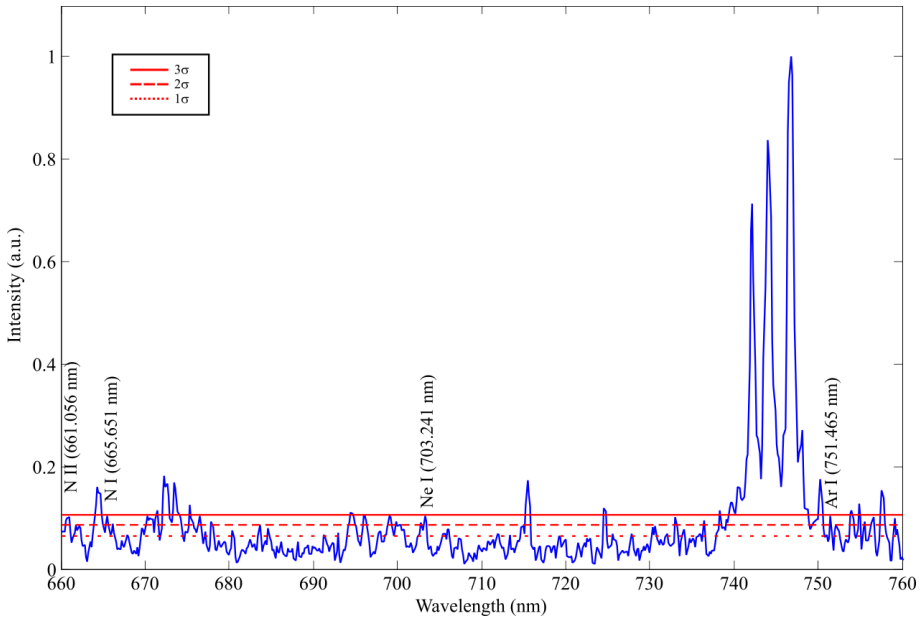
**Figure 6.6:** Lightning spectrum, correspondent to figure 6.4. Dotted red line represents the 1-sigma level. Dashed red line represents the 2-sigma level. Solid red line represents the 3-sigma level. Identified spectral lines over 2-sigma are shown

6.2).

The total broadening of an atomic or ionic spectral line, corresponds to the contribution of three factors: (1) the instrumental broadening, mainly related to the spectral resolution of SPEC1, (2) the Doppler broadening, which can be neglected when compared to Stark broadening resulting from collisions of neutral atoms with charged particles that dominate for plasma densities above $10^{14}$ cm$^{-3}$ (*Befeki*, 1976), and (3) the Stark broadening itself. The total broadening, $b$, which is the measured FWHM of N I spectral line 744.299 nm ($b = 7.8$ Å) can be approximated then by the expression 6.10 (*Miller*, 1987; *Whiting*, 1968):

$$b \simeq (\frac{d^2}{4} + g_{ins}^2)^{1/2} + \frac{d}{2} \tag{6.2}$$

which has an accuracy of 1 % (*Whiting*, 1968), where $d$ is the FWHM due

| T (K) | W (Å) | $N_e$ (cm$^{-3}$) |
|-------|-------|-------------------|
| 2,500 | 0.299 | 6.3202 10$^{16}$ |
| 5,000 | 0.368 | 5.1352 10$^{16}$ |
| 10,000 | 0.475 | 3.9784 10$^{16}$ |
| 20,000 | 0.628 | 3.0091 10$^{16}$ |
| 40,000 | 0.785 | 2.4073 10$^{16}$ |

**Table 6.2:** Electron impact widths of the N I spectral line 744.229 nm related to different electron temperatures (*Griem*, 1974) and estimated electron density extracted from N I spectral line 744.229 nm

to the Stark broadening and $g_{ins} = 5.6$ Å is the measured contribution of the instrumental function. If we consider an error of $\pm$ 5 % when measuring the instrumental FWHM, the error of the estimated $N_e$ (equation 6.9) is less than $\pm$ 10 %.

The estimated values of the electron density (table 6.2) are consistent if we compare them with those calculated from measuring the $H_\alpha$ spectral line, which electron densities range between $10^{16}$ to $10^{19}$ cm$^{-3}$ (*Walker*, 2015).

We presented these results during the 2nd Thunderstorm Effects on the Atmosphere-Ionosphere System (TEA-IS) Summer School in Collioure, France, in June 2014. The detection of these high resolution spectra, the further identification of the well-known lightning spectral lines and the estimation of the $N_e$ demonstrate the reliability of SPEC1.

## 6.3 Observation of a meteor spectrum

The emission spectrum of a meteor was recorded by the GRASSP v1.1 instrument during the observation of transient luminous events (TLEs) on the 16th of October 2014. The spectroscopic signal was recorded in the wavelength range from 695 to 795 nm, where the emission from atmospheric

oxygen and nitrogen dominated. The good spectral resolution of the spectrum (0.235 nm with 0.078 nm/pixel spectral dispersion) has allowed us to determine the physical conditions in the meteor plasma, to identify several emissions from atmospheric (N I, N II, O I) and meteoroid species (Ti I, Cr I, Fe I, Fe II, Zr I, Pd I, W I) and to estimate the upper limit of the temperature of the gaseous environment surrounding the meteoroid. Images recorded for this meteor from two different sites allowed calculating its atmospheric trajectory and the orbital parameters of the progenitor meteoroid. These data revealed that the particle belonged to the Orionid meteoroid stream. The results and conclusions of the analysis of these data were published in the journal *Icarus* on the 19th of November 2015 (*Passas et al.*, 2016a).

### 6.3.1 Introduction

Comet 1P/Halley is the parent of both the $\eta$-Aquariid and the Orionid meteor showers. Their activity period ranges, approximately, from April 19th to May 25th, and from October 2nd to November 7th, respectively (*Jenniskens*, 2006). The analysis of meteor events produced by debris from this comet can provide information about the physical properties of these meteoroids and their dynamics in the atmosphere, but also about their chemical nature if spectral data are available. Thus, meteor emission spectroscopy has proven to be a fundamental technique to analyze the physical conditions in meteor plasmas and the composition of meteoroids ablating in the atmosphere (*Borovicka*, 1993; *Jenniskens*, 2007; *Madiedo et al.*, 2013a).

Meteor spectra contain contributions from the meteoroid, but also from atmospheric species. In general, most lines associated to the meteoroid are produced by Fe I, but the contributions of other neutral and singly ionized chemical elements have been also identified (*Borovicka*, 1993, 1994; *Trigo-Rodríguez et al.*, 2009a; *Madiedo et al.*, 2013c,b). Besides, bands of different molecules (such as, for instance, CN, $N_2$, $C_2$, FeO and CaO), have been also observed (*Borovicka*, 1993; *Jenniskens et al.*, 1998; *Madiedo*, 2015).

This section analyzes a meteor high resolution emission spectrum serendipitously recorded in the framework of a transient luminous event (TLE) observing campaign conducted during the activity period of the Orionid meteor shower in 2014. The signal was obtained in the wavelength range between 695 and 795 nm. The meteor was simultaneously imaged from two different sites in Spain, which provided the atmospheric trajectory and radiant of this event, but also the orbital elements of the meteoroid.

### 6.3.2 Instrumentation

The meteor observing station at Sierra Nevada, Granada, Spain, located at 2,896 meters above mean sea level, 37.05° N latitude and 03.38° W longitude, employs an array of five low-lux CCD video cameras (models 902H Ultimate and 902H2, manufactured by Watec Co., Japan) with the aim to determine the atmospheric trajectory of meteor events and the heliocentric orbit of the progenitor meteoroids. These devices generate analogue interlaced imagery following the PAL video standard at a rate of 25 frames per second (fps) and with a resolution of 720 × 576 pixels. Aspherical optics with focal length ranging from 6 to 25 mm are attached to these cameras. With this configuration each device monitors an area in the night sky ranging from 62×50 to 14×11 degrees. A detailed description of this station is given in (*Madiedo and Trigo-Rodríguez*, 2008). This CCD camera array operates in a fully autonomous way by means of software developed for this purpose (*Madiedo*, 2014). To obtain the atmospheric trajectory and radiant of the meteor and the orbital elements of the progenitor meteoroid we have employed the AMALTHEA software (*Trigo-Rodríguez et al.*, 2009b; *Madiedo et al.*, 2013c), which follows the calculation methods described in *Ceplecha* (1987).

The GRanada Sprite Spectrograph and Polarimeter v1.1 (GRASSP hereinafter, figure 6.7) is a ground-based polarimeter and grating spectrograph sensitive in the wavelength range between 695 and 795 nm, both installed

on a remotely controlled telescope mount. It has been designed to measure simultaneously the polarization and the spectra of the light emitted from TLEs with a spectral resolution of R=$\lambda/\Delta\lambda = 3309$ ($\Delta\lambda = 0.235$ nm) measured at the central wavelength of 750 nm with a spectral dispersion of 0.078 nm/pixel.
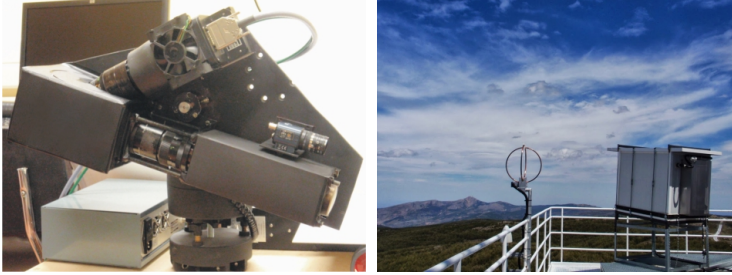


**Figure 6.7:** GRASSP instrument 0.23 nm resolution spectrograph (left) and housing together with a lightning detector (right) on the terrace of the 2.2 m dome of CAHA Observatory

The GRASSP intensified CCD (iCCD) slit spectrograph system main characteristics are fully described in *Parra-Rojas et al.* (2013b) and *Passas et al.* (2014), although it was upgraded in 2014 July to shift the former spectral range from 695 nm to 795 nm and to improve its spectral resolution. Moreover, we upgraded the analog to digital system too and we installed a Blackmagic Design Decklink Mini Recorder board, which increases the HD format support to 1080 (V) × 1920 (H) pixels instead of 576 (V) × 720 (H) pixels we used to have. Table 6.3 shows the main features of GRASSP v1.1 slit spectrograph.

The GRASSP instrument is also equipped with a field camera to discern the origin of the recorded spectrum. It consists of a Watec WAT-902H2 Ultimate with a 3005VX4 sensor 1/2" CCD low light monochrome camera of high sensitivity similar to the meteor station cameras installed at Sierra Nevada. Its field of view is 21.6 (H) × 17.4 (V) thanks to the f/1.4 and 16 mm focal length lens it has attached.

| | |
|---|---|
| Wavelength range | 695 nm - 795 nm |
| Spectral resolution | 0.235 nm |
| Dispersion | 0.078 nm/px |
| Time resolution | 10 $\mu$s - 30 ms |
| Slit size | 0.10 mm × 31.37 mm |
| Field of view | 0.03° × 6° |
| Frame rate | 25 fps |

**Table 6.3:** ICCD spectrograph features of GRASSP v1.1

The whole system was housed in an isothermal box which front face included a $80 \times 80$ cm$^2$ window with a mean transmittance of 69% in the band between 695 and 795 nm. It was located on the terrace of the 2.2 m dome of the German-Spanish Astronomical Center at Calar Alto, Sierra de Los Filabres, north of Almería (Andalucía, Southern Spain) fixed at 2,168 meters above mean sea level, 37.2231° N latitude and 2.5458° W longitude. The box was installed on an aluminum sloped fixed structure oriented to 45° azimuth from the north and 10° elevation in order to observe the western Mediterranean Sea zone (37°-50°N; 2°W-14°E) with an elevation of 10°-35° above the horizon, a region where the most TLE activity in Europe takes place (see figure 6.7).

**Figure 6.8:** Sum pixel intensity image of the Orionid meteor imaged from CAHA

### 6.3.3   Results

#### 6.3.3.1   Atmospheric path, radiant and orbit

Figure 6.8 shows a sum pixel intensity image of the meteor recorded from Calar Alto on the 16th October of 2014 at 01 h 19 m $40.4 \pm 0.1$ s UTC. The peak luminosity of the event was equivalent to a stellar magnitude of $-2.5 \pm 0.5$. The meteor was simultaneously imaged from a meteor observing station located at Sierra Nevada.

The geographic coordinates of both recording sites are shown in table 6.4. The triangulation of the atmospheric trajectory reveals that the luminous phase of the event began at $119.7 \pm 0.5$ km above mean sea level and ended at a height of $82.8 \pm 0.5$ km. The inclination of this trajectory with respect to the local vertical was $48.5° \pm 1.0''$, and the meteoroid struck the

| Station | Station name | Longitude (W) | Latitude (N) | Altitude (m) |
|---------|--------------|---------------|--------------|--------------|
| 1 | Calar Alto (CAHA) | 2° 32′ 46″ | 37° 13′ 25″ | 2168 |
| 2 | Sierra Nevada (OSN) | 3° 23′ 05″ | 37° 03′ 51″ | 2896 |

**Table 6.4:** Geographical coordinates of the sites where the meteor analyzed in this work was imaged

| $H_b$ (km) | $H_e$ (km) | $\alpha_g$ (°) | $\delta_g$ (°) | $V_\infty$ (km s$^{-1}$) | $V_g$ (km s$^{-1}$) | $V_h$ (km s$^{-1}$) |
|------------|------------|----------------|----------------|--------------------------|---------------------|---------------------|
| 119.7 ± 0.5 | 82.8 ± 0.5 | 91.7 ± 0.1 | 16.5 ± 0.1 | 68.1 ± 0.3 | 66.9 ± 0.3 | 40.9 ± 0.3 |

**Table 6.5:** Atmospheric trajectory and radiant data. $H_b$ and $H_e$: beginning and ending height of the meteor, respectively; $\alpha_g$, $\delta_g$: right ascension and declination of the geocentric radiant; $V_\infty$, $V_g$, $V_h$: observed pre–atmospheric, geocentric and heliocentric velocities, respectively

atmosphere with an initial velocity of 68.1 ± 0.3 km s$^{-1}$, and no significant deceleration was observed while the meteoroid penetrated the atmosphere.

The apparent radiant was located at the equatorial coordinates $\alpha_g = 91.92 \pm 0.07°$, $\delta_g = 16.65 \pm 0.09°$. The main parameters of this atmospheric path are summarized in table 6.5. The calculated orbital data of the progenitor meteoroid are listed in table 6.6.

| a (A.U.) | e | i(°) | $\omega$(°) | $\Omega$(°) | q (A.U.) | P (yr) | $T_J$ | $D_{SH}$ |
|----------|---|------|-------------|-------------|----------|--------|-------|----------|
| 8.7 ± 1.9 | 0.92 ± 0.01 | 165.9 ± 0.2 | 74.9 ± 1.0 | 22.40735 ± 10$^{-5}$ | 0.642 ± 0.005 | 25.82 | -0.35± 0.27 | 0.11 |

**Table 6.6:** Orbital parameters of the meteoroid.

### 6.3.3.2 Emission spectrum

Five consecutive frames of the spectrum were recorded while the meteor was passing through the spectrograph slit. To reduce long-slit spectroscopy data, we combined these frames in order to maximize the signal to noise ratio (SNR) by calculating the median value of each pixel. The spatial extension of the resulting spectrum is 1280 × 46 pixels, being the signal extracted from row 410 to row 455. We subtracted a combination of the bias frames from all images. Later we calculated the sky background as the mean value between 10 frames - previously bias-corrected- corresponding to five frames immediately before and after the caption.

Once the sky background was subtracted from the bias-corrected image, we calibrated it in wavelength using Ne, Ar and Kr lamps in order to straighten the curvature of the spectrum through a specific Matlab software we have developed, by associating the pixel coordinates in the ICCD with the absolute wavelength by comparison with emission data whose absolute wavelengths are well-known.

We calculated the calibration curve of the instrument using the response of a commercial continuum lamp according to the steps defined in *Fantz* (2006). To do so, we divided the spectral radiance of this calibrated source by the instrument response to the same calibrated lamp under the same calibration setting. The resulting curves (one for each row of the ICCD) are called the conversion factor spectral sensitivity, which define the calibration curves of the instrument.

Next, we enhanced the response of the ICCD edges by flux-calibrating the corrected spectrum image. To do so, we multiplied the response of every row of the ICCD image by its corresponding conversion factor spectral sensitivity curve of GRASSP instrument. Then, we corrected the resulting spectrum by the GRASSP instrument window and the air transmittances, as in *Gordillo-Vázquez et al.* (2011, 2012). The air transmittance for computing the $N_2$ 1PG synthetic spectra between 695 nm and 795 nm was

calculated using the MODTRAN code (*Anderson et al.*, 1993) as the atmospheric transmission model. We considered a mean source altitude of 100 km and a atmospheric path length of 700 km between the source (the Orionid meteor) and the GRASSP spectrograph located at 2.2 km altitude.

Considering that the first frame of the meteor spectrum was recorded 0.24 s after the Watec camera detection, we estimate that the altitude of the meteor at that time was $107.6 \pm 0.5$ km. By inspecting the resulting spectrum, and by assuming that the main contribution corresponds to line 777.194 nm of atomic oxygen, we have identified a Doppler blueshift of 0.2 nm in this spectral line, which implies a projected velocity of 77 km/s $\pm$ 27 km/s (corresponding to a dispersion rate of 0.78 Å) which is consequent with the velocity derived from the analysis of the atmospheric trajectory of the event.

### 6.3.3.3 Identified species

The next step is to identify which species could be emitting while the meteoroid was entering the Earth's atmosphere. First, we smoothed the blueshift-corrected spectrum to increase the SNR. Then, we calculated sigma as the root mean square value (RMS) for a dark image, previously wavelength and flux calibrated. To identify the emission lines of the meteoroid spectrum we only took into account the signal over an upper limit of 2-sigma.

We identified some species by modelling a synthetic spectrum combining well-known spectral lines (*Kramida et al.*, 2015) close to the peaks over 2-sigma, previously convolved with a gaussian of a standard deviation of 0.10 nm, corresponding to a system spectral resolution of 0.23 nm.

We also modelled a synthetic spectrum including the relative intensities of the atomic emission lines of O I, N I, N II for a gas temperature of 0.13788 eV ($\sim$ 1500 K). Then, we combined the above atomic synthetic spectra with a synthetic spectrum of the $N_2$ first positive system (*Gordillo-Vázquez et al.*, 2011, 2012; *Parra-Rojas et al.*, 2013b). Table 6.7 shows that

the mean wavelength difference between measured and modelled spectra is 0.9 Å, being the intensity measured in arbitrary units (A.U.).

In order to generate the synthetic spectrum of the $N_2$ first positive system between 695 nm and 795 nm we have assumed Boltzmann distributions for the populations of $N_2$ $(B^3\Pi_g)$ rotational and vibrational levels considering $T_{rot} = T_{vib} = T = 1500$ K, that is the calculated upper gas temperature limit obtained from the numerical solution of equation 6.6 below. The main contributions of the corrected spectrum over 2-sigma are listed in table 6.7, where contributions over 3-sigma are bold typefaced. The contributions over 3-sigma correspond to the emissions of atmospheric N I and O I, and the contributions over 2-sigma seem to correspond to the emissions of N I, N II and O I, but also to the meteoroid-forming species Ti I, Cr I, Fe I, Fe II, Zr I, Pd I and W I. We also find coincidences with several peaks below 2-sigma when we include spectral lines of the above identified species in the range between 695 nm and 795 nm.

### 6.3.3.4 Estimation of an upper limit of the gas temperature surrounding the meteor

In this section we estimate the gas temperature surrounding the meteor by means of the ionization degree of the plasma. It is well-known that the relative intensity of the spectrum lines are proportional to their densities as:

$$I_i = C \cdot N_i \cdot A_i \cdot h \cdot \nu_i \tag{6.3}$$

where, for each line of the spectrum, $I_i$ is the relative emission intensity of an atomic or ionic species in the i-th state of ionization, $C$ is a constant, $A_i$ is the Einstein's coefficient in $s^{-1}$ accounting for the probability of spontaneous emission between a given atom or ion excited electronic state and a lower energy state, $\nu_i$ is the frequency of the transition between atomic or ionic electronic states in $s^{-1}$, $h$ is the Planck's constant and $N_i$ is the

| Wavelength (nm) | | | Σ intensity (A.U.) | |
|---|---|---|---|---|
| Measured | Theory | Identification | Measured | Blend |
| 710.3 | 710.291 | Zr I | 0.09361 | 710.372 (Zr I) <br> 710.448 (W I) <br> 710.486 (W I) <br> 710.526 (W I) |
| 734.3 | 734.4695 | Ti I | 0.08957 | 734.396 (Zr I) <br> 734.394 (Fe I) <br> 734.449 (W I) |
| 740.7 | 740.7821 | O II | 0.09131 | 740.837 (Fe II) |
| 743.8 | 743.95532 | Fe II | 0.09312 | 743.719 (W I) |
| 746.0 | 746.036 | Fe I | 0.1143 | 745.927 (W I) <br> 746.219 (W I) <br> 746.231 (Cr I) |
| **746.6** | **746.831** | **N I** | **0.1893** | **746.578 (Fe I)** <br> **746.611 (W I)** <br> **746.757 (Zr I)** <br> **746.774 (W I)** <br> **746.822 (W I)** <br> **746.994 (Ti I)** <br> **747.041 (W I)** |
| 769.2 | 769.3254 | Ti I | 0.09693 | |
| 773.5 | 773.57981 | Fe II | 0.08958 | 773.629 (W I) <br> 773.767 (Fe I) |
| 776.2 | 776.224 | N II | 0.1062 | 776.298 (Cr I) <br> 776.397 (Pd I) |
| **777.2** | **777.194** | **O I** | **1** | **777.165 (W I)** <br> **777.169 (Cr I)** <br> **777.252 (W I)** <br> **777.348 (Fe II)** <br> **777.417 (O I)** <br> **777.468 (W I)** <br> **777.539 (O I)** <br> **777.673 (W I)** |

**Table 6.7:** Identified lines over 2-sigma and 3-sigma. Lines over 3-sigma are given in bold typeface. The *BLEND* column includes the surrounding spectral lines we found. If blended lines, the strongest feature is given in the *Theory* column
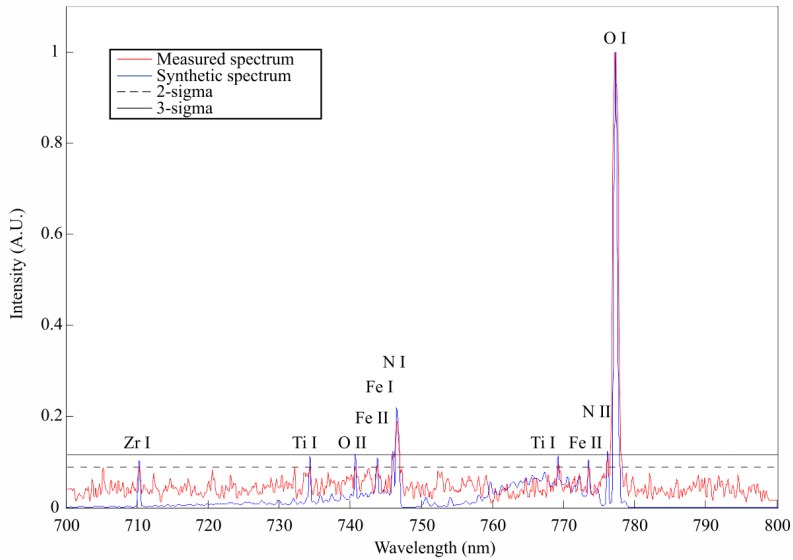
**Figure 6.9:** Details of a meteor spectrum (red line) from 695 nm and 795 nm, obtained with GRASSP v1.1 spectrograph on 2014 October 16th at 01:19:40 UTC. Flux is dimensionless. The blue line is a composition of a $N_2$ first positive system synthetic spectrum at $T_{rot} = T_{vib} = T = 1500$ K, at an altitude between 99 and 108 km, combined with a synthetic spectrum of N I, N II, O I, Ti I, Cr I, Fe I, Fe II, Zr I, Pd I and W I atomic lines convolved with a gaussian curve of sigma 0.10 nm
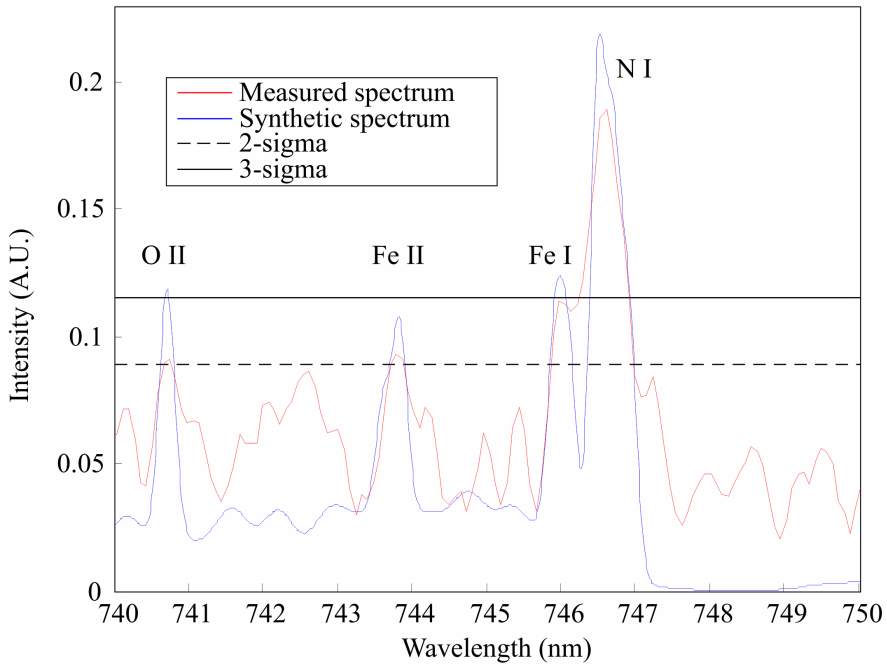
**Figure 6.10:** Details of a meteor spectrum (red line) from 740 to 750 nm, obtained with GRASSP v1.1 spectrograph on 2014 October 16th at 01:19:40 UTC. Flux is dimensionless. The blue line is a composition of a $N_2$ first positive system synthetic spectrum at $T_{rot} = T_{vib} = T = 1500$ K, at an altitude between 99 and 108 km, combined with a synthetic spectrum of N I, N II, O I, Ti I, Cr I, Fe I, Fe II, Zr I and W I atomic lines convolved with a gaussian curve of sigma 0.10 nm. Notice that the strongest features of N I at 742.364 and 744.229 nm can not be found, although atomic lines of Fe have been identified

| Altitude (km) | Ionization degree | $n_e(max)(cm^{-3})$ | $T_{gas}(max)(K)$ |
|---|---|---|---|
| 107.6± 0.5 | 0.5442 | $3.0208 \cdot 10^{12}$ | 1594.6911 |
| 105.6 ± 0.5 | 0.4752 | $4.3034 \cdot 10^{12}$ | 1600.8048 |
| 103.6 ± 0.5 | 0.2443 | $6.1298 \cdot 10^{12}$ | 1547.9219 |
| 101.6 ± 0.5 | 0.3566 | $8.7046 \cdot 10^{12}$ | 1618.1201 |
| 99.6 ± 0.5 | 0.2637 | $1.2322 \cdot 10^{13}$ | 1610.6464 |

**Table 6.8:** Altitude, ionization degree, electron density and gas temperature estimated for each frame of the meteor spectrum video

density of ground or excited atoms or ions in the i-th state of ionization. We have identified two nitrogen lines in the meteor spectrum, corresponding to different ionization stages. If we consider that the main contributions are due only to nitrogen, then we can calculate an approximate value of the ionization degree of the plasma for each frame. We define the ionization degree as:

$$\frac{N_{i+1}}{N_{i+1} + N_i} = \frac{1}{1 + \frac{I_i \cdot A_{i+1} \cdot \nu_{i+1}}{I_{i+1} \cdot A_i \cdot \nu_i}} \tag{6.4}$$

where $I_i$ is the relative emission intensity of the N I line at 746.831 nm, and $I_{i+1}$ is the relative emission intensity of the N II line at 776.224 nm. The values of $I_i$ and $I_{i+1}$ vary within the frame, so we have calculated the rate $I_{i+1}/I_i$ and the ionization degree for each frame, as shown in the second column of table 6.8.

If we consider the gas to be in thermal equilibrium —at least locally— so that the electron and gas temperatures have similar values ($T_e = T$), we

can calculate the ionization degree of the plasma using the Saha equation:

$$\frac{n_e \cdot N_{i+1}}{N_i} = \frac{g_e \cdot g_{i+1} \cdot (2\pi m_e k_B T_e)^{3/2}}{g_i \cdot h^3} e^{\frac{-\chi_i}{k_B T_e}} \qquad (6.5)$$

where $n_e$ is the electron density, $N_i$ is the density of ground or excited atoms or ions in the i-th state of ionization, $g_i$ is the degeneracy or multiplicity of the considered atom or ion excited states, being $g_e$=2, $m_e$ is the mass of an electron, $\chi_i$ is the energy needed to ionize an atom in the ground state or in a given excited state. For N I in the excited state with excitation energy 11.99 eV (connected to the transition 746.831 nm) the value of $\chi_i$ needed for its ionization is 2.54 eV, $k_B$ is the Boltzmann constant; $T$ is the temperature of the gas and $h$ is the Planck's constant.

The ionization degree is defined then as a function of the electron density and the gas temperature:

$$\frac{N_{i+1}}{N_{i+1} + N_i} = \frac{1}{1 + \frac{n_e \cdot g_i \cdot h^3}{g_e \cdot g_{i+1} \cdot (2\pi m_e k_B T_e)^{3/2}} e^{\frac{-\epsilon_{i+1} + \epsilon_i}{k_B T_e}}} \qquad (6.6)$$

being $\epsilon_i$ and $\epsilon_{i+1}$ the energies of the states $i$ and $i + 1$. Considering that the electron density could never exceed the gas density at a known altitude, we can calculate an upper limit of the electron temperature for a given ionization degree and altitude. The gas density at altitudes between 99.6 and 107.6 km is between $1.2322 \cdot 10^{13}$ cm$^{-3}$ and $3.0208 \cdot 10^{12}$ cm$^{-3}$ (*Marsh et al.*, 2013); the corresponding maximum electron density is shown in the third column of table 6.8. The fourth column of table 6.8 is computed by solving equation 6.6 numerically for T; figure 6.11 plots the function in equation 6.6 for the electron density levels corresponding to 99.6 to 107.6 km altitude. According to figure 6.11 and table 6.8, we found that the upper limit of the gas temperature surrounding the meteor was $1500 \pm 100$ K.
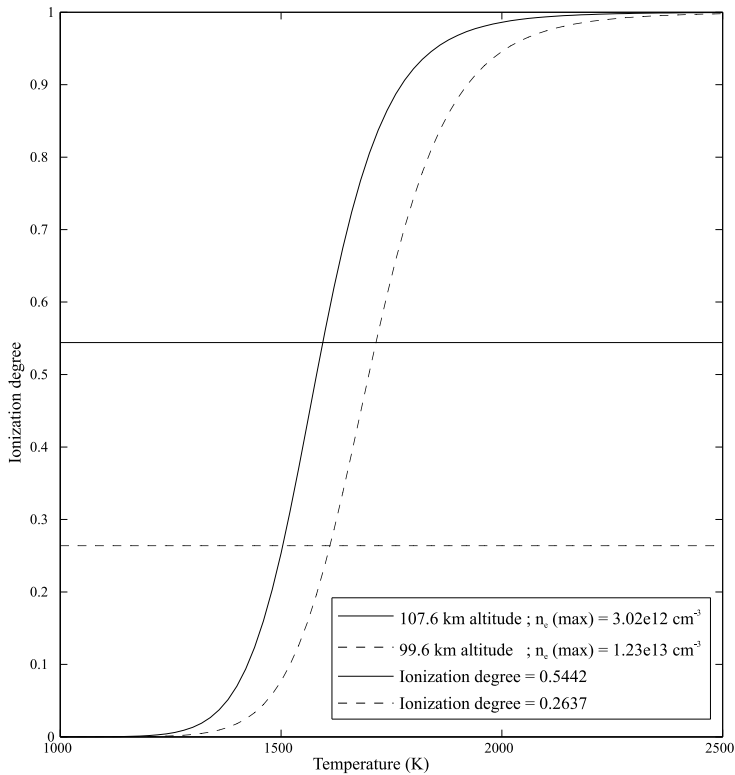
**Figure 6.11:** Gas temperature calculated as a function of a given ionization degree and altitude. Dashed lines correspond to the ionization degree of the gas at 99.6 km altitude. Solid lines correspond to the ionization degree of the gas at 107.6 km altitude

### 6.3.4 Discussion

#### 6.3.4.1 Meteoroid source

The event discussed here was recorded during the activity period of the Orionids. It was registered about 5 days before the maximum of this meteor shower, which took place on October 21st at around 20:16 UTC according to the International Meteor Organization [www.imo.net/live/orionids2014]. In order to validate the association of the progenitor meteoroid with the Orionid meteoroid stream, we have compared the orbit of this stream (table 7 in *Jenniskens* (2006)) with the orbital data of the meteoroid listed in table 4. This comparison has been performed, as usual, by calculating the value of the Southworth & Hawkins $D_{SH}$ dissimilarity function (*Southworth and Hawkins*, 1963). This function measures the "distance" between both orbits (*Williams*, 2011). The computed value of $D_{SH}$ yields 0.11, which is below the cut-off value of 0.15 usually adopted to establish a valid link (*Lindblad*, 1971a,b). This result confirms that the meteor belonged to the Orionid shower.

#### 6.3.4.2 Photometric analysis

The lightcurve of the meteor is shown in figure 6.12.

As can be noticed, it exhibited no flares during its atmospheric path. This means that the meteoroid experienced a quasi-continuous fragmentation process without suffering any sudden disruption as it penetrated denser atmospheric regions. This smooth curve can be employed to calculate the initial (pre–atmospheric) mass $m_\infty$ of the particle by means of the classical meteor luminous equation:

$$m_\infty = 2 \int_{t_e}^{t_b} \frac{I}{\tau v^2} dt, \qquad (6.7)$$

where $I$ is the time-dependent luminosity of the meteor, which is related
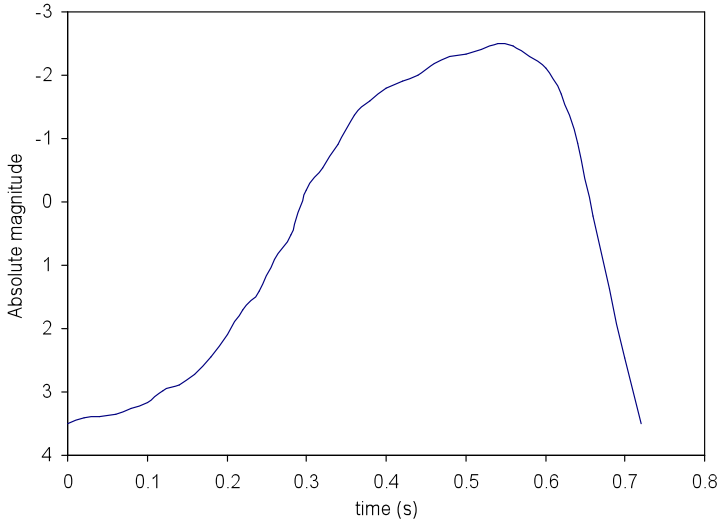
**Figure 6.12:**  Lightcurve (absolute magnitude vs. time) of the Orionid meteor analyzed in the text

to its absolute magnitude M by means of the equation

$$I = 10^{-0.4 \times M}. \tag{6.8}$$

The parameters $t_b$ and $t_e$ are the times corresponding to the beginning and the end of the luminous path, respectively, and $\tau$ is the luminous efficiency (i.e., the fraction of the kinetic energy of the meteoroid that is converted into light during the ablation process). This efficiency has been estimated by employing the relationships given by *Ceplecha and McCrosky* (1976). In this way, we have obtained that $m_\infty = 0.23 \pm 0.03$ g. If spherical shape is assumed for this particle and by taking into account the average bulk density d $= 0.9$ g cm$^{-3}$ obtained for Orionid meteoroids (*Babadzhanov and Kokhirova*, 2009), the diameter of the meteoroid yields $0.78 \pm 0.04$ cm.

243

### 6.3.5   Summary and conclusions

We have analyzed the high resolution emission spectrum of a magnitude -2.5 ± 0.5 meteor serendipitously recorded by the GRASSP instrument on the 16th of October 2014. The signal covers the wavelength range between 695 nm and 795 nm. The triangulation of the event has provided its atmospheric path and radiant, and the orbital elements of the progenitor meteoroid were also obtained. These data reveal that the particle belonged to the Orionid meteoroid stream.

In the spectrum, which has a spectral dispersion of 0.078 nm/pixel, we have identified the contributions of the atmospheric species N I, N II and O I. The emission of meteoroid species Ti I, Cr I, Fe I, Fe II, Zr I, Pd I and W I was also identified above the 2-sigma level. An upper limit temperature of around 1500 K has been obtained for the gas surrounding the meteor.

## 6.4   Observation of sprites and halos spectra

Here we present the first high spectral resolution (0.235 nm) spectra of sprites. These spectra were recorded in Europe in August and September of 2015, September to December of 2016 and during January 2017. The use of high-spectral resolution has allowed us to resolve for the first time the internal (vibro-rotational) structure of the sprite molecular $N_2$ first positive system and to quantify the local gas (rotational) temperature of the mesosphere under the influence of sprites. The temperatures of the explored region of the mesosphere range between 149 K ± 10 K and 226 K ± 20 K. The recorded spectroscopic data also provide valuable quantitative information on the concentrations of some of the vibrational levels of the $B^3\Pi_g$ electronic state of molecular nitrogen involved in transient red-near infrared optical emissions from sprites. The analysis of the recorded TLE images has enabled us to determine the elevation angle of GRASSP v2.1. With these data we could estimate the altitudes of the region of TLEs recorded with

our spectrograph (equipped with a horizontally oriented slit), ranging between 65 km and 74 km. These results have been submitted to Nature Communications.

### 6.4.1  Introduction

Soon after the publication of the first TLE images (of a sprite) in 1990 (*Franz et al.*, 1990), the interest of the international community in TLE spectroscopic features started. The simultaneous works by *Mende et al.* (1995) and *Hampton et al.* (1996) reported the first spectroscopic studies of the $N_2$ first positive band system (1PG, $B^3\Pi_g \rightarrow A^3\Sigma_u^+$) from the "body" of sprites occurring at altitudes between 70 km and 90 km. These early spectral investigations of TLEs used regular (30 fps) video recording in the visible and near infrared (NIR) spectral range (550 nm - 840 nm) and low (above 6 nm) spectral resolutions. Unfortunately, the number of spectroscopic campaigns of TLEs since the mid 1990s has been scarce. Later results by *Morrill et al.* (1998) and *Bucsela et al.* (2003) reported spectroscopic investigations of the low altitude "tendrils" (blurred motion of rapidly moving point-like structures (*Liu and Pasko*, 2005), *Stenbaek-Nielsen et al.* (2007)) of sprites at 53 km and 57 km covering from 600 nm up to 900 nm with low spectral resolutions of 7 nm and 11 nm, respectively. More recently *Kanmae et al.* (2007) reported altitude–resolved sprite spectra of the $N_2$ 1PG with an imaging (vertical) slit spectrograph within 640 nm - 820 nm with 3 ms (300 fps) temporal and $\sim$3 nm spectral resolutions.

Regarding near ultraviolet (NUV) (below 400 nm) spectra of sprites, the only measurements available to date (without correction for instrument response function) are those reported by *Heavner et al.* (2010) focusing on optical emissions of the $N_2$ second positive band system (2PG, $C^3\Pi_u \rightarrow B^3\Pi_g$) from the "body" of sprites at 65 km altitude. This NUV sprite spectrum was recorded during the EXL98 observation campaign from an aircraft at 14 km altitude and using $\sim$4 nm spectral resolution and 60 fps recording rate.

High-speed (10,000 fps) slitless spectroscopy of sprite streamer heads and column-shaped glows were reported for the first time in 2010 from aircraft observations including blue spectral features (*Kanmae et al.*, 2010a) and from ground-based facilities (*Kanmae et al.*, 2010b) with the spectra consisting only of the $N_2$ 1PG due to the atmospheric absorption of the blue component through the long line of sight.

The different types of TLEs occurring in the Earth's atmosphere from the lower stratosphere to the upper mesosphere can be considered as natural probes to learn about the properties of the middle and upper atmosphere of our planet through remote determination of key properties such as the gas temperature or the degree of excitation and ionization of atoms and molecules caused by TLEs in the atmosphere. In this regard, systematic spectroscopic campaigns of optical emissions from all sort of TLEs can allow us to remotely determine important atmospheric properties that would be difficult to obtain in other ways. Unfortunately the spectrographs used in the dispersed TLE spectroscopic campaigns carried out so far were originally designed for aurora spectroscopy (*Hallinan et al.*, 1985) and the best spectral resolution achieved to date is $\sim$3 nm that it is not enough to spectrally resolve the different low-lying vibrational transitions of the $N_2$ 1PG.

The lack of TLE spectroscopic observations with high-spectral resolution motivated us to build a TLE-dedicated instrument called *GRAnada Sprite Spectrograph and Polarimeter (GRASSP)* that incorporates a 0.235 nm resolution spectrograph (with a spectral dispersion of 0.078 nm/pixel) covering the wavelength range between 695 nm and 795 nm (*Passas et al.*, 2016b). GRASSP is in operation for ground-based systematic imaging and spectroscopic surveys of all sort of TLEs in Europe since October 2012 when the first GRASSP version (*Parra-Rojas et al.*, 2013b) was deployed in the Calar Alto Astronomical Observatory ($37°13'23''$N $2°32'45''$W) placed at 2,168 m above mean sea level in southeast Spain from where imaging of distant TLEs (*Passas et al.*, 2014) and meteor spectroscopy (*Passas et al.*, 2016a) with GRASSP were carried out. An upgraded version of GRASSP

is now available and relocated (since May 2015) in Castellgalí (Barcelona, $41°40'36''$ N $1°50'24''$ E) placed at 275 m above mean sea level and close to the Ebro valley.

As we describe below, GRASSP has allowed us to resolve for the first time the vibrational bands of $N_2$ 1PG in transient air plasma spectra generated by TLEs and to remotely determine the gas temperature in the mesosphere. Furthermore, we present quantitative measurements of the relative vibrational concentrations of the emitting electronic state $N_2(B^3\Pi_g, v)$ from carrot, single-column and column-like sprites and compare with previous measurements. Finally, we have calculated the approximate altitudes of the TLE regions whose spectra are recorded and we have correlated them with the derived gas temperatures.

### 6.4.2   2015 Data and Spectroscopic Analysis

TLE activity during the 2015 campaign was relatively high in south-western Europe. However, the number of spectra of sprites recorded with GRASSP v2.0 from Castellgalí, Spain, was low. A total of 3 spectra were recorded with the spectrograph with good signal to noise ratio (SNR), obtained from carrot and column-like sprites occurring at distances between 350 km and 800 km from the observation site. In general, spectra are only present in one frame due to the low available temporal resolution and the peaked brightness profile of sprites.

#### 6.4.2.1   August 2015

The spectrum of two distant carrot-like sprites were recorded at 01:15:26 UTC and 01:20:55 UTC, respectively, on the 24th of August 2015 over a thunderstorm in northern Italy occurred at almost 800 km distance (see figures 6.13 and 6.14). The $N_2$ 1PG (2, 0) rovibronic band spectra of these sprites were fitted with synthetic spectra following previously described procedures (*Parra-Rojas et al.*, 2013b).
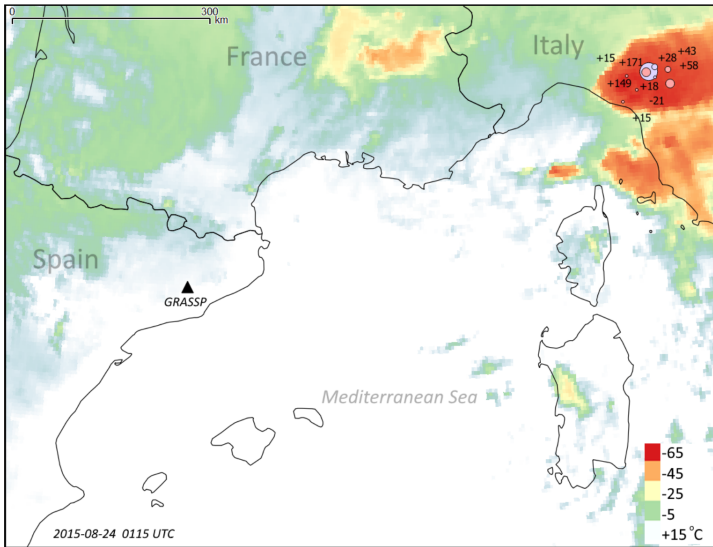
**Figure 6.13:** Location of the detected carrot-like sprites during the 2015 spectroscopic campaign, recorded on the 24th of August 2015. The location of GRASSP v2.0 in Castellgalí (black triangle) and the thunderstorm systems (reddish shadows) with the parent strokes as received by METEORAGE are shown (circles and numbers indicate the parent lightning position and corresponding peak intensities, respectively)

Figure 6.15 shows good agreement between the recorded (green line) and fitted synthetic (blue line) spectra of the two carrot sprite spectra observed at 01:15:26 UTC (left column) and 01:20:55 UTC (right column) on the 24th of August, 2015 using spectral resolutions of 0.15 nm (top), 0.20 nm (middle) and 0.24 nm (bottom). Due to the long slant path (around 800 km) the spectroscopic signal from TLEs can be strongly affected by absorption from various atmospheric constituents ($O_2$, $H_2O$, $CO_2$). To quantify this effect, we have estimated atmospheric transmittance using MODTRAN4 (*Anderson et al.*, 1993) from the visible optical range up to 2000 nm (where there is significant absorption due to water vapor) and with the observing site (Castellgalí, Spain) at only 275 m above mean sea level. All spectra shown in figure 6.15 clearly exhibit the expected three main peaks of the (2,
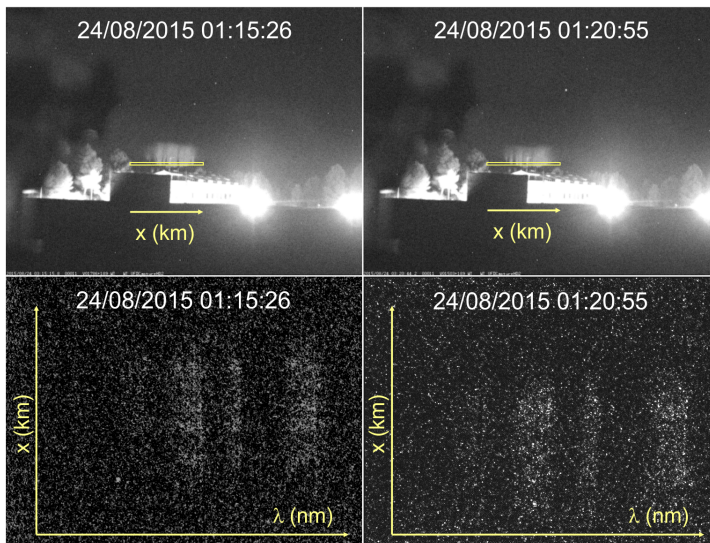
**Figure 6.14:** Scene camera images with the spectrograph slit superimposed showing sprites and their related spectra recorded at, 01:15:26 UTC on the 24th of August, 2015 (1st column) and 01:20:55 UTC on the 24th of August, 2015 (2nd column), respectively

0) band of the $N_2$ 1PG located, respectively, in the spectral positions 774.8 - 775.4 nm (band head peak), 773.5 - 774.1 and 771.0 - 771.6 nm (*Simek*, 1994). We estimated the altitude of the section of the sprite that generated the spectrum on the 24th of August 2015 at 01:15:26 UTC to range between 71.4 and 73.3 km. The parent lightning occurred at about 770 km distance, with the rotational gas temperature ($T_{rot}$) from the fitted spectra in figure 6.15 (left) being 185 K ± 10 K. Similarly, we estimated the altitude of the section of the sprite that generated the spectrum on the 24th of August 2015 at 01:20:55 UTC to range between 70.2 and 72.1 km. The parent lightning occurred at about 762 km distance, being the rotational gas temperature ($T_{rot}$) from the fitted spectra in figure 6.15 (right) 190 K ± 11 K. Figure 6.16 shows the full (green line) spectra recorded by GRASSP v2.0 and the corresponding fitted spectra (blue line) of the carrot-like sprite captured at 01:15:26 UTC on the 24th of August 2015 using spectral resolutions of 3 nm (top) and 0.45 nm (middle). The bottom panel shows a convolved spectrum (from the full recorded spectrum) with 0.45 nm resolution fitted with a synthetic spectrum (blue line) of the same spectral resolution. The gas temperatures used to generate the fitted synthetic spectra are the ones derived from the rotational fits of the (2, 0) band (see figure 6.15), that is, 185 K. The synthetic spectra are for neutral $N_2$ only and it includes six $\Delta v = 2$ rovibronic band transitions marked in the plots of the $N_2(B^3\Pi_g \rightarrow A^3\Sigma_u^+)$ electronic transition.

The spectra in figure 6.16 clearly show that 3 nm spectral resolution previously used (*Kanmae et al.*, 2007) is not sufficient to properly resolve the $(v', v'')$ rovibrational band structure.

### 6.4.2.2   September 2015

On the 28th September 2015, a close column-like sprite spectrum was recorded at 04:07:44 UTC over a thunderstorm in the south of the Balearic islands at almost 350 km from the observation site according to parent lightning location provided by LINET (see figures 6.17 and 6.18). From this capture,
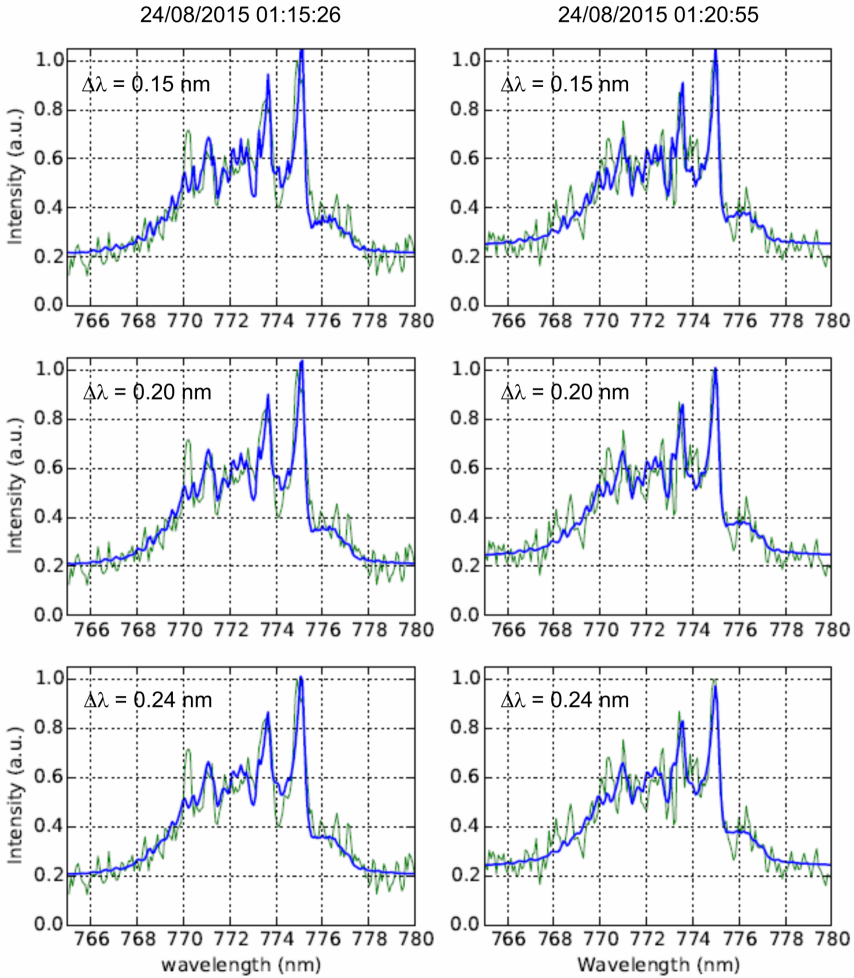
**Figure 6.15:** Spectral fitting (blue line) of recorded (green line) carrot and multi-column sprite spectra recorded at, respectively, 01:15:26 UTC on the 24th of August, 2015 (first column) and 01:20:55 UTC on the 24th August, 2015 (second column). The spectra correspond to the (2, 0) rovibronic transition of the $N_2(B^3\Pi_g \rightarrow A^3\Sigma_u^+)$ system using a spectral resolution of 0.235 nm and synthetic spectra using spectral resolutions of 0.15 nm (top), 0.20 nm (middle) and 0.24 nm (bottom)

251
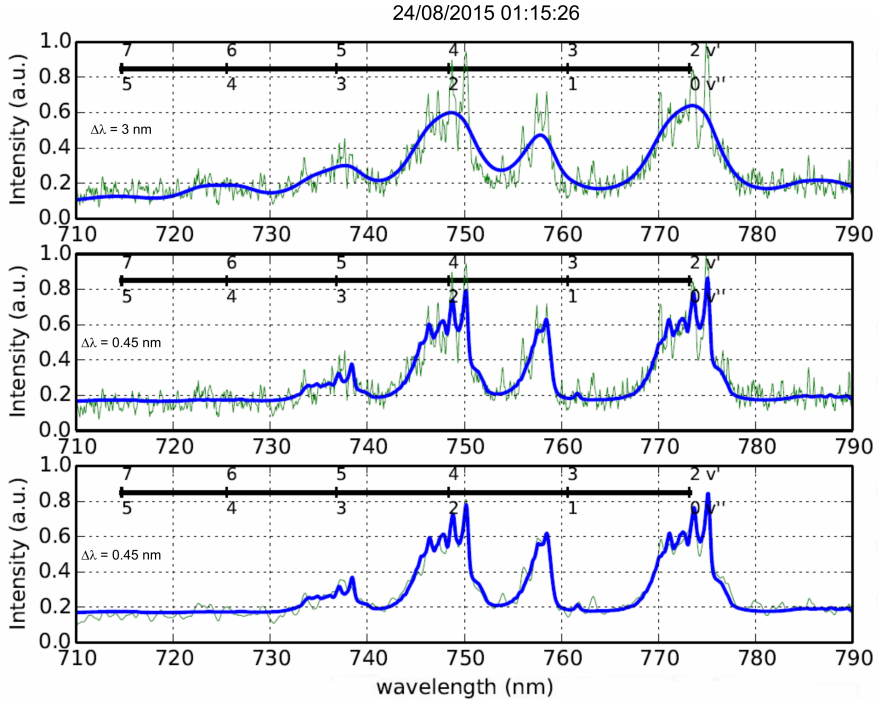
**Figure 6.16:** Spectral fitting (blue line) between 710 nm and 790 nm of the carrot sprite spectra (green line) recorded at 01:15:26 UTC on the 24th August, 2015. The upper and middle panels show the recorded spectra fitted with, respectively, 3 nm and 0.45 nm spectral resolutions. The bottom panel shows a convolved spectrum (from the full recorded spectrum) with 0.45 nm resolution fitted with a synthetic spectrum (blue line) of the same spectral resolution. The different rovibronic bands $(v', v'')$ of the $N_2(B^3\Pi_g \rightarrow A^3\Sigma_u^+)$ system are marked. All plots use $T_{rot} = 185$ K extracted from previous rotational fitting of the $(2, 0)$ band (see figure 6.15). The original recorded spectra is normalized to the $(2, 0)$ band head peak (774.8 nm - 775.4 nm). Notice that 3 nm spectral resolution previously used (*Kanmae et al.*, 2007) is not sufficient to properly resolve the $(v', v'')$ rovibrational band structure

we obtained a total of four different spectra simultaneously, corresponding to four different columns of the sprite. Unfortunately, only two of them showed a good SNR. We called these two good-SNR spectra as *Bottom* and *Up* as their positions in the iCCD spectral image (see figure 6.18).
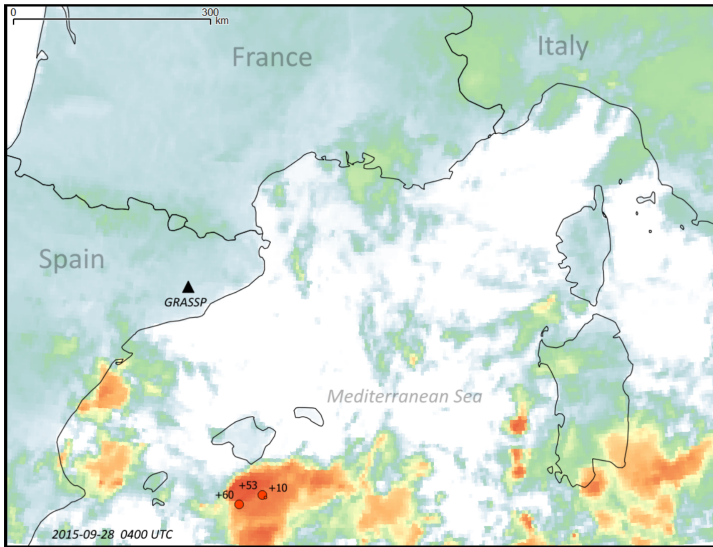


**Figure 6.17:** Location of the detected carrot-like sprites during the 2015 spectroscopic campaign, recorded on the 28th September 2015. The location of GRASSP v2.0 in Castellgalí (black triangle) and the thunderstorm systems (reddish shadows) with the parent strokes as received by METEORAGE are shown (circles and numbers indicate the parent lightning position and corresponding peak intensities, respectively)

Figure 6.19 shows the two good-SNR spectra of this multi-column sprite between 765 nm and 780 nm. In particular, recorded (green line) spectra of the so-called *Bottom* (first column) and *Up* (second column) sections of the multi-column sprite are represented together with the corresponding fitted (blue line) spectra using spectral resolutions of 0.15 nm (top), 0.20 nm (middle) and 0.24 nm (bottom). The recorded spectra are a bit noisier (specially the spectrum of the *Up* section) than the ones of the carrot sprites

253
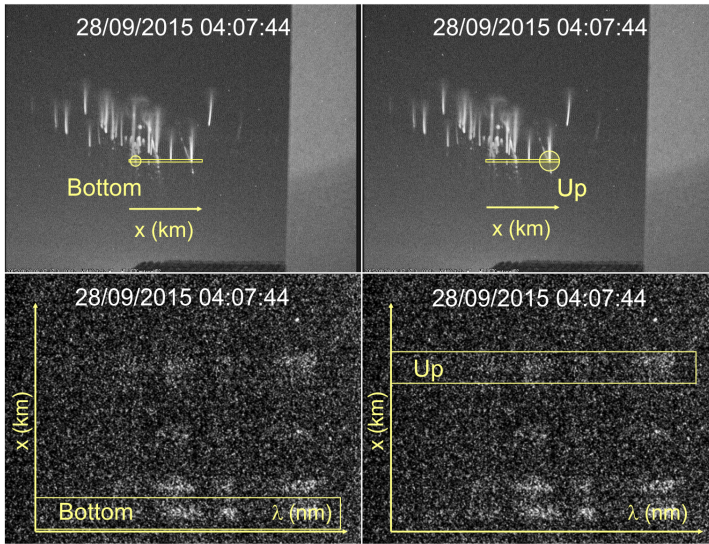
**Figure 6.18:** Scene camera image with the spectrograph slit superimposed showing sprites and their related spectrum recorded at 04:07:44 UTC on the 28th September 2015

recorded in August 2015 because the available optical signal is weaker. We estimated the altitude of the section of the sprite that generated the spectrum to range between 65.9 and 66.8 km. Even though, the spectral fit of the (2, 0) rovibronic transition in the recorded multi-column spectra remains quite reasonable with clear visibility of the three main peaks of the (2, 0) band of the $N_2$ 1PG. The rotational gas temperatures ($T_{rot}$) derived from the synthetic spectra fitting to single-column spectra shown in figure 6.19 are 149 K $\pm$ 10 K (*Bottom* section - first column) and 210 K $\pm$ 24 K (*Up* section - second column).

Figure 6.20 shows the full (green line) spectra recorded by GRASSP v2.0 and the corresponding fitted spectra (blue line) of the column-like sprite captured at 04:07:44 UTC on the 28th September 2015 using spectral resolutions of 3 nm (top) and 0.45 nm (middle). The bottom panel shows a convolved spectrum (from the full recorded spectrum) with 0.45 nm resolution fitted with a synthetic spectrum (blue line) of the same spec-

tral resolution. The gas temperatures used to generate the fitted synthetic spectra are the ones derived from the rotational fits of the (2, 0) band. The synthetic spectra are for neutral $N_2$ only and it includes six $\Delta v = 2$ rovibronic band transitions marked in the plots of the $N_2(B^3\Pi_g \rightarrow A^3\Sigma_u^+)$ electronic transition.

### 6.4.3    2016 and Early 2017 Data and Spectroscopic Analysis

The TLE spectroscopic campaigns during 2016 and January 2017 were more fruitful than the one of 2015. GRASSP v2.1 recorded a total of 41 events up to the end of January 2017. The spectra belonged to carrot and column-like sprite as well as to precursory halos to some of the detected sprites. Only the most significant results are shown.

#### 6.4.3.1    September 2016

We recorded six sprite spectra between 14th - 15th of September, 2016 over southeastern France (area around 4-8°E and 43-46°N). Figure 6.21 shows the related thunderstorm and figure 6.22 shows the scene camera images of the four best SNR spectra.

Figure 6.23 shows the spectral fitting (blue line) of TLEs recorded spectra (green line) at 23:47:20 UTC on the 14th of September, 2016 (halo - top left), 23:55:35 UTC on the 14th of September, 2016 (multi-column carrot sprite - top right), 01:12:59 UTC on the 15th of September, 2016 (carrot sprite - bottom left) and 01:16:38 UTC on the 15th of September, 2016 (carrot sprite - bottom right). The spectra correspond to the (2, 0) rovibronic transition of the $N_2(B^3\Pi_g \rightarrow A^3\Sigma_u^+)$ system using spectral resolutions of 0.235 nm. In all these spectra the three main peaks of the (2, 0) band of the $N_2$ 1PG are distinctly visible.

We estimated the altitudes of the section of the halo and sprite that generated the spectra on the 14th of September 2016 at 23:47:20 UTC and

23:55:35 UTC to range from 74.4 to 75.7 km and from 70.2 to 71.4 km, respectively. The related storm occurred at about 400 km distance, and we estimated the rotational temperature from the fitting of figure 6.23 to be 129 K and 175 K, respectively.

We also estimated the altitudes of the section of the carrot sprites that generated the spectra on the 15th of September 2016 at 01:12:59 UTC and 01:16:38 UTC to range from 72.2 to 73.5 km and from 72.7 to 74.1 km, respectively. The related storm occurred at about 540 km distance, and we estimated the rotational temperature from the fitting of figure 6.23 to be 154 K and 210 K, respectively. Figures 6.24, 6.25, 6.26 and 6.27, show the spectral fitting between 710 nm and 790 nm of the spectra in figure 6.23. The top and bottom panels show the recorded spectra fitted with, respectively, 3 nm and 0.24 nm spectral resolutions. The different rovibronic bands ($v'$, $v''$) of the $N_2(B^3\Pi_g \to A^3\Sigma_u^+)$ system are marked. All plots use the $T_{rot}$ extracted from previous rotational fitting of the (2, 0) band (see figure 6.23). Again, the spectra in top panels of figures 6.24, 6.25, 6.26 and 6.27, clearly show that 3 nm spectral resolution previously used (*Kanmae et al.*, 2007) is not sufficient to properly resolve the ($v'$, $v''$) rovibrational band structure. A considerable improvement is obtained when the observed spectra is fitted with a synthetic spectrum of 0.24 nm spectral resolution.
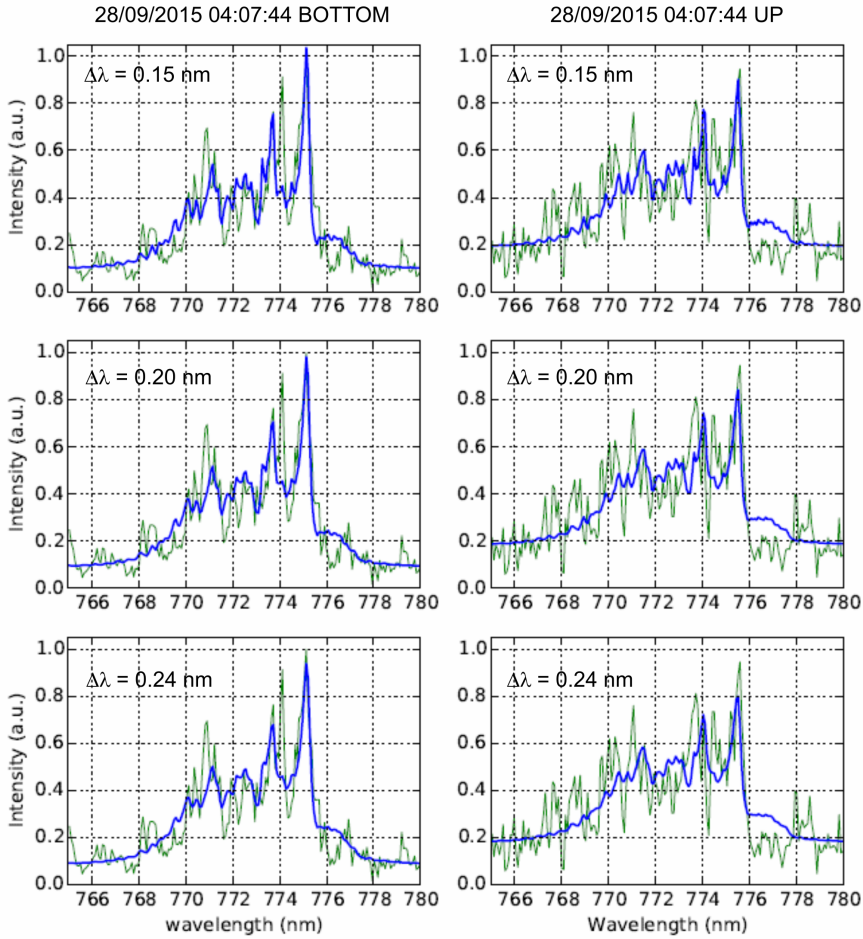
**Figure 6.19:** Spectral fitting (blue line) of recorded (green line) multi-column sprite spectra recorded at, 04:07:44 UTC on September 28, 2015 (*Bottom* - first column; *Up* - second column). The spectra correspond to the (2, 0) rovibronic transition of the $N_2(B^3\Pi_g \rightarrow A^3\Sigma_u^+)$ system using a spectral resolution of 0.235 nm and synthetic spectra using spectral resolutions of 0.15 nm (top), 0.20 nm (middle) and 0.24 nm (bottom)

257
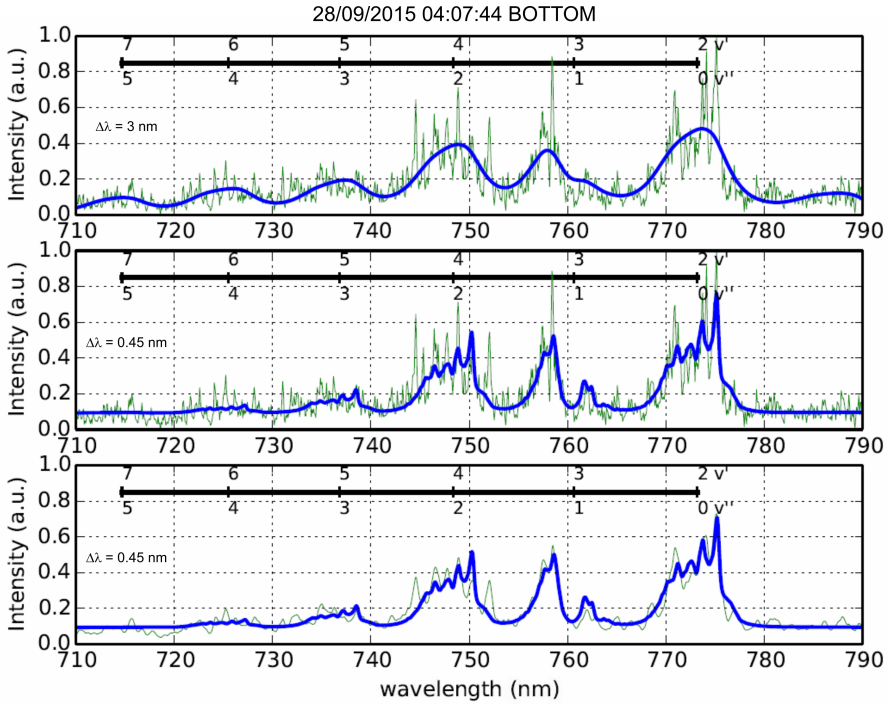
**Figure 6.20:** Spectral fitting (blue line) between 710 nm and 790 nm of the *Bottom* region of the multi-column sprite spectra (green line) recorded at 04:07:44 UTC on the 28th September 2015. The upper and middle panels show the recorded spectra fitted with, respectively, 3 nm and 0.45 nm spectral resolutions. The bottom panel shows a convolved spectrum (from the full recorded spectrum) with 0.45 nm resolution fitted with a synthetic spectrum (blue line) of the same spectral resolution. The different rovibronic bands ($v'$, $v''$) of the $N_2(B^3\Pi_g \to A^3\Sigma_u^+)$ system are marked. All plots use $T_{rot} = 149$ K extracted from previous rotational fitting of the (2, 0) band (see left column of figure 6.19). The original recorded spectra (green line - top and middle panels) is normalized to the (2, 0) band head peak (774.8 nm - 775.4 nm). Notice that 3 nm spectral resolution previously used (*Kanmae et al.*, 2007) is not sufficient to properly resolve the ($v'$, $v''$) rovibrational band structure
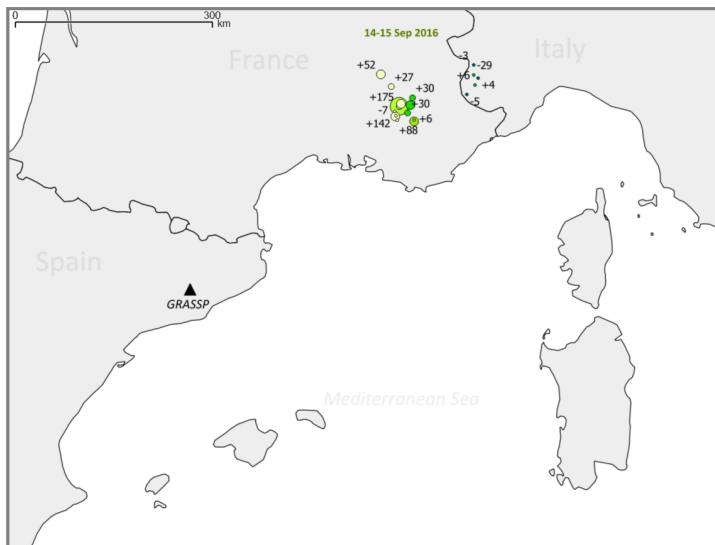
**Figure 6.21:** Location of the parent lightning of detected TLEs between 14th-15th of September, 2016 over southeastern France (area around 4-8°E and 43-46°N) with the parent strokes as received by METEORAGE (circles and numbers indicate the parent lightning position and corresponding peak intensities, respectively). The black triangle indicates the location of GRASSP in Castelgallí

**Figure 6.22:** Scene camera images (with the spectrograph slit superimposed) of TLEs detected between 14th - 15th September, 2016
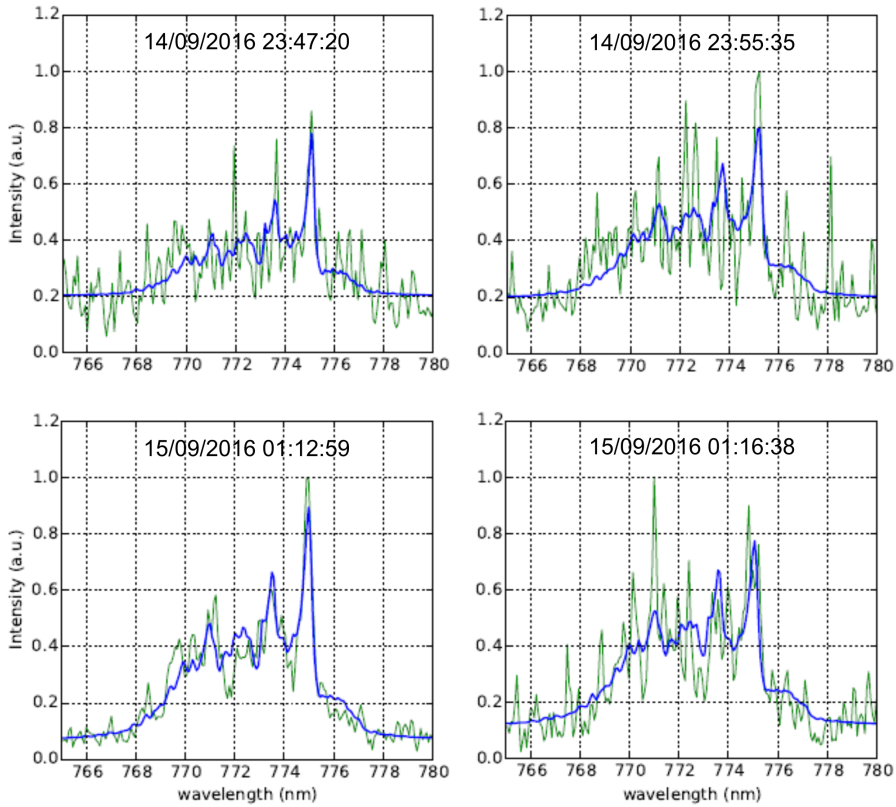
**Figure 6.23:** Spectral fitting (blue line) of recorded spectra (green line) of sprites and sprite halos on 14-15 September, 2016. The spectra correspond to the (2, 0) rovibronic transition of the $N_2(B^3\Pi_g \rightarrow A^3\Sigma_u^+)$ system using spectral resolutions of 0.24 nm (for sprites) and 0.18 nm (for halo - top left)
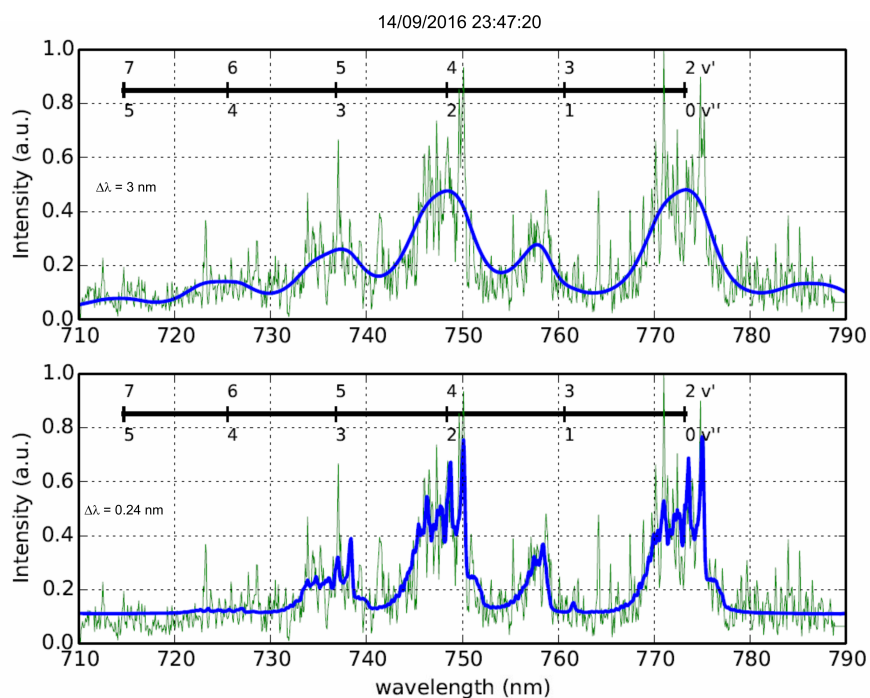
**Figure 6.24:** Spectral fitting (blue line) between 710 nm and 790 nm of the halo spectrum (green line) recorded at 23:47:20 UTC on the 14th of September, 2016. The top and bottom panels show the recorded spectra fitted with, respectively, 3 nm and 0.24 nm spectral resolutions. The different rovibronic bands $(v', v'')$ of the $N_2(B^3\Pi_g \rightarrow A^3\Sigma_u^+)$ system are marked. All plots use $T_{rot} = 129$ K extracted from previous rotational fitting of the (2, 0) band (see figure 6.23)
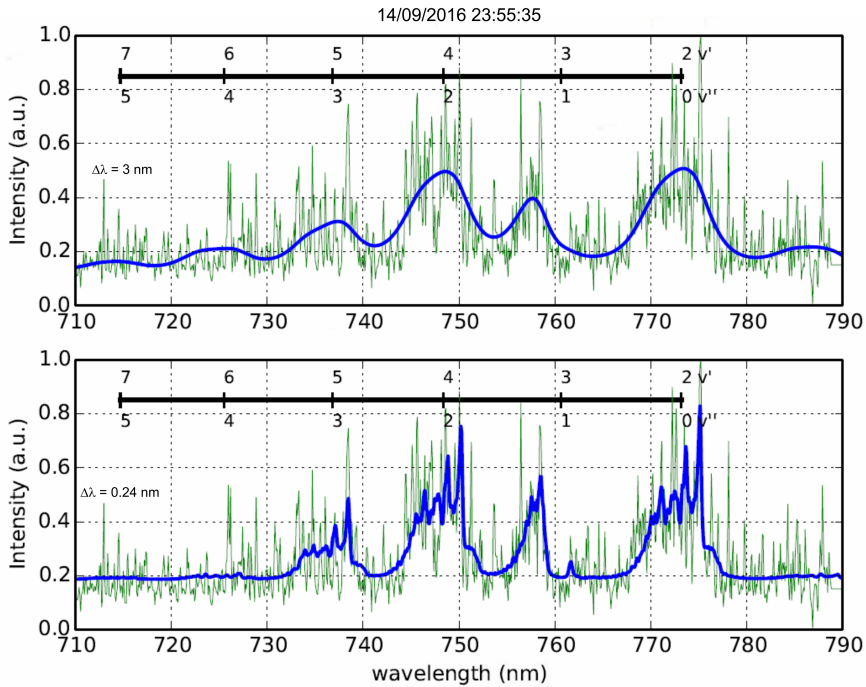
**Figure 6.25:** Spectral fitting (blue line) between 710 nm and 790 nm of the carrot sprite spectrum (green line) recorded at 23:55:35 UTC on the 14th of September, 2016. The top and bottom panels show the recorded spectra fitted with, respectively, 3 nm and 0.24 nm spectral resolutions. The different rovibronic bands $(v', v'')$ of the $N_2(B^3\Pi_g \rightarrow A^3\Sigma_u^+)$ system are marked. All plots use $T_{rot} = 175$ K extracted from previous rotational fitting of the (2, 0) band (see figure 6.23)
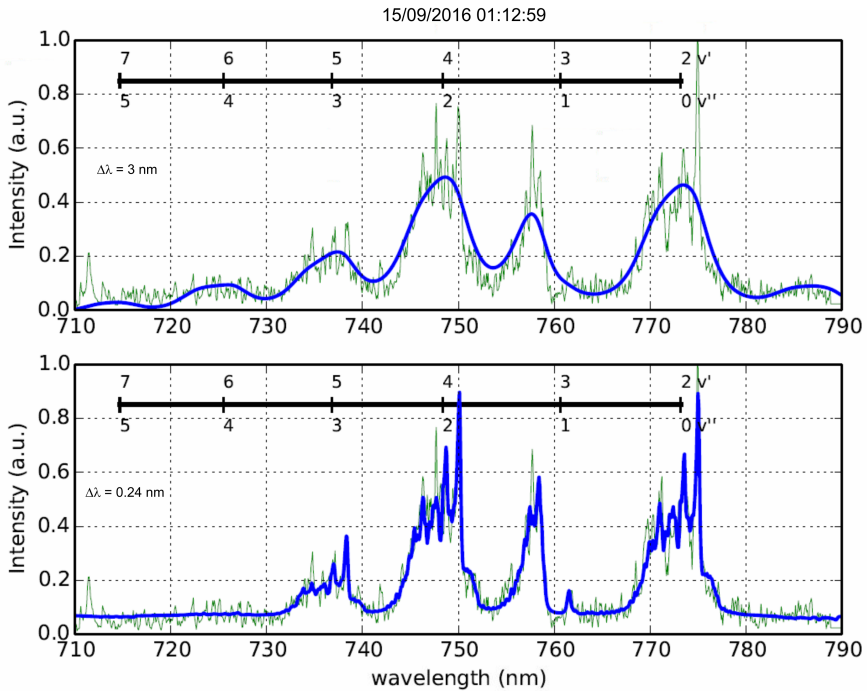
**Figure 6.26:** Spectral fitting (blue line) between 710 nm and 790 nm of the carrot sprite spectrum (green line) recorded at 01:12:59 UTC on the 15th of September, 2016. The top and bottom panels show the recorded spectra fitted with, respectively, 3 nm and 0.24 nm spectral resolutions. The different rovibronic bands $(v^{'}, v^{''})$ of the $N_2(B^3\Pi_g \rightarrow A^3\Sigma_u^+)$ system are marked. All plots use $T_{rot} = 154$ K extracted from previous rotational fitting of the $(2, 0)$ band (see figure 6.23)
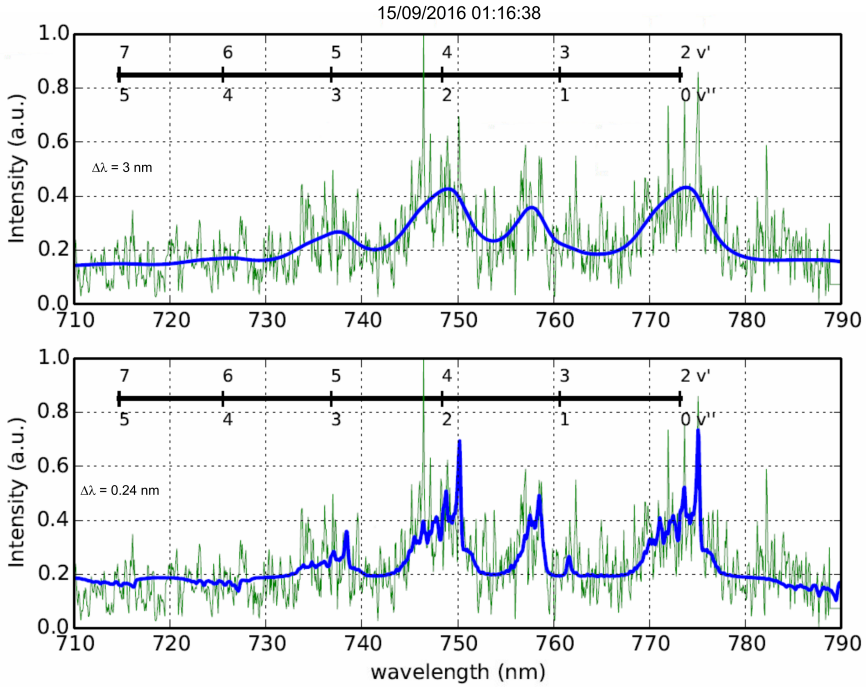
**Figure 6.27:** Spectral fitting (blue line) between 710 nm and 790 nm of the carrot sprite spectrum (green line) recorded at 01:16:38 UTC on the 15th of September, 2016. The top and bottom panels show the recorded spectra fitted with, respectively, 3 nm and 0.24 nm spectral resolutions. The different rovibronic bands $(v', v'')$ of the $N_2(B^3\Pi_g \to A^3\Sigma_u^+)$ system are marked. All plots use $T_{rot} = 210$ K extracted from previous rotational fitting of the (2, 0) band (see figure 6.23)

### 6.4.3.2 October 2016

Two carrot sprite spectra were recorded on the 21st of October, 2016 over east of Menorca island (Spain) at 01:24:19 UTC and 01:37:01 UTC. Figure 6.28 shows the location of the parent thunderstorm related to them. Figure 6.29 shows the scene image of the sprite recorded on October 21, 2016 at 01:24:19 UTC (left) and the synthetic fit of the (2, 0) band (blue solid line - right) using a spectral resolution of 0.24 nm that allows us to extract the rotational temperature superimposed to the recorded spectrum related to the upper glow region of the carrot sprite (green solid line - right). Unfortunately, none of these events showed a good SNR to properly fit the band between 710 and 790 nm.
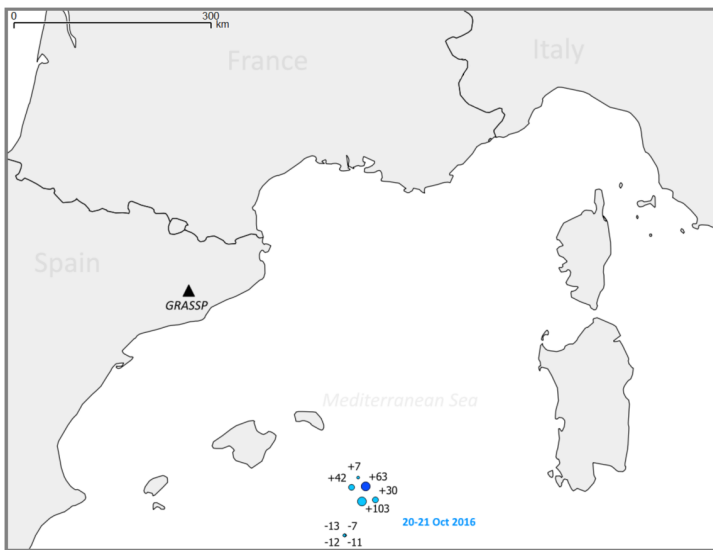


**Figure 6.28:** Location of the parent lightning of detected sprites and sprite halos on the 21st of October, 2016 over southeastern Balearic islands (area around 4-8°E and 43-46°N) with the parent strokes as received by METEOR-AGE are shown (circles and numbers indicate the parent lightning position and corresponding peak intensities, respectively). The black triangle indicates the location of GRASSP in Castelgallí
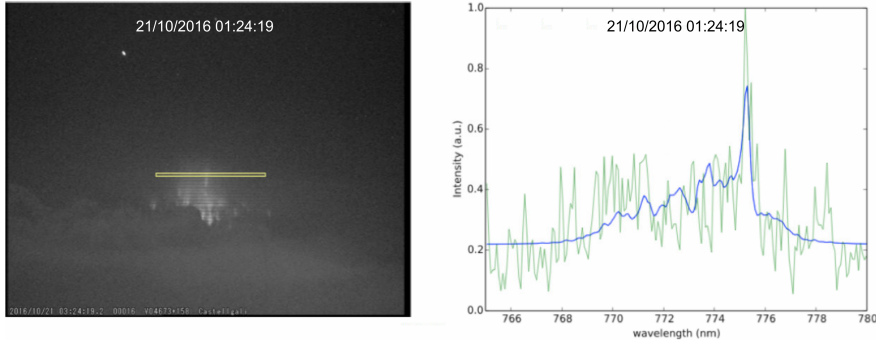
**Figure 6.29:** Scene camera image (left) (with spectrograph slit superimposed) and associated time integrated (40 ms) recorded spectrum (green solid line - right) and synthetic fit (blue solid line - right - using a spectral resolution of 0.24 nm) of the upper glow region of a carrot sprite detected by GRASSP at 01:24:19 UTC on the 21st of October, 2016

### 6.4.3.3    November 2016

A total of 19 sprite spectra were recorded in November 2016. However, only some of them showed good SNR.

The spectrum of a cluster of columniform sprites was recorded on the 16th of November, 2016 over southeastern Balearic islands (Spain) at 02:23:07 UTC. Figure 6.30 shows the location of the parent thunderstorm related to them. Figure 6.31 shows the scene image of the sprite recorded on the 16th of November at 02:23:07 UTC (left) and the synthetic fit of the (2, 0) band (blue solid line - right) using a spectral resolution of 0.24 nm that allows us to extract the rotational temperature superimposed to the recorded spectrum related to the upper glow region of the carrot sprite (green solid line - right). We estimated the altitude of the section of cluster of columniform sprites that generated the spectra on the 16th of November 2016 at 02:23:07 UTC to range from 70.4 to 71.5 km. The related storm occurred at about 470 km distance, and we estimated the rotational temperature from the fitting of figure 6.23 to be 164 K.
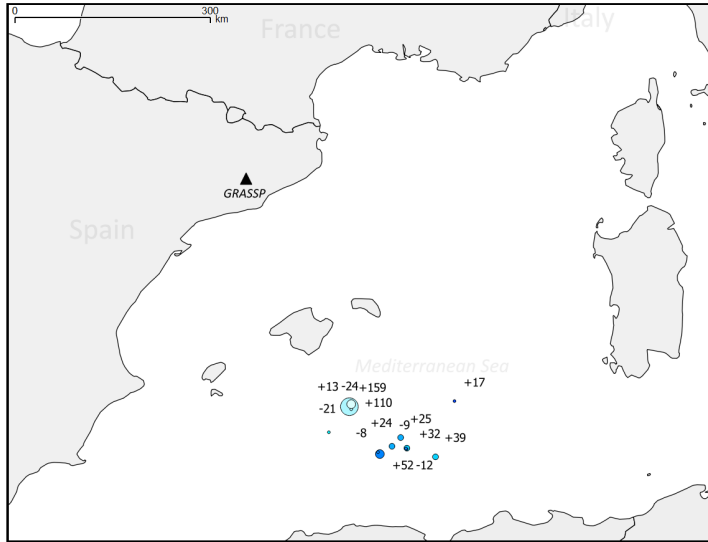
**Figure 6.30:** Location of the parent lightning of detected sprites on the 16th of November, 2016 over southeastern Balearic islands with the parent strokes as received by METEORAGE are shown (circles and numbers indicate the parent lightning position and corresponding peak intensities, respectively). The location of GRASSP in Castelgallí is indicated with a black triangle

Figure 6.32 shows the spectral fitting (blue line) between 710 nm and 790 nm of the spectra in figure 6.31 with 0.24 nm spectral resolution. The different rovibronic bands ($v'$, $v''$) of the $N_2(B^3\Pi_g \rightarrow A^3\Sigma_u^+)$ system are marked. The plot uses the $T_{rot}$ extracted from previous rotational fitting of the (2, 0) band (see figure 6.31).

#### 6.4.3.4   December 2016

A total of 11 sprite spectra were recorded in December 2016. Unfortunately, none of them showed good signal to noise ratio to estimate the rotational temperature of the mesosphere surrounding the TLEs.

Figure 6.33 shows two storm clusters between Valencia and Mallorca island (Spain) the night between 18th and 19th of December, 2016. Figure 6.34 shows the scene camera images (with the spectrograph slit superim-
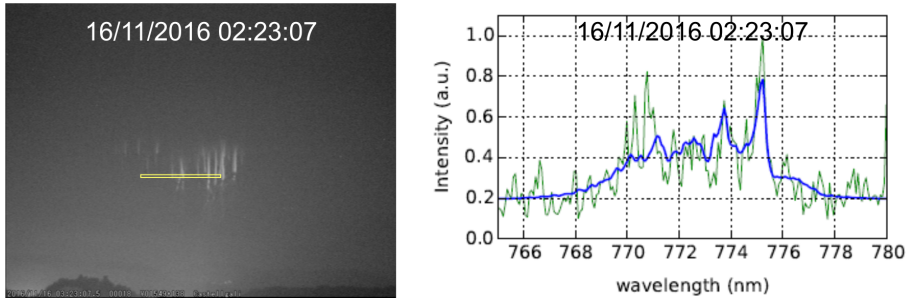
**Figure 6.31:** Scene camera image (left) (with spectrograph slit superimposed) and associated time integrated (40 ms) recorded spectrum (green solid line - right) and synthetic fit (blue solid line - right - using a spectral resolution of 0.24 nm) of the upper glow region of a carrot sprite detected by GRASSP at 02:23:07 UTC on the 16th of November, 2016
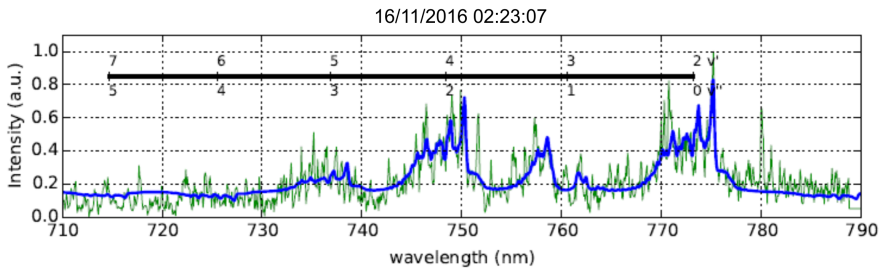


**Figure 6.32:** Spectral fitting (blue line) between 710 nm and 790 nm of the spectrum of the cluster of columniform sprites (green line) recorded at 02:23:07 UTC on the 16th of November, 2016 fitted with 0.24 nm spectral resolution. The different rovibronic bands $(v', v'')$ of the $N_2(B^3\Pi_g \rightarrow A^3\Sigma_u^+)$ system are marked. All plots use $T_{rot} = 164$ K extracted from previous rotational fitting of the (2, 0) band (see figure 6.31)

posed) of a sequential set of carrot and multi-column sprites detected at, respectively, 19:34:49 UTC on the 18th of December, 2016 (first row - left), 21:22:55 UTC on December 18, 2016 (firt row - right), 03:15:05 UTC on December 19, 2016 (second row - left), 04:08:18 UTC on December 19, 2016 (second row - right), 04:17:35 UTC on the 19th of December, 2016 (third row - left) and 04:50:11 UTC on the 19th of December, 2016 (third row - right).
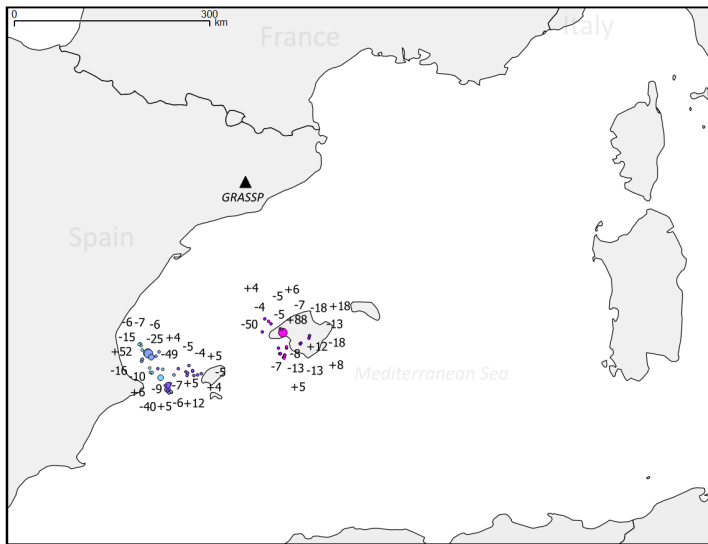


**Figure 6.33:** Location of the parent lightning of detected sprites between 18th and 19th of December, 2016 between Valencia and Mallorca island (Spain), as received by METEORAGE. The black triangle indicates the location of GRASSP in Castelgallí
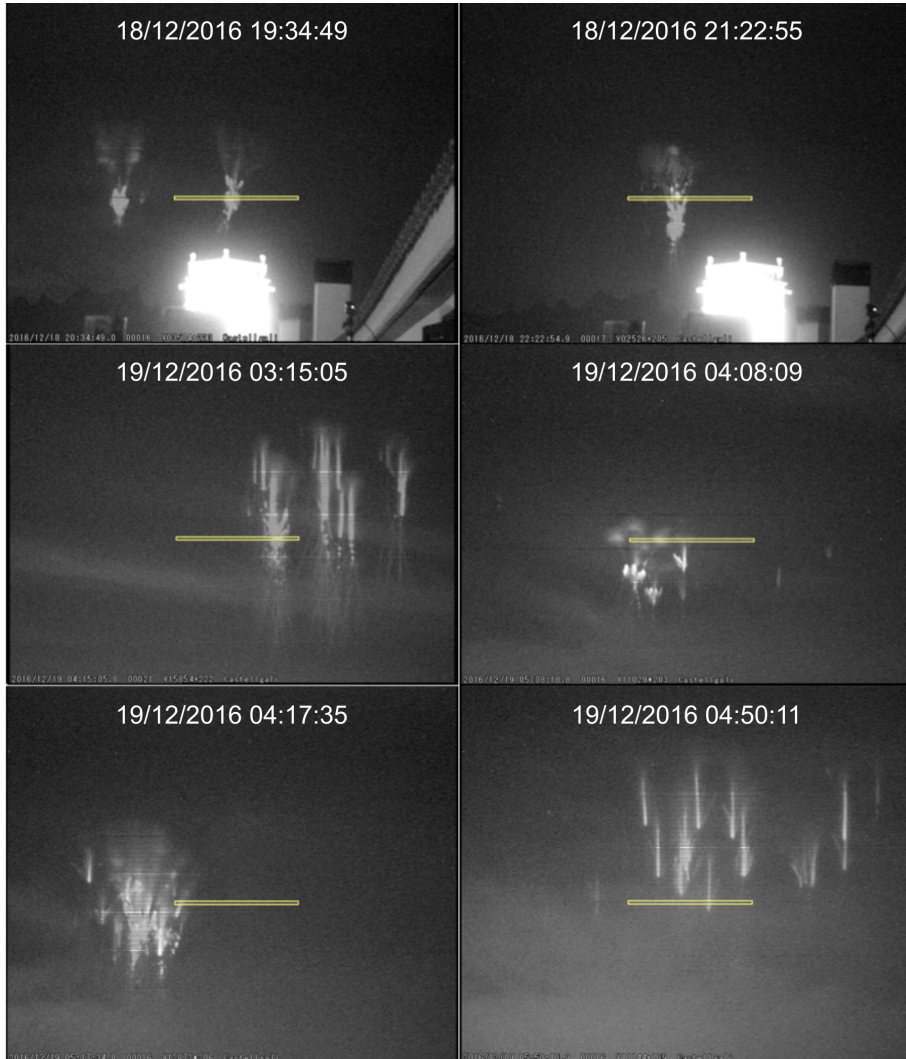
**Figure 6.34:** Scene camera images (with spectrograph slit superimposed) of a sequential set of carrot and multi-column sprites detected at, respectively, 19:34:49 UTC on the 18th of December, 2016 (first row - left), 21:22:55 UTC on the 18th of December, 2016 (firt row - right), 03:15:05 UTC on the 19th of December, 2016 (second row - left), 04:08:18 UTC on the 19th of December, 2016 (second row - right), 04:17:35 UTC on the 19th of December, 2016 (third row - left) and 04:50:11 UTC on the 19th of December, 2016 (third row - right)

#### 6.4.3.5  January 2017

Ten sprite spectra were recorded on the 17th of January, 2017. The related thunderstorm occurred over northern Algeria, as seen in figure 6.35. Two of them showed good SNR to estimate the rotational temperature of the mesosphere surrounding the TLE.

The first column of figure 6.36 shows the scene images of the sprites recorded at 23:37:52 UTC on the 17th of January, 2017 (first row - left), and 23:40:34 UTC on the 17th of January, 2017 (second row - left). The second column of figure 6.36 shows the recorded spectra related to these sprites (green solid line - right), and the synthetic fits of the (2, 0) band (blue solid line - right) using a spectral resolution of 0.24 nm that allows us to extract the rotational temperature of the plasmas.

We estimated the altitudes of the section of sprites that generated the spectra on the 17th of January, 2017 to range from 71.5 to 72.9 km and from 61.2 to 62.5 km, respectively. The parent lightning occurred at about 520 km and 460 km distance, respectively (data provided by AEMET).

The rotational gas temperatures ($T_{rot}$) derived from the 2017 fitted spectra in figure 6.36 are 226 K $\pm$ 17 K and 201 K $\pm$ 20 K, respectively. The calculated uncertainties of the derived gas temperatures correspond to the standard deviation $\sigma$ (square root of the variance) obtained from the numerical least-square fitting of synthetic spectra to the recorded spectra. These estimated uncertainties are probably underestimating the real error.

Figure 6.37 shows the full (green line) spectra recorded by GRASSP and the corresponding fitted spectra (blue line) of the multi-column sprites at 23:40:35 UTC on the 17th of January, 2017. The fitted spectra used a spectral resolution of 0.24 nm.
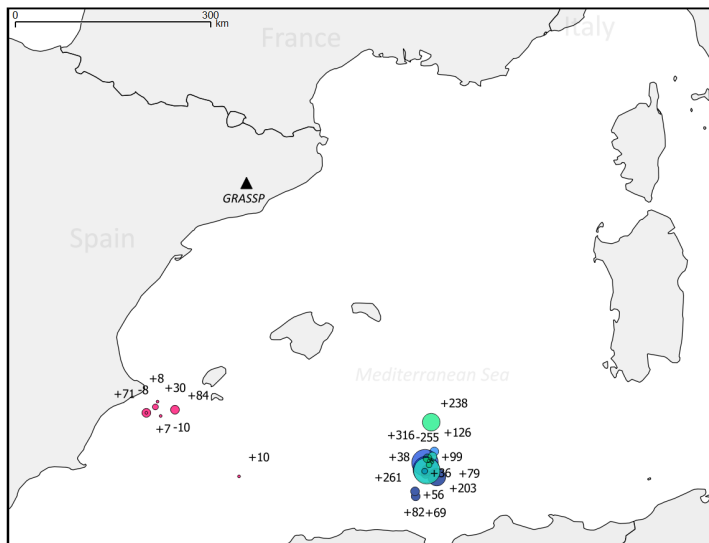
**Figure 6.35:** Location of the parent lightning of detected sprites between the 17th and the 18th January, 2017 between Valencia and Formentera island (Spain) and over northern Algeria, as received by AEMET. The black triangle indicates the location of GRASSP in Castelgallí
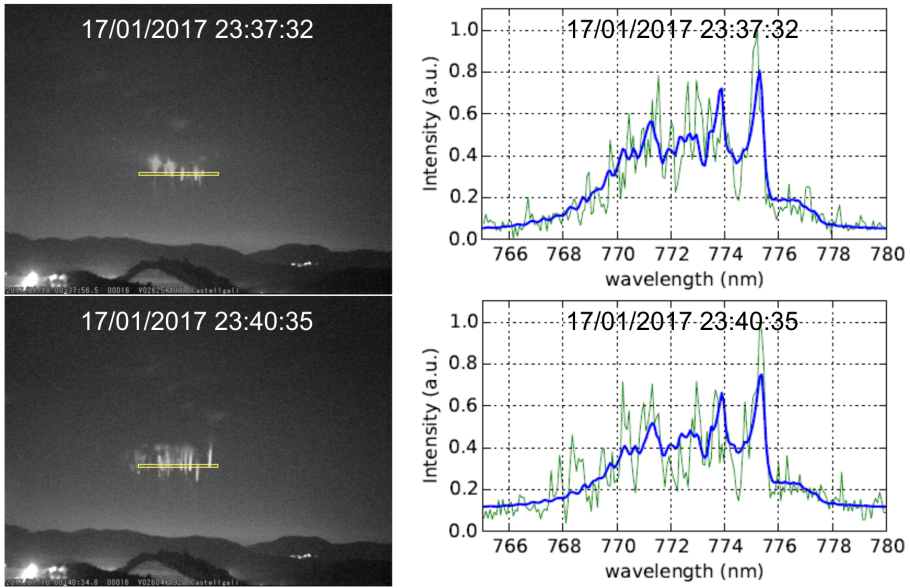
**Figure 6.36:** Scene images of the sprites recorded at 23:37:52 UTC on the 17th of January, 2017 (first row - left), and 23:40:34 UTC on the 17th of January, 2017 (second row - left). The second column shows the recorded spectra related to these sprites (green solid line - right), and the synthetic fits of the (2, 0) band (blue solid line - right) using a spectral resolution of 0.24 nm that allows us to extract the rotational temperature of the plasmas
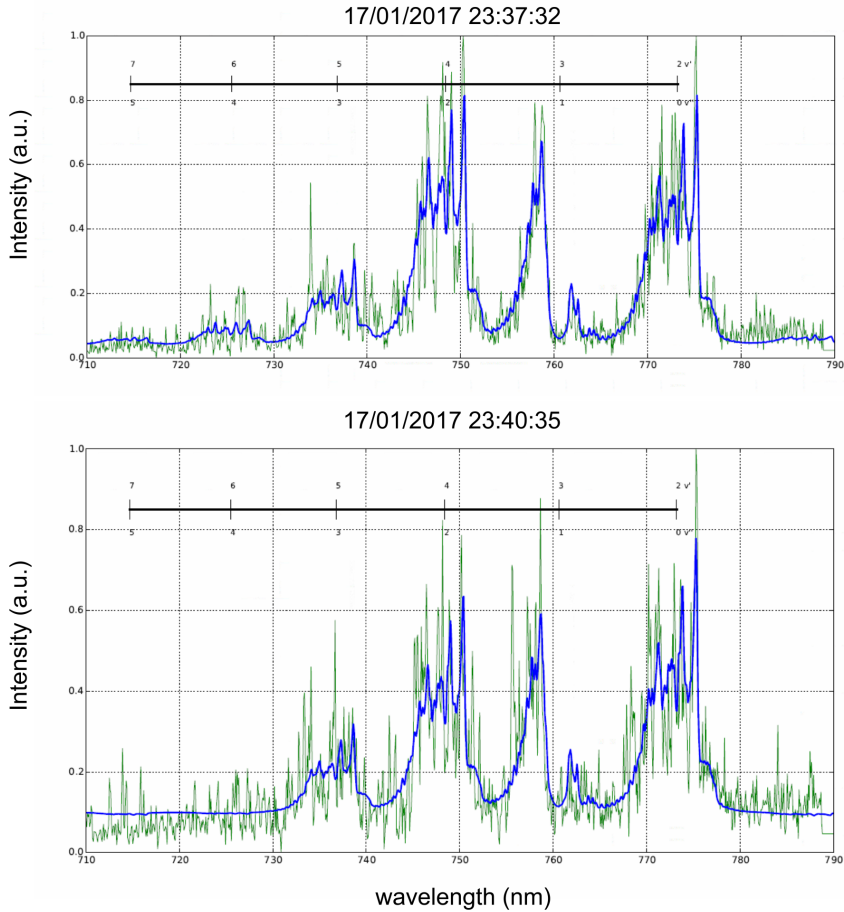
**Figure 6.37:** Spectral fitting (blue line) between 710 nm and 790 nm of the spectrum of the cluster of columniform sprites (green line) recorded at 23:37:32 UTC (top panel) and 23:40:34 UTC (bottom panel)on the 17th of January, 2017 fitted with 0.24 nm spectral resolution. The different rovibronic bands $(v', v'')$ of the $N_2(B^3\Pi_g \to A^3\Sigma_u^+)$ system are marked. The plots use $T_{rot} = 226$ K (top panel) and $T_{rot} = 201$ K (bottom panel) extracted from previous rotational fitting of the (2, 0) band (see figure 6.36)

275

### 6.4.4 Discussion

Sprite spectra recorded with GRASSP during the spectroscopic campaigns of 2015, 2016 and January 2017 from Spain are the first high resolution spectra ($< 0.5$ nm) of TLEs to date.

The spectral resolution used (0.235 nm) has allowed us to resolve the rovibrational structure of $\Delta v = 2$ bands of the $N_2$ 1PG within the explored spectral range (695 - 795 nm) from an almost sea level (275 m) observation site.

Figure 6.38 shows the different morphologies of recorded sprites covering a range of altitudes between 61.2 - 62.5 km (lower region of a multi-column sprite detected at 23:40:35 UTC on January 17, 2017 - see 4th row right of figure 6.38) and 71.5 - 72.9 km of the column sprite detected at 23:37:32 UTC on January 17, 2017 - see 4th row left of figure 6.38).

We captured high resolution spectra of full carrot sprites, single-column sprites (see yellow circles in the second row of figure 6.38) as well as multi-column sprites.

Figure 6.39 shows high resolution spectra of the (2, 0) band of the $N_2$ 1PG associated to each of the sprites in figure 6.38. We can see that the (2, 0) band is well resolved and that the spectra with the best signal to noise ratio (SNR) correspond to carrot sprites since they produce higher and more uniform optical signal in the spectrograph slit than the narrow regions of the recorded single and multi-column sprites. Contrarily to the assumed rotational (gas) temperatures reported in previous low resolution sprite spectra (*Mende et al.*, 1995; *Hampton et al.*, 1996), (*Kanmae et al.*, 2007), our high-resolution TLE spectroscopic campaigns have allowed us to extract the rotational temperature from the fitting shown in figure 6.39 of the recorded and synthetic spectra of the $N_2$ 1PG (2, 0) band. The calculation of the altitudes of the detected events make sprites a useful natural thermal probe of the mesosphere.
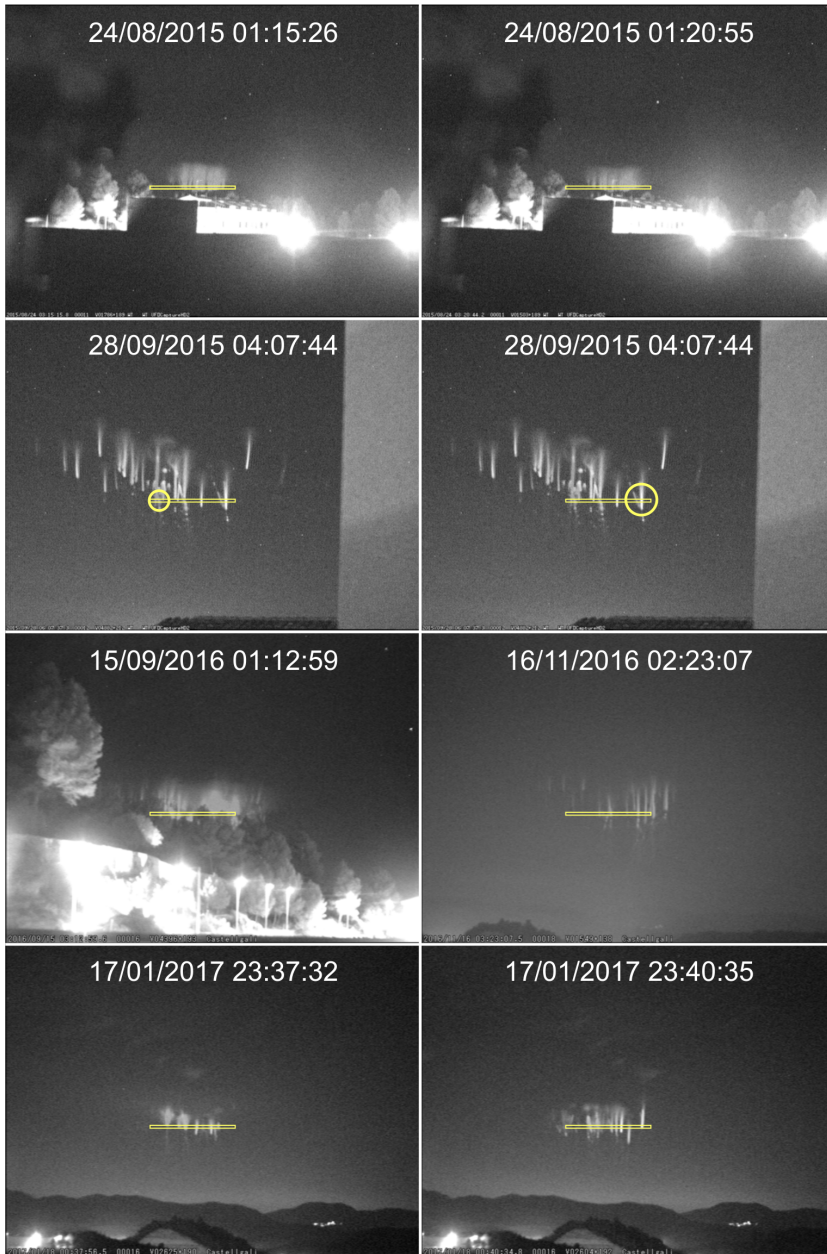
**Figure 6.38:** Scene camera images with the spectrograph slit superimposed showing sprites recorded on, respectively, August 24, 2015 (1st row), September 28, 2015 (2nd row), September 15, 2016 (3rd row left), November 16, 2016 (3rd row right), January 17, 2017 (4th row)

277
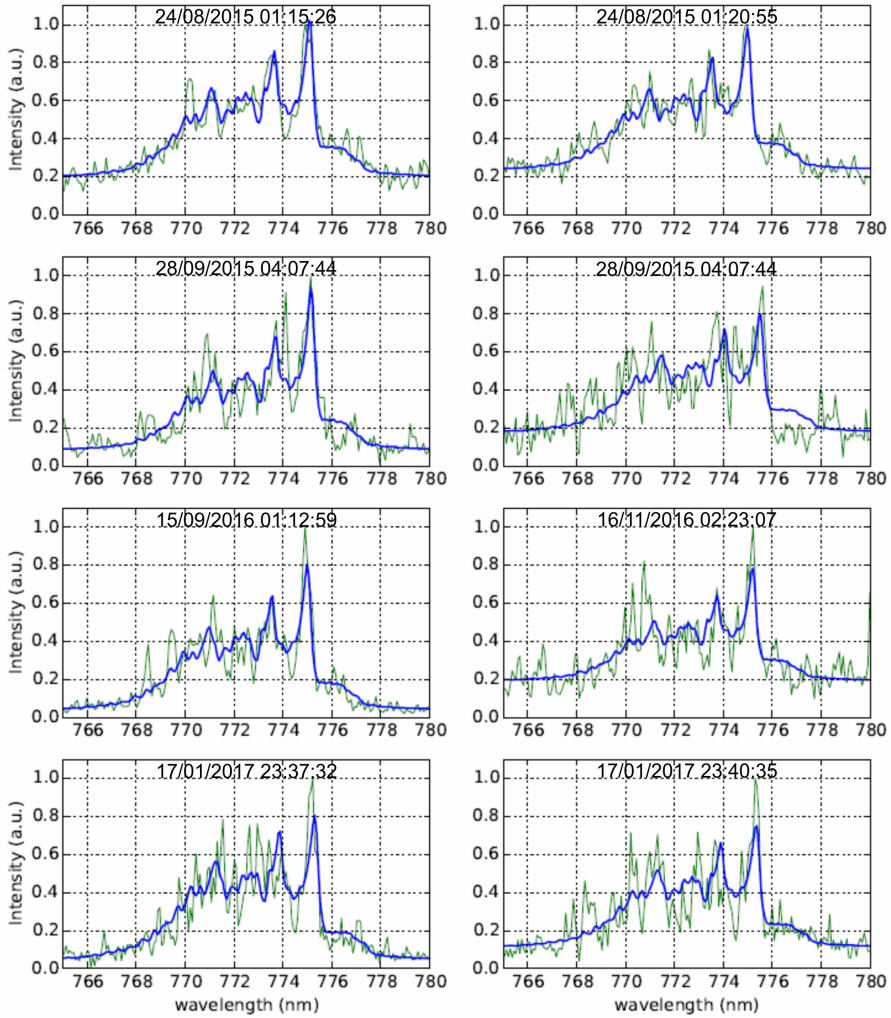
**Figure 6.39:** Spectral fitting (blue line) of recorded (green line) carrot and multi-column sprite spectra which images are shown in Fig. 6.38. The spectra correspond to the $(2, 0)$ rovibronic transition of the $N_2(B^3\Pi_g \to A^3\Sigma_u^+)$ system using a spectral resolution of 0.235 nm and synthetic spectra using 0.24 nm spectral resolution

Table 6.9 shows that the derived gas temperature fluctuates depending on the type of sprite probing different altitudes of the mesosphere. The mesospheric temperatures obtained from high-resolution spectra of sprites are in reasonable agreement with previous temperature measurements performed from 1978 to 1989 by two Rayleigh lidars (*Hauchecorne et al.*, 1991) in the south of France (44° N, 6° E and 44°N, 1° W) close to the site of our spectroscopic recordings. Table 6.9 also includes mesospheric temperatures recorded by the instrument SABER on board the satellite TIMED in the region, altitudes and times explored in this work. SABER provides temperature profiles from 20 to 105 km, retrieved from $CO_2$ 15 $\mu$m emission with 1.5 - 2 K errors in the 60-80 km range (*Remsberg et al.*, 2008; *García-Comas et al.*, 2008).

| Altitude (km) | $T_{rot}$ (K) | Spectrum of | Time and Date | $T_L$ (K) | $T_S$ (K) |
|---|---|---|---|---|---|
| 71.4 - 73.3 | 185 ± 10 | carrot | 01:15:26 UTC on Aug 24 , 2015 | 203.8 ± 2 | 201 ± 2 |
| 70.2 - 72.1 | 190 ± 11 | carrot | 01:20:55 UTC on Aug 24 , 2015 | 203.8 ± 2 | 201 ± 2 |
| 65.9 - 66.8 | 149 ± 10 | single column | 04:07:44 UTC on Sept 28 , 2015 | 222.8 ± 2 | 221 ± 2 |
| 65.9 - 66.8 | 210 ± 24 | single column | 04:07:44 UTC on Sept 28 , 2015 | 222.8 ± 2 | 221 ± 2 |
| 72.2 - 73.5 | 178 ± 10 | column-carrot | 01:12:59 UTC on Sept 15, 2016 | 209.2 ± 2 | 202 ± 2 |
| 70.4 - 71.4 | 164 ± 18 | multi-column | 02:23:07 UTC on Nov 16 , 2016 | 217.8 ± 2 | 211 ± 2 |
| 71.8 - 76.5 | 226 ± 17 | multi-column | 23:37:32 UTC on Jan 17, 2017 | 221.7 ± 2 | 226 ± 2 |
| 69.6 - 74.2 | 201 ± 20 | multi-column | 23:40:35 UTC on Jan 17, 2017 | 223.6 ± 2 | 226 ± 2 |

**Table 6.9:** Altitudes and rotational (gas) temperatures derived from high-resolution spectra of sprite events with different morphology captured through our 2015 (blue), 2016 and January 2017 (green) TLE spectroscopic campaigns in Spain. Also shown (two columns to the right) are $T_L$ and $T_S$. $T_L$ stands for the mean (for the fifteenth of each month) gas temperatures as derived from two Rayleigh lidars operated between 1978 and 1989 in the south of France (44° N, 6° E and 44°N, 1° W) (*Hauchecorne et al.*, 1991). $T_S$ stands for the gas temperature measured by the instrument SABER on board of the TIMED satellite in a region centered in the location of each of the sprite corresponding parent lightning (± 5° lat and ± 10° lon) within an altitude range between 66 km and 77 km and in a time interval ± 4 h with respect to the parent lightning occurrence time

Furthermore, temperatures in table 6.9 seem to follow the seasonal be-
haviour of the temperature of the mesosphere, being consistent with the
annual trend followed by the data obtained from the Spectral Airglow Tem-
perature Imager (SATI) (see figure 6.40), which is intended to analyze the
variation of the mesospheric and lower thermospheric temperatures (*López-
González et al.*, 2007) at 95 km (by measuring the rotational temperature
obtained from the $O_2$ atmospheric (0, 1) nightglow band) and 87 km (by
measuring the rotational temperature obtained from the OH (6, 2) band).

However, so far, we are not able to reproduce the complete annual cycle
of mesospheric temperatures since our data are still scarce. This reason
motivates us to plan future TLE spectrographic campaigns that will provide
the data to statistically characterize this layer of the atmosphere of the
Earth.

Sprites generally exhibit an upper (85 - 75 km) diffuse structure and a
lower (75 - 40 km) filamentary region where thousands of streamers develop
and where reduced electric fields can reach values of 400 - 600 Td (*Luque
and Ebert*, 2010) that activate complex nonequilibrium electron-driven ki-
netics in low pressure air (*Gordillo-Vázquez*, 2008; *Sentman et al.*, 2008;
*Parra-Rojas et al.*, 2015). In particular, the production of the $^5$P electronic
state of O I, whose radiative decay produces the 777.4 nm line, could be
activated by (1) electron impact dissociative excitation of $O_2$ (e + $O_2$ → O
+ O($^5$P) + e) generating ground state O I atoms and electronically excited
O($^5$P) atoms and (2) direct electron impact excitation of ground state free
ambient O I atoms producing electronically excited O($^5$P) atoms (e + O →
O($^5$P) + e). The rate coefficients of mechanisms (1) and (2) in low pressure
(mesospheric) dry air increase as the reduced electric field grows but the
production of O($^5$P) by dissociative excitation is always significantly higher
than the one by direct electron impact excitation from ground state oxygen
atoms. Therefore, it could be possible that 777.4 nm optical emissions ap-
pear in well-resolved sprite spectra. The possible 777.4 nm emission would
not be uniformly produced through the entire body of the sprite but only in
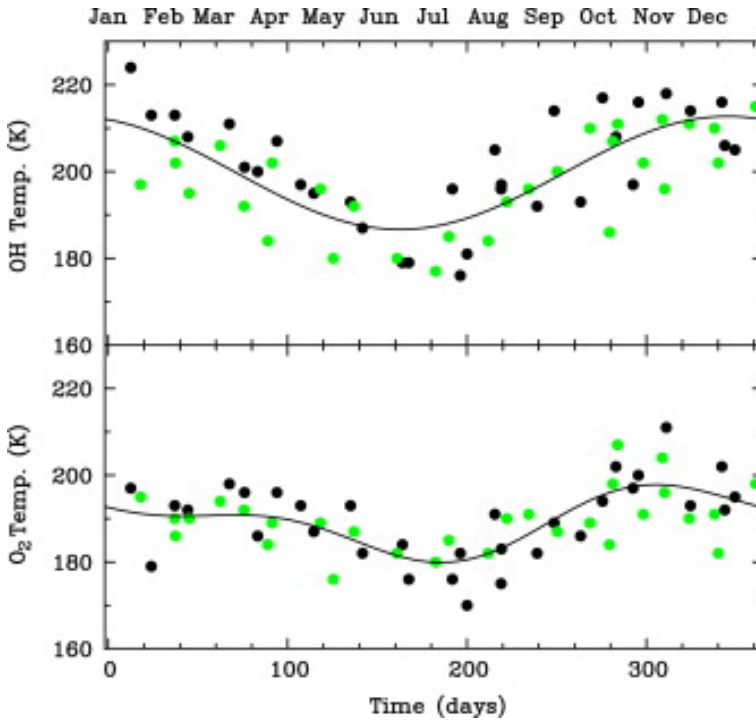
**Figure 6.40:** SATI monthly rotational temperatures. Black solid circles: from Oct 1998 to March 2002; green solid circles: from April 2002 to July 2006; solid lines: numerical fitting for the whole set of data (*López-González et al.*, 2007)

regions with high enough reduced electric fields like well developed streamers in sprites and/or in regions of sprites where streamer reconnection occur. However, none of the spectra of our detected sprites between 61 km and 74 km exhibit the characteristic 777.4 nm lightning emission feature that could be more probable in lower altitude (50 - 55 km) regions of sprites.

Figure 6.41 shows wide high resolution (0.235 nm) observed spectra (green line) of carrot sprites (panels 1 and 3), single column sprite (panel 2) and multi-column sprites (panel 4 and 5). The spectra with better SNR are those of carrot sprites while single and multicolumn sprite spectra are noisier. None of the spectra shown in figure 6.41 indicate the possible presence

of optical transitions associated to the (2, 0) band (around 785 nm) of $N_2^+$ Meinel emissions or to the 777.4 nm emission from the $^5$P electronic state of O I. The fit of high resolution (0.24 nm) synthetic spectra (blue line) to observed sprite spectra shown in figure 6.41 is very good for carrot sprites while it is reasonable for the others.

These fits allow us to derive the vibrational distribution function (VDF) or populations of the lower (from $v' = 2$ up to $v' = 7$) vibrational levels of the $B^3\Pi_g$ electronic state of $N_2$ that are shown in figure 6.42 for carrot (left) and single-column and multi-column (right) sprites, respectively. Each panel represents three different data sets: (1) VDF of the $B^3\Pi_g$ state from previous observations (squares and dashed green lines) reported by *Kanmae et al.* (2007) from spectra of carrot-like sprites at 71-75 km altitude using 3 nm spectral resolution; (2) model calculated sprite VDFs (open circles and dashed blue line) at 74 km altitude (*Luque and Gordillo-Vázquez*, 2011; *Gordillo-Vázquez et al.*, 2012) and (3) VDFs derived from fits to present spectroscopic observations for carrot spectra and single and multi-column sprite spectra using a spectral resolution of 0.24 nm. In particular, figure 6.41 (left) includes VDFs of carrot sprites at altitudes 71.4-73.3 km (detected at 01:15:26 UTC on 24 Aug, 2015 - red solid line) and 72.2-73.5 km (detected at 01:12:59 UTC on 15 Sep, 2016 - black solid line). Our carrot sprite VDFs deviate from previous observations for $v' = 3$ and $v' = 4$ while the agreement with VDF model predictions is reasonable except for $v' = 4$. Note that our two shown VDFs from carrot sprites observed at similar altitudes exhibit very close values (*Kanmae et al.*, 2007). The right panel of figure 6.41 includes VDFs from a single-column sprite at 65.9-66.8 km altitude (detected at 04:07:44 UTC on the 28th of September, 2015 - red solid line) and two multi-column sprites at 70.4-71.5 km (detected at 02:23:07 UTC on the 16th of November, 2016 - black solid line) and at 61.2-62.5 km (detected at 23:40:35 UTC on the 17th of January, 2017 - cyan solid line). The altitude dependence of the two multi-column sprite VDFs follows the trend reported by *Kanmae et al.* (2007) within a carrot sprite, that is, higher vibrational

population for sprites at higher altitudes. However the VDF of the single-column sprite occurring at $\simeq$ 66 km (lower than the multi-column sprites) does not follow the above mentioned altitude-dependent trend for $v' = 3$.

In summary, high-resolution systematic spectroscopic campaigns of TLEs have been carried out in Europe during 2015, 2016 and early 2017. It is the first time that the (2, 0), (3, 1), (4, 2) and (5, 3) rovibrational bands of the $N_2$ 1PG are well resolved in sprite spectra. We found that the rotational (gas) temperature derived from sprite spectra changes between 149 K $\pm$ 10 K at 65.9 - 66.8 km up to 226 K $\pm$ 17 K at 71.8 - 76.5 km. Therefore, the possibility to extract mesospheric local gas temperatures from high resolution sprite spectra makes sprites a natural thermal probe of (generally difficult to access) regions of the mesosphere located at different altitude. It is also found that the altitude dependence of vibrational populations in multi-column sprites is similar to the one previously reported within carrot sprites. However, the carrot sprite altitude dependent VDF trend is not completely fulfilled when comparing the VDFs from single-column and multi-column sprites recorded at various altitudes. No spectroscopic features of Meinel $N_2^+$ nor 777.4 nm (O I) optical emissions were found in any of our recorded high resolution spectra of sprites at the altitudes explored.
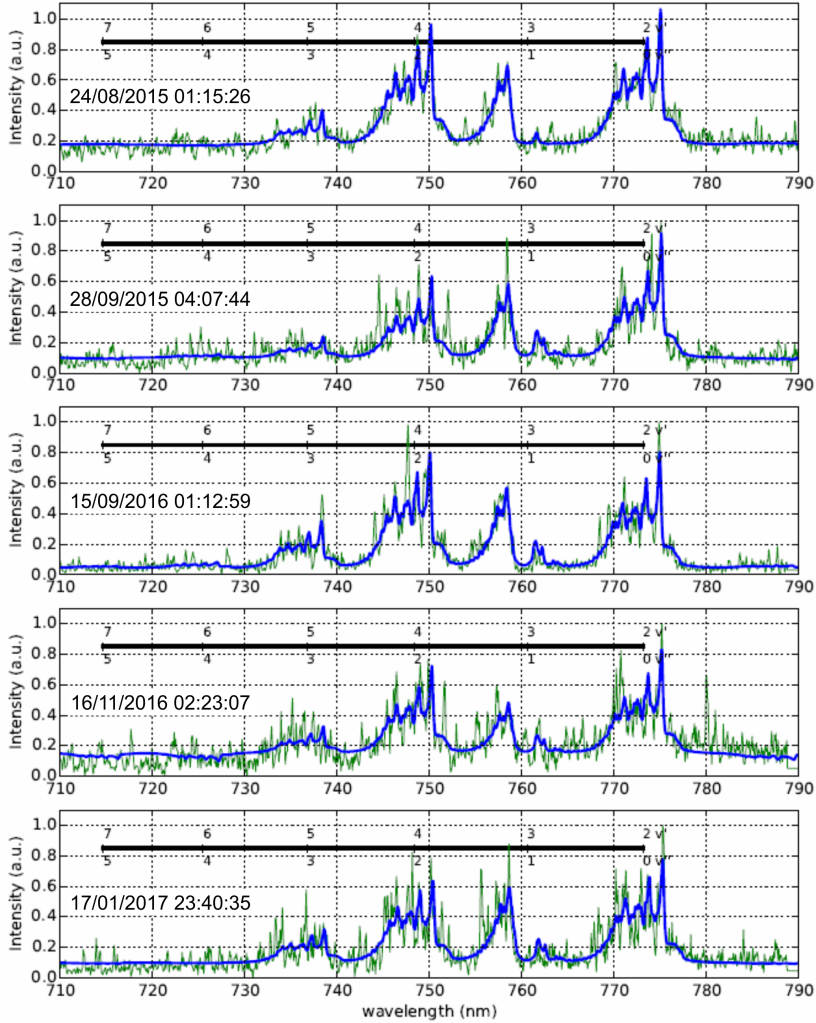
**Figure 6.41:** Spectral fitting (blue line) between 710 nm and 790 nm of the recorded (green line) spectra which images are shown in, respectively, 1st row-left (carrot sprite, $T_{rot}$ = 185 K ± 10 K), 2nd row left (multi-column sprite, $T_{rot}$ = 149 K ± 10 K), 3rd row left (carrot sprite, $T_{rot}$ = 178 K ± 10 K), 3rd row right (multi-column sprite, $T_{rot}$ = 164 K ± 18 K) and 4th row right (multi-column sprite, $T_{rot}$ = 201 K ± 20 K) of figure 6.38. The synthetic (fitted) spectra are generated using a spectral resolution of 0.24 nm. The different rovibronic bands $(v^{'}, v^{''})$ of the $N_2(B^3\Pi_g \rightarrow A^3\Sigma_u^+)$ system are marked. The used $T_{rot}$ are extracted from previous rotational fitting of the (2, 0) band (see figure 6.39). The original recorded spectra is normalized to the (2, 0) band head peak (774.8 nm - 775.4 nm)

284
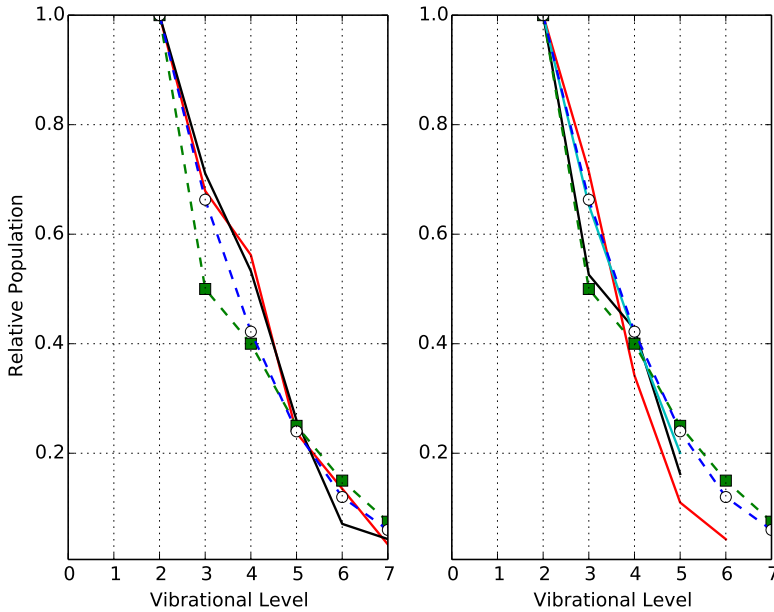
**Figure 6.42:** Relative populations of the vibrational levels (or vibrational distribution function (VDF)) of the $N_2(B^3\Pi_g, v')$ electronic state as obtained from recorded spectra of carrot-like (left panel - events recorded at 01:15:26 UTC on the 24th of August, 2015 and 01:12:59 UTC on the 15th of September, 2016) and column-like sprites (right panel - events recorded at 04:07:44 UTC on the 28th of September, 2015, 02:23:07 UTC on the 16th of November, 2016 and 23:40:35 UTC on the 17th of January, 2017). Each panel represents three different data sets: (1) altitude resolved VDFs derived from observations (squares and dashed green lines) reported by *Kanmae et al.* (2007) from spectra of carrot-like sprites recorded at 71-75 km altitude using 3 nm spectral resolution, (2) calculated sprite VDFs at 74 km altitude (*Luque and Gordillo-Vázquez*, 2011; *Gordillo-Vázquez et al.*, 2012) (open circles and dashed blue line) and (3) VDFs derived from fits to present spectroscopic observations (see first —red solid line, left— and third —black solid line, left— panels of figure 6.41 for carrot spectra and second —red solid line, right—, fourth —black solid line, right— and fifth —cyan solid line, right— panels of figure 6.41 for one single and two multi-column sprite spectra) using a spectral resolution of 0.24 nm

### 6.4.5  Methods

#### 6.4.5.1  Imaging, spectral acquisition and processing analysis

The GRASSP instrument currently consists of a medium-high resolution imaging slit spectrograph, aimed manually, but with remotely controlled internal subsystems.

GRASSP includes a wide-field Watec $1/2''$ CCD camera that records (at 25 fps) night images and helps to identify the origin of the recorded spectra. The Watec camera is a monochrome WAT-902H2 ultimate with a low light and high sensitivity CCD 3005VX4 sensor. An auto iris function allows the camera to produce visible images in light levels as low as 0.0001 lx with a signal-to-noise ratio better than 50 dB. Its FOV is 21.6 (H) x 17.4 (V) degrees thanks to the F#1.4 and 16 mm focal length lens it has attached.

GRASSP incorporates a slit spectrograph following a classical collimator/camera arrangement with an intermediate collimated beam and a monochrome intensified CCD L'Heritier LH 1300 ULL XVGA camera that provides the spectral pattern and allows to record weak spectra, due to its 90 dB adjustable gain. The CCD is a Sony ICX285AL interline solid-state image sensor of 1360 (H) x 1024 (V) pixels and 17.7 $\mu$m/px. The streak tube of the image intensifier is a Photonics Super Gen S25 photocathode (with spectral response up to 950 nm) equipped with a P20 phosphor, with a decay (persistence) time of tens of milliseconds. The Super Gen S25 sensitivity reaches its maximum value in the 700-800 nm spectral range and its quantum efficiency ranges between 11.6 % at 700 nm and 10.2 % at 800 nm. The spectrograph includes a horizontally oriented entrance slit of 31.47 mm length and variable width ranging between 0.08 and 0.10 mm that, when projected on the sky, has a FOV of 6 (H) $\times$ 0.03 (V) degrees. The dispersive element is a 1440 lines/mm and 70 mm $\times$ 70 mm aperture diffraction grating, with a blaze angle of 26.45° at 540 nm. It ranges a spectral band between 695 nm and 795 nm with a mean spectral resolution of 0.235 nm.

The complete calibration procedure of the GRASSP spectroscopic system consists of three stages: (1) a wavelength calibration (using argon and krypton spectral lamps), which assigns an absolute wavelength to each pixel of the iCCD; (2) a distortion correction, which straightens the raw curved spectrum; and (3) a flux calibration (using a halogen tungsten spectral lamp), which provides the spectral sensitivity (spectral response function) of the spectrograph. Both distortion correction and wavelength calibration are done whenever a TLE spectrum is recorded; the instrument response function was calculated just once at the IAA dependencies. Full spectral characterization and specifications of GRASSP are available in *Parra-Rojas et al.* (2013b) and *Passas et al.* (2016b), respectively.

### 6.4.5.2 Spectroscopic fitting procedure of $N_2$

The calculated synthetic spectrum includes the rovibronic bands for the $N_2$ 1PG that involve transitions between the upper electronic state $N_2(B^3\Pi_g)$ (with the orbital quantum number $\Lambda' = 1$) and the lower electronic state $N_2(A^3\Sigma_u^+)$ (with $\Lambda'' = 0$). The $N_2(A^3\Sigma_u^+)$ state (with spin-orbit constant $A_{v''} = 0$) belongs to the Hund's case ($b$). However, the coupling of the $N_2(B^3\Pi_g)$ electronic state is type Hund's case ($a$) for the lower rotational quantum number $J'$ values and Hund's case ($b$) for $J'$ values higher than 15 (*Herzberg*, 1950). Therefore, we have considered the intermediate Hund case coupling for the $N_2(B^3\Pi_g)$ state. In calculating the $N_2$ 1PG rovibronic band spectrum, we have taken into account the parity ($\Lambda$-type doubling) of the 3 sub-states $^3\Pi_{\Omega g}^{e,f}$ of the upper electronic state $N_2(B^3\Pi_g)$. Thus, the triplet fine structure of the $N_2(B^3\Pi_g \to A^3\Sigma_u^+)$ rovibronic band spectrum consists of a total of 27 branches divided into the 3 sub-bands $^3\Pi_{0g}^{e,f} \to {}^3\Sigma_u^+$, $^3\Pi_{1g}^{e,f} \to {}^3\Sigma_u^+$ and $^3\Pi_{2g}^{e,f} \to {}^3\Sigma_u^+$ with 9 branches, each denoted $P$, $Q$ and $R$ that correspond to $\Delta J = J' - J'' = $ -1, 0, +1, respectively. At medium spectral resolutions (0.1 - 0.5 nm) the small spin splitting causes the overlap of the three sub-bands producing the appearance of, depending on the $(v', v'')$ considered, 3 or 4 sub-band head peaks whose spectral positions for the (2,

0) band of the $N_2$ 1PG are 774.8 - 775.4 nm (band head peak), 773.5 - 774.1 and 771.0 - 771.6 nm (*Simek and DeBenedictis*, 1995), (*Simek*, 1994). The presence of atomic oxygen is considered by adding the 24 emission lines of atomic oxygen (O I) between 700 nm and 800 nm to the calculated rovibrational lines of the $N_2$ 1PG synthetic spectrum.

In order to compare the synthetic spectra with the observed (measured) spectra, each line of the synthetic spectrum needs to be convolved with an instrument function taking into account the finite spectral resolution of the spectrograph used. To model the instrument spectral broadening, we have used a combination of a Gaussian and a Lorentzian function, that is, a Voight function as (*Biloiu et al.*, 2007)

$$
S_{p,w}(\lambda) = p \frac{\sqrt{4\ln 2}}{\sqrt{\pi} w} \exp\left(-\frac{4\ln 2}{w^2}(\lambda - \lambda_{kl}^{J',J''})^2\right) + \frac{2}{\pi} \frac{(1-p)w}{w^2 + 4(\lambda - \lambda_{kl}^{J',J''})^2}
$$
(6.9)

where $p$ and $1 - p$ are the relative magnitudes of the Gaussian and Lorentzian functions contributions, respectively, $w$ is a parameter measuring the spectral resolution as the full width at half maximum (FWHM) of the line considered, and $\lambda_{kl}^{J',J''}$ is the central wavelength or the wavelength corresponding to the calculated (synthetic) rotational lines.

To correct for atmospheric absorption due to the long slant path (between 300 and around 800 km) the $N_2$ or $N_2$ and O synthetic spectrum are first multiplied by the atmospheric transmittance using MODTRAN (*Anderson et al.*, 1993), considering that the observing site (Castellgalí, Spain) is only at 275 m above sea level, and then convolved with the instrument spectral broadening function (6.9). The synthetic spectrum is then fitted by a non-linear least square technique to the recorded spectra corrected for the instrument function of GRASSP and for atmospheric absorption and scattering.

### 6.4.5.3 Procedure to estimate TLE altitudes

We apply the method suggested in *van der Velde and Montanyà* (2016). To do so, we need the spatial coordinates of the parent lightning of the TLEs and the elevation angle of the camera when recording the TLE spectra.

Several european lightning detection networks such as METEORAGE, LINET and AEMET provided the parent lightning coordinates matching the time-stamp of the recorded spectra.

We calculated the elevation angle ($\alpha$) of the region the slit overlapped the TLE from the stars recorded in the images. Unfortunately, our images have many hot pixels that are easily confused with stars. So the first step was to clean up the images from hot pixels. To do so, we built a hot–pixel mask by combining all video images we have got (see figure 6.43). This way we enhanced the hot pixels from the background. As hot pixels do not reach the same intensity value in all regions of the CCD, we had to build up the hot-pixel mask manually. Then we combined all the images of the same event, to enhance the stars from the background. Next, we subtracted the hot pixels mask from the TLE combined–image and we identified the stars position with the software *Cartes du Ciel*, as described in *van der Velde and Montanyà* (2016). Then, we changed the background image to the frame showing up the TLE with the superimposed slit, to obtain $\alpha$ by hovering the mouse over the slit position (see figure 6.44).

**Figure 6.43:** Combination of all the field video images recorded from Castell-galí to enhance the hot pixels of the CCD so we can discern them from stars
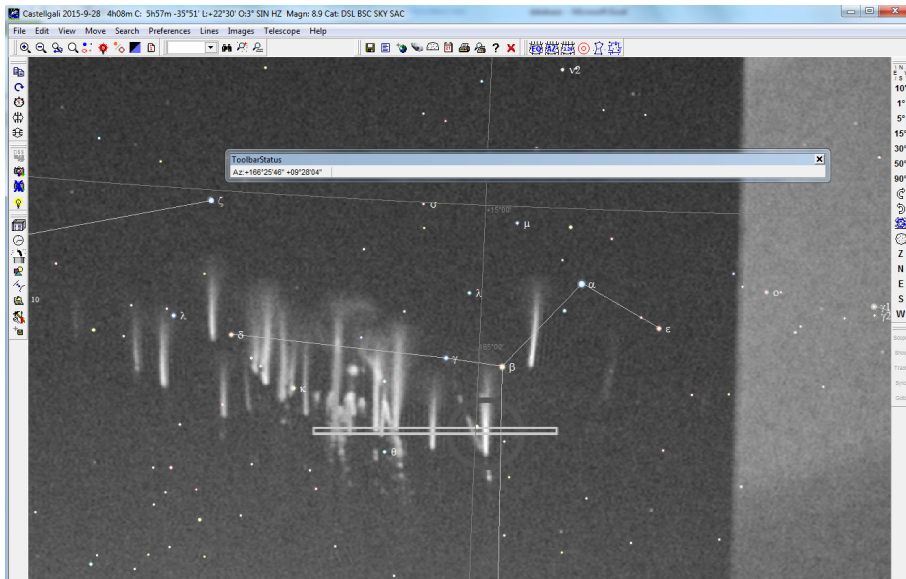
**Figure 6.44:** *Cartes du Ciel* software. Background image: columniform sprites captured on the 28th of September, 2015 at 04:07:44 UTC. The slit position is superimposed. The elevation angle for the slit position ranges between $9°22'$ and $9°29'$

We applied this elevation angle value to the equations defined in *van der Velde and Montanyà* (2016) to obtain the TLE altitude ($h$):

$$h = \frac{d \sin(\alpha + 0.5 \times \beta)}{\sin(90 - \beta - \alpha)} + h_{cam} \tag{6.10}$$

where $d$ is the distance in km from the observatory to the parent lightning projection above Earth surface, $\beta$ is the angle between the observatory and the TLE in degrees, measured from the center of Earth, $\alpha$ is the elevation angle of the TLE in degrees, which we have previously calculated and $h_{cam}$ is the height of the observatory in km . A MATLAB routine was developed to calculate $h$.
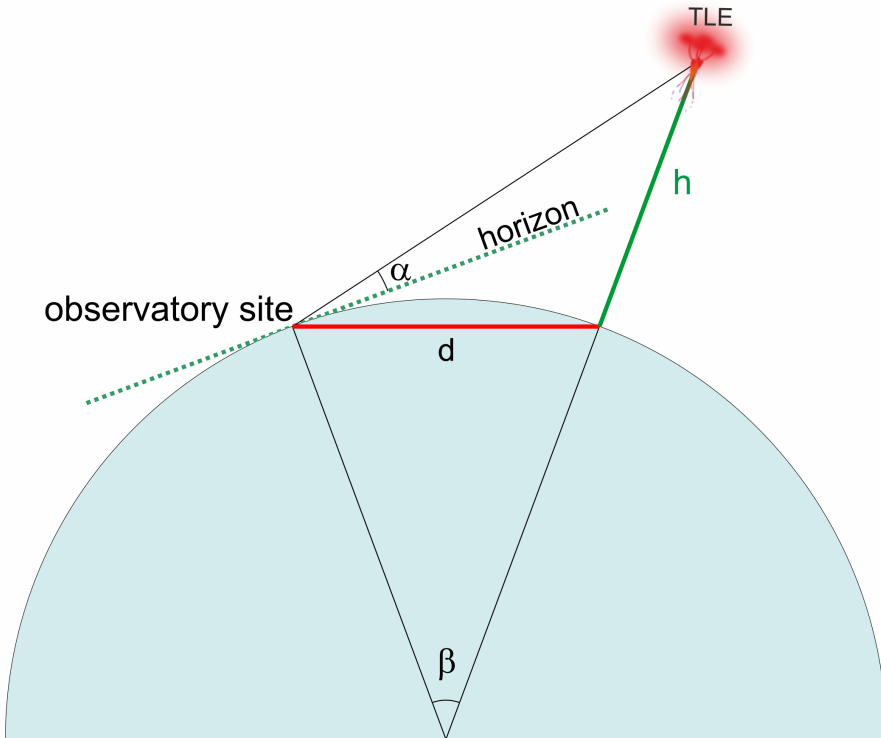


**Figure 6.45:** Geometry for the calculation of event altitude $h$ based on great circle $\beta$ and observed elevation angle $\alpha$ (*van der Velde and Montanyà*, 2016)

# Chapter 7

# Summary

*"April 11, 1982, on a night flight from Seattle to O'Hare, we broke out into a region of extremely clear air. There was a perfect line of nocturnal cumuli some 15–20 miles to the north and parallel to the airway. It seemed as if a giant smoke screen had been made there. Only occasional lightning in the clouds was observed, save for the eastern end, which was slightly higher. There the activity was more frequent. While the three of us were observing and commenting on the cloud formation, a brilliant white–blue spire shot upward some 2,000 feet above the cloud top. Around the arrow–straight finger core, there appeared to be an ionized glow. We referred to it as a lightning spike. The duration was approximately 1/4 – 1/2 s. No fingers were observed from the bolt here."*

– Albert Malgarin, retired captain of the United Airlines, *Journal of Geophysical Research, September 30, 1989*

## 7.1   Summary

We have developed and characterized the GRAnada Sprite Spectrograph and Polarimeter (GRASSP), the first ground–based instrument designed to simultaneously measure the polarization and the spectra of the light emitted from TLEs with medium–high spectral resolution in an automatic

and systematic way. This instrument is intended to be a ground support of the Atmosphere-Space Interaction Monitor (ASIM), an approved ESA project to be installed in the International Space Station (ISS) which will be launched in late 2017 – early 2018, with the objective to observe TLEs that occur in the Earth's upper atmosphere accompanied by thunderstorms in the lower atmosphere. GRASSP will also support from ground the Tool for the Analysis of RAdiation from lightNIng and Sprites (TARANIS) mission of the Centre National d'Études Spatiales (CNES), which will be launched in late 2018.

As GRASSP is a custom instrument, we have also designed and developed the software tools to control its inner subsystems and to reduce GRASSP spectroscopic data. Besides, to make measurements reliable, we have calibrated all versions of the spectrograph and the polarimeter in our dependencies.

So far, we have developed four different versions of GRASSP spectrograph and installed them within two different locations: SPEC1 —with a spectral resolution from 0.47 to 0.61 nm and covering a spectral range from 660 nm to 760 nm— and SPEC2 —with a spectral resolution from 0.21 to 0.26 nm and covering a spectral range from 695 nm to 795 nm—.

Before installing SPEC1 within GRASSP, we tested its capabilities by comparing the spectrum of a low pressure air lamp plasma recorded both with SPEC1 and a commercial Jobin Yvon Horiba FHR1000 spectrometer, confirming its reliability. We published these results in the *Journal of Geophysical Research: Space Physics* on July 2013 (*Parra-Rojas et al.*, 2013b) where we commented on the convenience of using one or another technique for TLE rotational (gas) temperature determination depending on the altitude and available spectral resolution.

When we tested SPEC1 reliability, we installed it within the first version of GRASSP (GRASSP v1.0) in October 2012 at the terrace of the 2.2 m dome of the German–Spanish Astronomical Center (CAHA) at Calar Alto, Sierra de Los Filabres, north of Almería (Andalucía, Southern Spain), where

its housing is still fixed at 2,168 meters above mean sea level, 37.2231° N latitude and 2.5458° W longitude, aiming to an azimuth from 35° to 55° that is, to the western Mediterranean Sea zone, a region where TLE activity in Europe seemed to be frequent. GRASSP v1.0 worked automatically in a methodical way: by consulting a real–time lightning database provided by the Spanish Meteorology Agency (AEMET), a telescope mount aimed automatically the spectrograph (the polarimeter was not operative then) to the region of the sky where a TLE was predicted to appear. The spectral range of GRASSP v1.0 spectrograph (SPEC1) was 100 nm (660 nm to 760 nm) with a mean spectral resolution of $R = \lambda/\Delta\lambda = 1247$ ($\Delta\lambda = 0.58$ nm). This version of GRASSP worked until July 2014, when we decided to upgrade the system since we noticed that the triplet of OI around 777.19 nm could be involved in the chemical processes taking place in TLEs (*Parra-Rojas et al.*, 2013b). We presented images of sprites and halos from August to November 2013, captured by GRASSP v1.0, in the journal *IEEE Transactions on Plasma Science* on June 2014 (*Passas et al.*, 2014). Unfortunately, we did not capture any TLE spectrum within this period. On the other hand, the night of 9th – 10th July 2013, GRASSP v1.0 captured 49 spectra of lightning light scattered on clouds. We identified emissions from atmospheric species (Ar I, N I, Ne I and O I) taking into account the spectral signal over an upper limit of 2 and 3-sigma. As the spectral resolution of SPEC1 was 0.58 nm and the N I triplet over 744 nm was well resolved, we could estimate the electron density ($N_e$) for different temperatures when analyzing the Stark (pressure) broadening of N I spectral line at 744.229 nm within the hypothesis of considering that it was isolated. We presented these results during the 2nd Thunderstorm Effects on the Atmosphere-Ionosphere System (TEA-IS) Summer School in Collioure, France, in June 2014. The detection of these high resolution spectra, the further identification of the well-known lightning spectral lines and the estimation of the $N_e$ demonstrated the reliability of SPEC1.

The second version of GRASSP (GRASSP v1.1) worked in CAHA from September 2014 to February 2015. The upgrade of the system consisted of developing and installing a new spectrograph (SPEC2) with a spectral range from 695 to 795 nm and a mean spectral resolution of R = $\lambda/\Delta\lambda$ = 3309 ($\Delta\lambda$ = 0.235 nm). GRASSP v1.1 recorded the emission spectrum of a meteor during the observation of transient luminous events (TLEs) on 2014 October 16th. The good spectral resolution of the spectrum (0.078 nm/pixel spectral dispersion) allowed us to determine the physical conditions in the meteor plasma, to identify several emissions from atmospheric (N I, N II, O I) and meteoroid species (Ti I, Cr I, Fe I, Fe II, Zr I, Pd I, W I) and to estimate the upper limit of the temperature of the gaseous environment surrounding the meteoroid. Images recorded for this meteor from two different sites allowed us to calculate its atmospheric trajectory and the orbital parameters of the progenitor meteoroid. These data revealed that the particle belonged to the Orionid meteoroid stream. The results and conclusions of the analysis of these data were published in the journal *Icarus* the 19th November 2015 (*Passas et al.*, 2016a).

The third version of GRASSP (GRASSP v2.0) was installed in May 2015 at Castellgalí (Barcelona, Spain), at 275 meters above the mean sea level, 41.6768° N latitude and 1.8399° E longitude to improve GRASSP statistics of spectroscopy of TLEs. From this place we manually aimed GRASSP v2.1 between -60° NW and 170° NW, spinning around 230° azimuth with an elevation from -10° to 60°, increasing the likelihood of TLE detection. This compact version of GRASSP included the previous version of GRASSP spectrograph, SPEC2, and worked until May 2016. In the summer campaign of 2015, GRASSP v2.0 recorded a total of 3 TLE spectra, being the first time a TLE spectrum had been recorded with medium–high resolution. We presented these results during the final TEA-IS international conference in Copenhagen, Denmark in June 2016. We published the main parameters, design features, and optical characterization of GRASSP v2.0 in the *Applied*

*Optics* journal, with the honour of being the cover of the number of August 2016.

The last version of GRASSP, (GRASSP v2.1) was installed in Castellgalí in May 2016 and has been working there since then. The upgrade of the system consisted of installing an industrial PC due to the failure of the former one. Since the installation of GRASSP v2.1, we have detected 41 medium–high resolution TLE spectra.

The last version of GRASSP includes the first medium–high resolution spectrograph designed to analyze the spectrum of TLEs in the visible–near infrared band (695 nm – 795 nm) with a spectral resolution of 0.235 nm, so we can estimate for the first time the rotational temperature of the gas surrounding TLEs among other characteristics. We submitted to *Nature Communications* the scientific results on medium–high resolution recorded with this version of GRASSP.

The last version of GRASSP will also bear (from July 2017) the first polarimeter designed to achieve the type and degree of polarization of the light emitted by TLEs by calculating the four Stokes parameters of TLEs optical emissions in a single shot. The optical characterization of the GRASSP polarimeter was recently finished and we plan to field the polarimeter during the 2017 summer campaign.

# 7. SUMMARY

# Chapter 8

# Conclusions

*"This flight, on March 29, 1979, from Omaha to Mt. Vernon,
Illinois, had just leveled at 41,000 ft msl, and to the left at about 40
miles were two or three isolated cells. One cell had two lightning
strokes which shot straight up from the tops of the storm, which
were about 39,000 ft msl. It is estimated that the lightning strokes
shot up 4,000–6,000 ft above the tops."*

  – Larry Fuerst, Lear jet pilot, *Journal of Geophysical Research,*
*September 30, 1989*

## 8.1    Conclusions

- We have developed and characterized the GRAnada Sprite Spectrograph and Polarimeter (GRASSP), the first ground–based instrument designed to simultaneously measure the polarization and the spectra of the light emitted from TLEs with medium–high spectral resolution in an automatic and systematic way.

- We have developed four different versions of the GRASSP instrument.

- We have developed two different versions of the GRASSP spectrograph: SPEC1 and SPEC2.

299

- The spectral resolution of SPEC1 ranges from 0.47 to 0.61 nm with a spectral range from 660 nm to 760 nm.

- The spectral resolution of SPEC2 ranges from 0.21 to 0.26 nm with a spectral range from 695 nm to 795 nm.

- We confirmed the reliability of SPEC1 by comparing the spectrum of a low pressure air lamp plasma recorded both with SPEC1 and a commercial Jobin Yvon Horiba FHR1000 spectrometer. We published these results in the *Journal of Geophysical Research: Space Physics* on July 2013 (*Parra-Rojas et al.*, 2013b).

- We presented images of sprites and halos from August to November 2013, captured by GRASSP v1.0, in the journal *IEEE Transactions on Plasma Science* on June 2014 (*Passas et al.*, 2014).

- We recorded 49 spectra of light from lightning scattered on clouds with SPEC1 and identified emissions from atmospheric species (Ar I, N I, Ne I and O I). We could estimate the electron density ($N_e$) for different temperatures when analyzing the Stark (pressure) broadening of N I spectral line at 744.229 nm within the hypothesis of considering that it was isolated. We presented these results during the 2nd Thunderstorm Effects on the Atmosphere-Ionosphere System (TEA-IS) Summer School in Collioure, France, in June 2014.

- We recorded the emission spectrum of a meteor with SPEC2 and determined the physical conditions in the meteor plasma, identified several emissions from atmospheric (N I, N II, O I) and meteoroid species (Ti I, Cr I, Fe I, Fe II, Zr I, Pd I, W I) and estimated the upper limit of the temperature of the gaseous environment surrounding the meteoroid. We calculated the atmospheric trajectory and the orbital parameters of the progenitor meteoroid, belonging the particle to the Orionid meteoroid stream. We published the results and conclusions

of the analysis of these data in the journal *Icarus* the 19th November 2015 (*Passas et al.*, 2016a).

- We published the main parameters, design features, and optical characterization of GRASSP v2.0 in the *Applied Optics* journal, with the honour of being the cover of the number of August 2016.

- We carried out the first high-resolution systematic spectroscopic campaigns of TLEs.

- We recorded 44 TLE medium-high resolution spectra with SPEC2, being the first time that the (2, 0), (3, 1), (4, 2) and (5, 3) rovibrational bands of the $N_2$ 1PG are well resolved in sprite spectra.

- We found that the rotational (gas) temperature derived from sprite spectra changes between 149 K $\pm$ 10 K at 65.9 - 66.8 km up to 226 K $\pm$ 17 K at 71.8 - 76.5 km.

- We found that the altitude dependence of vibrational populations in multi-column sprites is similar to the one previously reported within carrot sprites. We found that the carrot sprite altitude dependent VDF trend is not completely fulfilled when comparing the VDFs from single-column and multi-column sprites recorded at various altitudes.

- We did not find any spectroscopic features of Meinel $N_2^+$ nor 777.4 nm (O I) optical emissions in any of our recorded high resolution spectra of sprites at the altitudes explored.

- We presented these results during the final TEA-IS international conference in Copenhagen, Denmark in June 2016 and we have submitted them to *Nature Communications*.

- We have designed and developed the first TLE polarimeter designed to determine the type and degree of polarization of the light emitted

by TLEs by calculating the four Stokes parameters of TLEs optical emissions in a single image acquisition.

- We have calibrated all versions of the spectrograph and the polarimeter in our dependencies.

- We have developed two software packages to both control all GRASSP subsystems and to reduce the spectroscopic data.

# Chapter 9

# Future Work

*"The observation 6 or 7 years ago was in the area of southwest of Saint Louis flying at 35,000 – 37,000 feet over mean sea level, a little after sunset. [...] The lightning display was one of the most intense seen in 20 years of airline flying. There was both cloud-to-ground and cloud-to cloud lightning. Lightning was emitted from the top of one of the higher clouds in the vicinity. The height that the lightning rose above the cloud could not be estimated because there was no real vertical referene frame; however, it did continue upward for several thousand feet."*

*– Duane Eisenbeiss, airline pilot, Journal of Geophysical Research, September 30, 1989*

## 9.1   Future Work

For future work we have planned to develop a new application software to automatically identify the frames of the L'Heritier video recordings including good SNR spectra. At the moment the final user has to search these frames manually from the data repository, which entails a significant loss of time.

We have also planned to embed the modelling algorithms that extract the rotational temperature within the data reduction code, so the final user

can reduce the data and also extract valuable information, controlling all process. At the moment an operator reduces the data and passes the results to the scientist, who fits the spectrum to models and extracts the information.

As the goal of this thesis is to perform systematic TLEs observational campaigns from ground to statistically analyze the nature of this kind of transient air plasmas, we have planned to build up a database of TLE spectra to be shared online through our group's website (www.trappa.es).

When we fully characterize TLEs from 695 nm to 795 nm with high spectral resolution, we have planned to shift the grating of the spectrograph to statistically characterize TLEs within the 370 nm – 470 nm corresponding to the second positive system of $N_2$ emitting in blue.

Polarimetric campaigns in coordination with imaging and spectroscopy of TLEs will be conducted as from July 2017 onwards.

# References

ADACHI, T., FUKUNISHI, H., TAKAHASHI, Y., HIRAKI, Y., HSU, R.R., SU, H.T., CHEN, A.B., MENDE, S.B., FREY, H.U. & LEE, L.C. (2006). Electric field transition between the diffuse and streamer regions of sprites estimated from ISUAL/array photometer measurements. *Geophys. Res. Lett.*, **33**, L17803. 28

ANDERSON, G. & KLUGMANN, D. (2014). A european lightning density analysis using 5 years of atdnet data. *Natural Hazards and Earth System Sciences*, **14**, 815–829. xv, 38

ANDERSON, G.P., CHETWYND, J.H., THERIAULT, J.M., ACHARYA, P., BERK, A., ROBERTSON, D.C., KNEIZYS, F.X., HOKE, M.L., ABREU, L.W. & SHETTLE, E.P. (1993). MODTRAN2: suitability for remote sensing. In A. Kohnle & W. B. Miller, ed., *Society of Photo-Optical Instrumentation Engineers (SPIE) Conference Series*, vol. 1968 of *Presented at the Society of Photo-Optical Instrumentation Engineers (SPIE) Conference*, 514. 234, 248, 288

ARMSTRONG, R.A., SHORTER, J.A., TAYLOR, M.J., SUSZCYNSKY, D.M., LYONS, W.A. & JEONG, L.S. (1998). Photometric measurements in the SPRITES '95 and '96 campaigns of nitrogen second positive (399.8 nm) and first negative (427.8 nm) emissions. *J. Atm. Sol.-Terr. Phys.*, **60**, 787. 23, 26

ARMSTRONG, R.A., SUSZCYNSKY, D., LYONS, W.A. & NELSON, T.E. (2000). Multi-color photometric measurements of ionization and energies in sprites. *Geophys. Res. Lett.*, **27**, 653–656. 23

ARNONE, E., KERO, A., DINELLI, B.M., ENELL, C.F., ARNOLD, N.F., PAPANDREA, E., RODGER, C.J., CARLOTTI, M., RIDOLFI, M. & TURUNEN, E. (2008). Seeking sprite-induced signatures in remotely sensed middle atmosphere $NO_2$. *Geophys. Res. Lett.*, **35**, L05807. 27

ASHMORE, S.E. (1950). Unusual Lightning. *Weather*, **5**, 331. 3

BABADZHANOV, P.B. & KOKHIROVA, G.I. (2009). Densities and porosities of meteoroids. *AA*, **495**, 353–358. 243

BARRINGTON-LEIGH, C.P. & INAN, U.S. (1999). Elves triggered by positive and negative lightning discharges. *Geophys. Res. Lett.*, **26**, 683–686. 17

BEFEKI, G. (1976). *Principle of Laser Plasmas*. Wiley. 224, 225

BERING, E.A., BENBROOK, J.R., BHUSAL, L., GARRETT, J.A., PAREDES, A.M., WESCOTT, E.M., MOUDRY, D.R., SENTMAN, D.D., STENBAEK-NIELSEN, H.C. & LYONS, W.A. (2004a). Observations of transient luminous events (TLEs) associated with negative cloud to ground (-CG) lightning strokes. *Geophys. Res. Lett.*, **31**, L05104. 11

BERING, E.A., III, BHUSAL, L., BENBROOK, J.R., GARRETT, J.A., JACKSON, A.P., WESCOTT, E.M., MOUDRY, D.R., SENTMAN, D.D., STENBAEK-NIELSEN, H.C. & LYONS, W.A. (2004b). The results from the 1999 sprites balloon campaign. *Adv. Space Res.*, **34**, 1782. 15

BILOIU, C., SUN, X., HARVEY, Z. & SCIME, E. (2007). An alternative method for gas temperature determination in nitrogen plasmas: Fits of the bands of the first positive system ($B^3\Pi_g \rightarrow A^3\Sigma_u$). *J. Appl. Phys.*, **101**, 073303. 288

BLAES, P.R., MARSHALL, R.A. & INAN, U.S. (2016). Global occurrence rate of elves and ionospheric heating due to cloud-to-ground lightning. *Journal of Geophysical Research: Space Physics*, **121**, 699–712, 2015JA021916. 17

BOECK, W.L. & VAUGHAN JR., O.H. (1990). Lightning Observations from the STS-32 Space Shuttle Mission. In *EOS Trans. AGU*, vol. 71, 1241. xiii, 6, 7

BOECK, W.L., VAUGHAN JR., O.H., BLAKESLEE, B., R.AND VONNEGUT, BROOK, M. & MCKUNE, J. (1991a). Lightning to the Upper Atmosphere: A Vertical Light Pulse from the Top of a Thunderstorm as Seen by a Payload Bay TV Camera of the Space Shuttle. In *Proc. Int. Aerospace Lightning Conference,NASA; NASA Conference Publ.*, vol. 1058, 8pp. 6, 10, 17, 18

BOECK, W.L., VAUGHAN JR., O.H. & BLAKESLEE, R. (1991b). Low Light Level TV Images of Terrestrial Lightning as Viewed From Space. In *EOS Trans. AGU*, vol. 72, P21C–1. 6, 10, 16, 17, 18

BOECK, W.L., VAUGHAN, O.H.J., BLAKESLEE, R., VONNEGUT, B. & BROOK, M. (1992). Lightning induced brightnening in the airglow layer. *Geophys. Res. Lett.*, **19**, 99–102. xiv, 16

BOECK, W.L., VAUGHAN, O.H., BLAKESLEE, R.J., VONNEGUT, B., BROOK, M. & MCKUNE, J. (1995). Observations of lightning in the stratosphere. *J. Geophys. Res.*, **100**, 1465. 6, 11

BÓR, J. (2013). Optically perceptible characteristics of sprites observed in Central Europe in 2007 - 2009. *J. Atm. Solar-Terrestrial Phys.*, **92**, 151–177. 11, 13, 14

Borovicka, J. (1993). A fireball spectrum analysis. *AA*, **279**, 627–645. 227

Borovicka, J. (1994). Line identifications in a fireball spectrum. *AA*, **103**, 83–96. 227

Boys, C.V. (1926). Progressive Lightning. *Nature*, **118**, 749–750. 2

Bucsela, E., Morrill, J., Heavner, M., Siefring, C., Berg, S., Hampton, D., Moudry, D., Wescott, E. & Sentman, D. (2003). $N_2(B^3\Pi_g)$ and $N_2^+(A^2\Pi_u)$ vibrational distributions observed in sprites. *J. Atm. Sol.-Terr. Phys.*, **65**, 583. 23, 25, 245

Ceplecha, Z. (1987). Geometric, dynamic, orbital and photometric data on meteoroids from photographic fireball networks. *Bulletin of the Astronomical Institutes of Czechoslovakia*, **38**, 222–234. 228

Ceplecha, Z. & McCrosky, R.E. (1976). Fireball end heights: A diagnostic for the structure of meteoric material. *Journal of Geophysical Research*, **81**, 6257–6275. 243

Chen, A.B., Kuo, C.L., Lee, Y.J., Su, H.T., Hsu, R.R., Chern, J.L., Frey, H.U., Mende, S.B., Takahashi, Y., Fukunishi, H., Chang, Y.S., Liu, T.Y. & Lee, L.C. (2008). Global distributions and occurrence rates of transient luminous events. *J. Geophys. Res. (Space Phys)*, **113**, A08306. 11, 20

Chern, R.J., Wu, A.M. & Lin, S.F. (2014). Ten-year Arctic and Antarctic observations of FormoSat-2. In *Proceedings of the 65th International Astronautical Congress (IAC 2014)*, IAC–14–B1.6.1 and IAC–14–B4.4.1, Toronto, Canada. 16, 29

Cummer, S.A. & Stanley, M. (1999). Submillisecond Resolution Lightning Currents and Sprite Development: Observations and Implications. *Geophys. Res. Lett.*, **26**, 3205. 14

Cummer, S.A., Li, J., Han, F., Lu, G., Jaugey, N., Lyons, W.A. & Nelson, T.E. (2009). Quantification of the troposphere-to-ionosphere charge transfer in a gigantic jet. *Nature GeoSci.*, **2**, 617 – 620. 20

Deehr, C.S. (1961). *A spectrophotometric study of the aurora of 27 November 1959 at College, Alaska.*. Alaska Univ. College Geophysical Inst., Alaska Univ. College Geophysical Inst. 24

Elsevier Publishing Company, ed. (1965). *Nobel Lectures Physics 1922–1941*. Nobel Foundation. xiii, 2

Everett, W.H. (1903). Rocket Lightning. *Nature*, **68**, 599. 2, 17

Fantz, U. (2006). Basics of plasma spectroscopy. *Plasma Sources Science and Technology*, **15**, S137. 90, 92, 107, 109, 233

Fischer, H., Birk, M., Blom, C., Carli, B., Carlotti, M., von Clarmann, T., Delbouille, L., Dudhia, A., Ehhalt, D., Endemann, M., Flaud, J.M., Gessner, R., Kleinert, A., Koopman, R., Langen, J., López-Puertas, M., Mosner, P., Nett, H., Oelhaf, H., Perron, G., Remedios, J., Ridolfi, M., Stiller, G. & Zander, R. (2008). MIPAS: an instrument for atmospheric and climate research. *Atmos. Chem. Phys.*, **8**, 21512188. xiv, 28

Fogle, B.T. (1966). *Noctilucent Clouds.*. Ph.D. thesis, University of Alaska Fairbanks. 25

Franz, R.C., Nemzek, R.J. & Winckler, J.R. (1990). Television Image of a Large Upward Electrical Discharge Above a Thunderstorm System. *Science*, **249**, 48. xiii, 5, 8, 11, 245

Frey, H.U., Mende, S.B., Hsu, R.R., Su, H.T., Chen, A.B., Lee, L., Fukunishi, H. & Takahashi, Y. (2004). The spectral signature of transient luminous events (TLE, sprite, elve, halo) as observed by ISUAL. In *AGU Fall Meeting Abstracts*, vol. 1:05, AE51A–05. 28

Frey, H.U., Mende, S.B., Cummer, S.A., Li, J., Adachi, T., Fukunishi, H., Takahashi, Y., Chen, A.B., Hsu, R.R., Su, H.T. & Chang, Y.S. (2007). Halos generated by negative cloud-to-ground lightning. *Geophys. Res. Lett.*, **34**, L18801. 15

Fukunishi, H., Takahashi, Y., Kubota, M., Sakanoi, K., Inan, U.S. & Lyons, W.A. (1996). Elves: Lightning-induced transient luminous events in the lower ionosphere. *Geophys. Res. Lett.*, **23**, 2157. 16

Fullekrug, M., Mareev, E.A. & Rycroft, M.J. (2006). *Sprites, Elves and Intense Lightning Discharges*. Springer. 13

Furuya, R.S. (2010). Subaru Data Reduction Cookbook: Long-Slit Spectroscopic Observations with FOCAS. [Online; accessed 13-March-2017]. 96, 195

García-Comas, M., López-Puertas, M., Marshall, B.T., Wintersteiner, P.P., Funke, B., Bermejo-Pantaleón, B., Mertens, C.J., Remsberg, E.E., Gordley, L.L., Mlynczak, M.G. & Russell, J.M. (2008). Errors in Sounding of the Atmosphere using Broadband Emission Radiometry (SABER) kinetic temperature caused by non-local-thermodynamic-equilibrium model parameters. *J. Geophys. Res.*, **113**. 279

Glatthor, N., Höpfner, M., Leyser, A., Stiller, G.P., von Clarmann, T., Grabowski, U., Kellmann, S., Linden, A., Sinnhuber, B.M., Krysztofiak, G. & Walker, K.A. (2017). Global carbonyl sulfide (ocs) measured by mipas/envisat during 2002–2012. *Atmospheric Chemistry and Physics*, **17**, 2631–2652. 27

Gordillo-Vázquez, F.J. (2008). Air plasma kinetics under the influence of sprites. *J. Phys. D*, **41**, 234016. 280

GORDILLO-VÁZQUEZ, F.J., PEREA, A., MCKIERNAN, A.P. & AFONSO, C.N. (2005). Electronic temperature and density of the plasma produced by nanosecond ultraviolet laser ablation of lif. *Applied Physics Letters*, **86**, 181501. 224

GORDILLO-VÁZQUEZ, F.J., LUQUE, A. & SIMEK, M. (2011). Spectrum of sprite halos. *J. Geophys. Res. (Space Phys)*, **116**, A09319. 233, 234

GORDILLO-VÁZQUEZ, F.J., LUQUE, A. & SIMEK, M. (2012). Near infrared and ultraviolet spectra of TLEs. *J. Geophys. Res. (Space Phys)*, **117**, A05329. xxxvii, 219, 233, 234, 282, 285

GREEN, B.D., FRASER, M.E., RAWLINS, W.T., JEONG, L., BLUMBERG, W.A.M., MENDE, S.B., SWENSON, G.R., HAMPTON, D.L., WESCOTT, E.M. & SENTMAN, D.D. (1996). Molecular excitation in sprites. *Geophys. Res. Lett.*, **23**, 2161. 25

GRIEM, H.R. (1974). *Spectral Line Broadening by Plasmas*. Academic Press, New York. xxxix, 226

HALLINAN, T.J., STENBAEK-NIELSEN, H.C. & DEEHR, C.S. (1985). Enhanced aurora. *J. Geophys. Res.*, **90**, 8461–8475. 24, 31, 246

HAMPTON, D.L., HEAVNER, M.J., WESCOTT, E.M. & SENTMAN, D.D. (1996). Optical spectral characteristics of sprites. *Geophys. Res. Lett.*, **23**, 89. 23, 24, 35, 245, 276

HARDMAN, S.F., DOWDEN, R.L., BRUNDELL, J.B., BAHR, J.L., KAWASAKI, Z.I. & RODGER, C.J. (2000). Sprite observations in the Northern Territory of Australia. *J. Geophys. Res.*, **105**, 4689. 11

HAUCHECORNE, A., CHANIN, M.L. & KECKHUT, P. (1991). Climatology and trends of the middle atmospheric temperature (33 - 87 km) as seen by rayleigh lidar over the south of France. *J. Geophys. Res.*, **96**, 15297–15309. xl, 279

HEAVNER, M.J. (2000). *Optical Spectroscopic Observations of Sprites, Blue Jets, and Elves: Inferred Microphysical Processes and their Macrophysical Implications*. Ph.D. thesis, University of Alaska Fairbanks. 23, 26

HEAVNER, M.J., MORRILL, J.S., SIEFRING, C., SENTMAN, D.D., MOUDRY, D.R., WESCOTT, E.M. & BUCSELA, E.J. (2010). Near-ultraviolet and blue spectral observations of sprites in the 320-460 nm region: $N_2$ (2PG) emissions. *J. Geophys. Res. (Space Phys)*, **115**, A00E44. 26, 245

HERZBERG, G. (1950). *Molecular Spectra and Molecular Structure I. Spectra of Diatomic Molecules*. Van Nostrand Reinhold Co., New York, USA. 70, 287

HOESS, P. & FLEDER, K. (2000). Time Integrated Phosphor Behavior in Gated Image Intensifier Tubes. *Proc. SPIE*, **4128**, 23–28. 78, 95

HOVENIER, J.W., VAN DER MEE, C.V.M. & DOMKE, H. (2004). *Transfer of Polarized Light in Planetary Atmospheres*. Springer. 146

HU, W., CUMMER, S.A., LYONS, W.A. & NELSON, T.E. (2002). Lightning charge moment changes for the initiation of sprites. *Geophys. Res. Lett.*, **29**, 1279. 14

HUANG, E., WILLIAMS, E., BOLDI, R., HECKMAN, S., LYONS, W., TAYLOR, M., NELSON, T. & WONG, C. (1999). Criteria for sprites and elves based on Schumann resonance observations. *J. Geophys. Res.*, **104**, 16943. 14

INAN, U.S. (1990). VLF heating of the lower ionosphere. *Geophys. Res. Lett.*, **17**, 729732. 16

INAN, U.S., BELL, T.F. & RODRIGUEZ, J.V. (1991). Heating and ionization of the lower ionosphere by lightning. *Geophys. Res. Lett.*, **18**, 705–708. 16

IOPTRON (2010). GoToNovaTM 8401 Hand Controller Instruction Manual. [Online; accessed 13-March-2017]. 161

JENNISKENS, P. (2006). *Meteor Showers and their Parent Comets*. Cambridge University Press. 227, 242

JENNISKENS, P. (2007). Quantitative meteor spectroscopy: Elemental abundances. *Advances in Space Research*, **39**, 491–512. 227

JENNISKENS, P., LACEY, M., ALLAN, B.J., SELF, D.E. & PLANE, J.M.C. (1998). Feo "orange arc" emission detected in optical spectrum of leonid persistent train. *Earth, Moon, and Planets*, **82**, 429–438. 227

JING, Y., XIUSHU, Q., GUANGSHU, Z., YANG, Z. & TONG, Z. (2008). Red sprites over thunderstorms in the coast of shandong province, china. *Chinese Science Bulletin*, **53**, 1079–1086. 11

KANMAE, T. (2014). *Spectroscopic study of sprites*. Ph.D. thesis, University of Alaska. xvii, 71

KANMAE, T., STENBAEK-NIELSEN, H.C. & MCHARG, M.G. (2007). Altitude resolved sprite spectra with 3 ms temporal resolution. *Geophys. Res. Lett.*, **34**, L07810. xxx, xxxi, xxxvii, 23, 30, 35, 245, 250, 252, 256, 258, 276, 282, 285

KANMAE, T., STENBAEK-NIELSEN, H.C., MCHARG, M.G. & HAALAND, R.K. (2010a). Observation of blue sprite spectra at 10,000 fps. *Geophys. Res. Lett.*, **37**, L13808. 23, 30, 246

KANMAE, T., STENBAEK-NIELSEN, H.C., MCHARG, M.G. & HAALAND, R.K. (2010b). Observation of sprite streamer head's spectra at 10,000 fps. *J. Geophys. Res. (Space Phys)*, **115**, A00E48. 30, 246

KELLER, D. (1977). Bernard Vonnegut in his office at the University at Albany 1977. University of Albany, State University of New York. xiii, 3

# REFERENCES

Kramida, A., Ralchenko, Y., Reader, J. & and NIST ASD Team (2015). NIST Atomic Spectra Database (ver. 5.3), [Online]. Available: http://physics.nist.gov/asd [2016, November 25]. National Institute of Standards and Technology, Gaithersburg, MD. 85, 106, 234

Krehbiel, P.R., Riousset, J.A., Pasko, V.P., Thomas, R.J., Rison, W., Stanley, M.A. & Edens, H.E. (2008). Upward electrical discharges from thunderstorms. *Nature Geoscience*, **1**, 233. 19

Kuo, C.L., Chen, A.B., Chou, J.K., Y Tsai, L., Hsu, R.R., Su, H.T., Frey, H.U., Mende, S.B., Takahashi, Y. & Lee, L.C. (2008). Radiative emission and energy deposition in transient luminous events. *J. Phys. D*, **41**, 234014. 13, 15, 17

Kuo, C.L., Chang, S.C., Lee, L.J., Huang, T.Y., Chen, A.B., Su, H.T., Hsu, R.R., Sentman, D.D., Frey, H.U., Mende, S.B., Takahashi, Y. & Lee, L.C. (2011). The 762 nm emissions of sprites. *J. Geophys. Res. (Space Phys)*, **116**, A01310. a01310. 11

Kuo, C.L., Su, H.T. & Hsu, R.R. (2015). The blue luminous events observed by isual payload on board formosat-2 satellite. *J. Geophys. Res. (Space Phys)*, **120**, 9795–9804. 19

Lindblad, B.A. (1971a). A computerized stream search among 2401 photographic meteor orbits. *Smithson. Contrib. Astrophys.*, 14–24. 242

Lindblad, B.A. (1971b). A stream search among 865 precise photographic meteor orbits. *Smithson. Contrib. Astrophys.*, 1–13. 242

Liu, N. & Pasko, V.P. (2005). Molecular nitrogen LBH band system far-UV emissions of sprite streamers. *Geophys. Res. Lett.*, **32**, L05104. 25, 245

López-González, M.J., García-Comas, M., Rodríguez, E., López-Puertas, M., Shepherd, M.G., Shepherd, G.G., Sargoytchev, S., Aushev, V.M., Smith, S.M., Mlynczak, M.G., Russell, J.M., Brown, S., Cho, Y.M. & Wiens, R.H. (2007). Ground-based mesospheric temperatures at mid-latitude derived from {O2} and {OH} airglow {SATI} data: Comparison with {SABER} measurements. *Journal of Atmospheric and Solar-Terrestrial Physics*, **69**, 2379 – 2390, vertical Coupling in the Atmosphere/Ionosphere System3rd IAGA/ICMA Workshop. xxxvi, 280, 281

Luque, A. & Ebert, U. (2010). Sprites in varying air density: Charge conservation, glowing negative trails and changing velocity. *Geophys. Res. Lett.*, **37**, L06806. 280

Luque, A. & Gordillo-Vázquez, F.J. (2011). Modeling and analysis of $N_2(B^3\Pi_g)$ and $N_2(C^3\Pi_u)$ vibrational distributions in sprites. *J. Geophys. Res. (Space Phys)*, **116**, A02306. xxxvii, 282, 285

Lyons, W.A. (1993). A sensor system to monitor cloud-to-stratosphere electrical discharges. In *Final report, NASA contract NAS10-1194*. 10

Lyons, W.A. (1994). Characteristics of luminous structures in the stratosphere above thunderstorms as imaged by low-light video. *Geophys. Res. Lett.*, **21**, 875. 10

Lyons, W.A. (1996). Sprite observations above the U.S. High Plains in relation to their parent thunderstorm systems. *J. Geophys. Res.*, **101**, 29641. 14, 16

Lyons, W.A. & Armstrong, R.A. (2004). A review of electrical and turbulence effects of convective storms on the overlying stratosphere and mesosphere. In *AMS Symposium on Space Weather - Annual Meeting, Boston, American Meteorological Society.*. 7

Lyons, W.A. & Williams, E.R. (1993). Preliminary investigations of the phenomenology of cloud-to-stratospheric lightning discharges. In *Conf. Atmos. Elect., AMS*, St. Louis, MO. 10

Lyons, W.A., Nelson, T.E., Armstrong, R.A., Pasko, V. & Stanley, M.A. (2003a). Upward Electrical Discharges From Thunderstorm Tops. *Bulletin of the American Meteorological Society*, **84**, 445–454. 7

Lyons, W.A., Nelson, T.E., Williams, E.R., Cummer, S.A. & Stanley, M.A. (2003b). Characteristics of Sprite-Producing Positive Cloud-to-Ground Lightning during the 19 July 2000 STEPS Mesoscale Convective Systems. *Monthly Weather Review*, **131**, 2417. xiv, 21, 22

Mackenzie, T. & Toynbee, H. (1886). Meteorogical Phenomena. *Nature*, **33**, 245. 2, 17

Madiedo, J.M. (2014). Robotic systems for the determination of the composition of solar system materials by means of fireball spectroscopy. *Earth Moon and Planets*, **66**, 70–79. 228

Madiedo, J.M. (2015). The $\rho$-Geminid meteoroid stream: orbits, spectroscopic data and implications for its parent body. *Monthly Notices of the Royal Astronomical Society*, **448**, 2135–2140. 227

Madiedo, J.M. & Trigo-Rodríguez, J.M. (2008). Multistation Video Orbits of Minor Meteor Showers. *Earth Moon and Planets*, **102**, 133–139. 228

Madiedo, J.M., Trigo-Rodríguez, J.M., Konovalova, N., Williams, I.P., Castro-Tirado, A.J., Ortiz, J.L. & Cabrera-Caño, J. (2013a). The 2011 October Draconids outburst – II. Meteoroid chemical abundances from fireball spectroscopy. *Monthly Notices of the Royal Astronomical Society*, **433**, 571–580. 227

MADIEDO, J.M., TRIGO-RODRÍGUEZ, J.M., LYYTINEN, E., DERGHAM, J., PUJOLS, P., ORTIZ, J.L. & CABRERA-CAÑO, J. (2013b). On the activity of the γ-Ursae Minorids meteoroid stream in 2010 and 2011. *Monthly Notices of the Royal Astronomical Society*, **431(2)**, 1678–1685. 227

MADIEDO, J.M., TRIGO-RODRÍGUEZ, J.M., WILLIAMS, I.P., ORTIZ, J.L. & CABRERA-CAÑO, J. (2013c). The Northern χ-Orionid meteoroid stream and possible association with the potentially hazardous asteroid 2008XM1. *Monthly Notices of the Royal Astronomical Society*, **431**, 2464–2470. 227, 228

MALAN, D.J. (1937). Sur les Decharges Orageuses dans la Haute Atmosphère. *C. R. Acad. Sci.*, **205**, 812–813. 2

MARSH, D.R., MILLS, M.J., KINNISON, D.E., LAMARQUE, J.F., CALVO, N. & POLVANI, L.M. (2013). Climate change from 1850 to 2005 simulated in CESM1(WACCM). *Journal of Climate*, **26(19)**, 7372–7391. 240

MARSHALL, R.A., DA SILVA, C.L. & PASKO, V. (2015). Elve doublets and compact intracloud discharges. *Geophys. Res. Lett*, **42**, 61126119. 17

MENDE, S., FREY, H., HSU, R.R., SU, H.T., CHEN, A., LEE, L.C., FUKUNISHI, H. & TAKAHASHI, Y. (2004). . In *EOS Trans. Am. Geophys. Union 85 (Fall Meet. Suppl.)*. 28

MENDE, S.B., RAIRDEN, R.L., SWENSON, G.R. & LYONS, W.A. (1995). Sprite spectra; N₂ 1 PG band identification. *Geophys. Res. Lett.*, **22**, 2633. 23, 24, 35, 70, 245, 276

MENDE, S.B., CHANG, Y.S., CHEN, A.B., FREY, H.U., FUKUNISHI, H., GELLER, S.P., HARRIS, S., HEETDERKS, H., HSU, R.R., LEE, L.C., SU, H.T. & TAKAHASHI, Y. (2006). *Spacecraft Based Studies of Transient Luminous Events*, vol. 225 of *NATO Science Series II: Mathematics, Physics and Chemistry*. Springer Netherlands. 28

METEORAGE (2017). Meteorage, Lightning Information and Solutions. [Online; accessed 13-March-2017]. 171

MILLER, M. (1987). *in Inductively Coupled Plasmas in Analytical Atomic Spectrometry*. VCH, New York. 225

MISHCHENKO, M., HOVENIER, J.W. & TRAVIS, L. (2000). *Light Scattering by Nonspherical Particles*. Elsevier. 120, 122, 123

MONTANYÀ, J., VAN DER VELDE, O., ROMERO, D., MARCH, V., SOLÀ, G., PINEDA, N., ARRAYÁS, M., TRUEBA, J.L., REGLERO, V. & SOULA, S. (2010). High-speed intensified video recordings of sprites and elves over the western mediterranean sea during winter thunderstorms. *J. Geophys. Res. (Space Phys)*, **115**, n/a–n/a, a00E18. xiv, 12, 13

MORRILL, J., BUCSELA, E., SIEFRING, C., HEAVNER, M., BERG, S., MOUDRY, D., SLINKER, S., FERNSLER, R., WESCOTT, E., SENTMAN, D. & OSBORNE, D. (2002). Electron energy and electric field estimates in sprites derived from ionized and neutral N₂ emissions. *Geophys. Res. Lett.*, **29**, 1462. 23, 26

MORRILL, J.S., BUCSELA, E.J., PASKO, V.P., BERG, S.L., HEAVNER, M.J., MOUDRY, D.R., BENESCH, W.M., WESCOTT, E.M. & SENTMAN, D.D. (1998). Time resolved N₂ triplet state vibrational populations and emissions associated with red sprites. *J. Atm. Sol.-Terr. Phys.*, **60**, 811. 23, 25, 245

MYOKEI, K., MATSUDO, Y., ASANO, T., SUZUKI, T., HOBARA, Y., MICHIMOTO, K. & HAYAKAWA, M. (2009). A study of the morphology of winter sprites in the Hokuriku area of Japan in relation to cloud charge height. *J. Atm. Sol.-Terr. Phys.*, **71**, 597. 11

NEMZEK, R.J. & WINKLER, J.R. (1989). Observation and Interpretation of Fast Sub-visual Light Pulses from the Night Sky. *Geophys. Res. Lett.*, **16, 9**, 10151018. xiii, 4, 31, 36, 116

NEUBERT, T., RYCROFT, M., FARGES, T., BLANC, E., CHANRION, O., ARNONE, E., ODZIMEK, A., ARNOLD, N., ENELL, C.F., TURUNEN, E., BÖSINGER, T., MIKA, Á., HALDOUPIS, C., STEINER, R.J., VAN DER VELDE, O., SOULA, S., BERG, P., BOBERG, F., THEJLL, P., CHRISTIANSEN, B., IGNACCOLO, M., FÜLLEKRUG, M., VERRONEN, P.T., MONTANYA, J. & CROSBY, N. (2008). Recent Results from Studies of Electric Discharges in the Mesosphere. *Surveys in Geophysics*, 14. 11

OFFROY, M., FARGES, T., GAILLARD, P., KUO, C.L., CHEN, A.B., HSU, R. & TAKAHASHI, Y. (2015). Multivariate analysis of dim elves from isual observations. *Journal of Geophysical Research: Atmospheres*, **120**, 7454–7466, 2014JD023012. 13, 15

ORVILLE, R.E. (1968). Spectrum of the lightning stepped leader. *J. Geophys. Res.*, **73**, 6999–7008. 222

ORVILLE, R.E. & SALANAVE, L.E. (1970). Lightning Spectroscopy–Photographic Techniques. *Appl. Opt.*, **9**, 1775–1781. 222

PARRA-ROJAS, F.C., LUQUE, A. & GORDILLO-VÁZQUEZ, F.J. (2013a). Chemical and electrical impact of lightning on the Earth mesosphere: The case of sprite halos. *J. Geophys. Res.*, **118**, 1–25. 70

PARRA-ROJAS, F.C., PASSAS, M., CARRASCO, E., LUQUE, A., TANARRO, I., SIMEK, M. & GORDILLO-VÁZQUEZ, F.J. (2013b). Spectroscopic diagnostics of laboratory air plasmas as a benchmark for spectral rotational (gas) temperature determination in TLEs. *J. Geophys. Res.*, **118**, 4649–4661. 36, 37, 73, 229, 234, 246, 247, 287, 294, 295, 300

PARRA-ROJAS, F.C., LUQUE, A. & GORDILLO-VÁZQUEZ, F.J. (2015). Chemical and thermal impact of sprite streamers in the Earth mesosphere. *Submitted to J. Geophys. Res.*. 280

PASKO, V.P. (2008). Blue jets and gigantic jets: transient luminous events between thunderstorm tops and the lower ionosphere. *Plasma Phys. Controlled Fusion*, **50**, 124050. 19

PASKO, V.P. (2010). Recent advances in theory of transient luminous events. *J. Geophys. Res. (Space Phys)*, **115**, A00E35. 8

PASKO, V.P., INAN, U.S. & BELL, T.F. (1998). Spatial structure of sprites. *Geophys. Res. Lett.*, **25**, 2123. 219

PASKO, V.P., STANLEY, M.A., MATHEWS, J.D., INAN, U.S. & WOOD, T.G. (2002). Electrical discharge from a thundercloud top to the lower ionosphere. *Nature*, **416**, 152–154. xiv, 20, 21

PASSAS, M., SÁNCHEZ, J., PARRA-ROJAS, F.C., LUQUE, A. & GORDILLO-VÁZQUEZ, F.J. (2011). Diseño e implementación de un instrumento de diagnosis de plasmas debidos a eventos luminosos transitorios en la mesosfera terrestre. In *XXXIII Reunión Bienal de la Real Sociedad Española de Física*, vol. IV, 76. 72

PASSAS, M., SÁNCHEZ, J., LUQUE, A. & GORDILLO-VÁZQUEZ, F.J. (2014). Transient Upper Atmospheric Plasmas: Sprites and Halos. *IEEE Transactions on Plasma Science*, **42**. xxvii, 11, 217, 218, 220, 229, 246, 295, 300

PASSAS, M., MADIEDO, J.M. & GORDILLO-VÁZQUEZ, F.J. (2016a). High resolution spectroscopy of an Orionid meteor from 700 to 800 nm. *Icarus*, **266**, 134–141. 74, 227, 246, 296, 301

PASSAS, M., SÁNCHEZ, J., SÁNCHEZ-BLANCO, E., LUQUE, A. & GORDILLO-VÁZQUEZ, F.J. (2016b). GRASSP: a spectrograph for the study of transient luminous events. *Appl. Opt.*, **55**, 6436–6442. 79, 246, 287

QUINTEN, M. (2012). *A Practical Guide to Optical Metrology for Thin Films*. Wiley. 93

REMSBERG, E.E., MARSHALL, B.T., GARCÍA-COMAS, M., KRUEGER, D., LINGENFELSER, G.S., MARTIN-TORRES, J., MLYNCZAK, M.G., RUSSELL, J.M., SMITH, A.K., ZHAO, Y., BROWN, C., GORDLEY, L.L., LÓPEZ-GONZÁLEZ, M.J., LÓPEZ-PUERTAS, M., SHE, C.Y., TAYLOR, M.J. & THOMPSON, R.E. (2008). Assessment of the quality of the Version 1.07 temperature-versus-pressure profiles of the middle atmosphere from TIMED/SABER. *Journal of Geophysical Research: Atmospheres*, **113**, n/a–n/a, d17101. 279

SÃO SABBAS, F.T., TAYLOR, M.J., PAUTET, P.D., BAILEY, M., CUMMER, S., AZAMBUJA, R.R., SANTIAGO, J.P.C., THOMAS, J.N., PINTO, O., SOLORZANO, N.N., SCHUCH, N.J., FREITAS, S.R., FERREIRA, N.J. & CONFORTE, J.C. (2010). Observations of prolific transient luminous event production above a mesoscale convective system in argentina during the sprite2006 campaign in brazil. *J. Geophys. Res. (Space Phys)*, **115**, n/a–n/a, a00E58. 11

SALANAVE, L.E. (1961). The Optical Spectrum of Lightning. *Science*, **134**, 1395–1399. 222

SENTMAN, D.D. & WESCOTT (1994). *Red sprites and blue jets*. University of Alaska, Fairbanks, Alaska Univ. College Geophysical Inst. 6, 10, 69

SENTMAN, D.D. & WESCOTT, E.M. (1993). Observations of upper atmospheric optical flashes recorded from an aircraft. *Geophys. Res. Lett.*, **20**, 2857. 10

SENTMAN, D.D., WESCOTT, E.M., OSBORNE, D.L., HAMPTON, D.L. & HEAVNER, M.J. (1995). Preliminary results from the Sprites94 aircraft campaign: 1. Red sprites. *Geophys. Res. Lett.*, **22**, 1205. 10, 11, 25

SENTMAN, D.D., STENBAEK-NIELSEN, H.C., McHARG, M.G. & MORRILL, J.S. (2008). Plasma chemistry of sprite streamers. *J. Geophys. Res. (Atmos.)*, **113**, D11112. 280

SIEFRING, C.L., MORRILL, J.S., SENTMAN, D.D. & HEAVNER, M.J. (2010). Simultaneous near-infrared and visible observations of sprites and acoustic-gravity waves during the EXL98 campaign. *J. Geophys. Res. (Space Phys)*, **115**, A00E57. xiv, 27

SIMEK, M. (1994). On the use of the numerical simulations of the first positive system of $N_2$: III. numerical thermometer on (v',0) bands, v' = 0-3. *Research Report IPPCZ-345*, 1–31. 250, 288

SIMEK, M. & DEBENEDICTIS, S. (1995). On the use of the numerical simulation of the first positive system of $n_2$: Ii. fast $t_{rot}$ estimation from the partially resolved (3,0) band. *Plasma Chem. Plasma Proc.*, **15**, 451–463. 36, 70, 288

SONOTACO (2017). UFO Capture, software for unknown universe. [Online; accessed 13-March-2017]. xxiv, 188

SOULA, S., VAN DER VELDE, O., MONTANYÀ, J., HUET, P., BARTHE, C. & BÓR, J. (2011). Gigantic jets produced by an isolated tropical thunderstorm near Réunion Island. *J. Geophys. Res.*, **116**, D19103. 20

SOUTHWORTH, Z. & HAWKINS, R.E. (1963). Statistics of meteor streams. *Smithsonian Contributions to Astrophysics*, **7**, 261. 242

STENBAEK-NIELSEN, H.C., McHARG, M.G., KANMAE, T. & SENTMAN, D.D. (2007). Observed emission rates in sprite streamer heads. *Geophys. Res. Lett.*, **34**, L11105. 25, 245

STOKES, G.G. (1851). On the composition and resolution of streams of polarized light from different sources. *Transactions of the Cambridge Philosophical Society*, **IX**, 399. 118

SU, H.T., HSU, R.R., CHEN, A.B.C., LEE, Y.J. & LEE, L.C. (2002). Observation of sprites over the Asian continent and over oceans around Taiwan. *Geophys. Res. Lett.*, **29**, 1044. 11

Su, H.T., Hsu, R.R., Chen, A.B., Wang, Y.C., Hsiao, W.S., Lai, W.C., Lee, L.C., Sato, M. & Fukunishi, H. (2003). Gigantic jets between a thundercloud and the ionosphere. *Nature*, **423**, 974. 20

Suszcynsky, D.M., Roussel-Dupré, R., Lyons, W.A. & Armstrong, R.A. (1998). Blue-light imagery and photometry of sprites. *J. Atm. Sol.-Terr. Phys.*, **60**, 801. 23, 26

Suzuki, T., Hayakawa, M., Hobara, Y. & Kusunoki, K. (2012). First detection of summer blue jets and starters over northern kanto area of japan: Lightning activity. *Journal of Geophysical Research: Space Physics*, **117**, n/a–n/a, a07307. 19

Trigo-Rodríguez, J.M., Madiedo, J.M., Williams, I.P. & Castro-Tirado, A.J. (2009a). The outburst of the κ Cygnids in 2007: clues about the catastrophic break up of a comet to produce an Earth-crossing meteoroid stream. *Monthly Notices of the Royal Astronomical Society*, **392**, 367–375. 227

Trigo-Rodríguez, J.M., Madiedo, J.M., Williams, I.P., Castro-Tirado, A.J., Llorca, J., Vitek, S. & Jelinek, M. (2009b). Observations of a very bright fireball and its likely link with comet C/1919 Q2 Metcalf. *Monthly Notices of the Royal Astronomical Society*, **394**, 569–576. 228

van der Velde, O.A. & Montanyà, J. (2016). Statistics and variability of the altitude of elves. *Geophysical Research Letters*, **43**, 5467–5474, 2016GL068719. xxxviii, 17, 289, 292

van der Velde, O.A., Lyons, W.A., Nelson, T.E., Cummer, S.A., Li, J. & Bunnell, J. (2007). Analysis of the first gigantic jet recorded over continental North America. *J. Geophys. Res. (Atmos.)*, **112**, D20104. 20

Vaughan, O.H. (2017). Otha H. Vaughan's facebook profile. xiii, 4

Vaughan Jr., O.H. (1993a). MSFC Shuttle Lightning Research. In *31th AIAA Aerospace Sciences Meeting*, AIAA–93–0853, St. Louis, MO. 6, 10

Vaughan Jr., O.H. (1993b). Observations of nocturnal thunderstorms and lightning displays as seen during recent space shuttle missions. In *AMS Severe Storms Conf.*, AIAA–93–0853, St. Louis, MO. 6, 10

Vaughan Jr., O.H. (1994a). Observations of Nocturnal Thunderstorms and Lightning Displays as Seen During Recent Space Shuttle Missions. In *Preprints, Fifth Symposium on Global Change Studies, AMS*, 355–359, Nashville TN. 6

Vaughan Jr., O.H. (1994b). Observations of Nocturnal Thunderstorms and Lightning Displays as Seen During Recent Space Shuttle Missions. In *32nd AIAA Aerospace Sciences Meeting, Reno NV*, AAIA–94–0480, Reno NV. 6

Vaughan Jr., O.H. & Vonnegut, B. (1989). Recent observations of lightning discharges from the top of a thundercloud into the air above. *J. Geophys. Res.*, **94 D11**, 13,179–13,182. 3

Vaughan Jr., O.H., Blakeslee, R.J., Boeck, W.L., Vonnegut, B., Brook, M. & McKune Jr., J. (1992). A Cloud to Space Lightning as Recorded by the Space Shuttle Payload Bay TV Cameras. *Mon. Weath. Rev.*, **120**, 1459. 6, 10

Vonnegut, B. & Atkinson, B.M. (1958). Motion-picture lapse photography from high altitude balloons. *J. Meteor.*, **15**, 232–234. 3

Vonnegut, B., Vaughan Jr., O.H. & Brook, M. (1989). Nocturnal photographs taken from a U-2 airplane looking down on top of clouds illuminated by lightning. *Bull. Amer. Meteor. Soc.*, **70, 10**, 1263–1271. 3

Walker, T.D. (2015). *A 21st Century Investigation of the Lightning Spectrum*. Ph.D. thesis, School of Graduate Studies of the University of Alabama in Huntsville, U.S.A. 222, 226

Wallace, L. (1964). The Spectrum of Lightning. *Astrophysical Journal*, **139**, 994. 222

Wescott, E.M., Sentman, D., Osborne, D., Hampton, D. & Heavner, M. (1995). Preliminary results from the Sprites94 aircraft campaign: 2. Blue jets. *Geophys. Res. Lett.*, **22**, 1209. xiv, 10, 18, 19

Wescott, E.M., Sentman, D.D., Heavner, M.J., Hampton, D.L., Osborne, D.L. & Vaughan, O.H. (1996). Blue starters: Brief upward discharges from an intense Arkansas thunderstorm. *Geophys. Res. Lett.*, **23**, 2153. xiv, 19, 20

Wescott, E.M., Sentman, D.D., Heavner, M.J., Hampton, D.L., Lyons, W.A. & Nelson, T. (1998). Observations of 'Columniform' sprites. *J. Atm. Sol.-Terr. Phys.*, **60**, 733. 25

Wescott, E.M., Sentman, D.D., Stenbaek-Nielsen, H.C., Huet, P., Heavner, M.J. & Moudry, D.R. (2001a). New evidence for the brightness and ionization of blue starters and blue jets. *J. Geophys. Res.*, **106**, 21549. 18, 26

Wescott, E.M., Stenbaek-Nielsen, H.C., Sentman, D.D., Heavner, M.J., Moudry, D.R. & Sabbas, F.T.S. (2001b). Triangulation of sprites, associated halos and their possible relation to causative lightning and micrometeors. *J. Geophys. Res.*, **106**, 10467. 15, 26

Wescott, L.W., Wescott, E.M., Stenbaek-Nielsen, H.C., Sentman, D.D., Moudry, D.R., Heavner, M.J. & Sao Sabbas, F.T. (1999). Triangulation of sprites and elves from the nasa 1999 sprites balloon campaign. *EOS Supplement*, **80**, F216. 15

Whiting, E.E. (1968). An empirical approximation to the Voigt profile. *J. Quant. Spectros. and Radiat. Transf.*, **8**, 1379–1384. 225

# REFERENCES

WILLIAMS, E.R. (1998). The positive charge reservoir for sprite-producing lightning. *J. Atm. Sol.-Terr. Phys.*, **60**, 689. 14

WILLIAMS, E.R., LYONS, W.A., HOBARA, Y., MUSHTAK, V.C., ASENCIO, N., BOLDI, R., BR, J., CUMMER, S.A., GREENBERG, E., HAYAKAWA, M., HOLZWORTH, R.H., KOTRONI, V., LI, J., MORALES, C., NELSON, T.E., PRICE, C., RUSSELL, B., SATO, M., STORI, G., SHIRAHATA, K., TAKAHASHI, Y. & YAMASHITA, K. (2010). Ground-based detection of sprites and their parent lightning flashes over africa during the 2006 amma campaign. *Quarterly Journal of the Royal Meteorological Society*, **136**, 257–271. 11

WILLIAMS, I.P. (2011). The origin and evolution of meteor showers and meteoroid streams. *Astronomy and Geophysics*, **52**, 2.20–2.26. 242

WILSON, C.T.R. (1925). The electric field of a thundercloud and some of its effects. *Proc. Phys. Soc. London*, **37**, 32D. 2, 3

WILSON, C.T.R. (1956). A Theory of Thundercloud Electricity. *Proc. R. Meteorol. Soc. London*, **236**, 297–317. 5

WINCKLER, J.R., FRANZ, R.C. & NEMZEK, R.J. (1993). Fast Low-Level Light Pulses From the Night Sky Observed With the SKYFLASH Program. *J. Geophys. Res.*, **98**, 8775–8783. 31, 36, 116

YAIR, Y., ISRAELEVICH, P., DEVIR, A.D., MOALEM, M., PRICE, C., JOSEPH, J.H., LEVIN, Z., ZIV, B., STERNLIEB, A. & TELLER, A. (2004). New observations of sprites from the space shuttle. *J. Geophys. Res. (Atmos.)*, **109**, D15201. 11

YAIR, Y., PRICE, C., GANOT, M., GREENBERG, E., YANIV, R., ZIV, B., SHEREZ, Y., DEVIR, A., BR, J. & STORI, G. (2009). Optical observations of transient luminous events associated with winter thunderstorms near the coast of israel. *Atmospheric Research*, **91**, 529–537. 11

YANG, J. & FENG, G. (2012). A gigantic jet event observed over a thunderstorm in mainland china. *Chinese Science Bulletin*, **57**, 4791–4800. 20

# Declaration

I herewith declare that I have produced this thesis without the prohibited assistance of third parties and without making use of aids other than those specified; notions taken over directly or indirectly from other sources have been identified as such. This thesis has not previously been presented in identical or similar form to any other Spanish or foreign examination board.

The thesis work was conducted from 2010 to 2017 under the supervision of Dr. Francisco J. Gordillo Vázquez and Dr. Alejandro Luque Estepa.

Granada, May 17, 2017

**REFERENCES**

# Curriculum Vitae

## Personal information

Date of birth:  12th March 1980

Place of birth: Granada, Spain

## Education and employment

2010-2017:  Software Engineer at the Instituto de Astrofísica de
            Andalucía (IAA-CSIC)
            Granada, Spain

2008-2009:  M. Sc. degree in Physics and Physical Technologies
            at the University of Cantabria, Santander, Spain
            Dissertation: "Desarrollo de un Sistema de Diagno-
            sis de Turbulencia con Sonda Langmuir–Mach móvil"

2007-2009:  Research fellow at University of Cantabria, Santander,
            Spain
            Title: "Mecanismos del Transporte Turbulento en
            Plasmas Confinados Magnéticamente y su Descripción
            Probabilística"

1998-2006: Telecommunication Engineer at the Higher Technical School of Engineering of Seville, Spain

Final Project: "Infraestructura de Telecomunicaciones para Alojamientos Universitarios en el Campus del Carmen en Huelva"

# Short stays

Oct. 2008 - Dec. 2008:  Asociación EURATOM/CIEMAT para
la Fusión, Madrid, Spain
Project: "Diseño e instalación de sistemas ópticos para la posterior captura de imágenes del plasma en TJ-II con cámaras rápidas y redacción de tesis de máster"

Dec. 2007 - Dec. 2007:  Asociación EURATOM/CIEMAT para
la Fusión, Madrid, Spain
Project: "Control remoto de cámaras rápidas para tratamiento digital de imágenes de turbulencias en plasmas"

# Participation in publicly financed R&D projects

Mar. 2017 - Feb. 2021:  Instituto de Astrofísica de Andalucía (IAA-CSIC), Granada, Spain
Title: "Science and Innovation with Thunderstorms (SAINT)"
Funding Entity: "H2020-MSCA-ITN-2016 (Marie Curie Innovative Training Networks – ITN"

Jan. 2016 - Dec. 2018:  Instituto de Astrofísica de Andalucía (IAA-CSIC), Granada, Spain
Title: "Contribución del IAA a la explotación científica de ASIM"
Funding Entity: "ESP2015-69909-C5-2-MINECO"

Jan. 2014 - Dec. 2016:  Instituto de Astrofísica de Andalucía (IAA-CSIC), Granada, Spain
Title: "Atmospheric Space Interactions Monitor (ASIM). FM Manufacturing and Scientific Return: The IAA contribution"
Funding Entity: "ESP2013-48032-C5-5-R"

Jan. 2012 - Dec. 2014:  Instituto de Astrofísica de Andalucía (IAA-CSIC), Granada, Spain
Title: "Atmospheric Space Interactions Monitor (ASIM): The IAA contribution"
Funding Entity: "AYA2011-29936-546-C05-02-MINECO"

May 2011 - Jun. 2016:  Thunderstorm Effects in the Atmosphere–Ionosphere System (TEA–IS) Network

Title: "Severe thunderstorm processes and their effects on the atmosphere–ionosphere system (TEA–IS)"
Reference: 09-RNP-101 European Science Foundation (ESF) Research Networking Programmes

Mar. 2011 - Mar. 2015: Instituto de Astrofísica de Andalucía (IAA-CSIC), Granada, Spain
Title: "Modelización y espectroscopía de sprites: impacto en la naturaleza química y eléctrica de la atmósfera terrestre"
Reference: FQM–5965

Jun. 2010 - Dec. 2011: Instituto de Astrofísica de Andalucía (IAA-CSIC), Granada, Spain
Title: "Atmospheric Space Interactions Monitor (ASIM): The IAA contribution"
Funding Entity: "AYA2009-14027-C05-02-MICINN"

Jan. 2007 - Aug. 2009: Universidad de Cantabria, Santander, Spain
Title: "Mecanismos del Transporte Turbulento en Plasmas Confinados Magnéticamente y su Descripción Probabilística"
Funding Entity: "ENE2006-15244-C03-03"

# REFERENCES

# Publications

## Journal papers

- Gordillo-Vázquez F. J., **Passas M.**, Luque A. and Sánchez del Río J., Van der Velde, O. and Montanyá, J. , *High spectral resolution spectroscopy of sprites: A natural probe of the mesosphere*, Nature Communications (submitted)

- **Passas M.**, Sánchez del Río J., Sánchez-Blanco E., Luque A. and Gordillo-Vázquez F. J., *GRASSP: a spectrograph for the study of transient luminous events*, Applied Optics, 55, 23, 6436-6442, doi: 10.1364/AO.55.006436, 2016

- **Passas M.**, Madiedo J. M. and Gordillo-Vázquez F. J., *High resolution spectroscopy of an Orionid meteor from 700 to 800 nm*, Icarus, 266, 134-141, doi: 10.1016/j.icarus.2015.11.020, 2016

- **Passas M.**, Sánchez del Río J., Luque A. and Gordillo-Vázquez F. J., *Transient Upper Atmospheric Plasmas: Sprites and Halos*, IEEE Transactions on Plasma Science, Vol. 42, 134-141, doi: 10.1109/ /TPS.2014.2329320, 2014

- Parra-Rojas F. C., **Passas M.**, Carrasco E., Luque A., Tanarro I., Simek M. and Gordillo-Vázquez F. J., *Spectroscopy diagnostics of laboratory air plasmas as a benchmark for spectral rotational (gas) temperature determination in TLEs*, J. Geophys. Res. - Space Physics, 118, 4649-4661, doi: 10.1002/jgra.50433, 2013

## Conference proceedings

- **Passas M.**, Gordillo-Vázquez F. J., Luque A., Sánchez del Río J., Van der Velde O. and Montanyá J., *Espectroscopía de alta resolución de TLEs como sonda natural de la mesosfera*, XXXVI Reunión Bienal de la Real Sociedad Española de Física, Santiago de Compostela, España, 2017 [poster presentation + conference proceedings]

- **Passas M.**, Sánchez del Río J., Pérez-Invernón F. J., Luque A. and Gordillo-Vázquez F. J., Van der Velde O., Montanyá J., *GRASSP instrument: First high resolution spectra of TLEs in Europe*, Final TEA-IS international conference, Copenhague, Denmark, 2016

- **Passas M.**, Sánchez del Río J., Parra-Rojas F. C., Luque A. and Gordillo-Vázquez F. J., *GRASSP Instrument Status and First Results*, 2nd. TEA-IS summer school, Collioure, France, 2014

- **Passas M.**, Sánchez del Río J., Parra-Rojas F. C., Luque A. and Gordillo-Vázquez F. J., *GRASSP (GRanada Sprite*

*Spectrograph and Polarimeter) design and implementation*, XXXI Int. Conf. Phenomena in ionized gases (ICPIG), Granada, Spain, 2013

- Parra-Rojas F.C., **Passas M.**, Carrasco E., Luque A., Tanarro I., Simek M. and Gordillo-Vázquez F.J., *Spectroscopy diagnostics of laboratory air plasmas as a benchmark for spectral rotational (gas) temperature determination in TLEs*, XXXI Int. Conf. Phenomena in ionized gases (ICPIG), Granada, Spain, 2013

- Parra-Rojas F.C., **Passas M.**, Carrasco E., Luque A., Tanarro I., Simek M. and Gordillo-Vázquez F.J., *Astrophysical, geophysical and other natural plasmas*, XXXI Int. Conf. Phenomena in ionized gases (ICPIG), Granada, Spain, 2013

- **Passas M.**, Sánchez del Río J., Parra-Rojas F. C., Luque A. and Gordillo-Vázquez F. J., *Diseño e implementación de un espectrógrafo y un polarímetro para la diagnosis de plasmas de aire producidos por eventos luminosos transitorios en la mesosfera terrestre*, III Encuentro sobre Ciencias Planetarias y Exploracin del Sistema Solar, Madrid Spain, 2013

- **Passas M.**, Sánchez del Río J., Parra-Rojas F. C., Luque A. and Gordillo-Vázquez F. J., *GRASSP (GRanada Sprite Spectrograph and Polarimeter) design and implementation*, European Geosciences Union General Assembly, Vienna, Austria, 2013

- **Passas M.**, Sánchez del Río J., Parra-Rojas F. C., Luque A. and Gordillo-Vázquez F. J., *Design and implementation of an automatic instrument to diagnose air plasmas produced by earth mesosphere transient luminous events*, 1st. TEA-IS summer school, Torremolinos, Spain, 2012

- Parra-Rojas F.C., **Passas M.**, Carrasco E., Luque A. Tanarro I., Simek M. and Gordillo-Vázquez F.J., *Diagnostics of hollow cathode low pressure air discharges as a tool for understanding Halo spectral features in the Earth mesosphere*, 1st. TEA-IS summer school, Torremolinos, Spain, 2012

- Parra-Rojas F.C., Luque A., **Passas M.** and Gordillo-Vázquez F.J., *Kinetics of $CO_2$ and nitrogen oxides in air plasmas produced by the action of sprites and halos in the Earth mesosphere*, 1st. TEA-IS summer school, Torremolinos, Spain, 2012

- **Passas M.**, Sánchez del Río J., Parra-Rojas F. C., Luque A. and Gordillo-Vázquez F. J., *Diseño e implementación de un espectrómetro para la diagnosis de plasmas de aire producidos por eventos luminosos transitorios en la mesosfera terrestre*, XXXIII Reunión Bienal de la Sociedad Española de Física, Santander, Spain, 2011

- Parra-Rojas F.C., **Passas M.**, Luque A. and Gordillo-Vázquez F.J., *Cinética de $CO_2$ en plasmas de aire producidos por la acción de Sprites y Halos en la mesosfera terrestre*, XXXIII Reunión Bienal de la Sociedad Española

de Física, Santander, Spain, 2011

- **Passas M.**, Castellanos O., Seníes J. M. and Anabitarte E., *Two-Dimensional Turbulence Analysis using High-Speed Visible Imaging in SLPM Plasmas*, 36th EPS Conference on Plasma Physics, Sofia, Bulgaria, 2009

- Anabitarte E., Castellanos O., **Passas M.**, and Sentíes J. M., *First experimental results of statistical properties of turbulence plasma fluctuations in the SLPM upgrade*, 35th EPS Conference on Plasma Physics, Hersonissos, Greece, 2008

## Others

- Gordillo-Vázquez F.J., Luque A., Parra-Rojas F.C. and **Passas M.**, *Plasmas en atmósferas planetarias*, Revista Española de Física, Vol. 35, pp. 3, 2011

# REFERENCES

# Presentations

## 2017

- **Passas M.**, Gordillo-Vázquez F. J., Luque A., Sánchez del Río J., Van der Velde O. and Montanyá J., *Espectroscopía de alta resolución de TLEs como sonda natural de la mesosfera*, XXXVI Reunión Bienal de la Real Sociedad Española de Física, Santiago de Compostela, España, 2017 [poster presentation + conference proceedings]

## 2016

- **Passas M.**, Sánchez del Río J., Pérez-Invernón F. J., Luque A., Gordillo-Vázquez F. J., Van der Velde O. and Montanyá J., *GRASSP instrument: First high resolution spectra of TLEs in Europe*, Final TEA-IS international conference, Copenhague, Denmark, 2016 [Oral + poster presentation + conference proceedings]

## 2014

- **Passas M.**, Sánchez del Río J., Parra-Rojas F. C., Luque A. and Gordillo-Vázquez F. J., *GRASSP Instrument Status*

*and First Results*, 2nd. TEA-IS summer school, Collioure, France, 2014 [Oral + poster presentation + conference proceedings]

## 2013

- **Passas M.**, Sánchez del Río J., Parra-Rojas F. C., Luque A. and Gordillo-Vázquez F. J., *GRASSP (GRanada Sprite Spectrograph and Polarimeter) design and implementation*, XXXI Int. Conf. Phenomena in ionized gases (ICPIG), Granada, Spain, 2013 [Oral + poster presentation + conference proceedings]

- **Passas M.**, Sánchez del Río J., Parra-Rojas F. C., Luque A. and Gordillo-Vázquez F. J., *Diseño e implementación de un espectrógrafo y un polarímetro para la diagnosis de plasmas de aire producidos por eventos luminosos transitorios en la mesosfera terrestre*, III Encuentro sobre Ciencias Planetarias y Exploracin del Sistema Solar, Madrid Spain, 2013 [Oral presentation + conference proceedings]

- **Passas M.**, Sánchez del Río J., Parra-Rojas F. C., Luque A. and Gordillo-Vázquez F. J., *GRASSP (GRanada Sprite Spectrograph and Polarimeter) design and implementation*, European Geosciences Union General Assembly, Vienna, Austria, 2013 [Poster presentation + conference proceedings]

## 2012

- **Passas M.**, Sánchez del Río J., Parra-Rojas F. C., Luque A. and Gordillo-Vázquez F. J., *Design and implementation of an automatic instrument to diagnose air plasmas produced by earth mesosphere transient luminous events*, 1st. TEA-IS summer school, Torremolinos, Spain, 2012 [Poster presentation + conference proceedings]

## 2011

- **Passas M.**, Sánchez del Río J., Parra-Rojas F. C., Luque A. and Gordillo-Vázquez F. J., *Diseño e implementación de un espectrómetro para la diagnosis de plasmas de aire producidos por eventos luminosos transitorios en la mesosfera terrestre*, XXXIII Reunión Bienal de la Sociedad Española de Física, Santander, Spain, 2011 [Poster presentation + conference proceedings]

## 2009

- **Passas M.**, Castellanos O., Seníes J. M. and Anabitarte E., *Two-Dimensional Turbulence Analysis using High-Speed Visible Imaging in SLPM Plasmas*, 36th EPS Conference on Plasma Physics, Sofia, Bulgaria, 2009 [Poster presentation + conference proceedings]